

Study of **EXPANDABLE,
TERMINAL DECELERATORS FOR
MARS ATMOSPHERE ENTRY**

By

**GOODYEAR AEROSPACE CORPORATION
AKRON, OHIO**

For

**JET PROPULSION LABORATORY
JPL CONTRACT NO. 951153**

**3 October 1966
Copy No. 26**

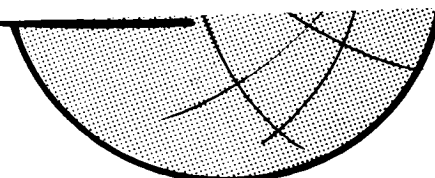
N67 12052
(ACCESSION NUMBER)
386
(PAGES)
CR-794/96
(NASA CR OR TMX OR AD NUMBER)

FACILITY FORM 3

(THRU)

(CODE)

(CATEGORY)



GOODYEAR AEROSPACE CORPORATION

AKRON 15, OHIO

STUDY OF EXPANDABLE, TERMINAL
DECELERATORS FOR MARS ATMOSPHERIC ENTRY

Volume II - Supporting Data and Technical Analysis

GER-12842

3 October 1966

Jay L. Musil

Goodyear Aerospace Corporation, Akron, Ohio

for

Jet Propulsion Laboratory, California Institute of Technology

Pasadena, Calif.

**This work was performed for the Jet Propulsion Laboratory,
California Institute of Technology, sponsored by
National Aeronautics and Space Administration under
Contract NAS7-100.**

ABSTRACT

The suitable application of expandable terminal decelerators for Mars atmosphere entry has been established on the basis of straightforward engineering techniques of analysis and design. By relating decelerator and entry vehicle performance and configuration characteristics to constraints associated with the operating environments, parametric formats were formulated that provided the required data. From these data integrated and meaningful tradeoffs were made. Analytical tools employed were point-mass trajectory computations, generalized strength/weight and configuration analyses, drag performances estimates, pressure distribution estimates, thermal analyses, and aerodynamic stability analyses. The results of this study have established that the suitable application of expandable terminal decelerators for Mars atmosphere entry are within the state of the art of expandable decelerator technology.

FOREWORD

The research described in this supporting technical data report (Volume II) was performed by Goodyear Aerospace Corporation, subsidiary of The Goodyear Tire & Rubber Company, Akron, Ohio, for the Jet Propulsion Laboratory, California Institute of Technology, under the authority of Contract No. 951153. The work was conducted from December 1965 to October 1966. Mr. James M. Brayshaw, Jr., was the Jet Propulsion Laboratory Technical Representative.

The work was performed under the general direction of Mr. R. L. Ravenscraft, manager of the Aero-Mechanical Engineering Division and Mr. Fred R. Nebiker, manager of the Recovery Systems Engineering Department. The program was directed by Mr. Jay L. Musil, project engineer.

Personnel contributing to this effort were Mssrs. A. P. Ahart, configuration, weight, and strength analyses; K. Birklein and J. W. Schlemmer, computer analyses; I. M. Jaremenko, pressure distribution analyses; and W. W. Sowa, thermal analyses.

This is Volume II of two volumes. Volume I presents the final summary report.

TABLE OF CONTENTS

	<u>Page</u>
FOREWORD	iii
LIST OF ILLUSTRATIONS	xi
LIST OF TABLES	xix
<u>Section</u>	<u>Title</u>
I	AERODYNAMIC PERFORMANCE AND STABILITY DATA
	1
	1. Aerodynamic Coefficient Data
	1
	2. Blunt Aerodynamic Shapes
	1
	3. Cones
	1
	4. Flared Skirts
	12
	5. Tension Shells
	12
II	AERODYNAMIC AND THERMAL ENVIRONMENT ANALYSES.
	19
	1. General
	19
	2. Atmospheric Environment
	19
	3. Surface Pressures on Decelerators in High-Speed Flows
	20
	4. Thermal Environment
	31
	a. Deployment Conditions
	31
	b. Heat Flux Rates
	34
III	STERILIZATION AND MATERIALS.
	43
	1. Sterilization Requirements Affecting Design . .
	43
	a. General
	43
	b. Sterilization Techniques
	43
	c. Spacecraft Design for Sterilization
	44
	d. Sterile Assembly of Spacecraft
	45
	e. Compatibility of Decelerator Materials with Spacecraft Sterilization
	46

<u>Section</u>	<u>Title</u>	<u>Page</u>
	<u>f.</u> Effects of Temperature and Sustained Load-ings	47
	2. Decelerator Materials and Coatings.	53
	<u>a.</u> General	53
	<u>b.</u> Fiber, Yarn, and Filament Material	59
	<u>c.</u> Woven Fabric Materials	60
	<u>d.</u> Fabric Coatings	64
	<u>e.</u> Joining Methods	66
	<u>f.</u> Material Selection and Qualification	70
IV	DECELERATOR ENVELOPE SIZE ESTABLISHED BY THERMAL REQUIREMENTS.	73
V	DECELERATOR SIZE DETERMINATION	85
VI	ANALYSIS RESULTS	101
VII	AUXILIARY GAS-INFLATION MEANS FOR MARS ENTRY DECELERATORS	135
	1. General	135
	2. Compressed Gas in Pressure Vessels.	135
	3. Residual Gas within the Decelerator	137
	4. Gas Generation by Burning Solid Fuel.	137
	5. Chemically Generated Gas.	138
	6. Auxiliary Compressors	139
	7. Ram-Air Inflation	139
	8. Package Bulk Factors for the Various Inflation Systems	139
VIII	TESTING REQUIREMENTS, TECHNIQUES, AND FACILITIES	141
	1. General	141
	2. Static Aerodynamic Coefficients and Aerodynamic Flow-Field Effects	141
	3. Decelerator Loads and Load Distribution	142
	4. Dynamic Stability	142
	5. Aerodynamic Heating	142

<u>Section</u>	<u>Title</u>	<u>Page</u>
	6. Testing Methods	143
	<u>a.</u> General	143
	<u>b.</u> Testing Facilities.	143
	<u>c.</u> Heating Techniques	147
IX	FREE-FLIGHT TEST SIMULATION	153
	1. General	153
	2. Description of Launch Vehicle System.	154
	<u>a.</u> General	154
	<u>b.</u> Booster Selection.	154
	3. Launch Vehicle Flight Characteristics	155
	4. Dispersion Controls	156
	5. Heat Transfer	158
	6. Test Vehicle Concept	159
	<u>a.</u> General	159
	<u>b.</u> AIRMAT in Simulation	159
	<u>c.</u> Design Considerations	160
	7. Instrumentation System	164
X	PRELIMINARY DESIGN, DEVELOPMENT, AND TESTING	167
	1. Objectives	167
	2. Preliminary Design.	167
	3. Preliminary Decelerator Analysis	168
	4. Development Program	169
	<u>a.</u> Five Phases	169
	<u>b.</u> Phase I - Test Evaluation of Decelerator Models	169
	<u>c.</u> Phase II - Test Evaluation of Larger-Scale Model	170
	<u>d.</u> Phase III - System Design and Mockup Testing	170
	<u>e.</u> Phase IV - Air-Drop Test	170
	<u>f.</u> Phase V - Flight Test.	171
	5. Schedule	171
	6. Documentation	173
	7. Customer Responsibilities	174
	<u>a.</u> Preliminary Design Phase.	174
	<u>b.</u> Development Program	175

<u>Appendix</u>	<u>Title</u>	<u>Page</u>
	LIST OF SYMBOLS	177
	LIST OF REFERENCES	183
A	DETAILED ANALYSIS OF DECELERATORS.	185
B	DYNAMIC ANALYSIS	221

LIST OF ILLUSTRATIONS

<u>Figure</u>	<u>Title</u>	<u>Page</u>
1	Axial Drag Characteristics for Mars Entry Vehicle .	2
2	Axial Force Coefficient vs Angle of Attack, 60-Deg Blunted Cone	2
3	Total Drag Coefficient for 120-Deg Blunt Cone	3
4	Axial Force Coefficient for 120-Deg Blunt Cone	3
5	Normal Force Coefficient vs Angle of Attack, 60-Deg Blunt Cone	4
6	Pitching Moment Coefficient vs Angle of Attack, 60-Deg Blunt Cone	5
7	C_N versus α for 120-Deg Blunt Cone	6
8	C_m versus α for 120-Deg Blunt Cone	7
9	Blunt Cone Shape, Pitch Damping Coefficient (Newtonian Theory)	8
10	Variations of $C_{m_q} + C_{m_\alpha}$ for Two Blunt Cone Models .	8
11	Static Aerodynamic Characteristics of Flared Bodies at $M = 8.0$	9
12	Static Stability of Flared Bodies at $M = 8.0$	10
13	Static Stability of Flared Bodies	10
14	Damping Moment Characteristics for Cones	11
15	Static Stability of Cones, Normal Force Curve Slope .	13
16	Static Stability of Cones, Center of Pressure	15
17	Tension Shell.	17

<u>Figure</u>	<u>Title</u>	<u>Page</u>
18	Initial Mars Entry Trajectories	22
19	Decelerator Deployment Envelope, VM7 Atmosphere .	23
20	Decelerator Deployment Envelope, VM8 Atmosphere .	24
21	Entry Capsule and Decelerator Configuration	26
22	JPL Capsule-Conical Flare Decelerator, Estimated Pressure Distribution.	27
23	JPL Capsule-BALLUTE Decelerator, Estimated Pressure Distribution.	28
24	Trailing BALLUTE Decelerator, Estimated Pressure Distribution	29
25	Deployment Conditions, VM7 Atmosphere	32
26	Deployment Conditions, VM8 Atmosphere	33
27	Stagnation Point Heat-Flux Rate	35
28	Local Heat-Flux Rate versus Unit Reynolds Number .	37
29	Heat-Flux Rate, Trajectory B1.	38
30	Heat-Flux Rate, Trajectory A4.	38
31	Heat-Flux Rate, Trajectory 22.	39
32	Heat-Flux Rate, Trajectory 19.	39
33	Heat-Flux Rate, Trajectory 37.	40
34	Heat-Flux Rate, Trajectory A1.	41
35	Heat-Flux Rate, Trajectory B3.	41
36	Typical Stress-Strain Curves for Dacron, Nylon, and Nomex	48
37	Strength Retained by Nylon, Dacron, and Nomex Yarns after Exposure to Hot, Dry Air.	49
38	Breaking Tenacity at Various Temperatures.	50

Figure	Title	Page
39	Shrinkage of Nylon, Dacron, and Nomex Exposed to Hot, Dry Air	52
40	Variation of Tensile Strength and Elongation of Nylon Fibers Irradiated in Nitrogen at 244 mu, 314 mu, and 369 mu	54
41	Variation of Tensile Properties with Incident Energy for Dacron Irradiated in Nitrogen with A-H6 Lamp . .	55
42	Variation of Tensile Strength and Ultimate Elongation of Nomex Irradiated in Nitrogen with Ultraviolet Light and with Visible Light (437 mu).	56
43	Degradation of Nomex after Exposure to Ultraviolet Radiation and Elevated Temperatures	57
44	Effects of Gamma Radiation on Nomex at 400 F (Top) and at 600 F (Bottom)	58
45	Strength Retention versus Temperature for Present and Future Fibers	63
46	Decelerator Fabric Envelope Weight Requires versus Initial Mach Number, Trajectory B1	75
47	Decelerator Fabric Envelope Weight Required versus Initial Mach Number, Trajectories A4 and 22	76
48	Decelerator Fabric Envelope Weight Required versus Initial Mach Number, Trajectory 37.	77
49	Decelerator Fabric Envelope Weight Required versus Initial Mach Number, Trajectories A1 and 19	78
50	Decelerator Fabric Envelope Weight Required versus Initial Mach Number, Trajectory B3	79
51	Six Steps in Determining Decelerator Size	81
52	Altitudes at which Various Decelerators Reach Mach Targets (M_t) as Functions of Initial Mach Numbers and Percent Initial $C_D A$ in VM7 Atmosphere.	83
53	Altitudes at which B1 and A4 Trajectory Decelerators Reach Mach Targets (M_t) (VM7 Atmosphere).	86

<u>Figure</u>	<u>Title</u>	<u>Page</u>
54	Altitudes at which B1 and A4 Trajectory Decelerators Reach Mach Targets (M_t) in VM7 Atmosphere	87
55	Altitudes at which Trajectory 22 Decelerators Reach Mach Targets in VM7 Atmosphere	88
56	Altitudes at which Trajectory 22 Decelerators Reach Mach Targets as Functions of Initial Mach Number and Percent Initial $C_D A$ in VM7 Atmosphere	89
57	Altitudes at which Various Decelerators Reach $M_t = 1.0$ as Functions of Original Mach Numbers and Percent of Initial $C_D A$ in VM8 Atmosphere	90
58	Altitudes at which Decelerators Reach Mach Targets (M_t) in VM8 Atmosphere in A1, B3, and 37 Trajectories	91
59	Altitudes at which Decelerators Reach Mach Targets (M_t) in VM8 Atmosphere at Trajectories A1, B3, and 37 with Initial Mach 5.0	92
60	Altitudes at which Decelerators Reach Mach Targets (M_t) in VM8 Atmosphere at Trajectories A1, B3, and 37 with Initial Mach 7.0	93
61	Altitudes at which Decelerators Reach Mach Targets (M_t) in VM8 Atmosphere at Trajectory 19	94
62	Altitudes at which Decelerators Reach Mach Targets as Functions of Initial Mach Numbers and Percent of Initial $C_D A$ in VM8 Atmosphere with JPL-19 Trajectory	95
63	Drag Coefficient Variation with Mach Number	96
64	Percent Drag Area versus Diameter for BALLUTE Decelerator Applied to Three Entry Configuration	97
65	Percent Drag Area versus Diameter for Inflatable Skirt Decelerator Applied to Three Entry Configuration	98
66	Drag Area versus Diameter of Trailing BALLUTE for Three Entry Capsule Configuration	99

<u>Figure</u>	<u>Title</u>	<u>Page</u>
67	Decelerator Diameter versus Deployment Mach Number for 18.5-Ft-Diameter Entry Capsule, Trajectory A1	102
68	Percent Decelerator to Total System Weight versus Deployment Mach Number for 18.5-Ft-Diameter Entry Capsule, Trajectory A1	103
69	Decelerator Diameter versus Deployment Mach Number for 12-Ft-Diameter Entry Capsule, Trajectory B3	104
70	Percent Decelerator to Total System Weight versus Deployment Mach Number for 12-Ft-Diameter Entry Capsule, Trajectory B3	105
71	Decelerator Diameter versus Deployment Mach Number for 16-Ft Entry Capsule Diameter, Trajectory 37	106
72	Percent Decelerator to Total System Weight versus Deployment Mach Number for 16-Ft-Diameter Entry Capsule, Trajectory 37	107
73	Decelerator Diameter versus Deployment Mach Number for 16-Ft-Diameter Entry Capsule, Trajectory 19 at 20,000 Ft	108
74	Percent Decelerator to Total System Weight versus Deployment Mach Number for 16-Ft Entry Capsule, Trajectory 19 at 20,000 Ft.	109
75	Decelerator Diameter versus Deployment, 16-Ft Diameter Entry Capsule, Trajectory 19 at 30,000 Ft	110
76	Percent Decelerator to Total Weight versus Deployment Mach Number, 16-Ft-Diameter Entry Capsule Trajectory 19 at 30,000 Ft.	111
77	Decelerator Diameter versus Deployment Mach Number for 18.5-Ft-Diameter Entry Capsule, Trajectory A4 at 20,000 Ft.	112
78	Percent Decelerator to Total Weight versus Deployment Mach Number, 18.5-Ft Diameter Entry Capsule, Trajectory A4 at 20,000 Ft	112

<u>Figure</u>	<u>Title</u>	<u>Page</u>
79	Decelerator Diameter versus Deployment Mach Number, 18.5-Ft-Diameter Entry Capsule, Trajectory A4 at 30,000 Ft	113
80	Percent Decelerator to Total Weight versus Deployment Mach Number, 18.5-Ft Entry Capsule Diameter, Trajectory A4 at 30,000 Ft	114
81	Decelerator Diameter versus Deployment Mach Number, 12-Ft Entry Capsule Diameter, Trajectory B1 at 20,000 Ft	115
82	Percent Decelerator to Total System Weight versus Deployment Mach Number, 12-Ft Diameter Entry Capsule, Trajectory B1 at 20,000 Ft	116
83	Decelerator Diameter versus Deployment Mach Number for 12-Ft Diameter Entry Capsule, Trajectory B1 at 30,000 Ft	117
84	Percent Decelerator to Total Weight versus Deployment Mach Number for 12-Ft Entry Capsule, Trajectory B1 at 30,000 Ft	118
85	Decelerator Diameter versus Deployment Mach Number for 16-Ft Diameter Entry Capsule, Trajectory 22 at 20,000 Ft	119
86	Percent Decelerator to Total Weight versus Deployment Mach Number for 16-Ft Entry Capsule, Trajectory 22 at 20,000 Ft	120
87	Decelerator Diameter versus Deployment Mach Number for 16-Ft Diameter Entry Capsule, Trajectory 22 at 30,000 Ft	121
88	Percent Decelerator to Total Weight versus Deployment Mach Number for 16-Ft Entry Capsule, Trajectory 22 at 30,000 Ft	122
89	Decelerator Envelope Unit Weight versus Deployment Mach Numbers at Trajectory A1 (Dacron)	123
90	Decelerator Envelope Unit Weight versus Deployment Mach Number, Trajectory A1 (Nomex)	124

<u>Figure</u>	<u>Title</u>	<u>Page</u>
91	Decelerator Envelope Unit Weight versus Deployment Mach Number, Trajectory B3	125
92	Decelerator Envelope Unit Weight versus Deployment Mach Number, Trajectory 19 at 20,000 Ft	126
93	Decelerator Envelope Unit Weight versus Initial Operating Mach Number, Trajectory 19 at 30,000 Ft	127
94	Decelerator Envelope Unit Weight versus Deployment Mach Number, Trajectory 37 (Dacron)	128
95	Decelerator Unit Weight versus Deployment Mach Number, Trajectory 37 (Nomex)	129
96	Decelerator Envelope Unit Weight versus Deployment Mach Number, Trajectory A4	130
97	Decelerator Envelope Unit Weight versus Deployment Mach Number at 20,000 Ft	131
98	Decelerator Envelope Unit Weight versus Deployment Mach Number, Trajectory B1 at 30,000 Ft	132
99	Decelerator Envelope Unit Weight versus Deployment Mach Number, Trajectory 22	133
100	Weights for Various Inflation Systems	136
101	Mach and Reynolds Numbers for Simulating Mars Flight in the Earth's Atmosphere	144
102	Mach Number and Temperature for Atmospheric Flight and for Various Laboratory Testing Methods	144
103	Mach and Reynolds Numbers for Various Laboratory Testing Methods	145
104	Rocket Boost Techniques for Simulation Tests	161
105	Preliminary Program Schedule	172

LIST OF TABLES

<u>Table</u>	<u>Title</u>	<u>Page</u>
I	Tension-Shell Aerodynamics	18
II	Characteristics of VM Atmospheres	21
III	Radiation Resistance: Effect of Exposure on Yarn Strength	59
IV	Effects of Environment on Natural and Manmade Textiles	61
V	Relative General Properal Properties of Elastomers	67
VI	Elastomeric Coatings	69
VII	Echo I and II Inflation Data	138
VIII	Experimental Techniques for Study of Expandable Decelerators	151

SECTION I - AERODYNAMIC PERFORMANCE AND STABILITY DATA

1. AERODYNAMIC COEFFICIENT DATA

Figures 1 through 10 include various aerodynamic coefficient data appropriate to the basic entry capsule configuration. These data include results of experimental and theoretical analytical studies conducted by JPL and NASA.

2. BLUNT AERODYNAMIC SHAPES

To support aerodynamic stability analyses for the Mars terminal decelerator program, Goodyear Aerospace investigated published data applicable to the decelerator configurations under study. Unfortunately, the meager data were of questionable accuracy. No available data relate to effects of flexibility on decelerator stability coefficients at angles of attack or for trailing decelerators. The following graphic information summarizes available data that more nearly relate to the configurations considered in the study.

Figures 11 through 16 are graphic summaries of published data on blunt aerodynamic shapes.

3. CONES

Plots of C_{N_α} and c_p versus Mach number present a fairly complete picture of the static stability of a cone in free stream. Experimental data given up to Mach 6.8 for cones of large angle (θ_s), agree with Newtonian theory. Several other theories predict supersonic stability characteristics; these, however, are of limited accuracy for large θ_s .

The effect of nose bluntness is negligible up to $r/D = 0.4$ where r = nose radius and D = cone base diameter, especially at $\theta_s \geq 30$ deg.

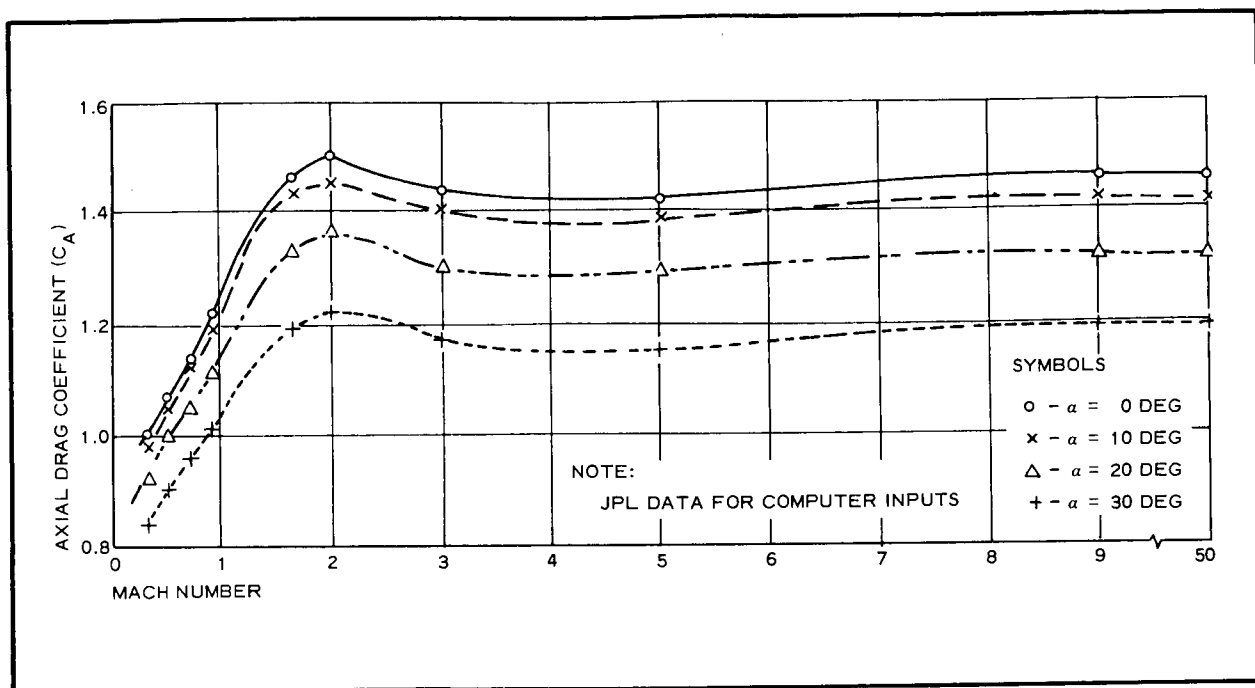


Figure 1 - Axial Drag Characteristics for Mars Entry Vehicle

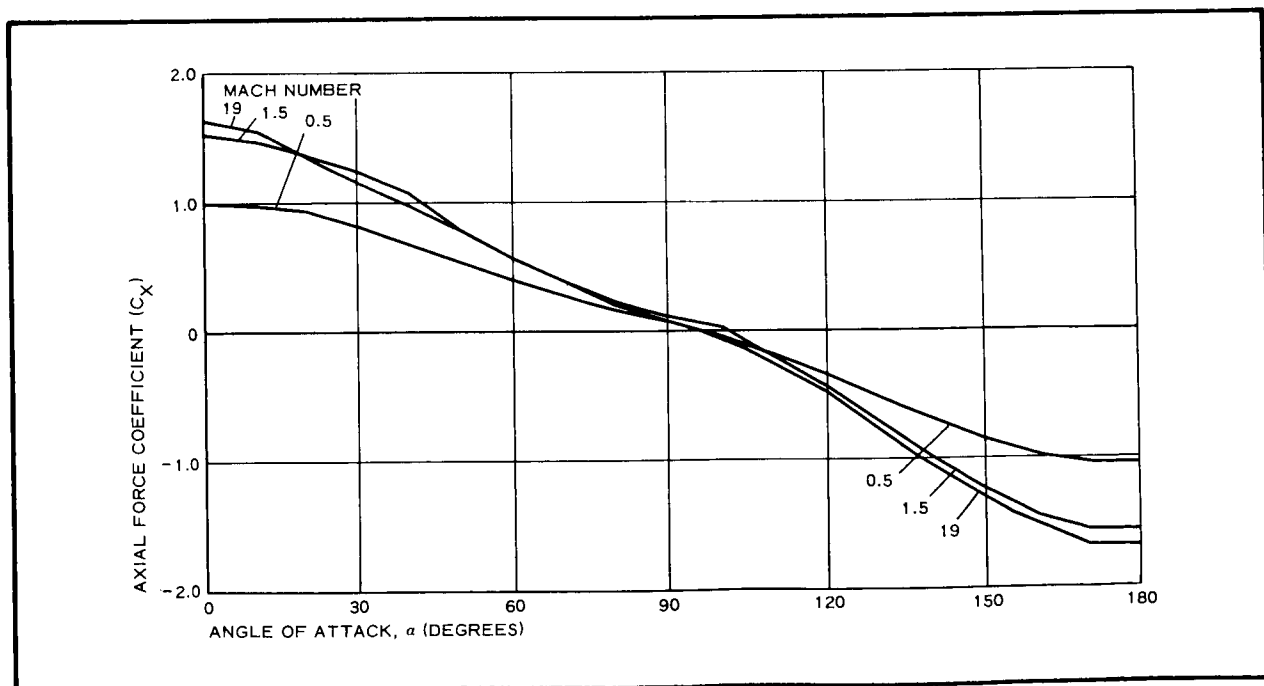


Figure 2 - Axial Force Coefficient vs Angle of Attack, 60-Deg Blunted Cone

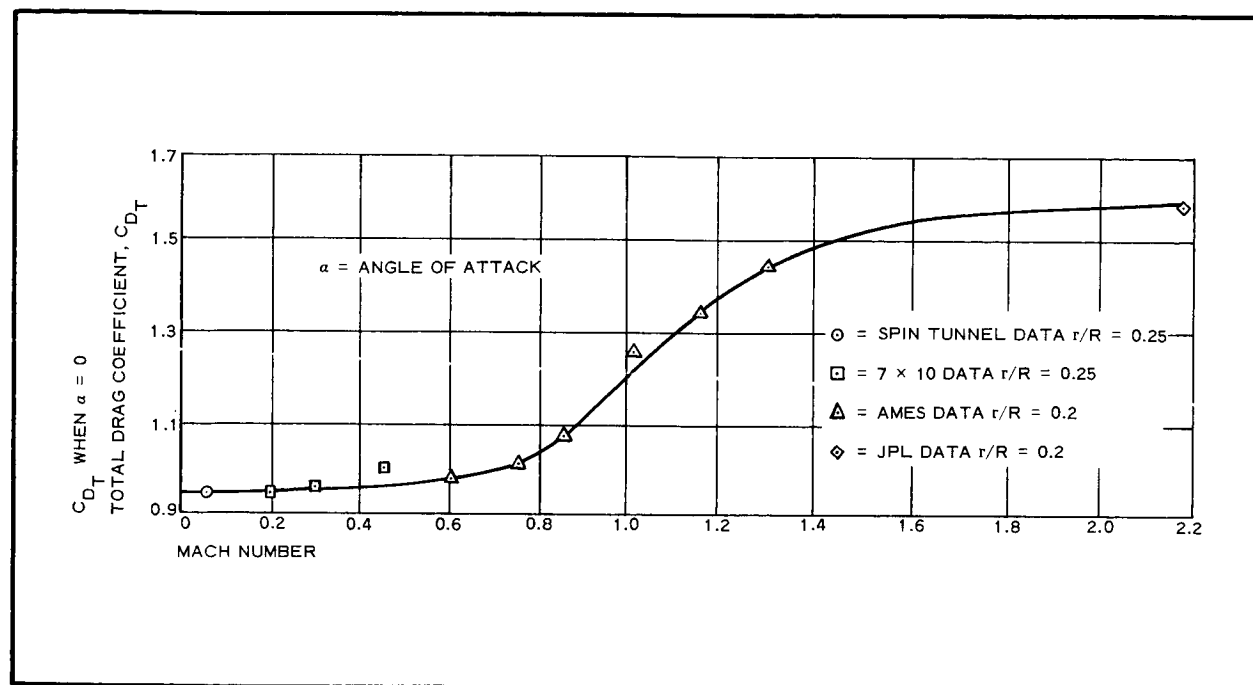


Figure 3 - Total Drag Coefficient for 120-Deg Blunt Cone

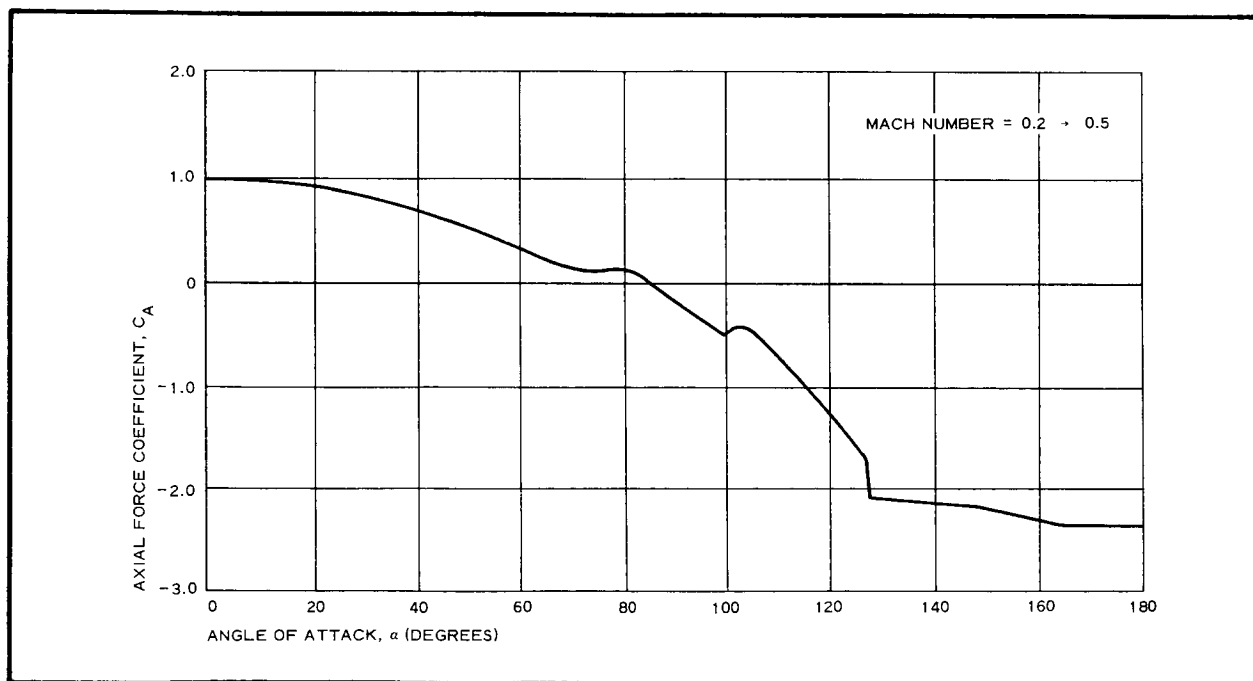


Figure 4 - Axial Force Coefficient for 120-Deg Blunt Cone

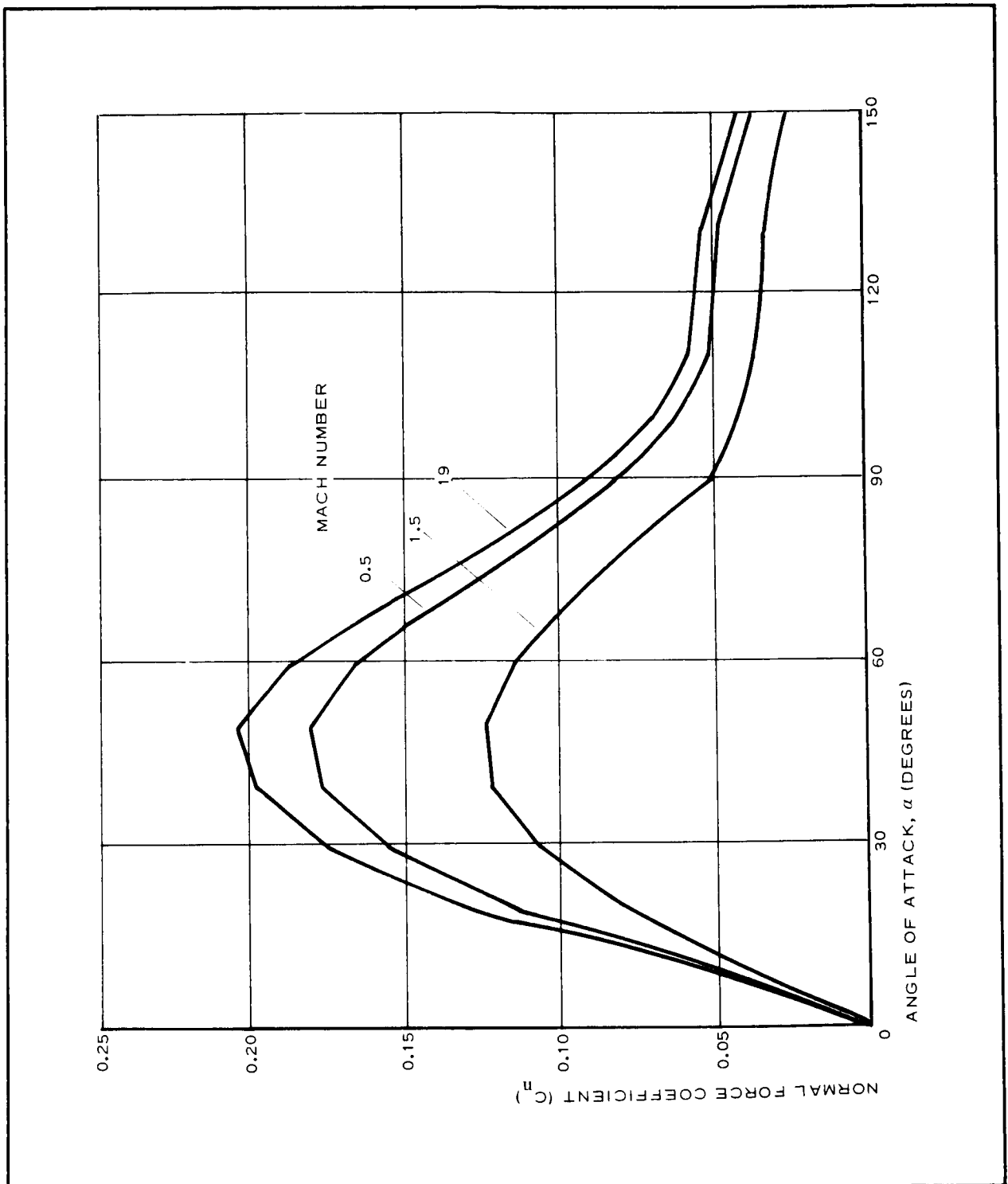


Figure 5 - Normal Force Coefficient vs Angle of Attack, 60-Deg Blunt Cone

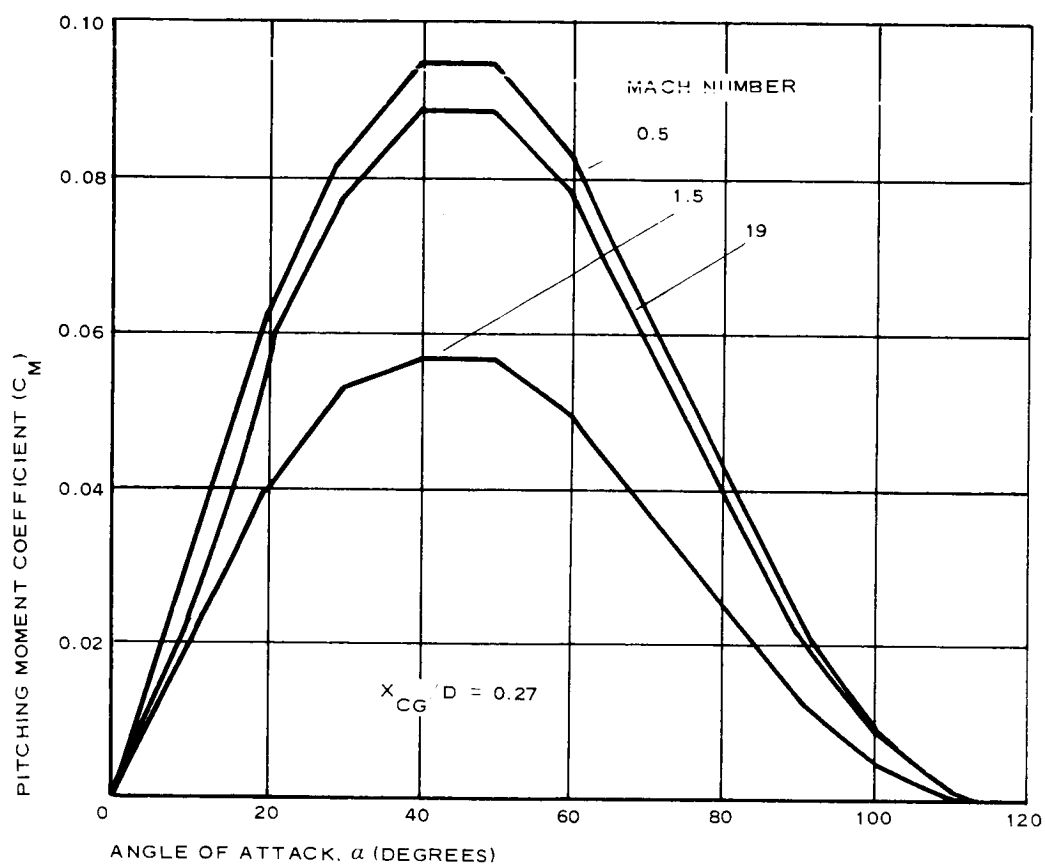
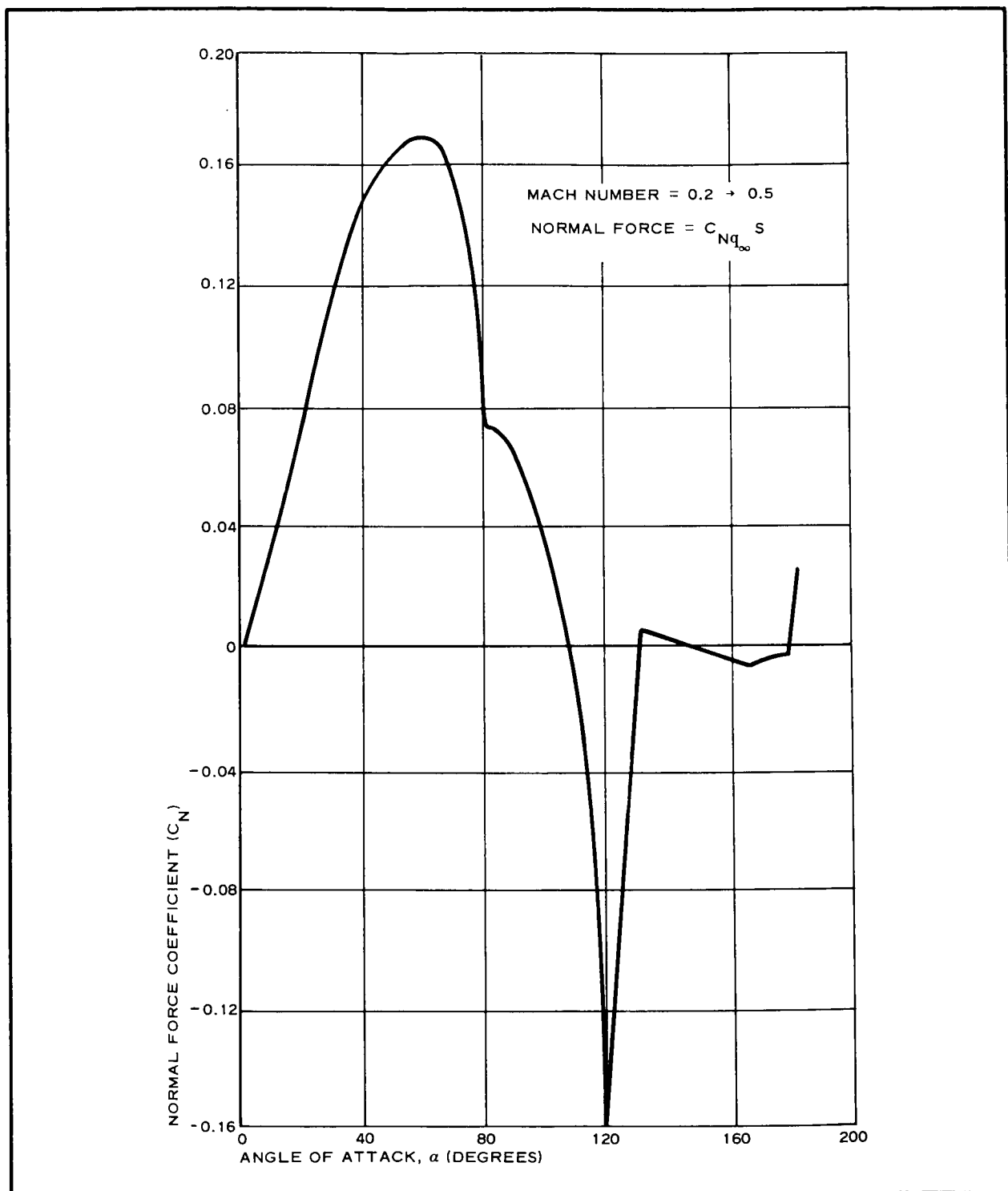
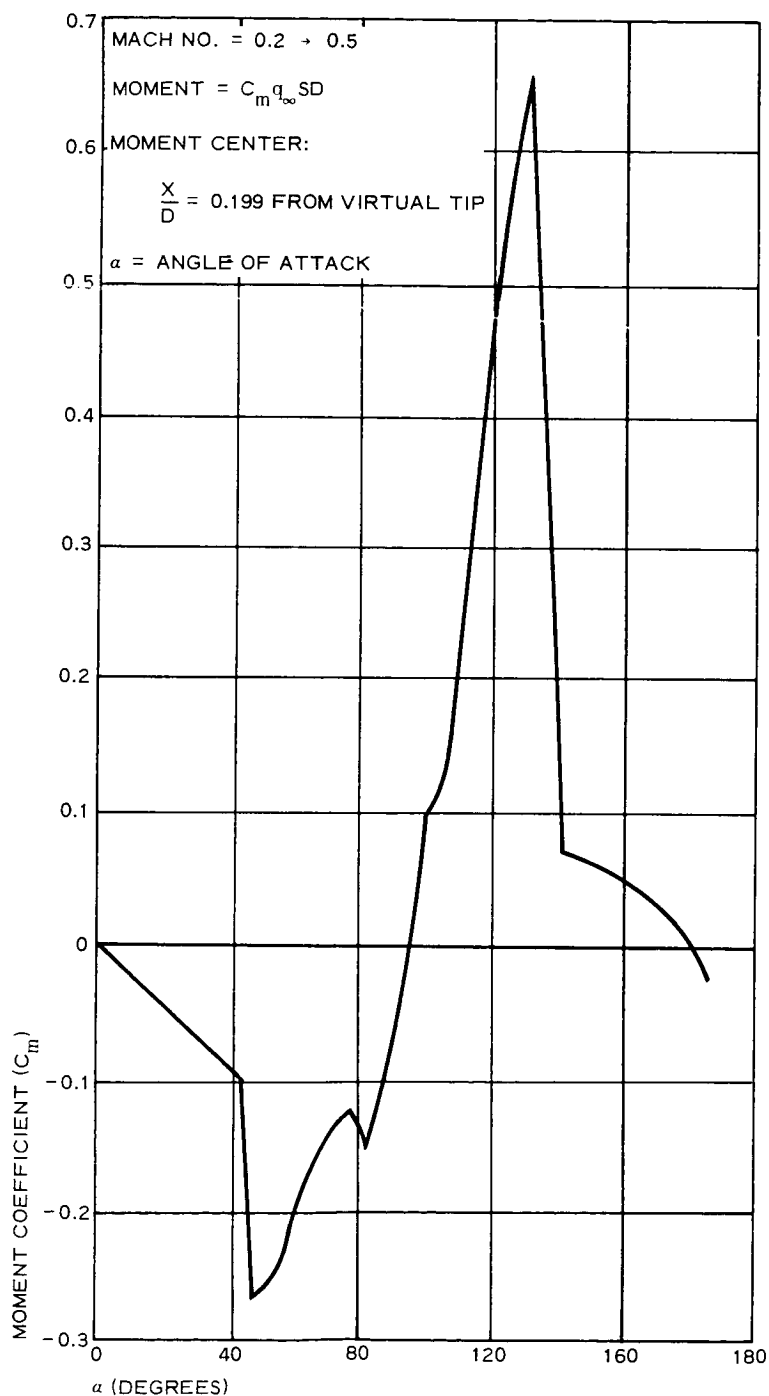


Figure 6 - Pitching Moment Coefficient vs Angle of Attack, 60-Deg Blunt Cone

Figure 7 - C_N versus α for 120-Deg Blunt Cone

Figure 8 - C_m versus α for 120-Deg Blunt Cone

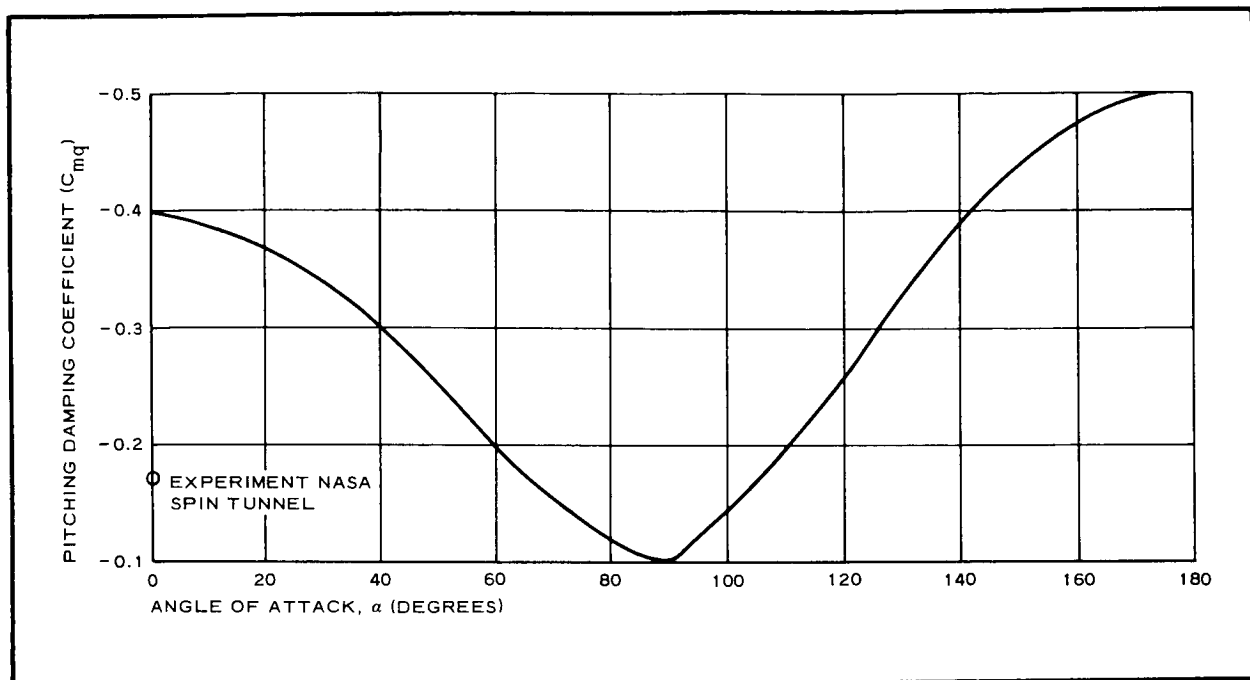


Figure 9 - Blunt Cone Shape, Pitch Damping Coefficient (Newtonian Theory)

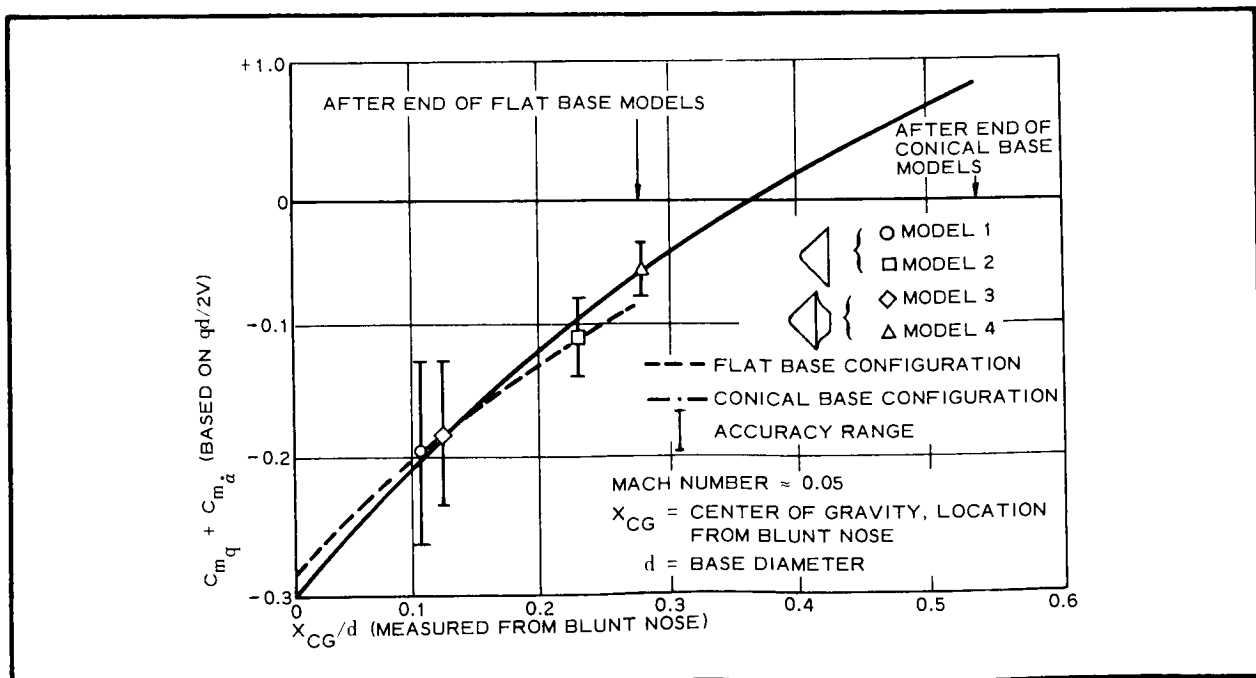


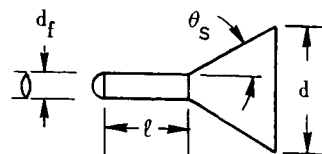
Figure 10 - Variations of $C_{mq} + C_{mq_\alpha}$ for Two Blunt Cone Models

REFERENCE: WADC TR-59-324, PART II

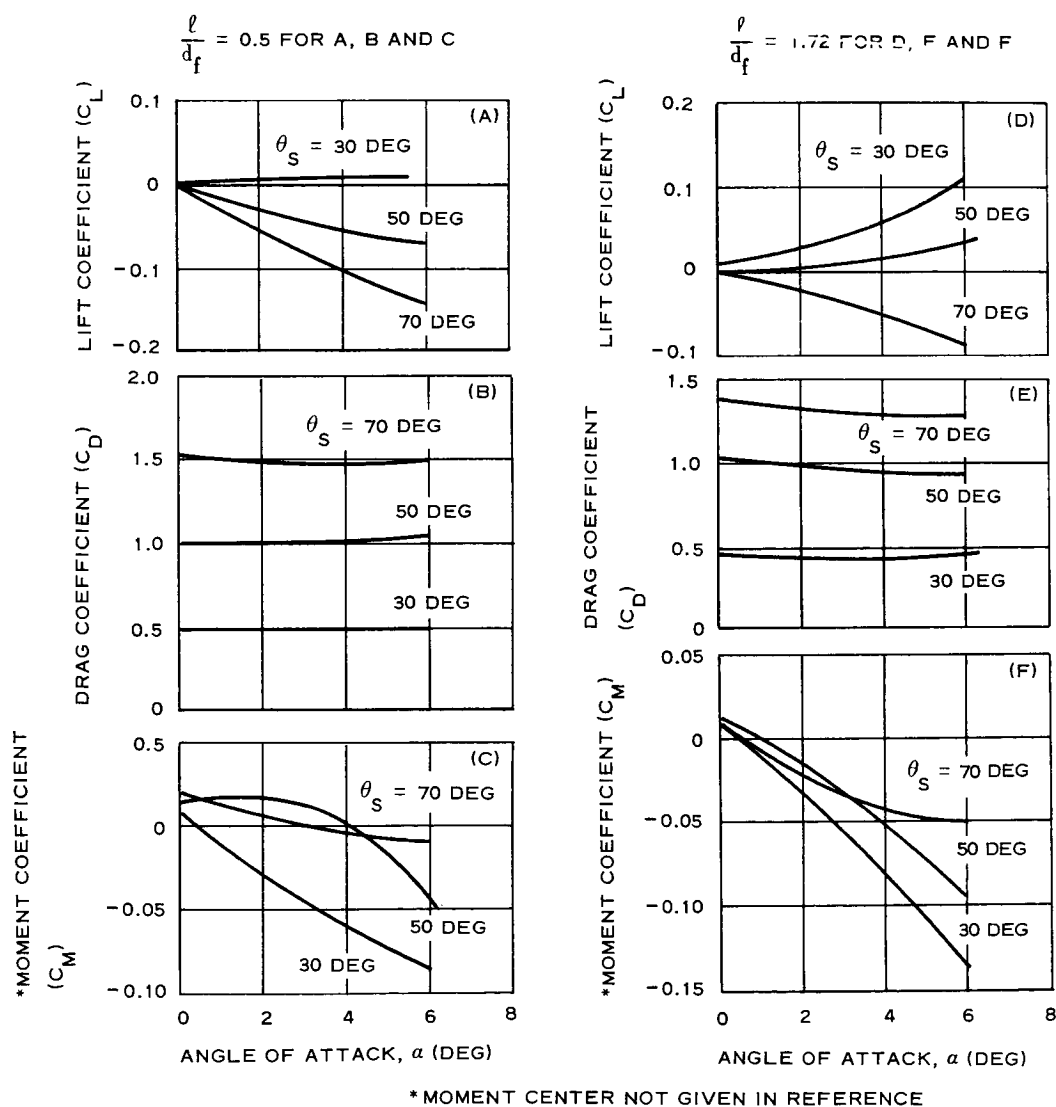
NOTES:

ALL COEFFICIENTS ARE REFERENCED TO S AND D WHEN

$$S = \frac{\pi D^2}{4} \quad \text{AND}$$

 $\theta_S = \text{FLARE HALF ANGLE}$ 

"APPLIES TO FIGURES 11, 12, AND 13."

Figure 11 - Static Aerodynamic Characteristics of Flared Bodies at $M = 8.0$

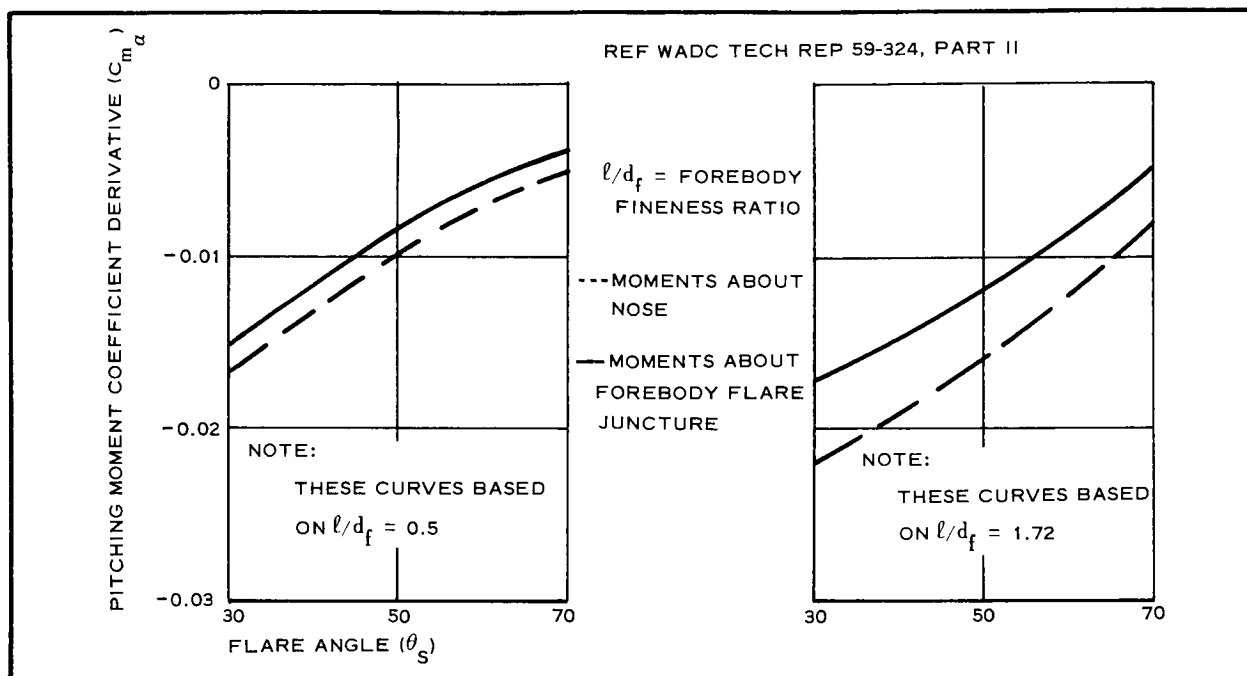
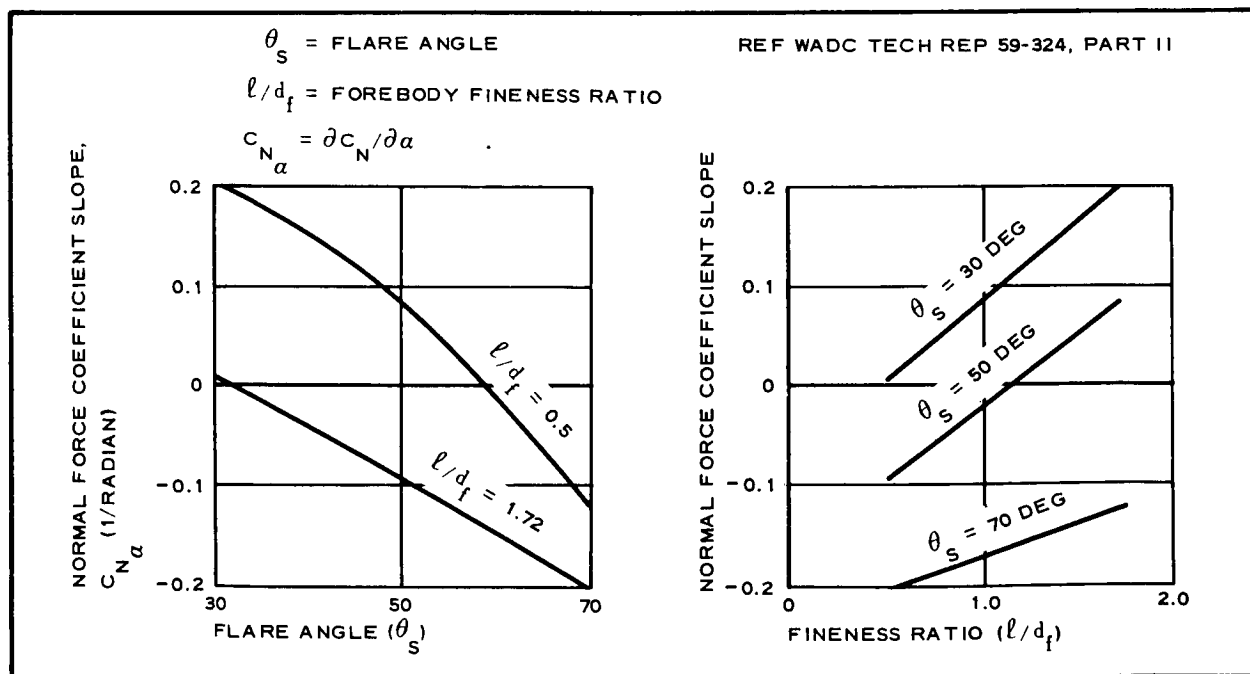
Figure 12 - Static Stability of Flared Bodies at $M = 8.0$ 

Figure 13 - Static Stability of Flared Bodies

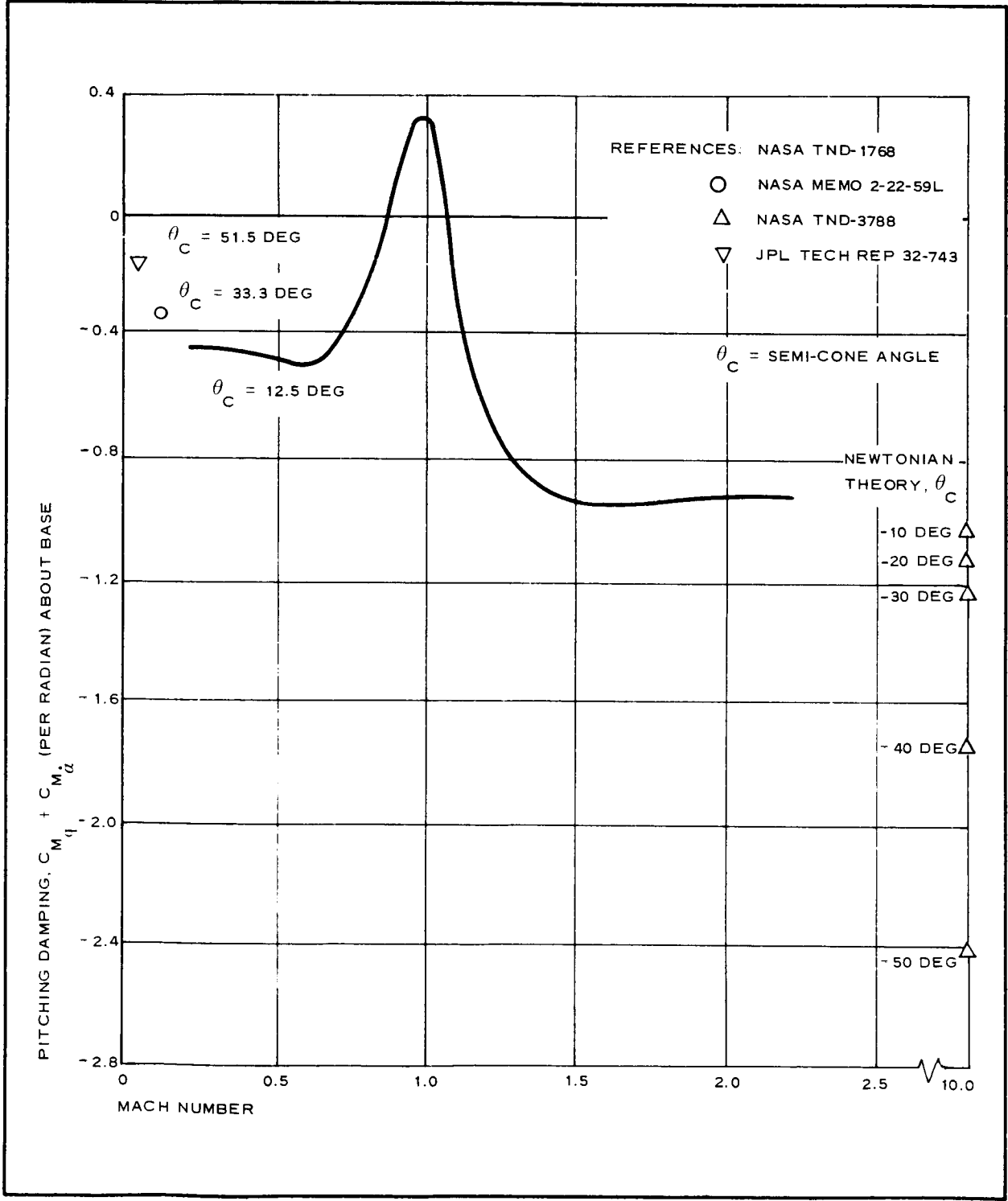


Figure 14 - Damping Moment Characteristics for Cones

Apparently, few, if any, tests have been made to evaluate R_N effects at low speeds.

Dynamic stability is an area where few tests have been conducted with cones of large θ_s . The plot of $C_{m_q} + C_{m_\alpha}$ test data for a cone of $\theta_s = 12.5$ deg is of questionable accuracy because of error in transferring the moment center to the cone base. The average variation of $C_{m_q} + C_{m_\alpha}$ with Mach number is based on test data about three reference centers. Prior to averaging, the transferred moments did not agree.

Several theories for damping moments at speeds above $M = 1.0$ exist and are in varying agreement with limited test data.

4. FLARED SKIRTS

The only static stability test data applicable to large decelerator-type flares are for $Mach = 8.0$. Graphs are presented in Figures 11, 12, and 13 for the static stability coefficient variation with flare angle and forebody fineness ratio.

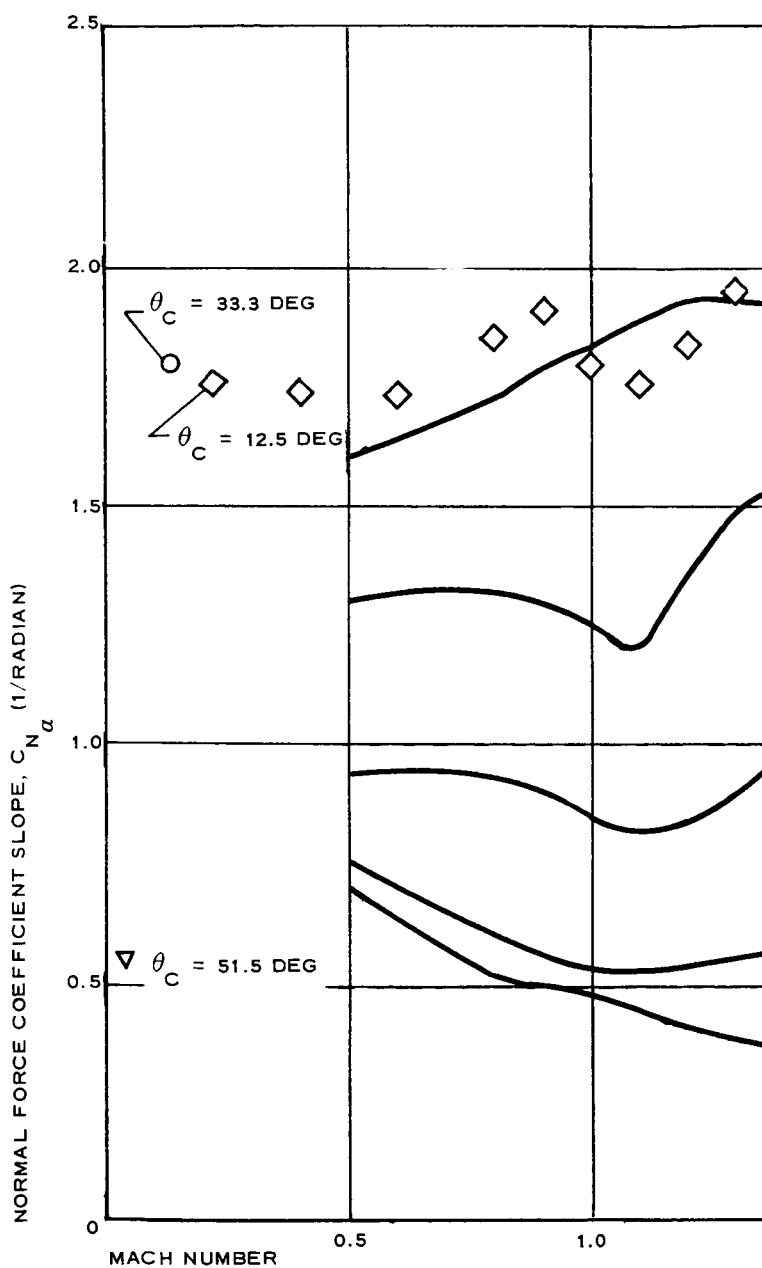
Much test data have been compiled by various government agencies for small flared skirts used for missile and re-entry body stability at very high speeds. These data, difficult to correlate because of many variations in forebody geometry, are of limited value in decelerator study.

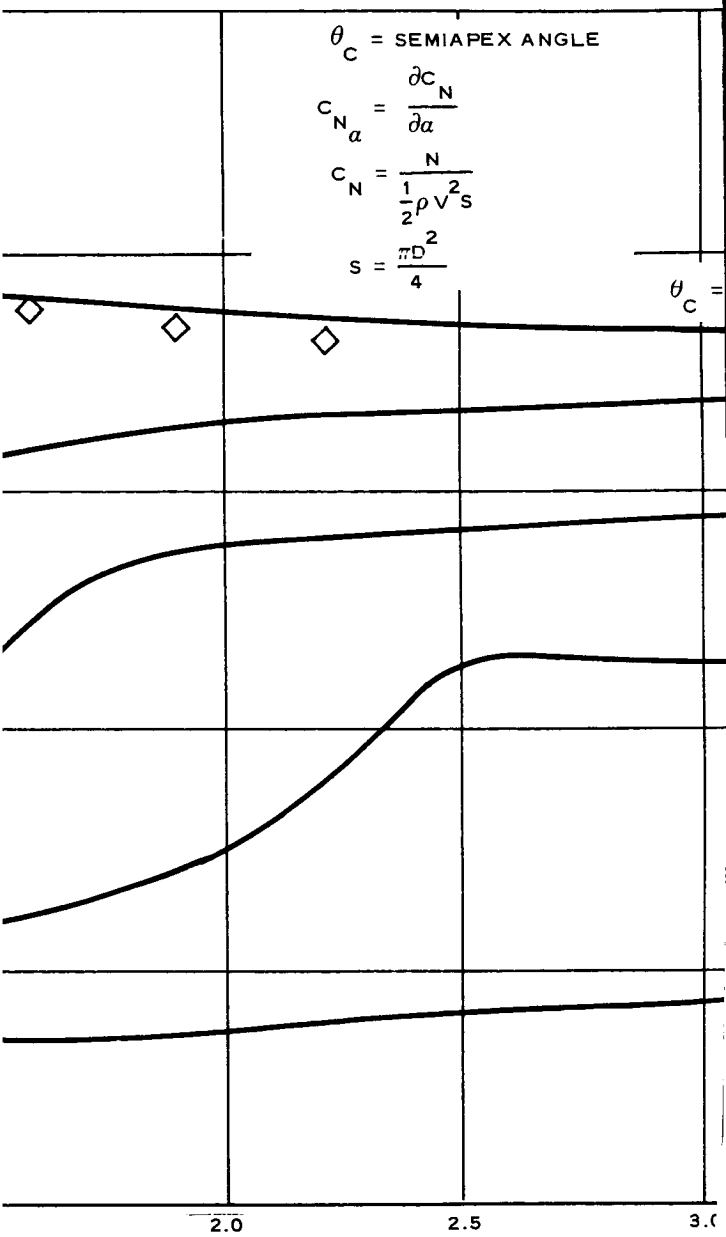
No dynamic stability test data were found for large flare angles and diameters at any speed.

5. TENSION SHELLS

The only stability test data for a tension-shell body came from a free-spinning wind tunnel test at $Mach 0.044$ and $R_N = 0.4 \times 10^4$ per diameter (see Figure 17).

The following stability data apply to the tension shell shown in Figure 17:





13

(2)

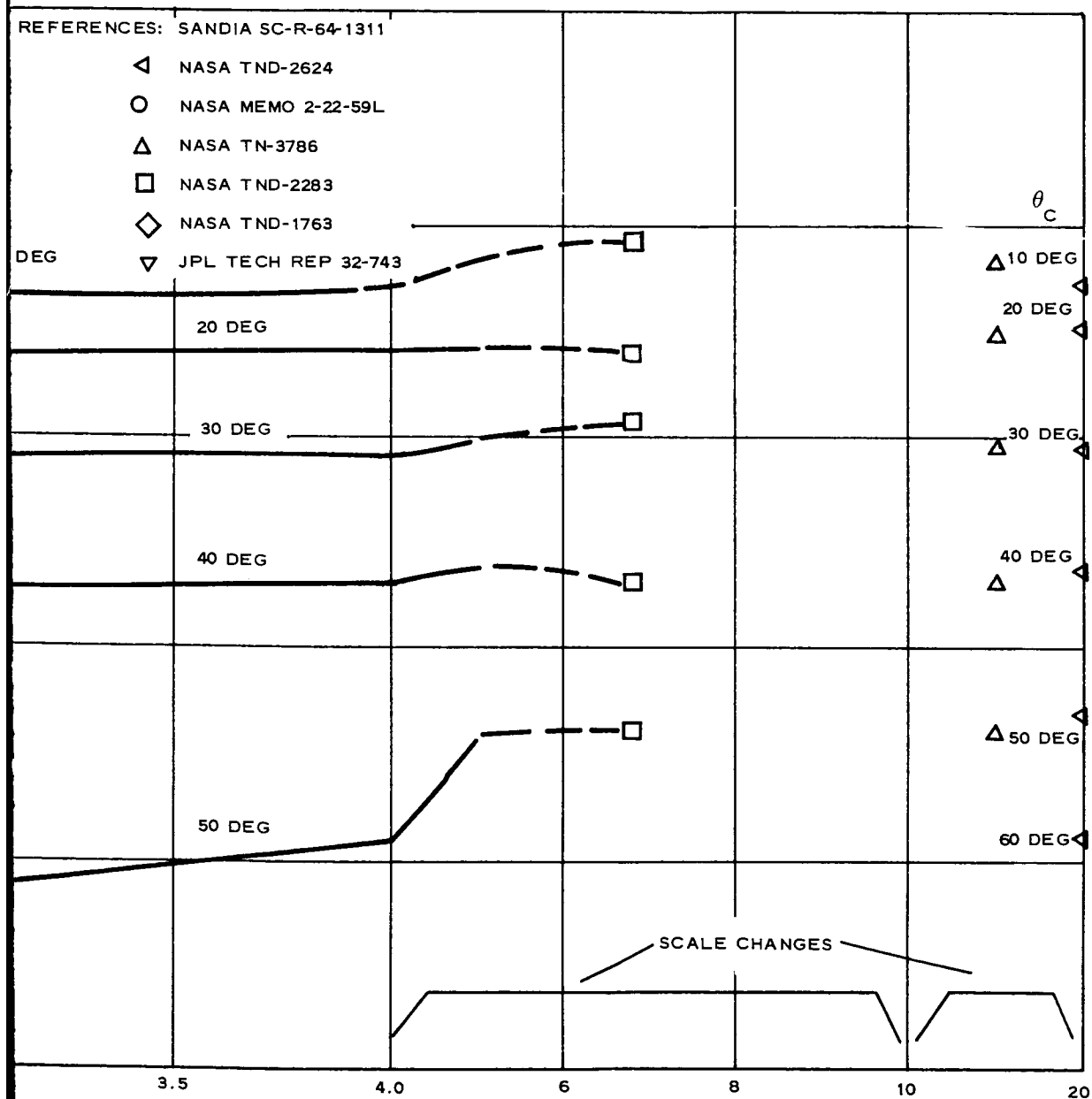
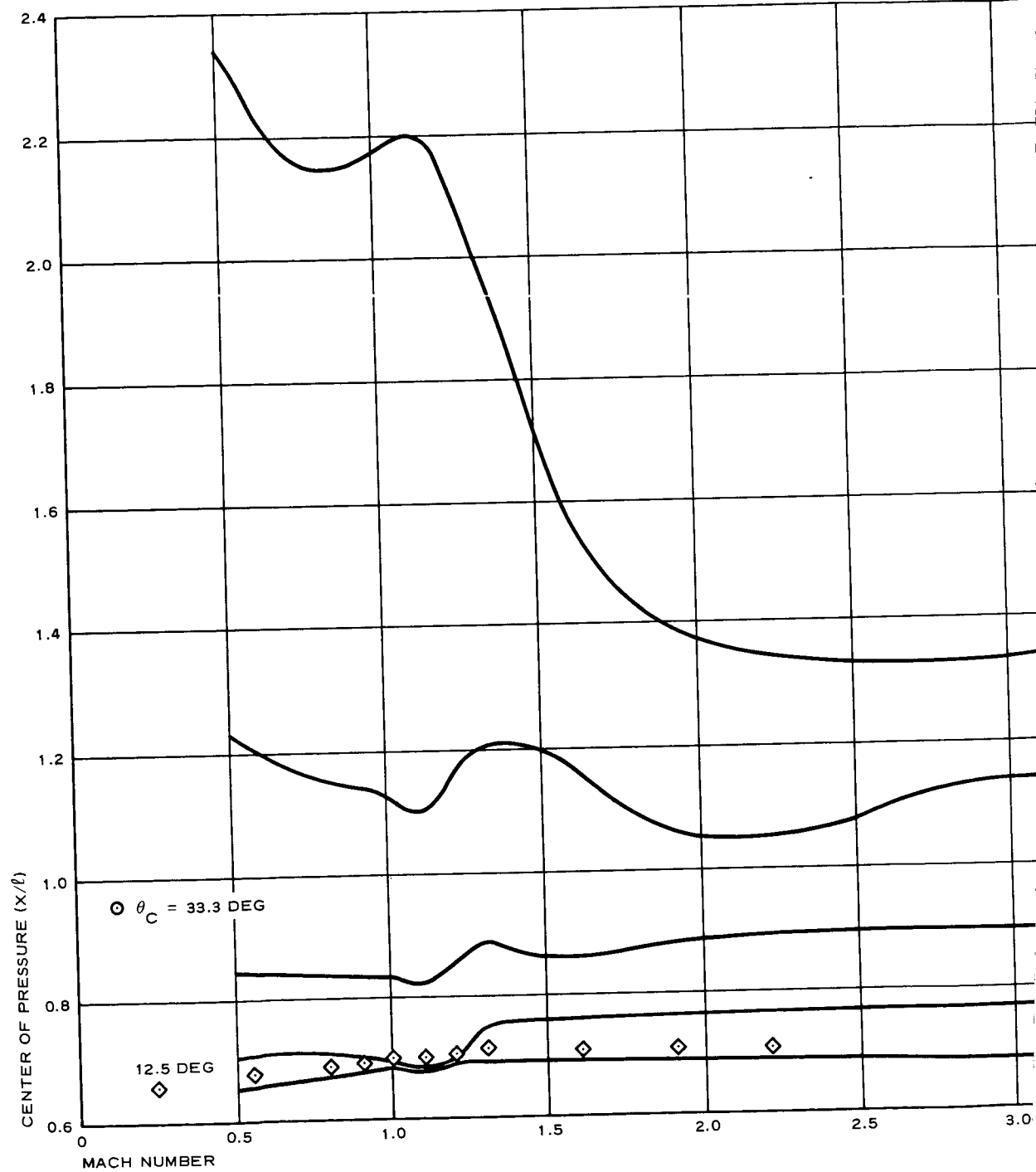


Figure 15 - Static Stability of Cones, Normal Force Curve Slope

14



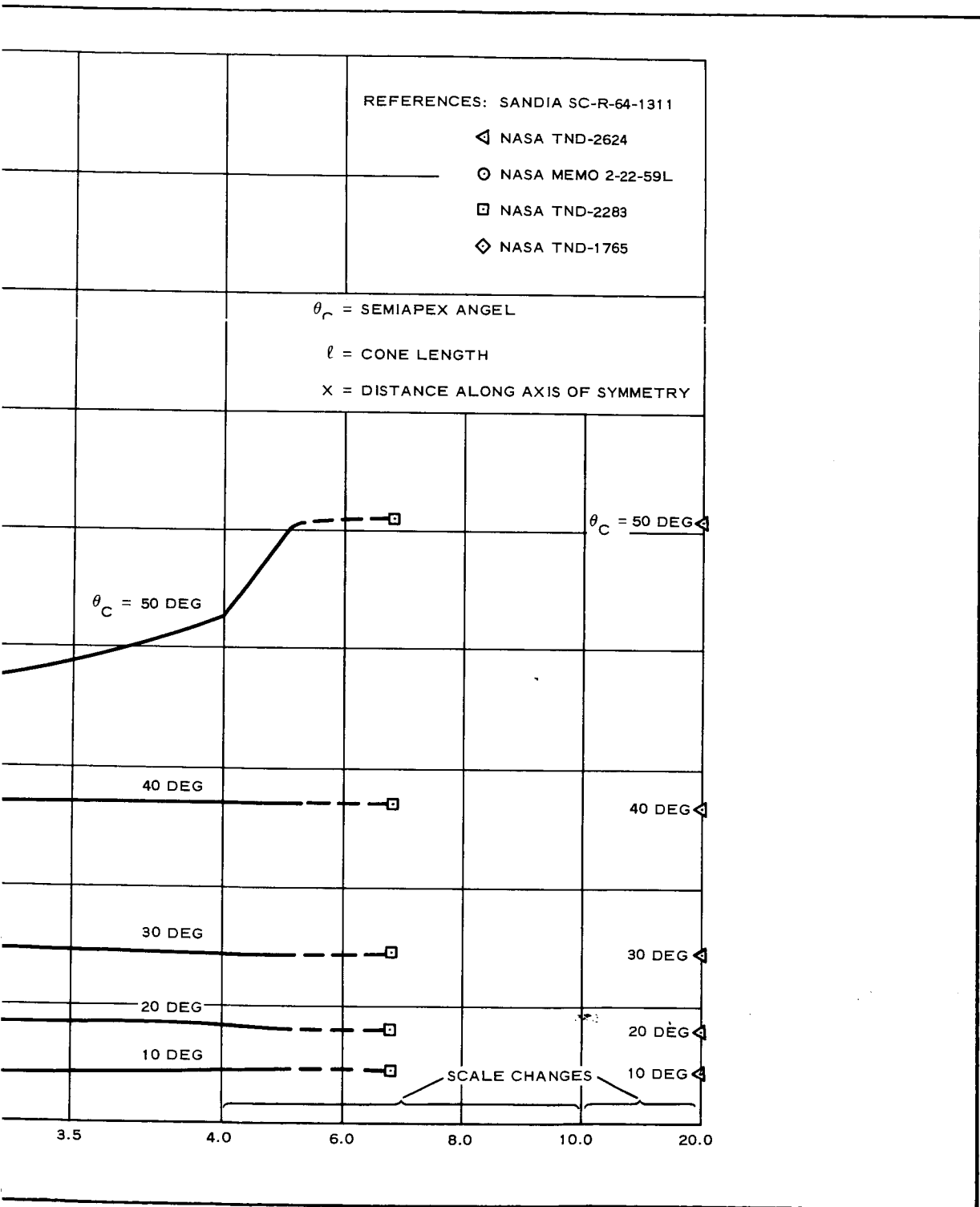


Figure 16 - Static Stability of Cones, Center of Pressure

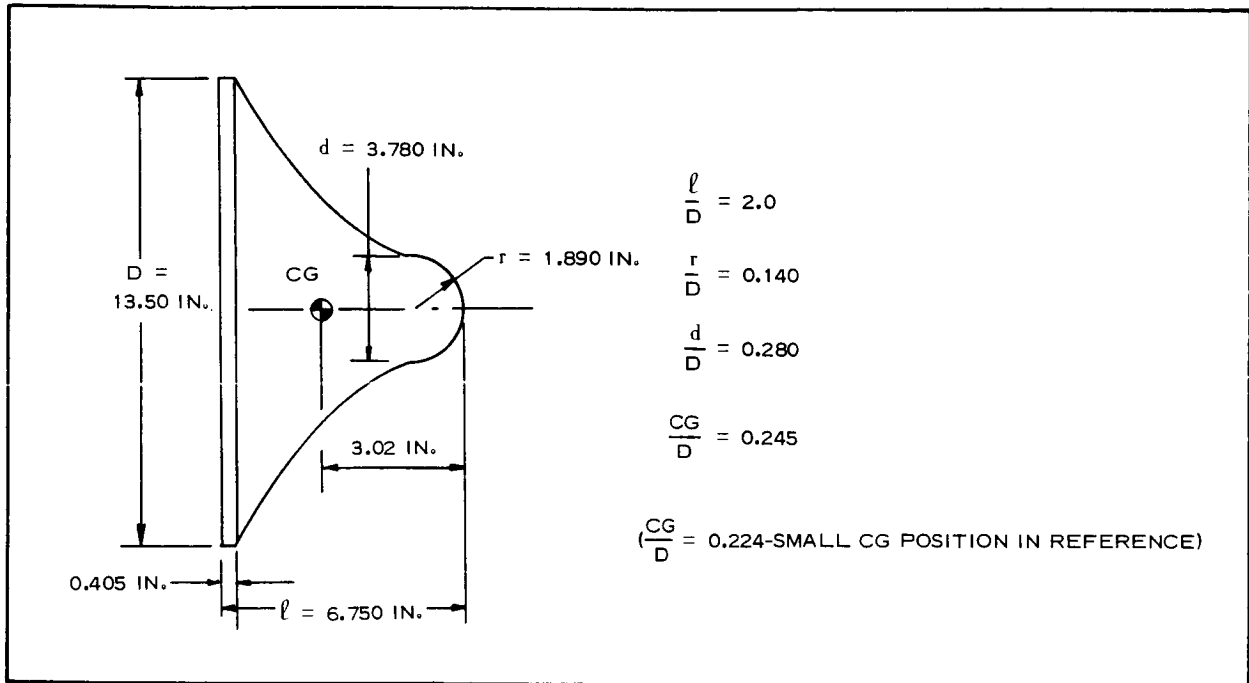


Figure 17 - Tension Shell

$$\left. \begin{aligned} C_{L_{\alpha}} &= -0.577 \text{ per radian} \\ C_{m_{\alpha}} &= -0.086 \text{ per radian} \\ C_{N_{\alpha}} &= +0.515 \text{ per radian} \end{aligned} \right\} \text{linear up to } \alpha = 40 \text{ deg}$$

$$C_D = 1.09$$

$$C_{m_q} = -0.097 \text{ per radian}$$

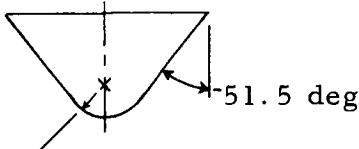
Moment center = cg

$$\left. \begin{aligned} \frac{cp}{D} &= 0.411 \\ \frac{cp}{l} &= 0.822 \end{aligned} \right\} \text{based on cg at } 0.245$$

Coefficients are based on D , $\pi D^2/4$, and qD/v .

Table I compares tension-shell aerodynamics with more familiar shapes.

TABLE I - TENSION-SHELL AERODYNAMICS

Body shape	C_{L_α}	C_{m_α}	C_{m_q}	$\frac{cp}{l}$ from nose	C_D
Blunted cone  $\frac{r}{D} = 0.235$	-0.330	-0.183	-0.148	0.591	0.880
Hemisphere	+0.620	-0.721	-0.281	0.420	0.450
Tension shell	-0.577	-0.086	-0.097	0.490	1.09

SECTION II - AERODYNAMIC AND THERMAL ENVIRONMENT ANALYSES

1. GENERAL

The following describes the range of aerodynamic loading and thermal environments the decelerator devices must be designed to face to perform successfully with structural integrity.

2. ATMOSPHERIC ENVIRONMENT

The variation of Mars atmospheric density with altitude below the tropopause is assumed to be in accordance with the adiabatic lapse-rate relation:

$$\rho_h = \rho_o \left(1 - \frac{\Gamma h}{T_o} \right)^{\frac{1}{\gamma - 1}}, \quad (1)$$

where

ρ_h = density at altitude

ρ_o = surface density,

Γ = adiabatic lapse rate K^+/km and $R/1000 ft$,

h = altitude,

T_o = surface temperature, and

γ = specific heat ratio.

Variation of static pressure with altitude is assumed to be in accordance with the reversible adiabatic process relation:

$$\frac{P_o}{P_1} = \left(\frac{T_o}{T_1} \right)^{\frac{\gamma}{\gamma - 1}}, \quad (2)$$

where

P_o = surface pressure,

P_1 = pressure altitude,

T_o = surface temperature, and

T_1 = stratospheric temperature.

Principles of gas dynamics for the inviscid ideal gas are assumed to be valid for the atmospheric properties listed in Table II. From JPL composite initial trajectories for VM7 and VM8 atmospheres, the deployment free-stream Mach numbers and altitudes are shown in Figure 18. For altitudes considered for the decelerator deployment, the variations in ambient pressure, temperature, and speed of sound are evaluated and plotted as bands of magnitudes versus altitude in Figures 19 and 20.

3. SURFACE PRESSURES ON DECELERATORS IN HIGH-SPEED FLOWS

Rapid techniques for estimating pressure distributions on decelerators in the high-speed flows are employed for analyses described in this section. One consists of the Newtonian impact law modified by replacing the constant of proportionality equal to 2.0 with the stagnation pressure coefficient behind the normal detached shock wave. In terms of the pressure ratios, the modified Newtonian relationships become:

$$\frac{P}{P_o} = \frac{P}{P_o} + \left(1 - \frac{P_\infty}{P_o} \right) \sin^2 \theta \quad (3)$$

where

P = local static pressure on surface,

TABLE II - CHARACTERISTICS OF VM ATMOSPHERES

Property	Symbol	Dimension	Atmosphere profile			
			VM3	VM4	VM7	VM8
Surface pressure	P_o	mb	10.0	10.0	5.0	5.0
		lb/sq ft	20.9	20.9	10.4	10.4
Surface density	ρ_o	(gm/cu cm) 10^5	1.365	2.57	0.68	1.32
		(slugs/cu ft) 10^5	2.65	4.98	1.32	2.56
Surface temperature	T_o	K	275	200	275	200
		R	495	360	495	360
Stratospheric temperature	T_s	K	200	100	200	100
		R	360	180	360	180
Acceleration of gravity at surface	g	cm/sec ²	375	375	375	375
		ft/sec ²	12.3	12.3	12.3	12.3
Composition						
CO ₂ (by mass)			28.2	70.0	28.2	100.0
CO ₂ (by volume)			20.0	68.0	20.0	100.0
N ₂ (by mass)			71.8	0.0	71.8	0.0
N ₂ (by volume)			80.0	0.0	80.0	0.0
A (by mass)			0.0	30.0	0.0	0.0
A (by volume)			0.0	32.0	0.0	0.0
Molecular weight	M	mol ⁻¹	31.2	42.7	31.2	44.0
Specific heat of mixture	C_p	cal/gm C	0.230	0.153	0.230	0.166
Specific heat ratio	γ		1.38	1.43	1.38	1.37
Adiabatic lapse rate	Γ	K/km	-3.88	-5.85	-3.88	-5.39
		R/1000 ft	-2.13	-3.21	-2.13	-2.96
Tropopause altitude	h_T	km	19.3	17.1	19.3	18.6
		kilo ft	63.3	56.1	63.3	61.0
Inverse scale height (stratosphere)	β	km ⁻¹	0.0705	0.193	0.0705	0.199
		ft ⁻¹ x 10^5	2.15	5.89	2.15	6.07
Continuous surface wind speed	v	ft/sec	155.5	155.5	220.0	220.0
Peak surface wind speed	v_{max}	ft/sec	390.0	390.0	556.0	556.0
Design vertical wind gradient	dv/dh	ft/sec/1000 ft	2	2	2	2

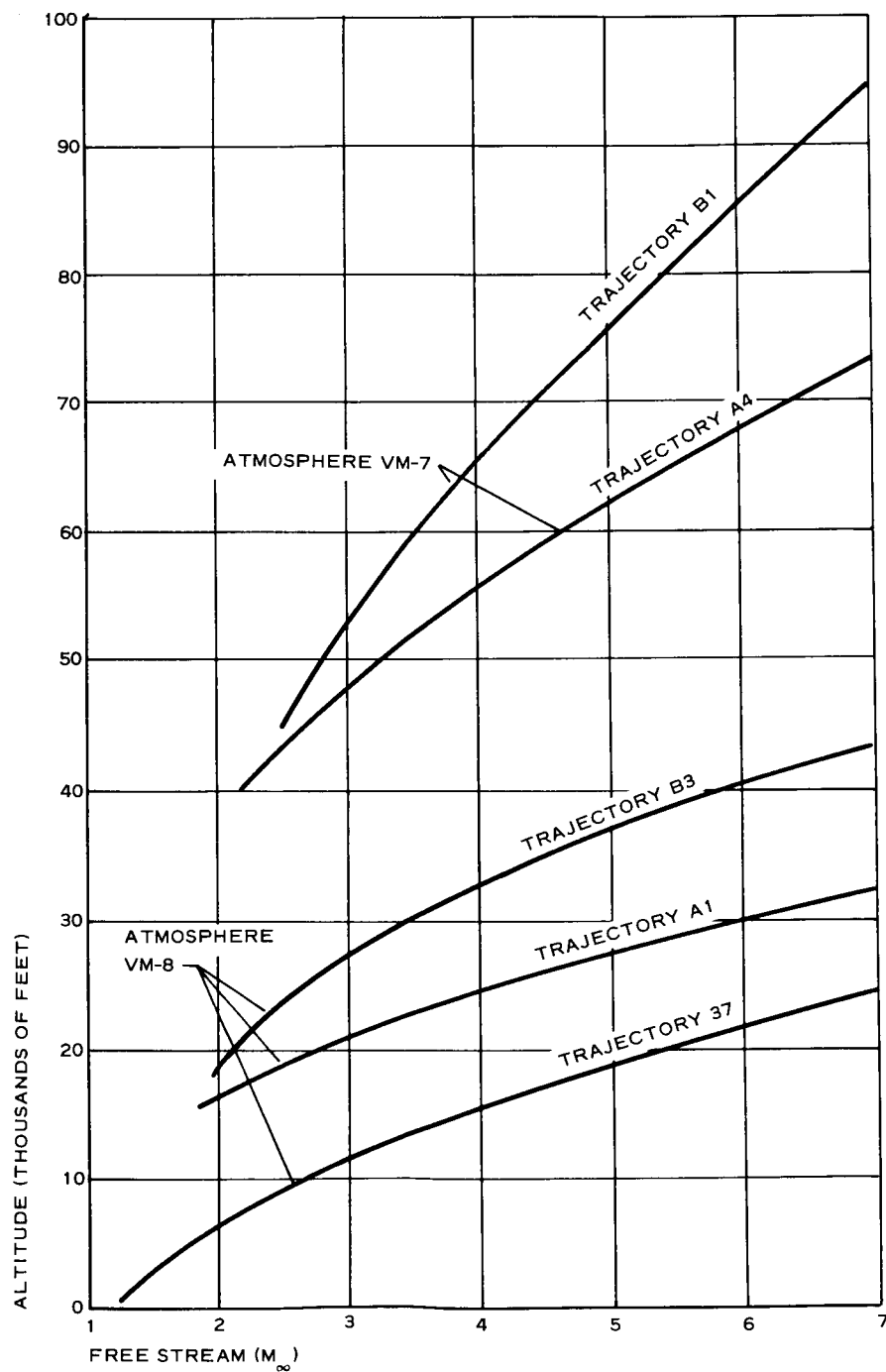


Figure 18 - Initial Mars Entry Trajectories

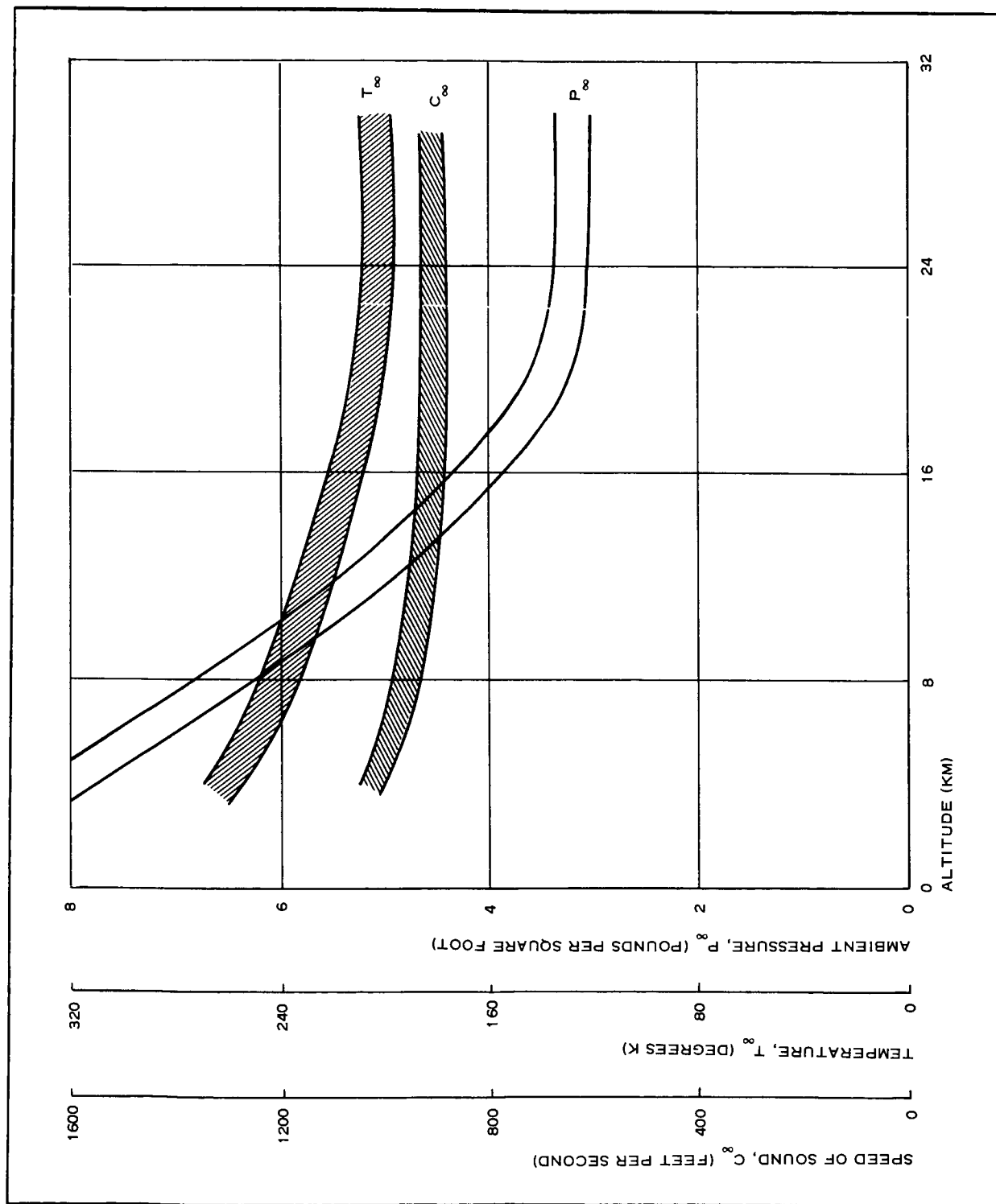


Figure 19 - Decelerator Deployment Envelope, VM7 Atmosphere

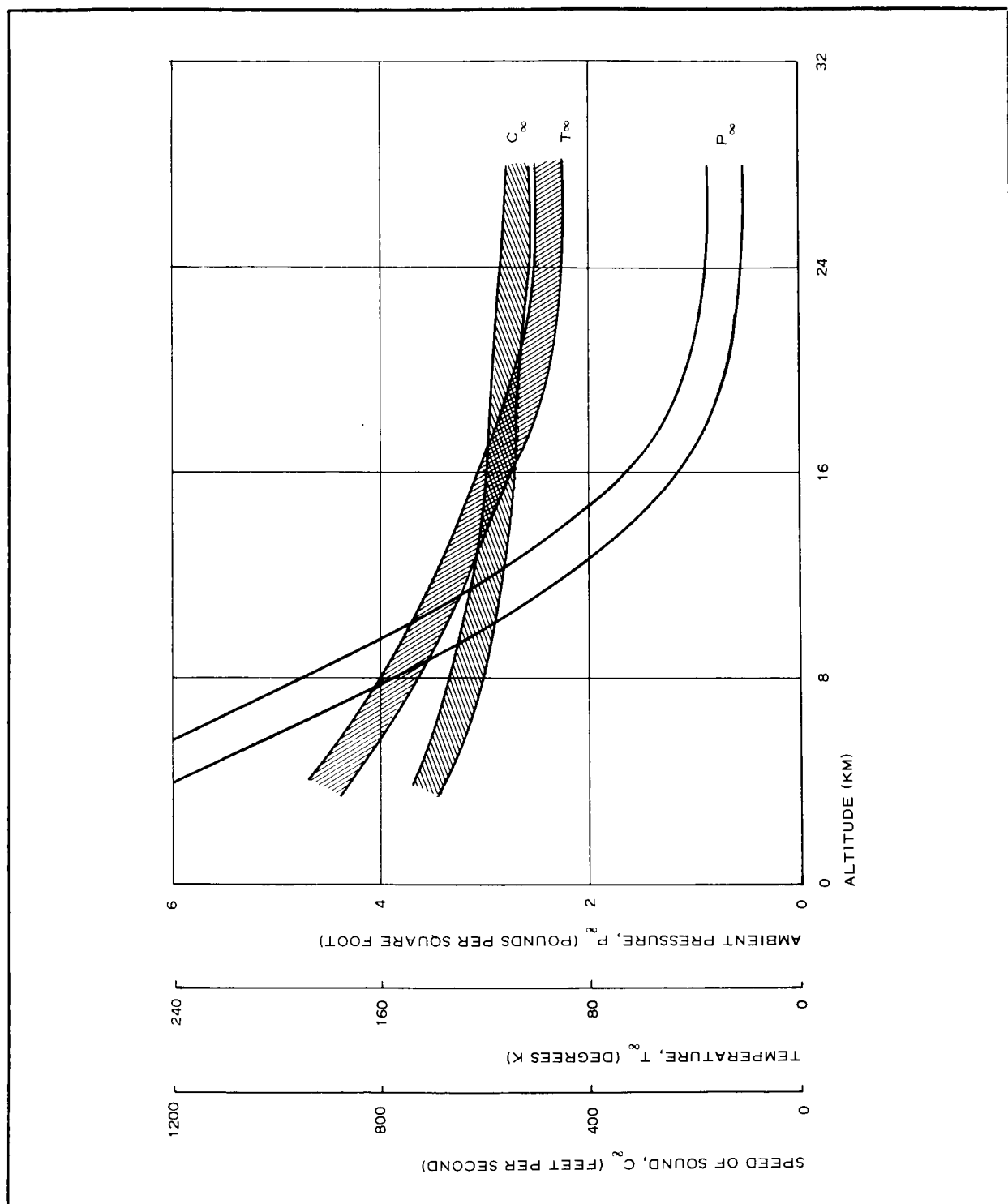


Figure 20 - Decelerator Deployment Envelope, VM8 Atmosphere

P_o = stagnation pressure behind normal shock,

P_∞ = free-stream static pressure, and

θ = local-surface inclination angle.

This approach has limitations, such as:

1. Existence and condition uniqueness require high supersonic flows.
2. Leading edge of the configuration should be blunted.
3. Accuracy decreases as surface slope with respect to stream decreases.
4. The effective value of specific heat (γ) changes significantly across the normal shock in equilibrium real-gas hypersonic flow, but it remains about constant over the leading edge of the blunt body downstream of the stagnation point.

The burble fence of a BALLUTE^a causes flow separation at the fence, a phenomenon similar to the presence of a forward-facing step in supersonic flow. This phenomenon is associated with a pressure plateau with its peak located at the fence and with the magnitude proportional to the local Mach number and the turning angle of the flow. The separation shock is assumed to be negligible with no local total pressure loss resulting from it.

For capsule-decelerator configurations shown in Figures 21 through 24, pressure distributions on the capsule also are considered because the systems are integrated. The capsule geometry and attached conical flare decelerator are shown in Figure 21. The shapes of this configuration and a BALLUTE up to about $Y/R_D \approx 1.0$, where separation begins because of the fence, are not slender; hence, the blunt body approach is justified for the indicated flow region.

^aTM, Goodyear Aerospace Corporation, Akron, Ohio.

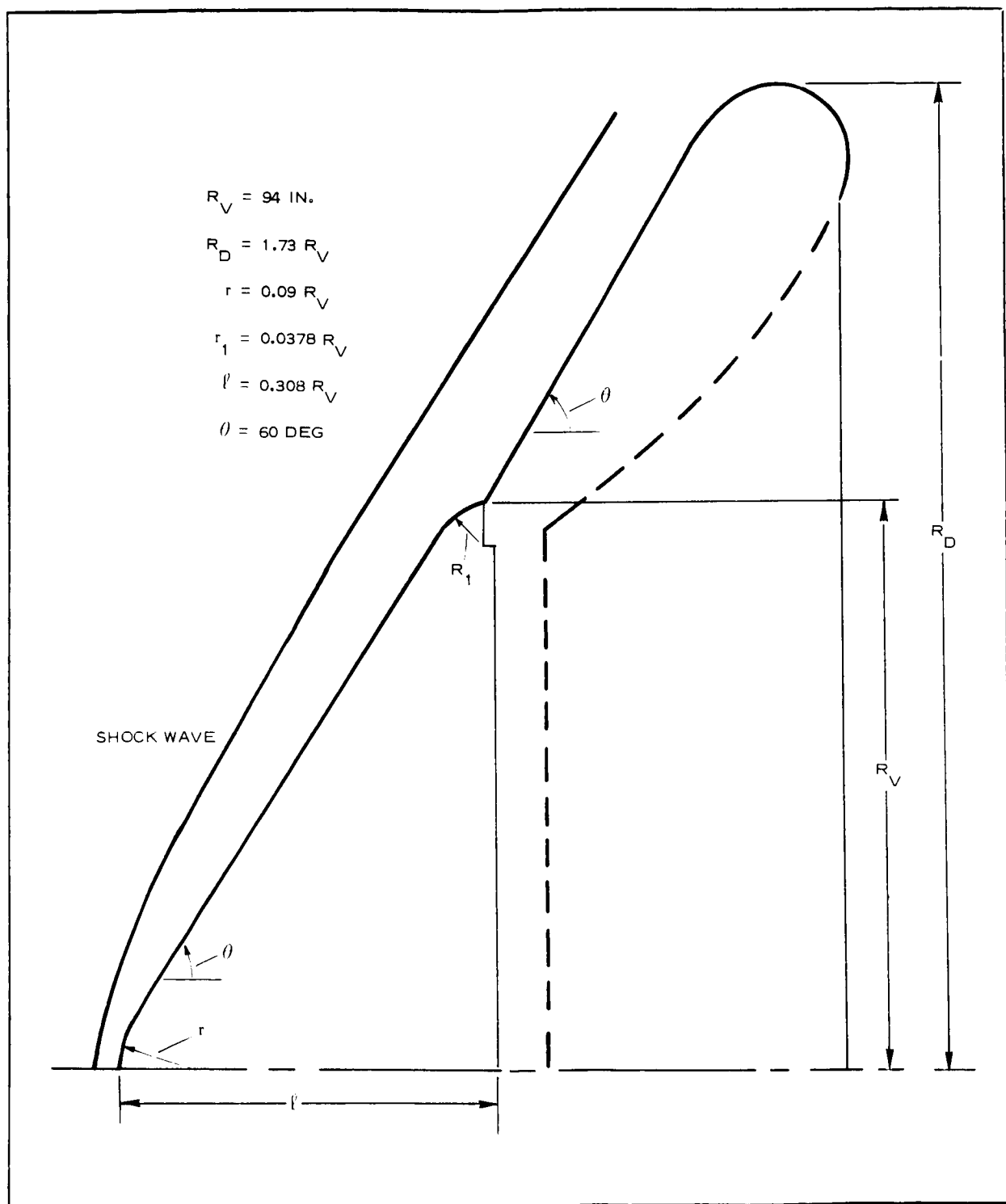


Figure 21 - Entry Capsule and Decelerator Configuration

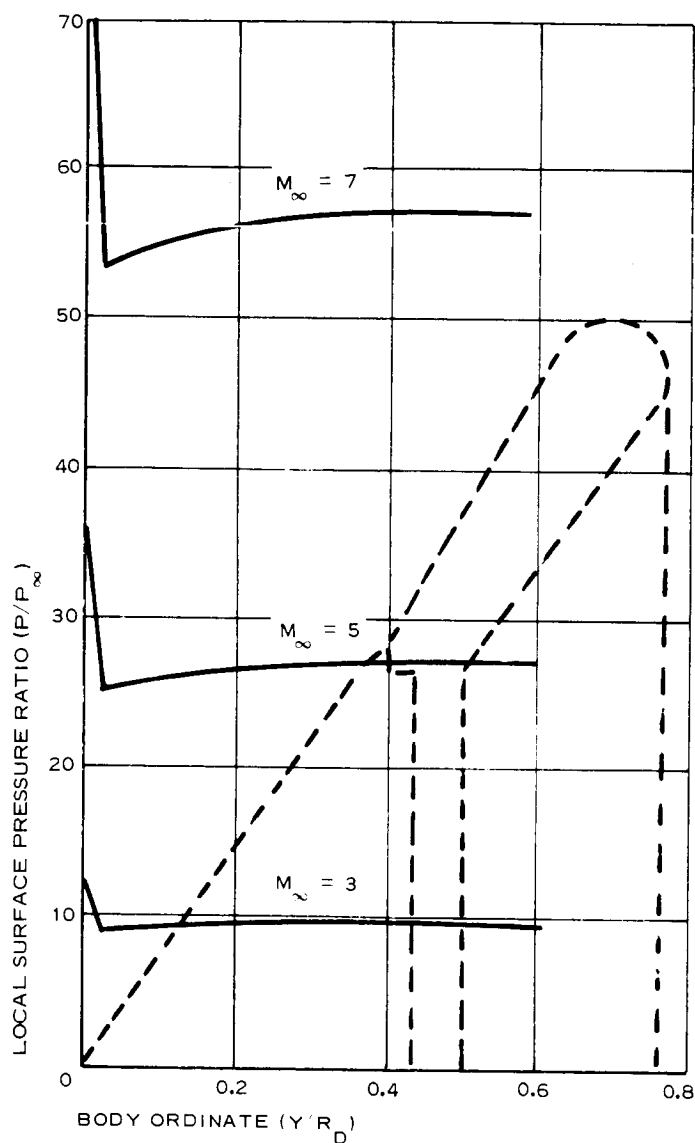


Figure 22 - JPL Capsule-Conical Flare Decelerator,
Estimated Pressure Distribution

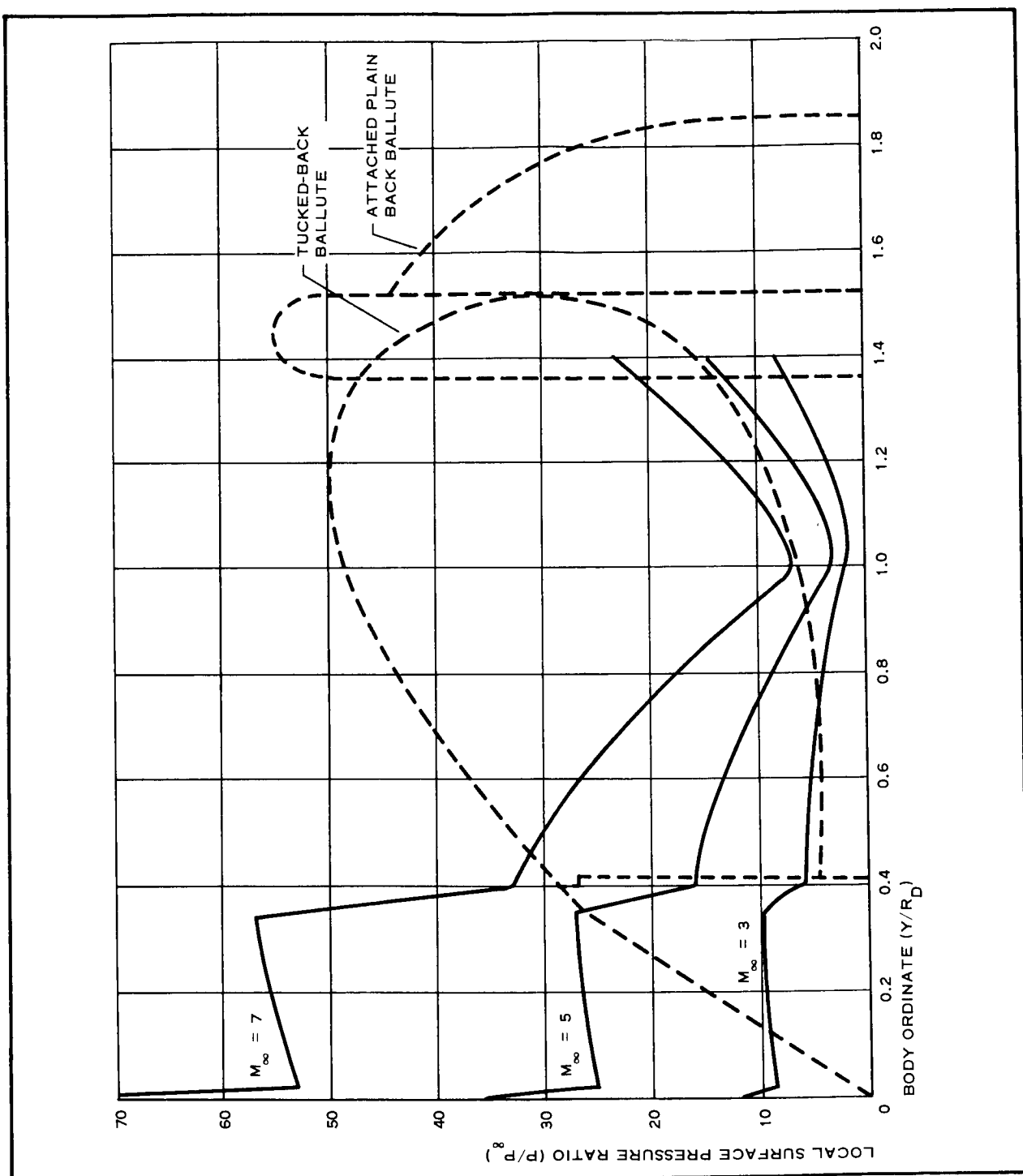


Figure 23 - JPL Capsule-BALLUTE Decelerator
Estimated Pressure Distribution

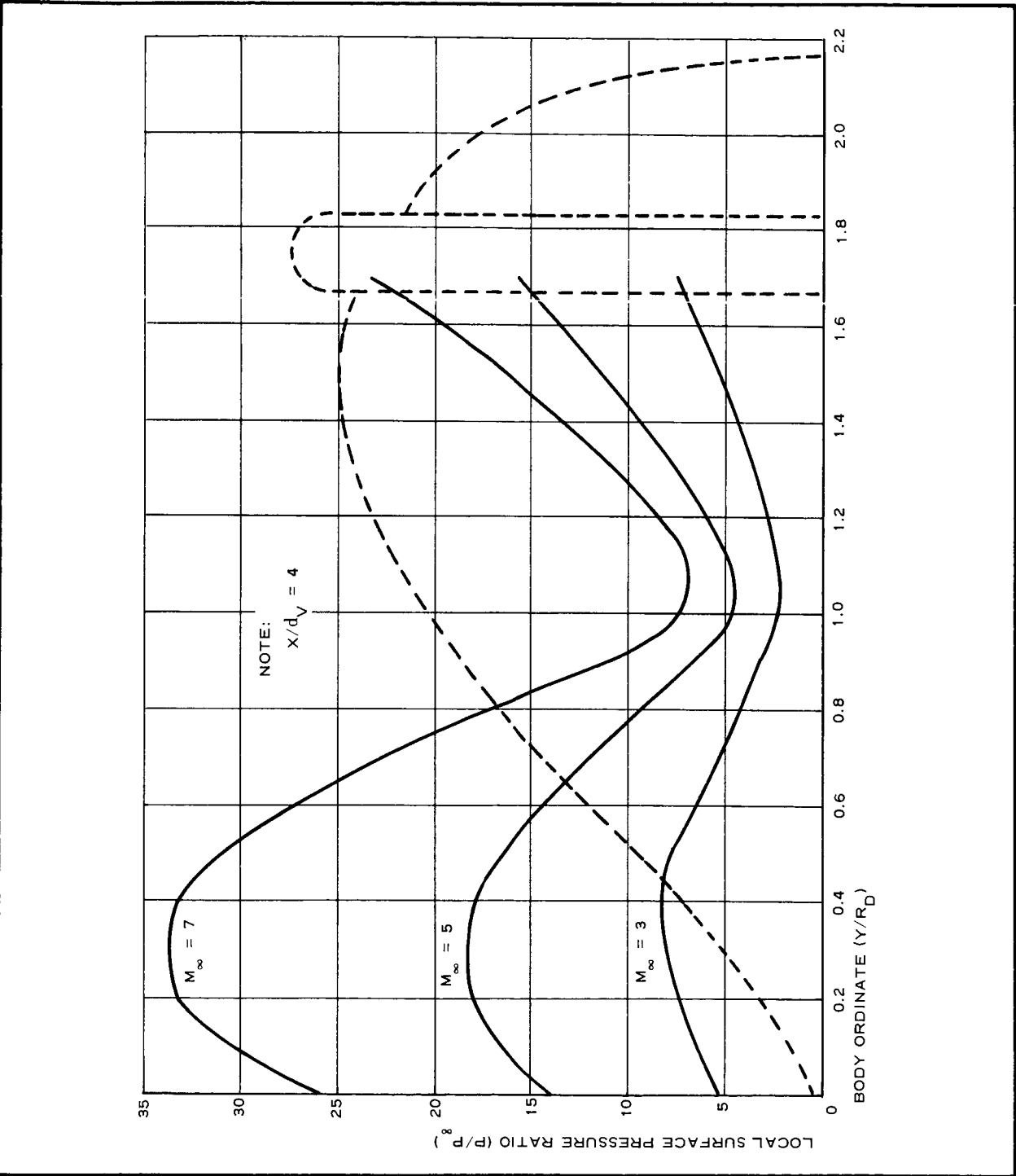


Figure 24 - Trailing BALLUTE Decelerator,
Estimated Pressure Distribution

No direct attempt was made in this study to investigate the shock-wave shape and structure, but a first order approximation for $M_\infty \approx 3$ shock shape is shown in Figure 21.

The resultant estimated pressure distribution over the capsule-conical flare configuration is shown in Figure 22. Similarly, Figure 23 presents an estimated pressure distribution for the capsule-attached BALLUTE configuration. For a BALLUTE trailing the capsule at $X/d_v \approx 4$, it is necessary to consider the effect of the capsule wake on the flow field of the BALLUTE. According to the available information the viscous wake width at this x/d is a function of the forebody shape and Mach number of the free stream as the principal variables. Thus, the forebody base radius at the flow conditions under consideration is related to wake half-width as follows:

$$0.6 \leq \frac{y_w}{R_v} \leq 0.8,$$

where

y_w = viscous wake half-width and

R_v = forebody base radius.

Based on wake geometry and on wake velocity "frozen" at the outer edge of the viscous wake at about $M \approx 3.0$ behind blunted bodies, associated pressure distributions are estimated in Figure 24.

Experience shows loading on the after part of a BALLUTE is inversely proportional to M_∞^2 . In terms of pressure ratios, estimated values are:

$\underline{M_\infty}$	$\underline{P/P_\infty}$
3	1.570
5	1.650
7	1.685

Results of this short inquiry are far from precise and are conservative. Knowledge of the Martian atmosphere is obtained from remote observations and indirect experiments that offer theoretical interpretations based on the physical processes occurring on the Earth.

4. THERMAL ENVIRONMENT

a. Deployment Conditions

Deployment of a first-stage decelerator for the Mars lander vehicle in the near surface region of the Martian atmosphere was initially established in Mach range $2 < M_D < 7$.

The approximate severity of aerodynamic heating may be estimated with deployment condition data illustrated in Figures 25 and 26. Data in Figure 25 are for the VM7 model atmosphere. Figure 26 data are for the VM8 model atmosphere. Lines of constant dynamic pressure and adiabatic wall temperature using a recovery factor of 0.9 are shown as functions of altitude and deployment Mach number. In general, deploying the first-stage decelerator at the low end of the Mach number range is not expected to produce significant aerodynamic heating in either atmosphere because of the potentially low thermal environment. However, as the deployment Mach number is increased to five or higher, the prospects of aerodynamic heating are increased. In the VM7 atmosphere, for example, at a deployment speed of Mach 5 and altitude of 65,000 ft, the adiabatic wall temperature becomes about 1500 F and dynamic pressure 60 psf. At Mach 7, the adiabatic wall temperature increases to about 3,000 F for deployment at 85,000 ft and approximately the same dynamic pressure.

With similar deployment conditions in the VM8 atmosphere, aerodynamic heating prospects encountered are approximately the same as for the VM7 model atmosphere. Thus, heating in the two model atmospheres will be about the same.

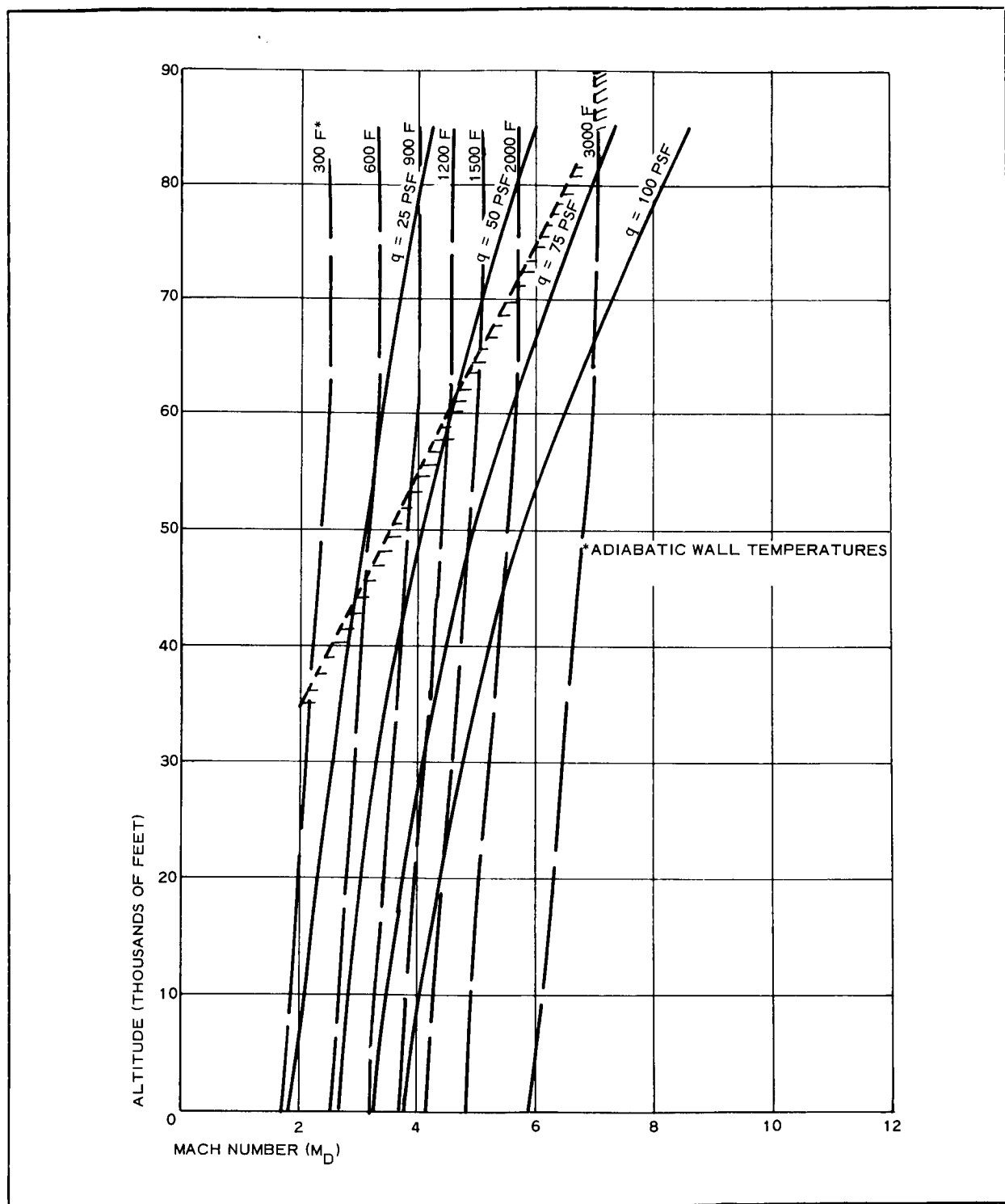


Figure 25 - Deployment Conditions, VM7 Atmosphere

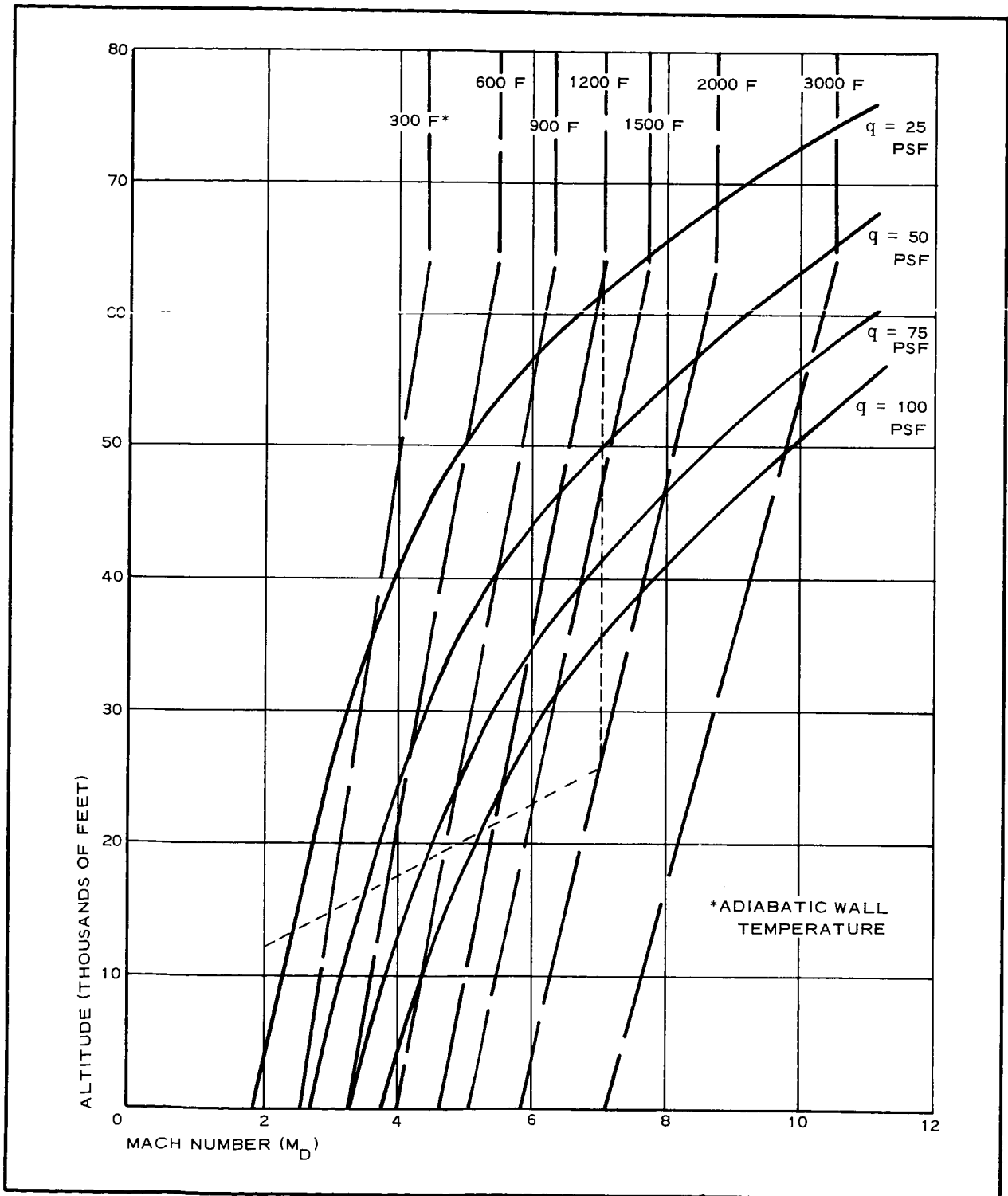


Figure 26 - Deployment Conditions, VM8 Atmosphere

Figure 25 and 26 show limits of the deployment envelope established from trajectory analysis to attain final-stage decelerator deployment conditions of about Mach 1 above 10,000 ft. It appears that the severest deployment cases ($5 < M_D < 7$) will encounter adiabatic wall temperature of about 3000 F and maximum dynamic pressures of 100 psf. Because these conditions are generated at the upper end of the deployment regime, these flight conditions must be examined more rigorously to determine the effect of aerodynamic heating on decelerator material.

b. Heat Flux Rates

The first-stage decelerators studied in this program were (1) attached conical flare, (2) attached plain-back BALLUTE, (3) tucked-back BALLUTE, (4) trailing BALLUTE. The single position directly amenable to heat-flux rate analysis for atmospheres other than air is the stagnation point of entry capsules. In particular,

$$\dot{q}_o = \bar{C} \left(\frac{P_o}{R_N} \right)^{1/2} (U_\infty)^N (1 - g_w) , \quad (4)$$

where

\dot{q}_o = Stagnation point heat flux rate, BTU/ft²-sec;

P_o = Stagnation point pressure, atmospheres;

R_N = Nose radius (feet);

U_∞ = Free-stream velocity divided by 10,000 fps;

g_w = Ratio of wall to total enthalpy;

\bar{C} = Constant depending on gas composition; and

N = Exponent depending on gas composition.^{1, a}

^aSuperior numbers in the text refer to items in the List of References.

This equation is well suited for estimating the stagnation point heat-flux rate during the deceleration profile. Thus, it appears appropriate first to generate this heating rate and then to estimate the heating rates further back on the body on the basis of the stagnation point heat-flux rates. Typical stagnation point heat-flux rates are shown in Figure 27 for VM7 and VM8 atmospheres, as functions of flight velocity. These rates depend on stagnation pressure, total enthalpy, and body geometry. After the trajectory has been specified, rates may be estimated from flow properties generated at the stagnation point as a function of velocity and altitude.

Heat-flux rates to the surface of interest (that is, the expandable flares or BALLUTES) then can be calculated from the generated stagnation-point heat flux rates. Simplest is Lee's distribution method.² Assuming a hemispherical blunt-nose body over which laminar flow exists on the forebody surface and assuming also a 60-deg half angle

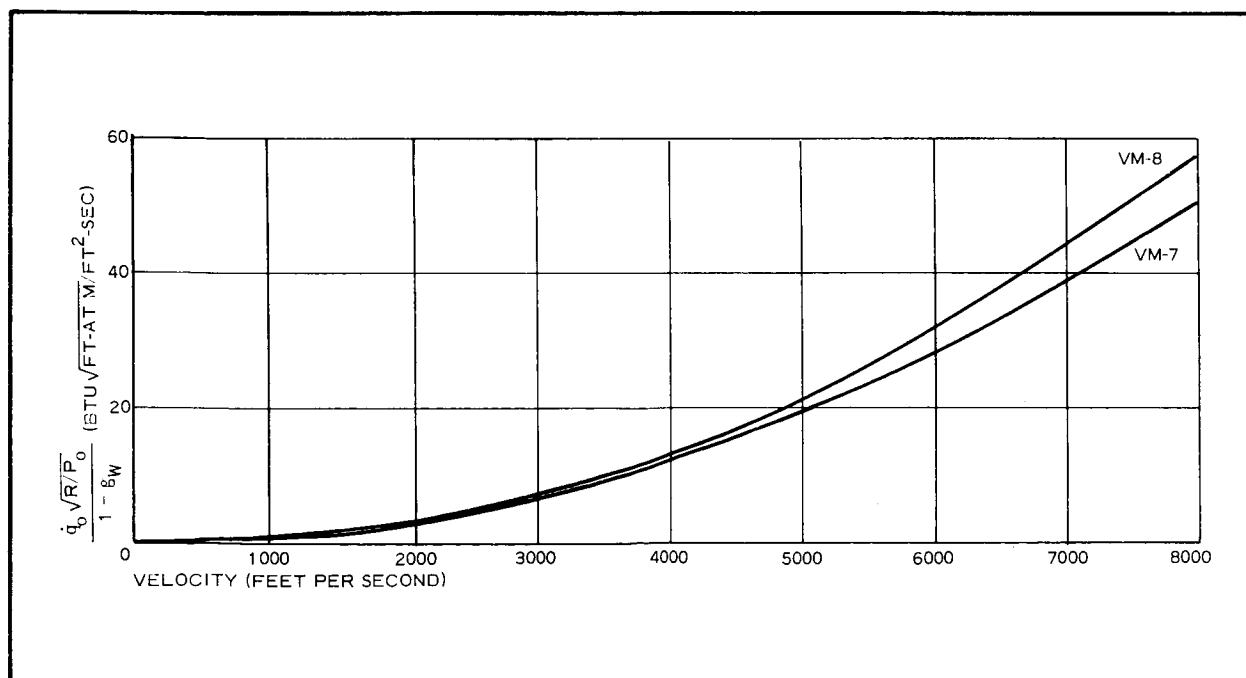


Figure 27 - Stagnation Point Heat-Flux Rate

with an expandable flare of similar geometry, the ratio of local heat-flux rate to stagnation point heat flux can be calculated using Lees' equation.

On the basis of a modified Newtonian pressure distribution over this forebody surface, an evaluation of the local heat-flux rate showed it to be approximately 25 percent of the stagnation-point rate. To confirm this estimated heat flux rate magnitude, Goodyear Aerospace surveyed reports of experimental heat-transfer data dealing with the testing of blunt face configurations somewhat similar to the present configurations. Data obtained are shown in Figure 28 as functions of unit Reynolds number. Single-point data for a hemispherical nose followed by half-angle flares of 30, 50, and 70 deg were obtained.³ These data showed that the local heat flux rate averages about 20 to 40 percent of the stagnation point heat-flux rate. The local heat-flux rate variation for the 40-deg half angle configuration was obtained.⁴ The upper curve was obtained for a solitary BALLUTE and the lower curve for a BALLUTE trailing in the wake of a leading body. The variation in local heat flux rate was again about 20 to 40 percent of the stagnation point heat-flux rate except with Reynolds numbers above 10^6 where rates begin to rise significantly.

Because of this cursory examination of local heat-flux rate distribution for various configurations, Goodyear Aerospace assumed that a local heat-flux rate of 0.3 of the stagnation-point heat-flux rate would be a representative value for estimating heat-flux rate profiles during deceleration of all configurations. Heat-flux rate profiles for various trajectories and atmospheres are shown in Figures 29 through 35 for a wall temperature of 70 F. These heat-flux rate profiles show the effect of increasing drag potential of the decelerator device. In terms of the heat-flux profile, because deployment conditions are identical, increasing decelerator drag potential decreases heating exposure time.

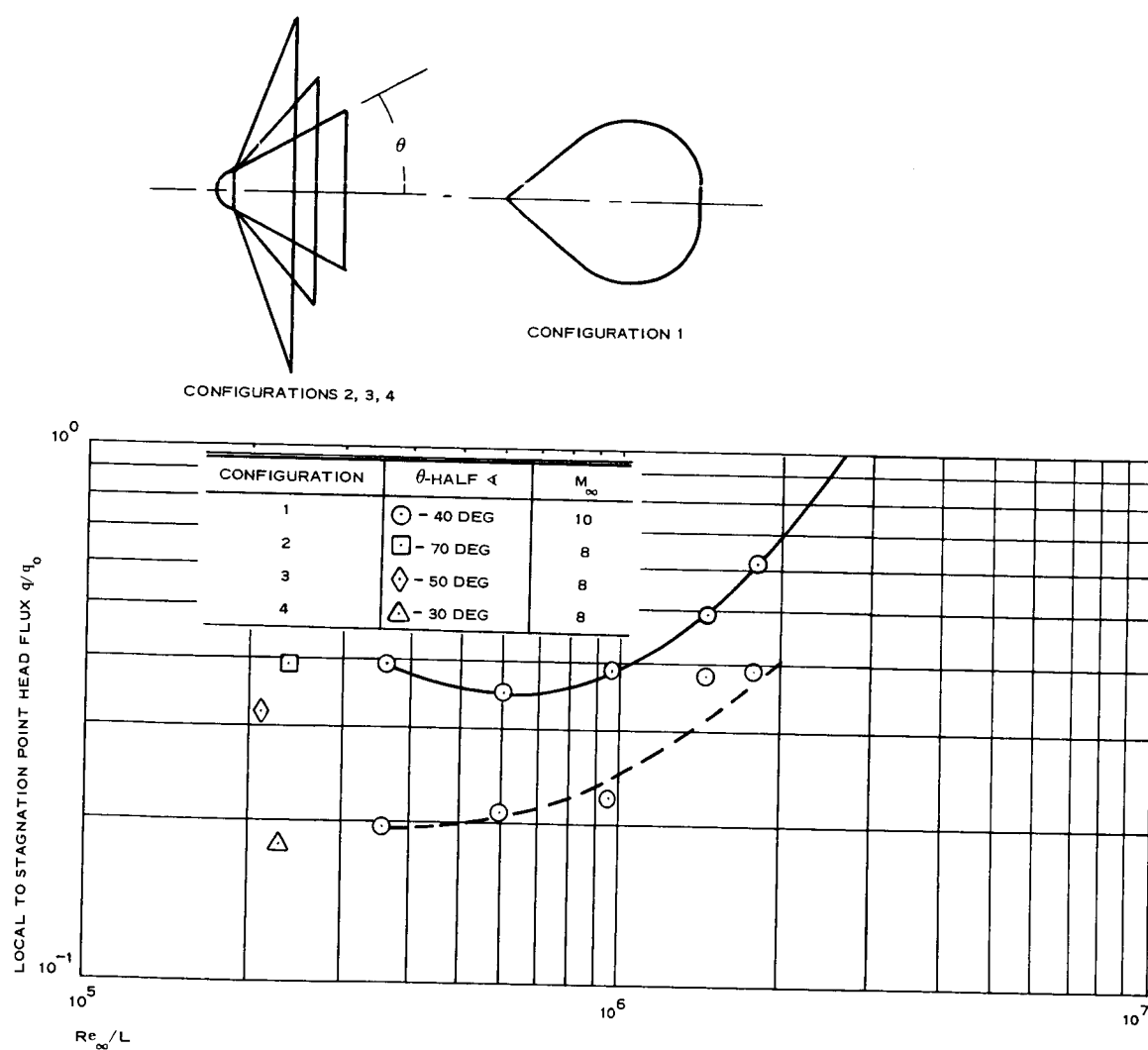


Figure 28 - Local Heat-Flux Rate versus Unit Reynolds Number

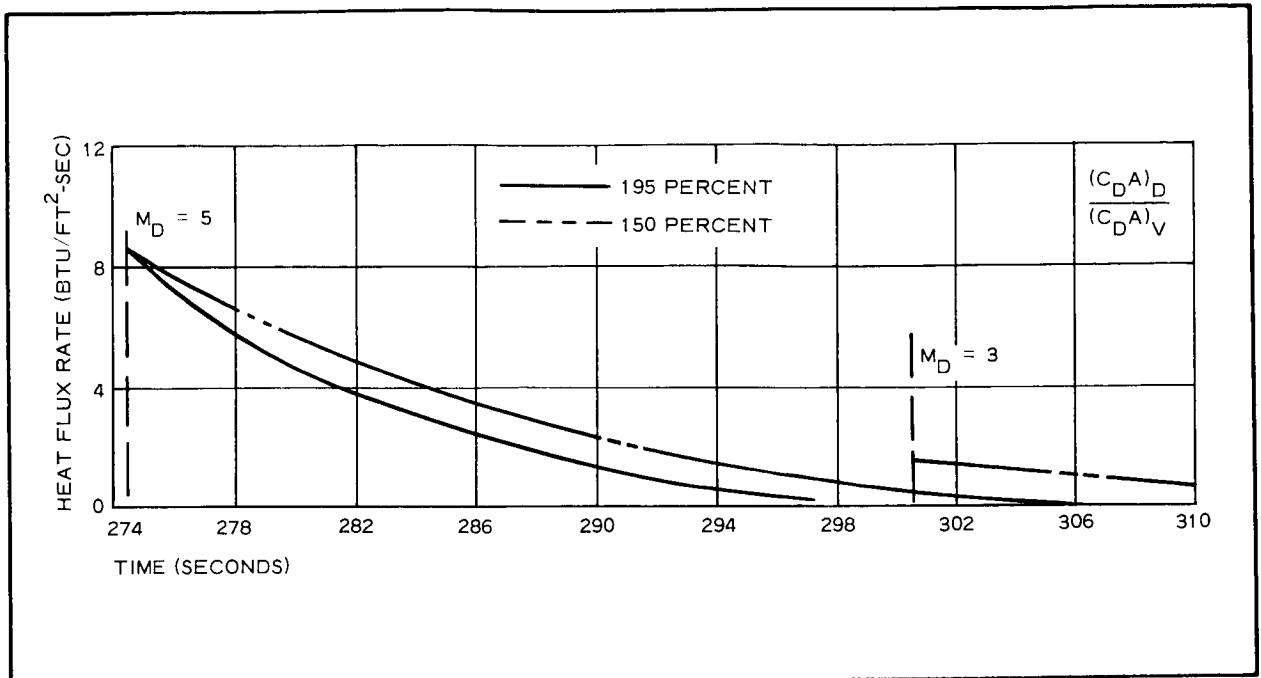


Figure 29 - Heat-Flux Rate, Trajectory B1

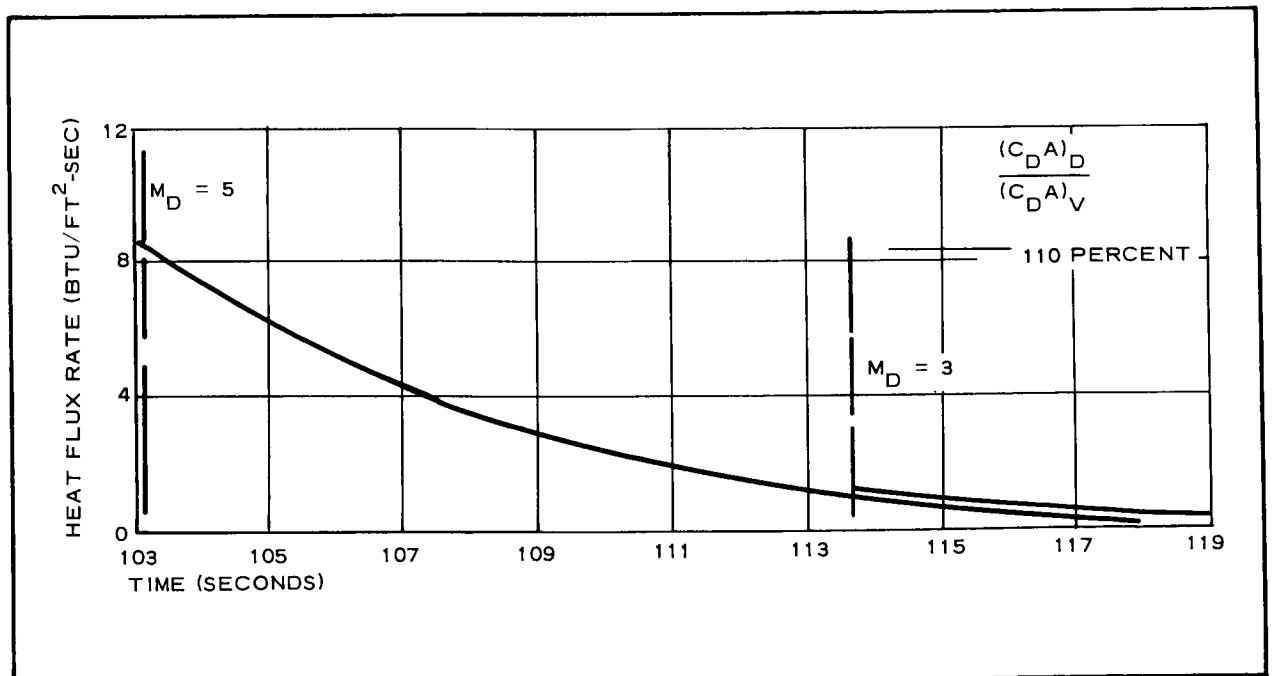


Figure 30 - Heat-Flux Rate, Trajectory A4

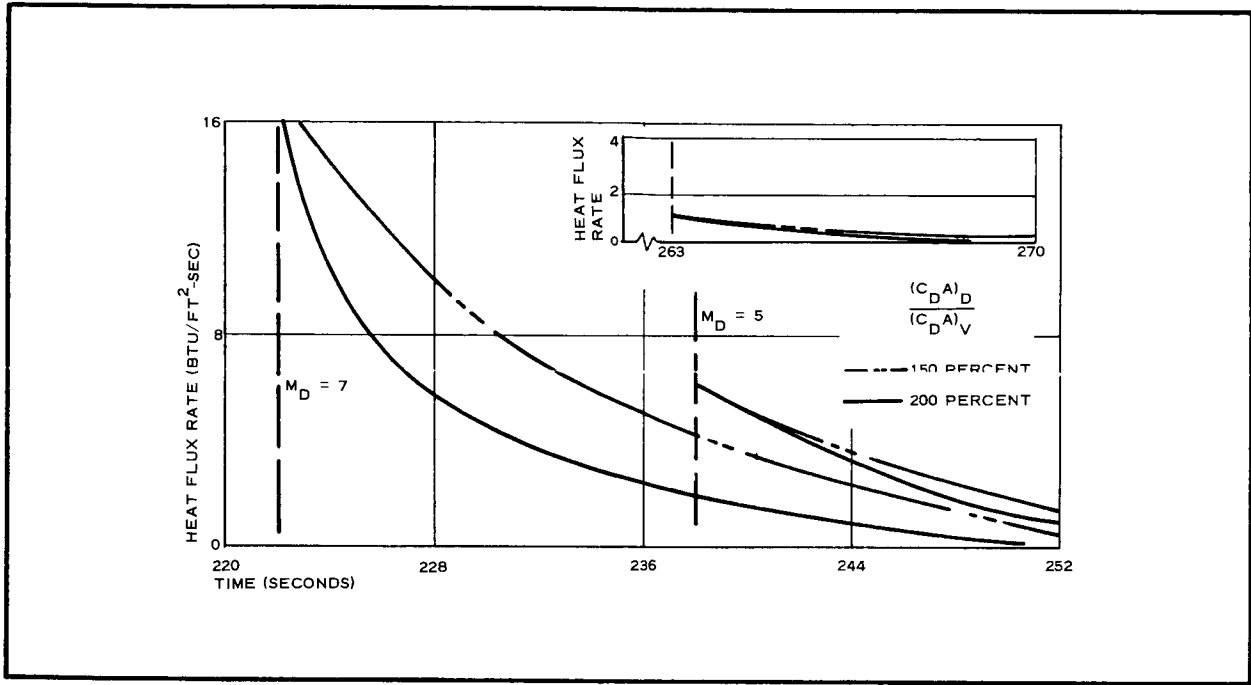


Figure 31 - Heat-Flux Rate, Trajectory 22

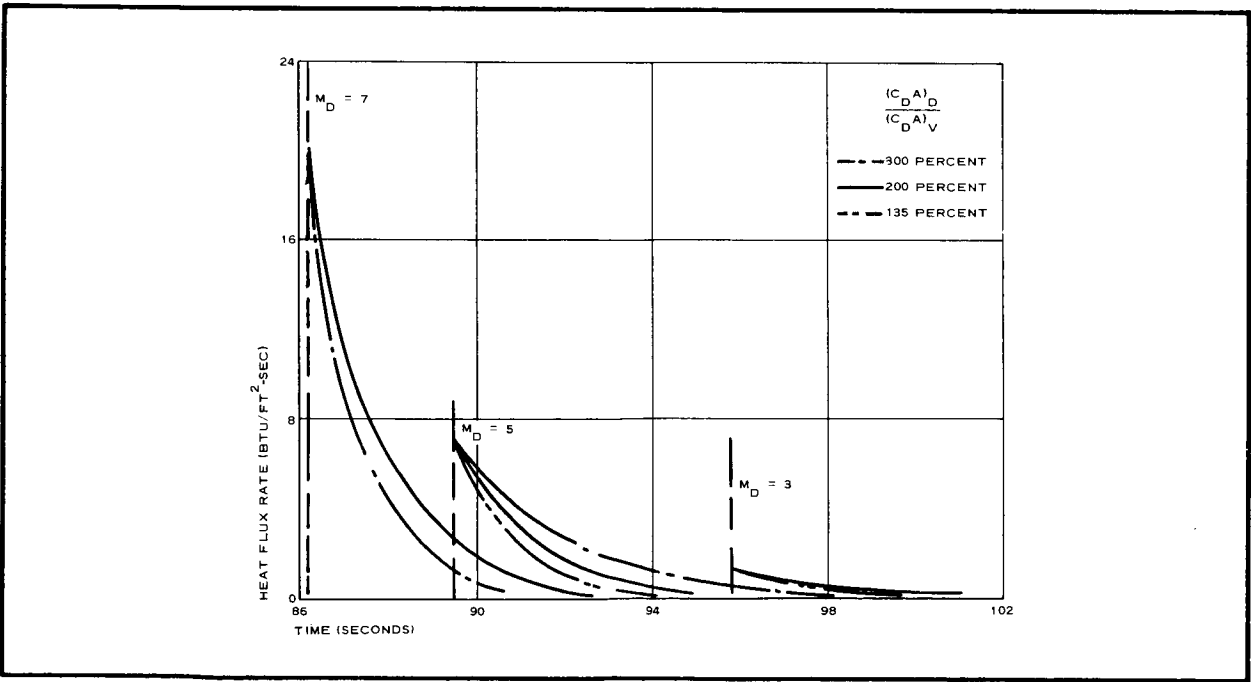


Figure 32 - Heat-Flux Rate, Trajectory 19

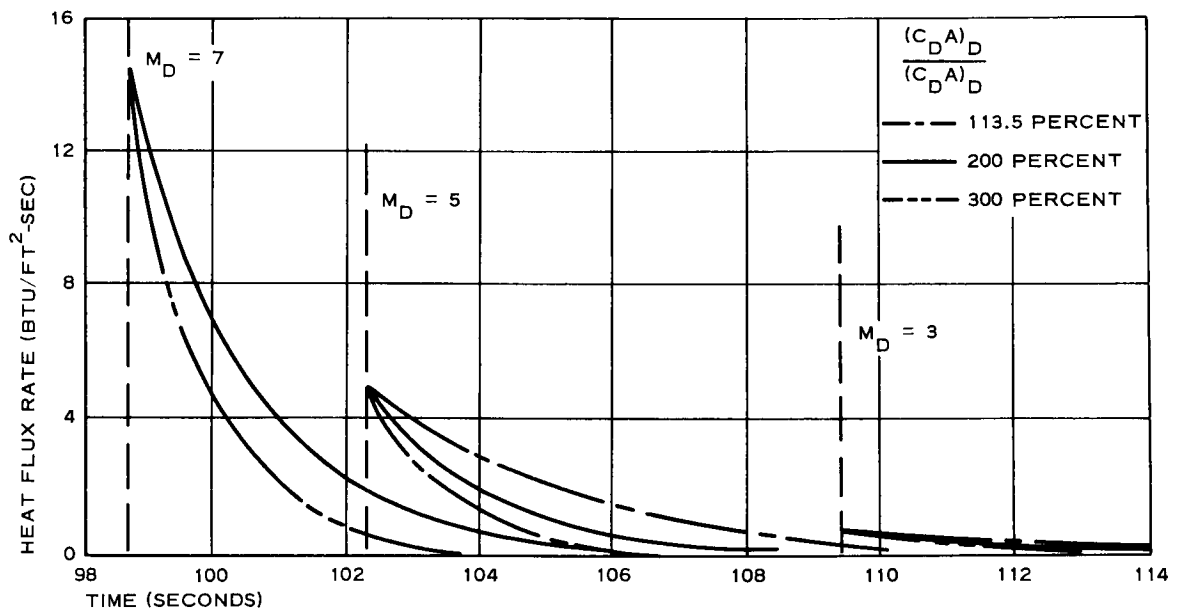


Figure 33 - Heat-Flux Rate, Trajectory 37

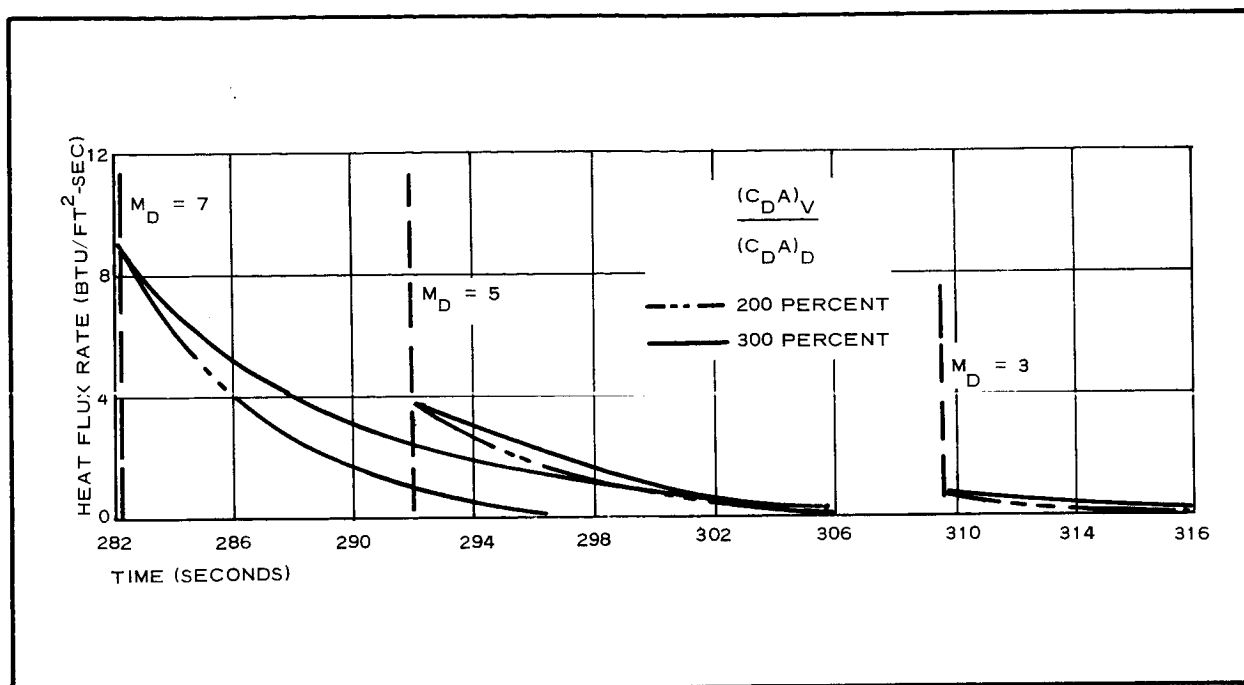


Figure 34 - Heat-Flux Rate, Trajectory A1

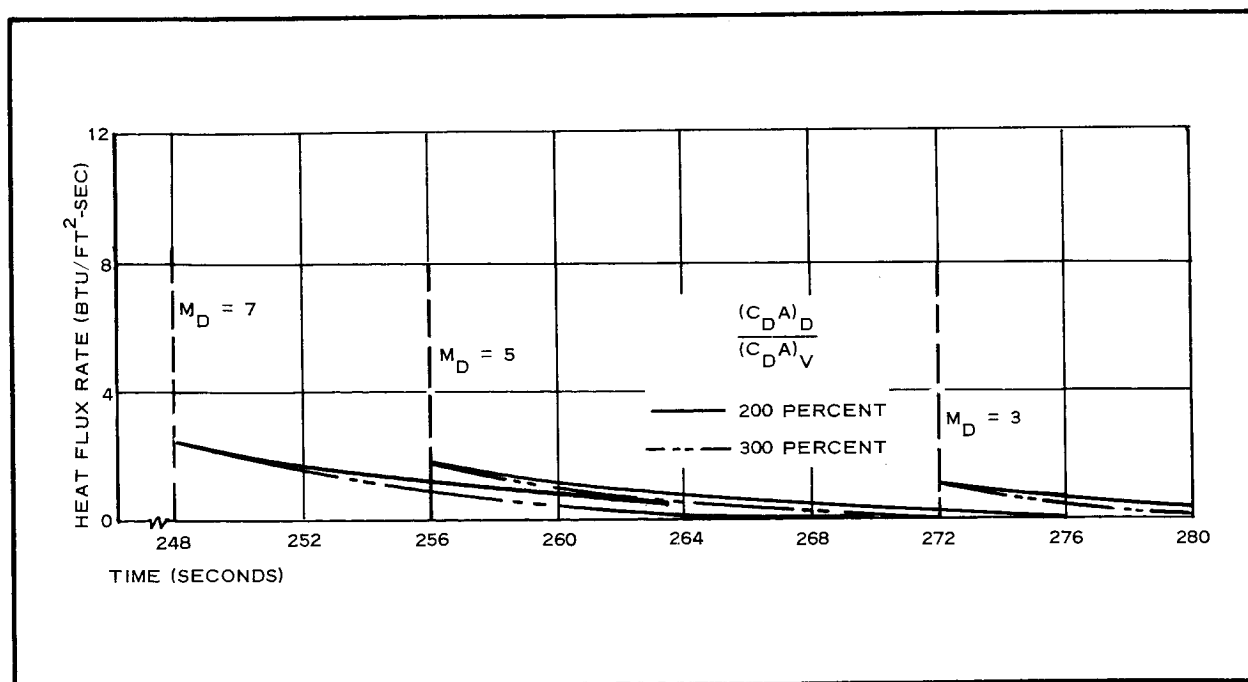


Figure 35 - Heat-Flux Rate, Trajectory B3

Maximum heat-flux rates encountered occur immediately at deployment and appear to be well within the capability of the fabrics. However, deployment at Mach 7 in trajectory 22 of the VM7⁷ atmosphere and trajectory 37 of the VM8 atmosphere indicate that the initial heat-flux rates may be quite substantial, although time of deceleration heating is quite short.

SECTION III - STERILIZATION AND MATERIALS

1. STERILIZATION REQUIREMENTS AFFECTING DESIGN

a. General

Planning to meet sterilization requirements for the Mars entry capsule requires these guide lines:

1. Sterilization techniques
2. Spacecraft design for sterilization
3. Sterile assembly techniques
4. Compatibility of materials and components with sterilization procedures

b. Sterilization Techniques

Dry heat is recommended for sterilization in most cases. JPL has established sterilization specifications for Type Approval and Flight Acceptance equipment for the Mars entry capsule.⁵ If the entry capsule could be encapsulated in a biological barrier with proper heat soak and kept within this barrier until just before landing, the sterilization requirement would be met. Voyager entry capsule design plans are proceeding with this technique.

Because of two factors, other sterilization techniques are being investigated, however. An entry capsule capable of surviving the heat soak may not be possible. If this is true, parts that cannot survive must be sterilized differently and inserted with sterile techniques into the capsule after heat soak. The second factor is the time relationship of various sterilization processes. As the number of organisms increases, time required to reach a given level of sterility

increases. A knowledge of initial contamination is required to determine final condition.

Among toxic chemicals that can be used in a gaseous state, ethylene oxide generally is preferred for surface sterilization of spacecraft. Currently, a blend of 12 percent ethylene oxide and 88 percent Freon 12 is suitable for spacecraft sterilization. Other compounds are available for special applications. Among these are formaldehyde, methyl bromide, betapropiolactane, ethylenimine, and paracetic acid. Available wipe-on disinfectants include plenol, quaternary bases, mustards, and organic solvents.

Radiation effectively sterilizes. Sufficient doses of ultraviolet below 3200 Å provide surface sterilization; however, penetration is poor. X-rays and gamma rays have greater penetrating powers, but these are detrimental to many spacecraft components.

Filtration is available for sterilizing liquids and gases. The smallest organisms known are from 0.01 to 0.1 μ . Filters with small pore size combined with a high dielectric constant across the filter used in a series can provide statistical assurance of sterility.

c. Spacecraft Design for Sterilization

Various research efforts have sought to determine compatibility of materials and components with sterilization methods and environments. The JPL approach to the entry capsule is to develop a qualified parts list for dry-heat sterilization and to design the capsule using this list. Design-around techniques will be used and other parts will be sterilized for insertion after heat soak in the capsule.

As a backup method for heat sterilizing the entire capsule, individual parts can be sterilized, assembled in a sterile environment, and inserted into the spacecraft after the major part of the spacecraft has been heat sterilized. Clean-room techniques with added biological considerations would be used.

Placing a sterile spacecraft or entry capsule on a planetary surface requires consideration of sterilization techniques from beginning of design. Sterilization must be integrated into each design phase.

These design concepts should include:

1. Minimum assembly contact points, voids in structure, and assembly steps
2. Maximum use of self-sterilizing components and materials or those rendered sterile during manufacture
3. Maximum assembly of the spacecraft prior to internal sterilization by dry heat.
4. Sterile assembly of the major subsystem, terminal surface sterilization, and emergency subsystem replacement or resterilization
5. Retention of payload encapsulation until an established distance from earth is reached.

A subsystem that must be designed from the beginning for sterilization is the spacecraft structure. Sharp edges and crevices must be held to a minimum to prevent collection of organisms. The maximum surface exposure must be attained for ease of surface sterilization. Efficient heat flow and dimensional stability must be obtained for ease of heat sterilization. Overall geometry must remain simple for ease of encapsulation.

d. Sterile Assembly of Spacecraft

Basic techniques of sterile assembly, derived from techniques developed in biological laboratories, are:

1. A biologically leak-tight enclosure
2. Sterilant and purge gas transfer apparatus

3. Monitoring equipment

4. Access and tools for assembling

Components to be assembled and the necessary tools first are sterilized internally. These articles then are placed in an enclosure, which is flooded with a sterilizing gas, usually a mixture of ethylene oxide and Freon 12. Gloves resistant to the sterilizing gas are used for access to the space or, in larger facilities, assembly technicians can enter the enclosure wearing sealed clothing with outside air source and exhaust capability. If the assembly does not include encapsulation, the assembled part must be sealed in a biologically leak-proof bag before the enclosure is purged and opened. To reduce the chance of leakage, the enclosure generally is kept at a slightly positive pressure with respect to the outside atmosphere. There seems to be no practical limit to the size of the enclosure.

e. Compatibility of Decelerator Materials with Spacecraft Sterilization

More materials and components suited to deployable inflatable decelerators for an entry capsule are compatible with sterilization requirements than expected. Some ancillary components are made inherently sterile internally during manufacturing or can be made sterile by simple changes in manufacturing. Most electronic parts fit this category.

Under JPL Contract BE4-229753, Cook Electric Co. of Chicago, Illinois, tested samples of candidate materials for deployable inflatable decelerator devices under conditions simulating sterilization test environments.

Silk was eliminated immediately and nylon was so seriously degraded by thermal sterilization that further testing was not considered. If the thermal sterilization could be mitigated, nylon probably would withstand the chemical sterilization without serious degradation.

E. I. du Pont de Nemours Company reports nylon has been subjected to ethylene oxide and to Freon 12, separately, at temperatures higher

than 104 F without serious degradation. Therefore, the combination probably would not be critically damaging. Nylon, after thermal cycling, was markedly stiffer and less flexible. In contrast to preliminary tests where adhesion of unscoured materials was observed, no adhesion of the nylon to itself or to the stainless steel plates was observed. No adhesion was observed with either dacron or Nomex.^a Thus, long-time packed storage at elevated temperature with or without vacuum should not be a serious concern for structures made of nylon, dacron, or Nomex. Dacron is a promising candidate for a sterilizable retardation system. Average strength losses of all dacron configurations from sterilization and vacuum exposures did not exceed 20 percent. Nomex is also a promising candidate material for the Mars entry retardation system. Average strength losses of all Nomex configurations from sterilization and vacuum exposures did not exceed five percent.

Depending on the specific material and the temperature-vacuum envelope, some stiffening and heat setting of folds and wrinkles could occur with possible adverse effects on deployment. Effects from folding and compacting were negligible.

f. Effects of Temperature and Sustained Loadings

(1) General Characteristics

Figures 36 and 37 present typical strength relationships for nylon, dacron, and Nomex under various conditions. These curves show optimum strength-to-weight characteristics for undegraded materials at room temperature are obtained with nylon, dacron, and Nomex, respectively. These yarns appear in the same order when listed according to sensitivity to initial elevated temperature values and sustained loads at room temperature (see Figure 37). Thus, after exposure to a preload temperature of

^aA high temperature polyamide produced by I. E. duPont deNemours and Co., Inc., Wilmington, Del.

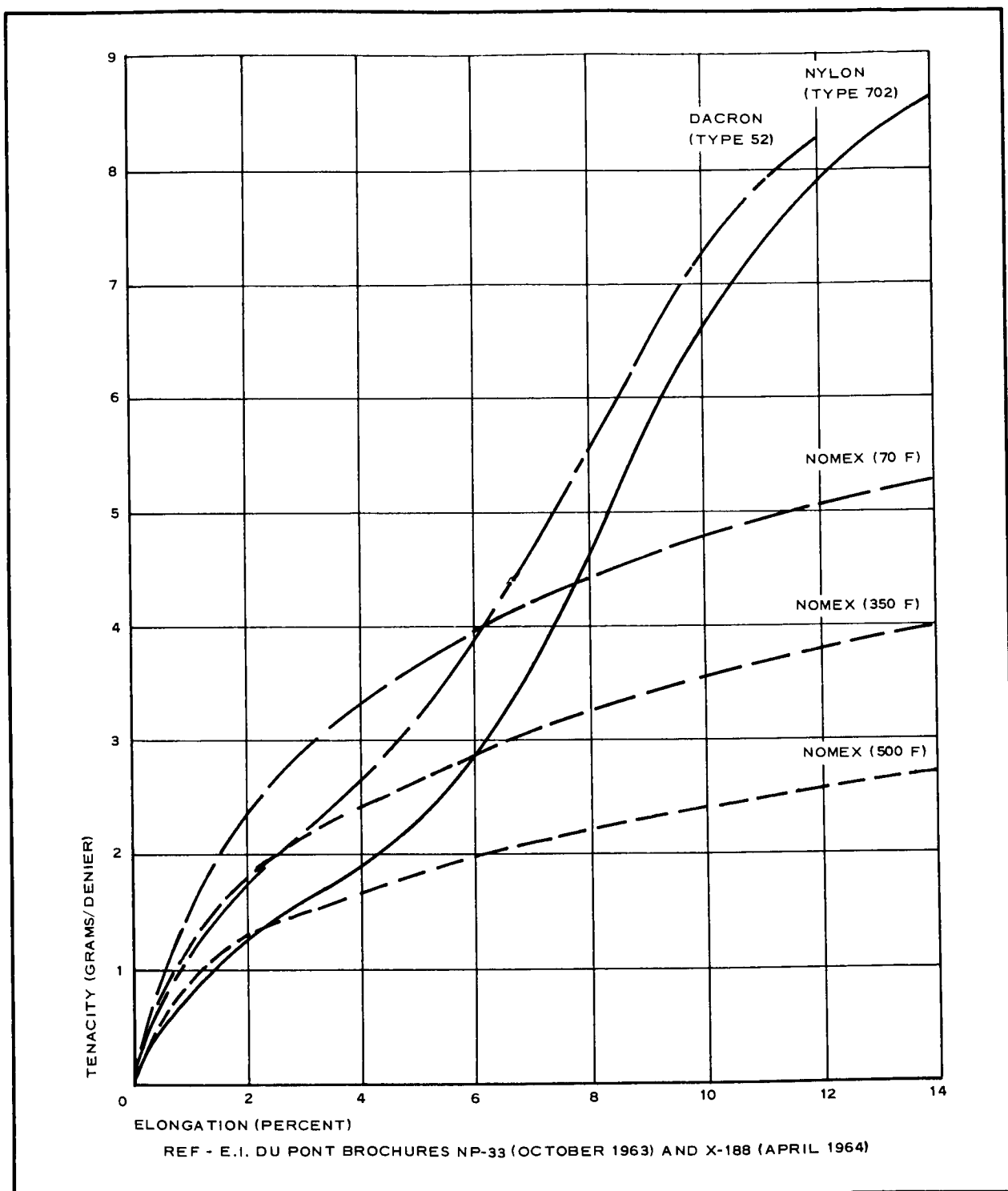


Figure 36 - Typical Stress-Strain Curves for Dacron, Nylon, and Nomex

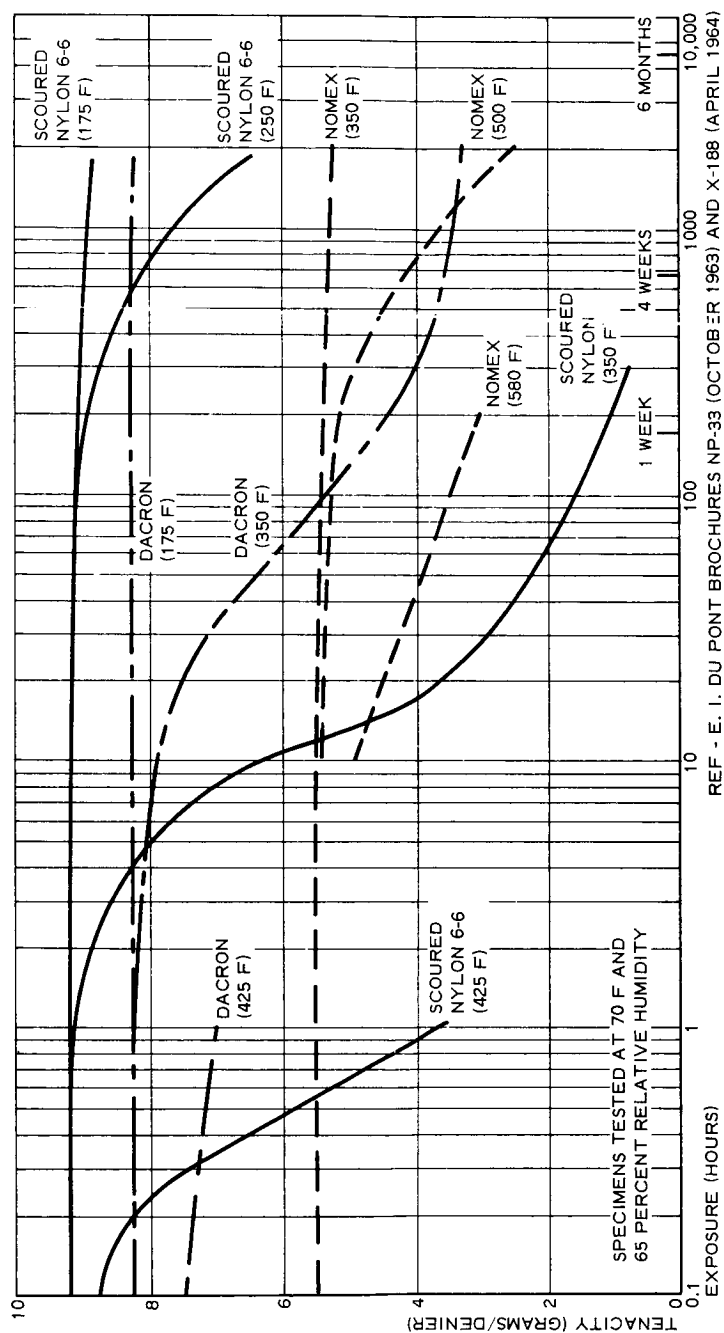
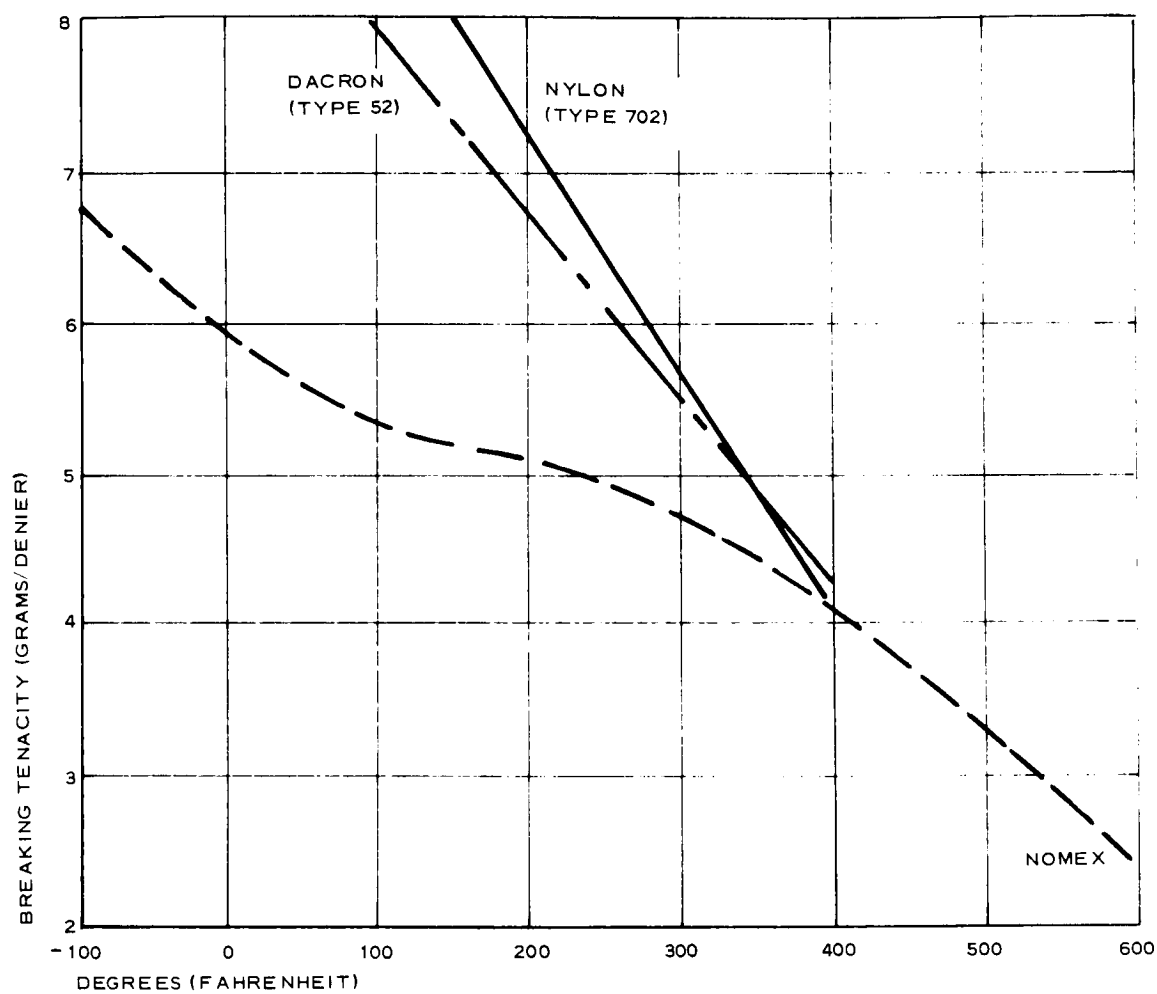


Figure 37 - Strength Retained by Nylon, Dacron, and Nomex Yarns after Exposure to Hot, Dry Air



REF - E. I. DU PONT BROCHURES NP-33 (OCTOBER 1963) AND X-188 (APRIL 1964)

Figure 38 - Breaking Tenacity at Various Temperatures

350 F, for example, dacron is superior to scoured nylon after a loading time of 5 hr and Nomex is superior to dacron after a loading time of 100 hr. These effects become more pronounced with exposure to higher preload temperatures, with dacron having almost twice the tenacity of scoured nylon after exposure to 425 F and a 1-hr loading. Nomex remains usable after exposure to preload temperatures up to 580 F and a continuous loading time of 200 hr.

Figure 38 indicates relative performance of nylon, dacron, and Nomex when subjected to a sustained load at an elevated temperature. At a temperature of about 400 F, nylon, dacron, and Nomex, respectively, exhibit the best initial properties. Above 400 F, Nomex is the only one of the three that will withstand a sustained load.

Somewhat less temperature sensitivity was observed in unscoured nylon compared with scoured nylon. This lessening apparently resulted from the protection of the manufacturing oils. Investigations showed no difference between scoured and unscoured dacron.

(2) Stiffness

At room temperatures, nylon is more flexible than dacron and both are more flexible than Nomex for elongations below approximately six percent (see Figure 36). When stressed to breaking, however, Nomex is the most flexible, with dacron and nylon approximately 50 percent stiffer.

(3) Shrinkage

Results of heat shrinkage of virgin fiber are shown in Figure 39. Dacron reaches about 25 percent shrinkage at about 440 F; nylon reaches 16 percent at the same temperature and Nomex only 4-1/2 percent at 600 F. These shrinkages occur in about 30 sec

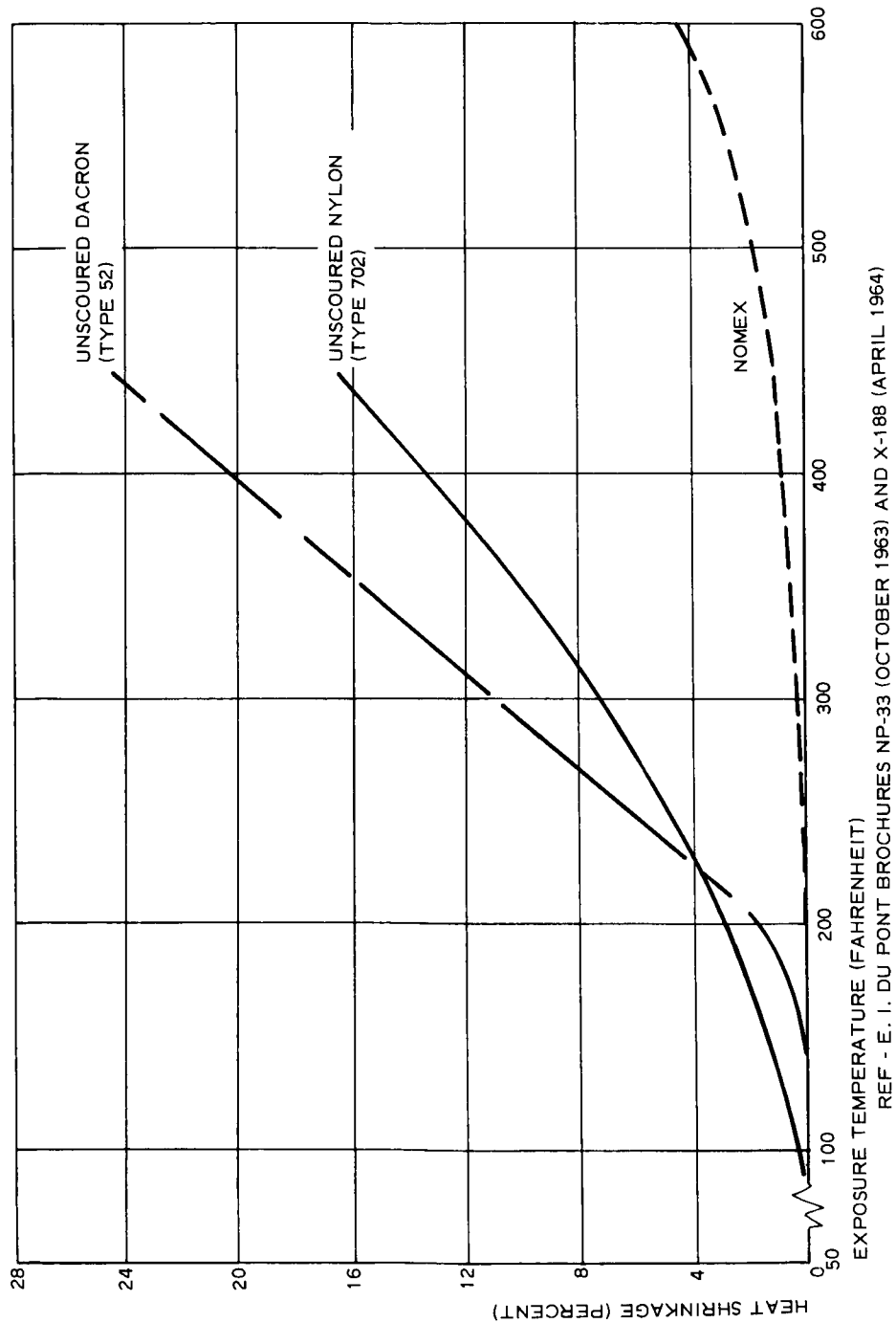


Figure 39 - Shrinkage of Nylon, Dacron, and Nomex
Exposed to Hot, Dry Air

from the time the yarn reaches temperature. While nylon will start shrinking from temperatures above 75 F, dacron does not start until temperatures above 140 F are obtained. The cross-over is at 4 percent shrinkage at 225 F. A heat-setting process must be specified in procurement of nylon and dacron before patterns are cut.

(4) Radiation Resistance

Nylon, dacron, and Nomex are degraded in tensile strength and elongation by irradiation with ultraviolet. Their responses, maximum and minimum, are not necessarily to the same wavelengths (see Figures 40 through 42). Nylon is least affected by 369 μ and most degraded by 244 μ ; dacron least by 369 μ and most by 314 μ ; Nomex least by 314 μ and most by 369 μ . Nomex has the best long-range resistances. Bar graphs (see Figure 43) show how ultraviolet radiation and elevated temperatures affect Nomex.

Gamma radiation results are presented for Nomex in Figure 44. Radiation resistance of Nomex, dacron, and nylon 6-6 is presented in Table III with respect to various radiation sources.

2. DECELERATOR MATERIALS AND COATINGS

a. General

Consideration of candidate materials for expandable terminal decelerators for Mars atmospheric entry must include woven fabrics of synthetic fibers and various coating materials for porosity reduction and heat protection of woven fabrics. Low predeployment volume, low weight, and high strength are required of the decelerator. These indicate flexible structures of woven fabrics will produce the best first-stage decelerator for the entry capsule.

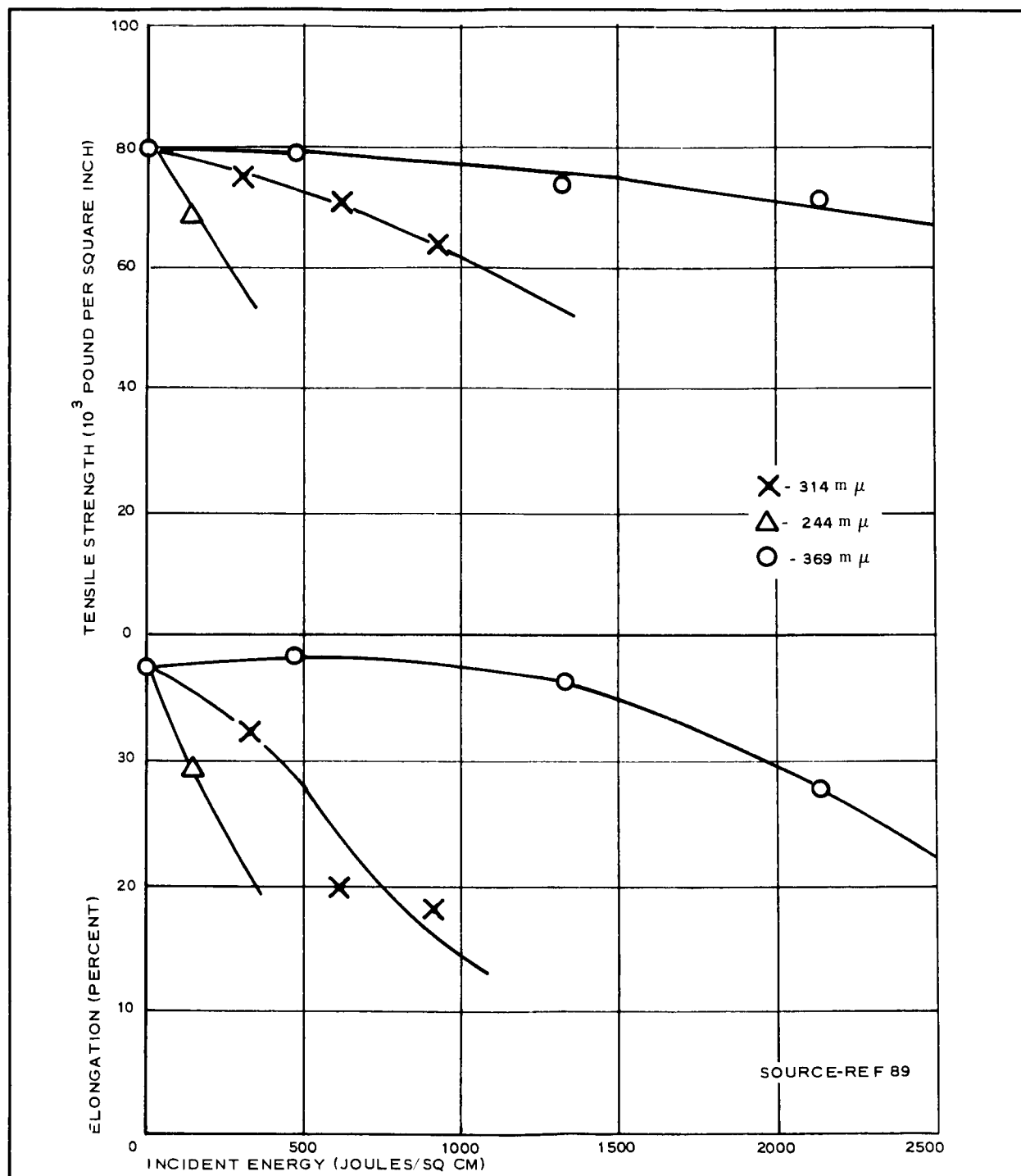


Figure 40 - Variation of Tensile Strength and Elongation of Nylon Fibers Irradiated in Nitrogen at 244 μ , 314 μ , and 369 μ

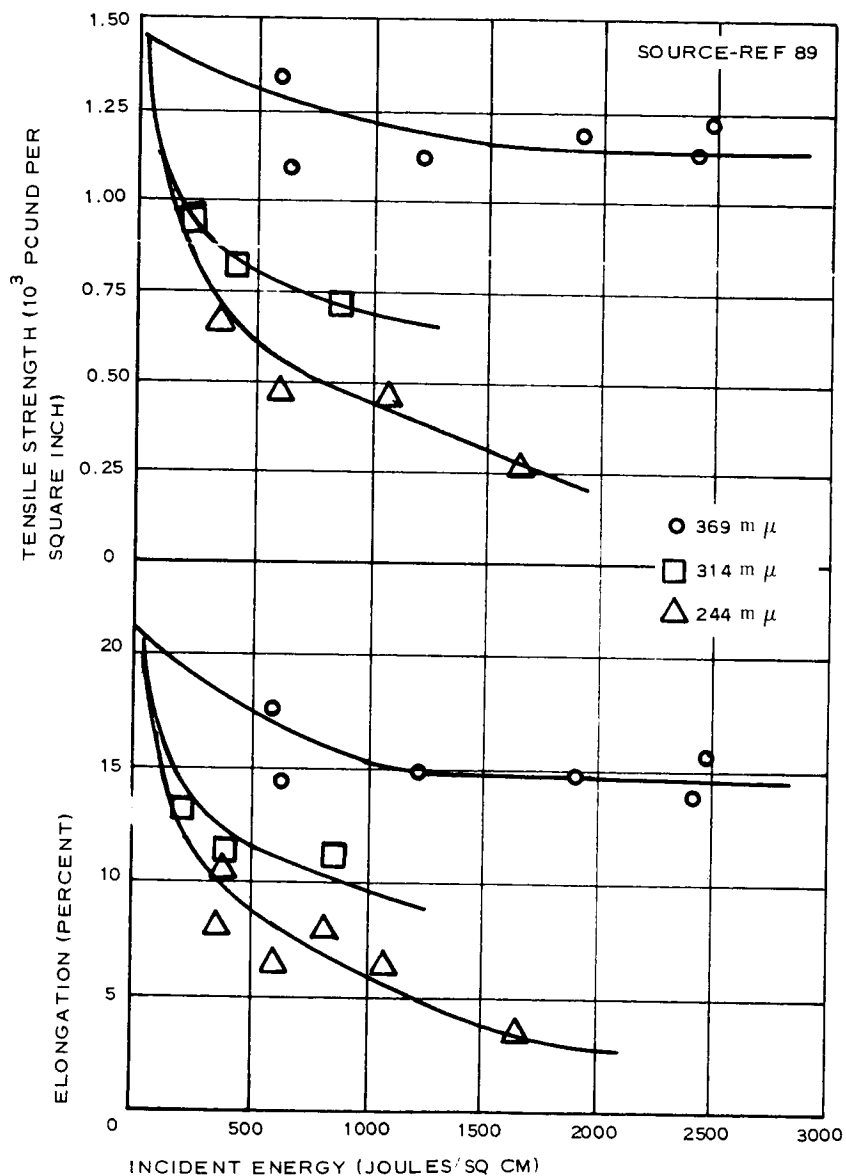


Figure 41 - Variation of Tensile Properties with Incident Energy for Dacron Irradiated in Nitrogen with A-H6 Lamp

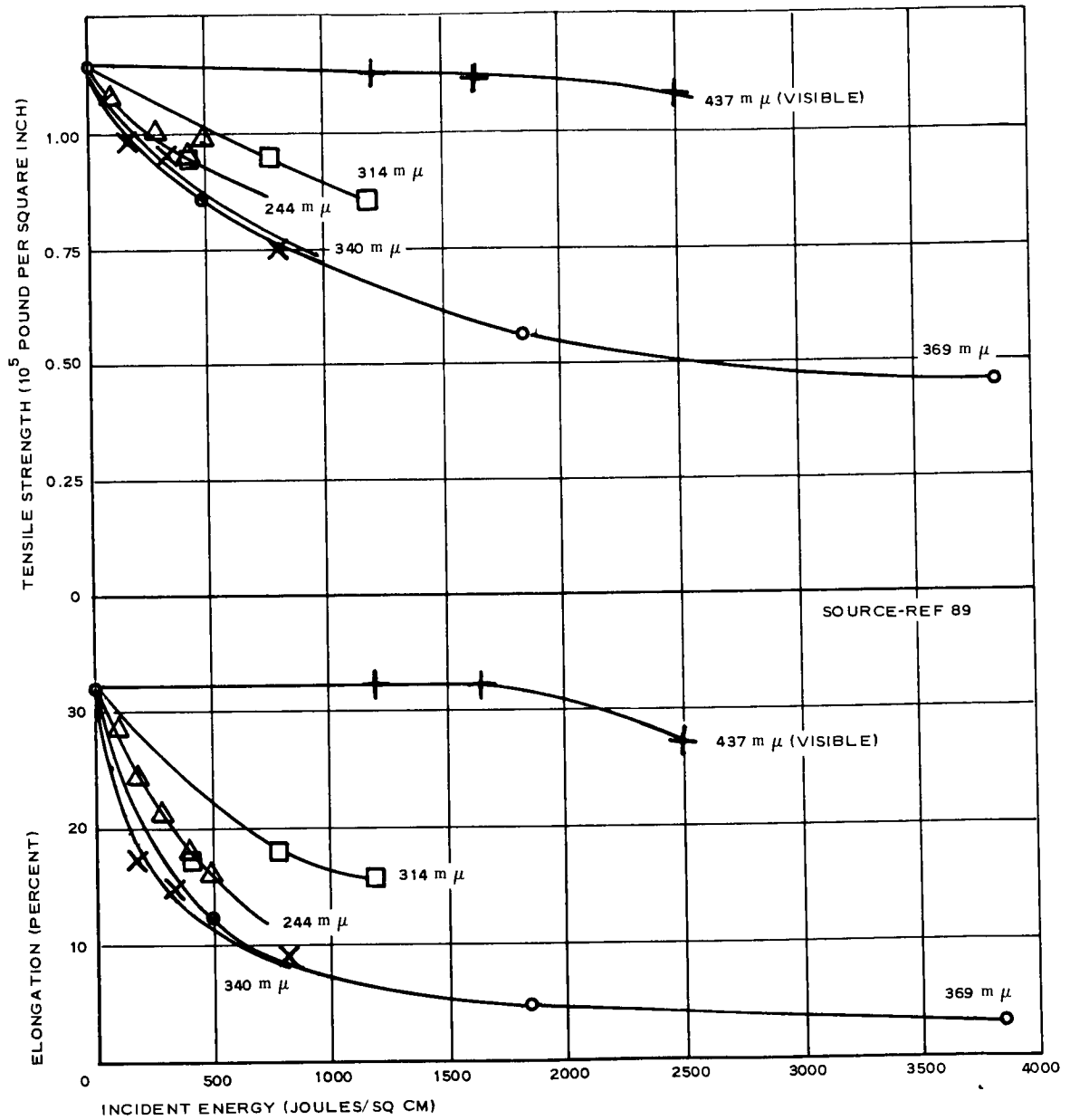


Figure 42 - Variation of Tensile Strength and Ultimate Elongation of Nomex Irradiated in Nitrogen with Ultraviolet Light and with Visible Light (437μ)

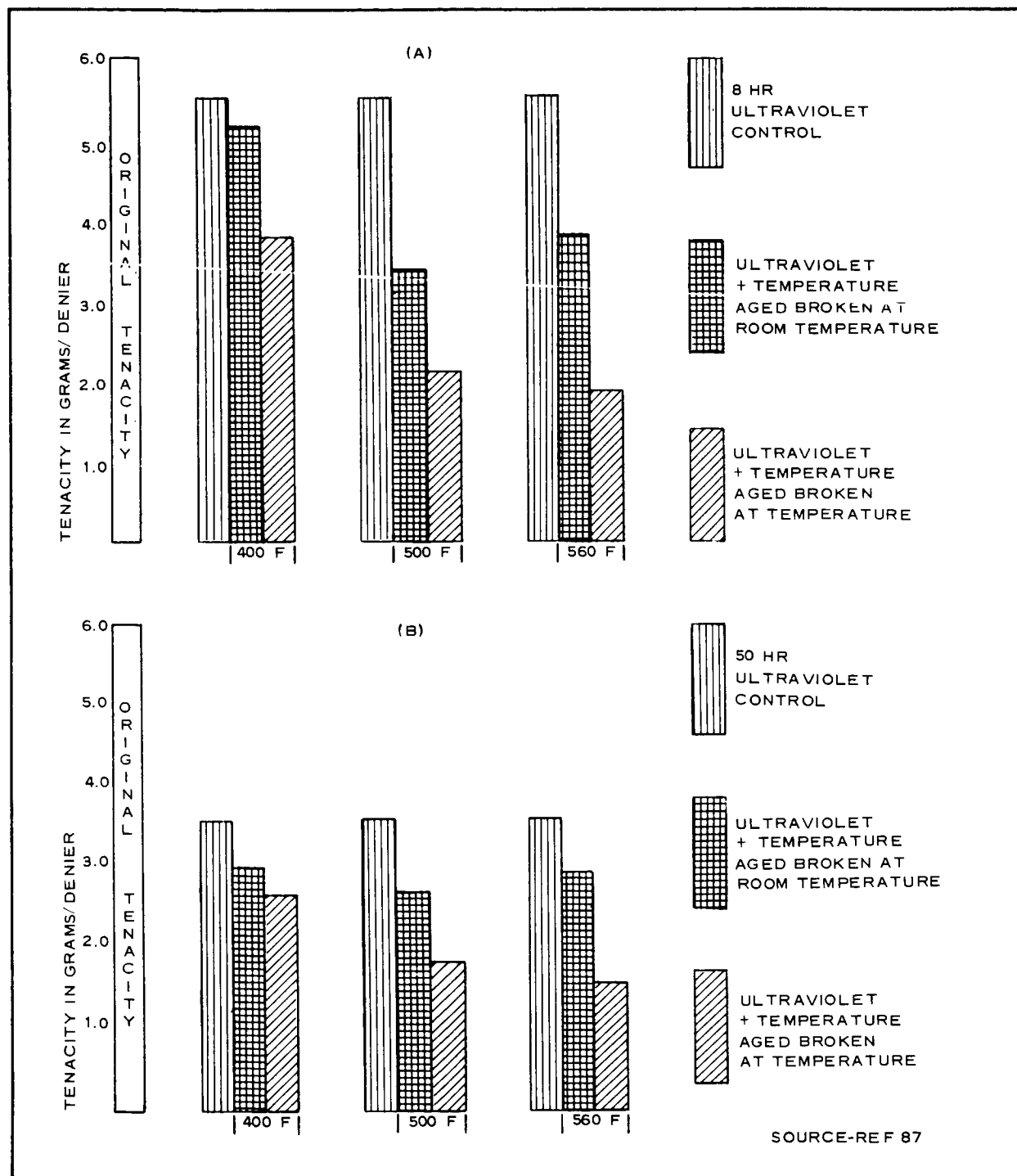


Figure 43 - Degradation of Nomex after Exposure to Ultraviolet Radiation and Elevated Temperatures

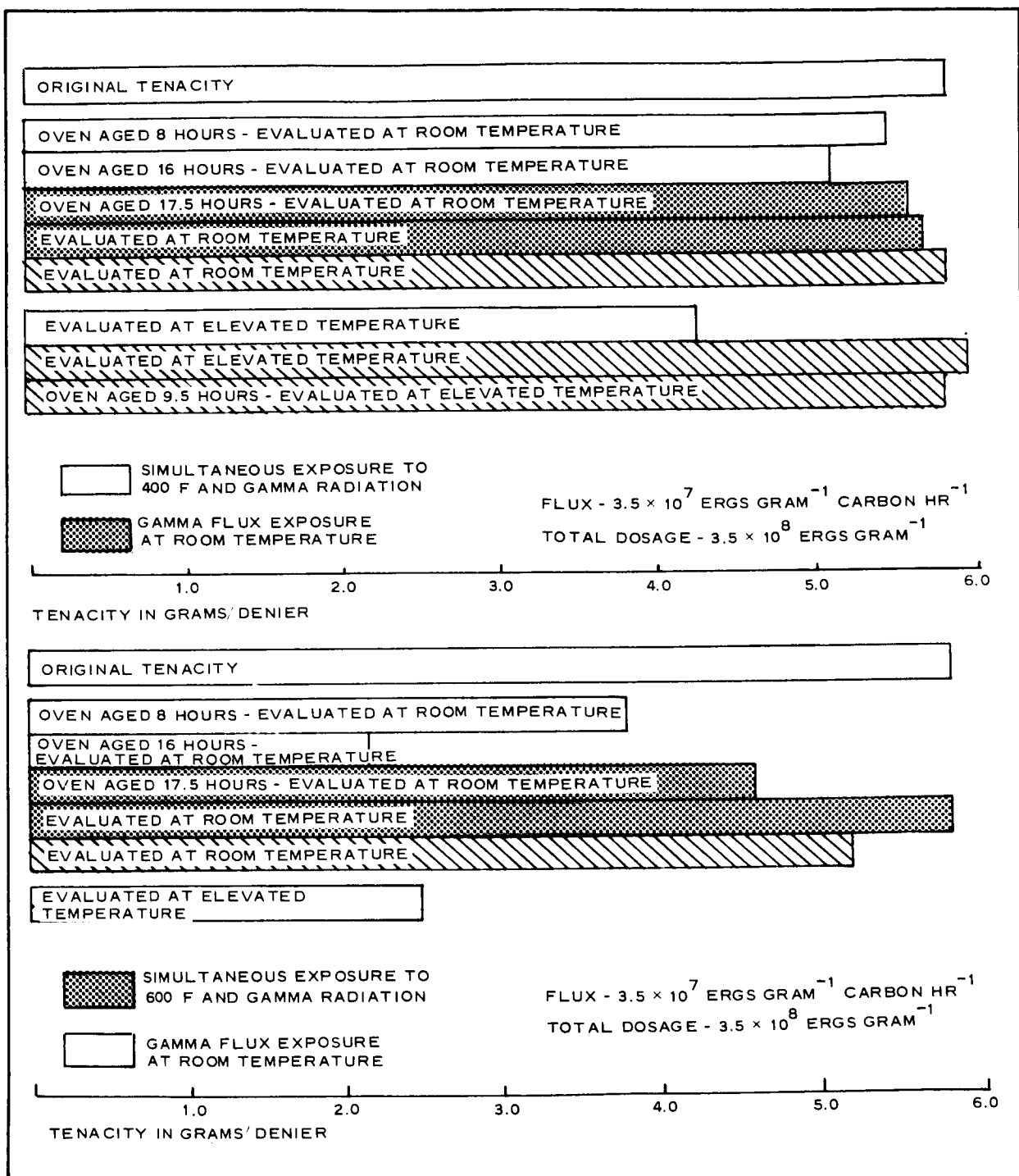


Figure 44 - Effects of Gamma Radiation on Nomex at 400 F (Top) and at 600 F (Bottom)

TABLE III - RADIATION RESISTANCE: EFFECT OF
EXPOSURE ON YARN STRENGTH⁶

Dosage	Tenacity retained (percent)		
	Nomex	Dacron	66 Nylon
β - Van de Graff			
200 mega reps	81	57	29
600 mega reps	76	29	0
X-rays (50 kv)			
50 hr	85	22	. . .
100 hr	73	0	. . .
250 hr	49	0	. . .
Brookhaven pile (50 C)			
200 mega reps	70	45	32
1000 mega reps	55	Radioactive	Crumbled
2000 mega reps	45	Radioactive	Crumbled

b. Fiber, Yarn, and Filament Material

Characteristics of woven fabrics are determined largely by the basic fiber or filament materials. Important fiber qualities for deployable decelerator materials include high strength, temperature resistance, high modulus of elasticity, flexibility, abrasion resistance, and chemical stability.

These basic properties when related to deployable, inflatable decelerators show that high modulus of elasticity and flexibility are contradictory and are difficult problems for textile technology and production. Available fibers with good temperature-resistance qualities also tend to have high modulus characteristics, making temperature resistance and flexibility difficult to attain in a single fabric.

Table IV summarizes effects of various environmental conditions on

man-made and natural textiles used or considered for aero-dynamic decelerators.

c. Woven Fabric Materials

(1) General

Available woven fabric materials applicable for deployable decelerator construction, in order of increasing strength and temperature resistance, are nylon, dacron, and Nomex.

Most current applications are filled by woven fabrics of nylon, dacron, or Nomex with or without coatings. Plastic film is suitable only for low-load, low-temperature applications. Although fiberglass has high basic strength, modulus, and temperature resistance, it is notoriously vulnerable to folding damage and interfilament abrasion. Fiberglass has been used successfully in rigid applications but has been disappointing in flexible-fabric applications.

(2) Operational Temperature Ranges

Decelerator materials are available for operation from 300 to 1500 F (see Figure 45) Substrate material recommended from 300 to 600 F is Nomex coupled with silicon or fluoroelastomers. Between 1000 to 1500 F, substrates of stainless steel or René 41 woven cloth coated with a high-temperature coating, such as CS-105 (Goodyear Aerospace), can be used.

In other operational temperature ranges, proved materials are now unavailable. An obvious area for development of suitable materials lies between 600 to 1000 F. At temperatures above 600 F, the strength of Nomex drops rapidly; below 1000 F, the penalty in strength-to-weight ratio paid in the use of stainless steel cloth is too severe.

A potential material to fill this void is fiberglass (see Figure 45).

TABLE IV - EFFECTS OF ENVIRONMENT ON NATU

Environment	Cotton	Silk	Viscose Rayon	F
Heat	Highly resistant to dry heat; yellows at 248 F; decomposes at 302 F; burns readily	Begins to decompose at 270 F; rapid disintegration above 300 F; burns readily	Loses strength above 300 F; decomposes at 350 F to 400 F; burns readily	Scorches about 200 F; cotton, cotton,
Age	Little or none	Slight yellowing and loss of tensile strength	Slight	Little or
Sunlight	Loses strength; formation of oxycellulose; tendency to yellowing	Loses tensile strength; affected more than cotton	Loses tensile strength after prolonged exposure; very little discoloration	Loses s to color
Chemicals	Disintegrated by hot dilute acids or cold conc. acids. Shells (mercerization) in caustics damaged by prolonged exposure in presence of air. Bleached by hypochlorites and peroxides, oxidized into oxycellulose by strong oxidizing agents.	Fairly resistant to weak acids; dissolved by strong acids except nitric. Insensitive to dilute alkali unless hot; dissolves in strong alkalis. Above pH11 and below pH3 stability decreases rapidly	Strong alkali causes swelling and reduces strength. Attached by strong oxidizing agents; not damaged by hypochlorite or peroxide bleaches	Disinteg lute or acids. shrinks ing. Re bleaches dyehous
Organic solvents	Resistant	Resistant	Generally insoluble; soluble in cuprammonium	Unaffected
Moths	Not attacked	Attacked slightly	Not attacked	Not atta
Mildew	Poor resistance unless	Attacked	Attacked	Same as
Environment	Dacron	Glass Fiber	Polyethylene	M
Heat	Highly resistant to degradation and discoloration; melts at 480 F	Will not burn; strength loss starts at 600 F, continues to limiting temp. of 1000-1500 F, softens 1500 F	5% shrinkage at 165 F; softens at 225 to 235 F; melts at 230 to 250 F; slow burning	Strength 200 F, melts 480 F
Age	Virtually none	None	Virtually none under normal conditions	Virtually
Sunlight	Loses strength on prolonged exposure; no discoloration	None	Prolonged exposure decreases tensile strength	Moderate
Chemicals	Good resistance to mineral acids except conc. sulfuric. Good resistance to weak alkali, moderate to strong alkali at room temp.; dissolves in hot strong alkali. General good resistance to other chemicals; excellent to bleaches and oxidizing agents.	Good resistance to all but hot strong acids. Attacked by hot solutions of weak alkalis and cold solutions of strong alkalis. Generally good resistance.	Very resistant to acids. Generally good resistance to caustics and other chemicals.	Good resistance to dilute acids. Becomes mineral alkalis. General to commercial
Organic solvents	Generally insoluble; soluble in some phenolic compounds	Insoluble	Insoluble, but swells in chlorinated hydrocarbons, aromatics	Insoluble in phenols
Moths	Not attacked	Not attacked	Not attacked	Not attacked
Mildew	Good resistance	Wholly resistant (binder may be attacked)	Good resistance	Good resistance

* Source: Reference 7

NATURAL AND MANMADE TEXTILES

Artisan	Nylon	Orlon
resists in ironing at 300 C higher than otherwise like viscose rayon	Yellow slightly at 300 F when exposed for 5 hr; melts at 482 F	Sticks at 455 F; slight loss in strength after 32 days in air at 275 F melts at 480 F
resistance to none	Virtually none	Virtually none
strength; tends to lose	Loses strength on prolonged exposure; no discoloration; bright yarn more resistant than semi-dull	Very resistant to degradation by ultraviolet light and atmosphere
resists in hot dilute cold concentrated Strong caustic as in mercerizing resistant to acids, phenols, and other reagents	Boiling in 5% HCl ultimately causes disintegration; dissolves in cold conc. sulfuric or nitric acids. Substantially inert to alkali. Generally good resistance to other chemicals	Good to excellent resistance to mineral acids. Fair to good resistance to weak alkalis. Not harmed by oils, greases, neutral salts and some acid salts
resistance to acids	Insoluble except in some phenolic compounds and conc. formic acid	Unaffected by common solvents
resistance to alkalis	Not attacked	Not attacked
resistance to cotton	Good resistance	Good resistance (coating may be attacked)
Mylar	Nomex HT-1	
resistance to reduced above 300 F; useful to 300 F, 2 F	Degrades above 700 F to friable char at 482 F; has 60 % room temp. structural strength	
resistance to none	Virtually none	
resistance to acids	Loses strength on prolonged exposure; surface turns bronze	
resistance to cold acids and alkalis. brittle in hot acids and alkalis. generally resistant to chemicals	Acid resistance better than nylon 6-6; not as good as Dacron or Orlon; degraded by strong alkali at elevated temperature	
resistance to degraded by acids and cresols	Highly resistant to most hydrocarbons	
resistance to alkalis	Not attacked	
resistance to acids	Good resistance	

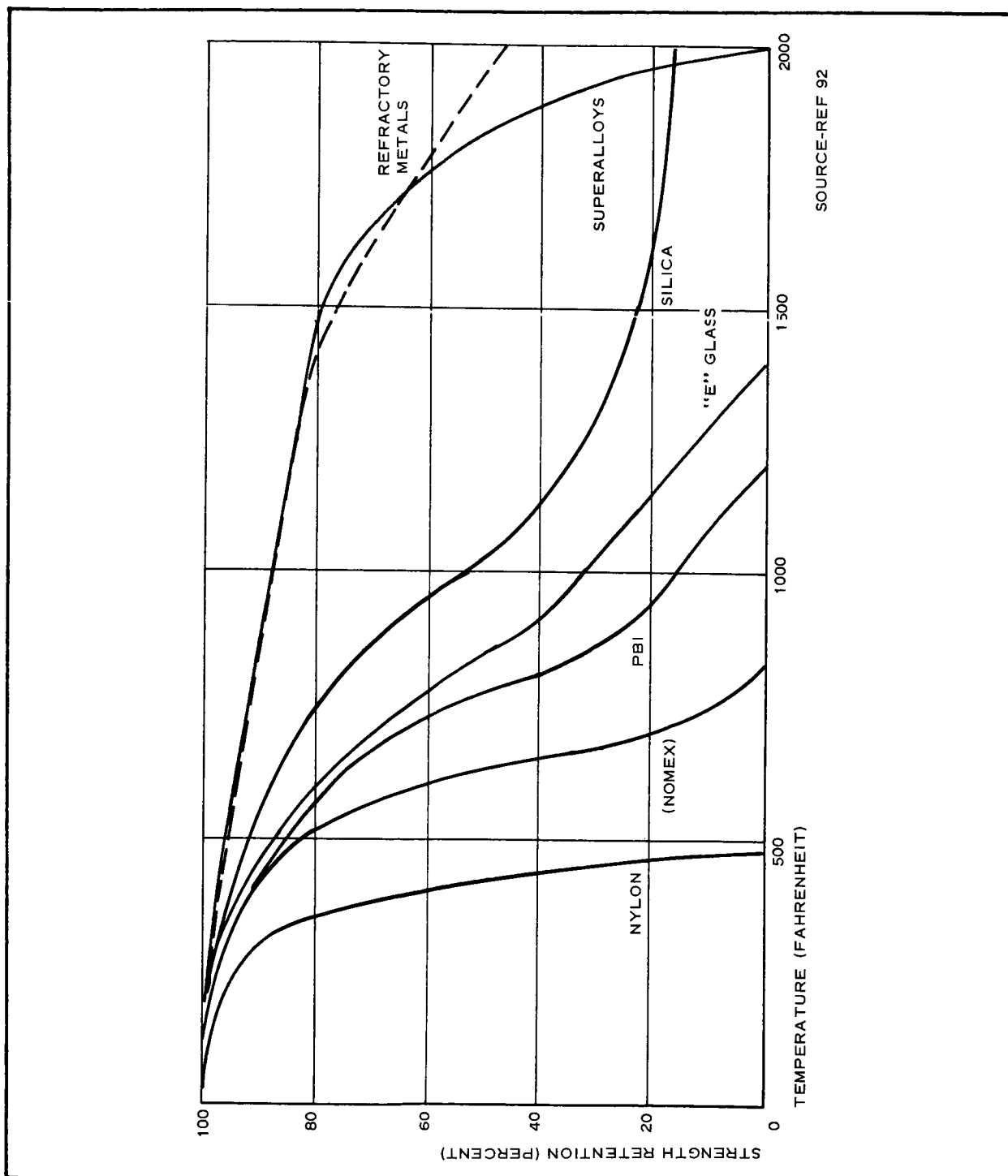


Figure 45 - Strength Retention versus Temperature for Present and Future Fibers

However, because of its self-destructive nature under flexing of pulsating loads, fiberglass does not lend itself to this application. Efforts have been underway for some time to minimize the abrasive nature of fiberglass, with moderate success. One approach to this problem has been to impregnate yarns with elastomers to prevent adjacent filaments in the yarn from rubbing. Another approach has been the development of Beta glass fiber.^a The Beta fiber is an extremely fine filament. Both methods have improved performance of fiberglass in flexible applications; however, this work must be continued to realize its potential.

Another possibility of filling the substrate-material void from 600 to 1000 F is to extend the capability of Nomex. The most practical way to do this is to protect the substrate so its temperature does not exceed 600 F. Coating the substrate with ablative offers this protection, but the thickness required and the associated rigidity of thermal insulators as they are now known make this use prohibitive. Development of low-temperature ablators has caused a considerable lag in development of high-temperature ablators. To obtain ablative materials that will satisfy the requirements for use on decelerators is a definite problem area that warrants investigation.

d. Fabric Coatings

Coatings are applied to reduce fabric porosity or to protect the basic fabric from high aerodynamic temperatures or other heat load, or both. No rigid line of demarcation exists between coatings for gas tightness and those for heat protection. Urethane and silicon rubbers have higher temperature resistance than neoprenes; however, any coating with a low thermal conductivity can render a limited heat protection. The formation of an insulating char is sometimes a usable mechanism. For transients, an aluminum metalizing can be adequate,

^aA product of Owens-Corning Fiberglass Corp., Toledo, Ohio

but when temperature requirements are high and fairly long, coating performance can become quite sophisticated. Heat protection can be afforded by combining mechanical and chemical reactions to the temperature through char formation, sublimation, and ablation.

Coating materials are available that perform satisfactorily to 1500 F. To 600 F, fluoroelastomers perform quite well for short periods of time. To 1000 F, silicones are available. Between 1000 and 1500 F, CS-105 high-temperature flexible coating is recommended. This coating, a silicon binder with a glass frit filler, has been used to 1500 F.

CS-105 coating resembles silicon elastomer at room temperature. As the temperature is raised, a thermal decomposition of the elastomer and fusing of the glass frit occur. The weight of decomposition is a time-temperature phenomenon that progresses slowly at 800 F and increases as the temperature rises. The glass frit does not fuse until 1100 to 1200 F has been reached. Hence, between approximately 800 to 1100 F the elastomer is decomposing and the glass frit does not fuse. During this transition phase, the coating is most susceptible to damage and the gas permeability increases. When the coating is subjected to a heat flux of such magnitude, it must traverse the critical temperature range in a relatively short time. The glass frit fuses before the silicon elastomer decomposes excessively, provides a carrier for the silicon residue, and forms an adequate gas barrier.

Elastomer coating materials applicable for reducing porosity in decelerator structure fabrics are described in Table V. Performance is evaluated for each material in a variety of environmental conditions so material limitations are readily apparent.

Some typical coatings, used or investigated for possible use in decelerators, are shown in Table VI. Neoprene, DC-131, and Viton have been used satisfactorily on flight-tested decelerators in the

low-to-medium temperature regime - that is, up to about Mach 2 and at altitudes above 70,000 ft.

The remainder of the listed coatings are potential candidates to extend the operating capability of state of the art fabrics. In many applications, ablative coating materials may be appropriate because of the short deceleration times characteristic of deployable decelerators.

The approach used to increase the temperature capability of the coating between the thermal degradation temperature of the elastomer and the desired operating temperature is to load the elastomer with a low-melting point inorganic material. As the temperature rises, a thermal decomposition of the elastomer occurs, and inorganic material changes to a very viscous fluid. The viscous fluid requires a high surface tension to hold the residue of the elastomer in suspension and to maintain a continuous film. After cooling, the material solidifies, forming a solid gas barrier with some flexibility although much less than the original unfired coating.

e. Joining Methods

Construction of foldable, packageable structures involves the classic problem of building compound shapes from plane material. Aerospace decelerators are assembled by sewing a multitude of individually patterned pieces of a plane fabric material. These pieces are seamed together, usually by sewing with threads of material similar to the fabric filaments. BALLUTE gore patterns, for example, are cut on the bias from "square" cloth that has equal or nearly equal strength and elongation in warp and fill. Gores are alternated right and left bias to balance out differences in elongation in the warp and fill directions. So far, BALLUTES and parachutes are of single-ply construction.

Joining methods include sewing, cementing, and, with metal fabrics, spot welding. With plastic film material, cementing is almost invariably involved, either a heat-sealing or solvent-sealing cementing or

TABLE V - RELATIVE GENERAL PROPERAL P

Elastomer types	Ten- sile	Tear	Abra- sion	Impact (fatigue)	Flame	Heat (F)	Cold (stiff)	Cold (brittle) (F)	Ozone	Radi- ation
Natural rubber	AB ⁺	B	AB	AB	D	CD ⁺ +250	B	B -80	D	BC
Styrene butadiene rubber (Buna S or GRS)	B	BC	AB	AB	D	C +275	BC	B -80 to -90	D	BC
Isobutylene iso- prene rubber (Butyl or GR-1)	C	B	B	C	D	BC +300	C	BC -50 to -80	AB	D
Chloroprene rubber (Neoprene or GR-M)	B	B	AB	B	B	C +300 F	C	BC -45 to -70	AB	CD
Polyurethane elastomers (Adi- prene, Chemigum SL, CX-1046)	A	A	A	B	CD	C +250	C	A -30 to -95	A	B
Nitrile butadiene rubber (Buna N)	BC	BC	AC	C	D	B +275	BC	BC -80 to -90	D	BC
Silicone rubbers	D	CD	CD	D	C	A +550	A	A -200	A	D
Chlorosulfonated polyethylene (Hypalon)	BC	BC	AB	BC	B	BC +325	C	B -70 to -80	A	BC
Fluorinated elas- tomers (Fluorel, Kel-F, Viton)	BC	BC	B	BD	A	A +450	D	BC +10 to -40	A	BC
Organic polysul- fide rubbers (Thiokol, GR-P)	D	D	D	D	D	C +200 to +275	C	B -60 to -80	A	BC

*Source - Reference 8

⁺A = exceptional, outstanding, or excellent; B = good; C = fair; D = poor.

PROPERTIES OF ELASTOMERS

Gas retention	Resistance - oil, weather, chemical	Unsuitable for	Specific gravity
B	Highly resilient, low hysteresis, general	Contact with oils, ozone, strong oxidizing agents.	0.93
B	General purpose rubber, not so resilient as natural, better resistance to aging.	Contact with oil, ozone, strong oxidizing agents.	0.94
A	Weather, heat, ozone, chemical, and solvent resistant, low air permeability.	Contact with oils.	0.92
AB	Weather resistant, fair oil resistance.	Temperature extremes, contact with aromatic oils and most fuels, long exposure to low temperatures	1.24
A (R. T.)	Superior abrasion resistance, sunlight and ozone resistance, good oil resistance.	Contact with steam or hot water	1.05 to 1.17
B	Medium to good oil resistance, fair fuel resistance	Contact with ozone, strong oxidizing agents.	0.99
B	Resistant to temperature extremes, fair oil resistance, properties constant from 60 F to 500 F.	Contact with high pressure steam, aromatic oils, fuels, abrasion.	1.25
AB	Weather, heat, ozone, and moderate oil resistance, good color possibilities.	Aromatic oils and most fuels.	1.10
A	Resistant to oxidizing acids, fuels containing up to 30 percent aromatics, ozone, weather; excellent oil resistance.	Contact with diester lubricants, uses where material must be easily flexed at temperatures below 0 F.	1.40 to 1.85
A	Excellent oil resistance, good resistance to aromatic fuels, excellent weather and ozone resistance.	Resistance to compression set particularly at temperatures above 100 F, uses where mercaptan odor would be objectionable, contact with oxidizing acids.	1.25 to

TABLE VI - ELASTOMERIC COATINGS

Coating	Vendor	Specific gravity	Specific heat	Thermal conductivity	Emis-sivity	Remarks
Neoprene 1137-C	Goodyear	1.30	0.35 Btu/lb-deg F	0.14 Btu/hr-ft-deg F		Low temperature coating
DC-131	Dow-Corning	0.94	0.3-0.35 Btu/lb-deg F	0.167 at room temperature Btu/hr-ft-deg F		
Viton	Du Pont	1.85 to 1.90	0.395 Btu/lb-deg F	0.117 at 300 F Btu/hr-ft-deg F		
CS-105	Goodyear				0.92 at 1000 F	High temperature coating
D-65	Dyna-Therm	1.1	0.25 (68 to 150 F) Btu/lb-deg F	0.053 at 150 F Btu/hr-ft-deg F		Ablator
RTV-88	General Electric	1.48	0.35 Btu/lb-deg F	0.18 at 200 F Btu/hr-ft-deg F		
RTV-560	General Electric	1.42		0.19 at 315 F Btu/hr-ft-deg F		Ablator
AVCOAT II	AVCO	1.0	0.43 (65 to 240 F) Btu/lb-deg F	0.10 at 250 F Btu/hr-ft-deg F		Ablator
DC-325	Dow-Corning	0.87	0.32 (77 to 200 F) Btu/lb-deg F	0.08 at 200 F Btu/hr-ft-deg F	0.90 at 70 F	Ablator

adhesive application. Soft fabrics usually are sewed. But cementing is sometimes practical, especially with an elastomer-coated cloth, and frequently this results in higher joint efficiencies. Combinations of cementing and sewing have been used. Cementing has been used for sealing holes made by sewing or preventing the slippage of stitching. Joining of metal cloth has been by multiple staggered row spot welding. The Air Force has reported sewing such fabric successfully with wire thread.

The development of the optimum seam for a specific application is a matter of design and test development. Involved are such factors as the cloth and its basic strength to be developed; the coating, and an orthogonal or biased seam. Variations are possible with number of parallel rows of stitches, number of stitches per inch, type of stitch, presence or absence of reinforcing tapes or webs, types of seams, and possible overlay of elastomeric coating. The final bulkiness of the seam is a consideration with its consequent influence on packageability and deployment.

Seams invariably cause problems. Seaming represents a sizeable part of construction cost and contributes significantly to the variation in quality of the finished article. The seam adds bulk and weight, reduces flexibility, adds distortions when the structure is loaded, and almost never can be designed to develop 100 percent material strength. Although cementing generally can produce a better joint, it also is affected more adversely by elevated temperature.

f. Material Selection and Qualification

Materials for decelerators are selected after analysis of design factors and fabrication technology. Static and dynamic loading, thermal loading, maximum size and weight of structure, and aerodynamic drag requirements dictate requirements for strength and temperature resistance. Material selected must meet these requirements after fabric strength-to-weight ratio, thickness, porosity, flexibility,

and coatings have been considered. Material selection usually will involve fiber or filament material and size, weave, seam construction, production sequence, and other production techniques. Different materials and fabrication techniques may be required for structure components.

SECTION IV - DECELERATOR ENVELOPE SIZE ESTABLISHED BY
THERMAL REQUIREMENTS

On the basis of heat-rating profiles developed in Section II, fabric weight requirements for several entry cases were estimated.

Fabric weight per unit surface area was estimated from heat-flux rate profiles on the basis of material heat capacity. This procedure, carried out in the deployment Mach range for Atmospheres VM7 and VM8, includes trajectories computed for different drag parameters using similar deployment conditions. The heat-balance procedure simply equated the cold-wall heat, presented above, and the heat capacity of the fabric material to the maximum temperature at which it retains load carrying capability. Hence,

$$q = \int \dot{q} d\tau$$
$$= \rho \delta (T_f - T_i)$$

where

q = heat flux (Btu/ft²),

\dot{q} = heat flux rate (Btu/ft²-sec),

c = specific heat of material (Btu/lb-deg F),

T_i = initial temperature - 70 F,

T_f = final maximum temperature (deg F),

δ = thickness of material (ft),

τ = time (sec), and

ρ = density of material (pcf).

This heat balance assumes that thermal conductivity of the fabric material is infinitely high and that outward surface radiation is zero. Infinite thermal conductivity is a poor assumption since the usual value of this fabric thermal parameter is quite low. Surface temperature would be expected to rise quickly while temperature at the back or interior surface would change little. However, heating rates appear so low and of such short duration that this assumption is realistic for a preliminary design weight estimate. In addition, as the outer surface temperature rises, incoming heat pulse decreases because of differential temperature reduction. Furthermore, as the surface temperature rises, the back radiation can be expected to increase. Because both factors have been neglected, it will be assumed that two trends either compensate for each other or produce conservative estimates of the fabric weight required. These results were supplemented with computer solutions (see Appendix B of Vol I) using transient one-dimensional heat conduction in the fabrics to account for these parameter variations. Such solutions yield more realistic design configurations for the temperature profiles in the materials.

Results of the computations are presented in Figures 46 through 52. Fabric weight requirements in the VM7 atmosphere are increased considerably over those required for the VM8 atmosphere. This is primarily caused by increased ambient temperatures associated with this atmosphere and secondarily to the more gradual decrease of density with altitude. In addition, most decelerations in the VM8 atmosphere take place at altitudes below 50,000 ft while those in the VM7 atmosphere are between 60,000 and 110,000 ft. As a result, deceleration times in the VM7 atmosphere are longer, a fact reflected in heat input to the fabric. Requirements thus are increased significantly in the upper deployment Mach regime.

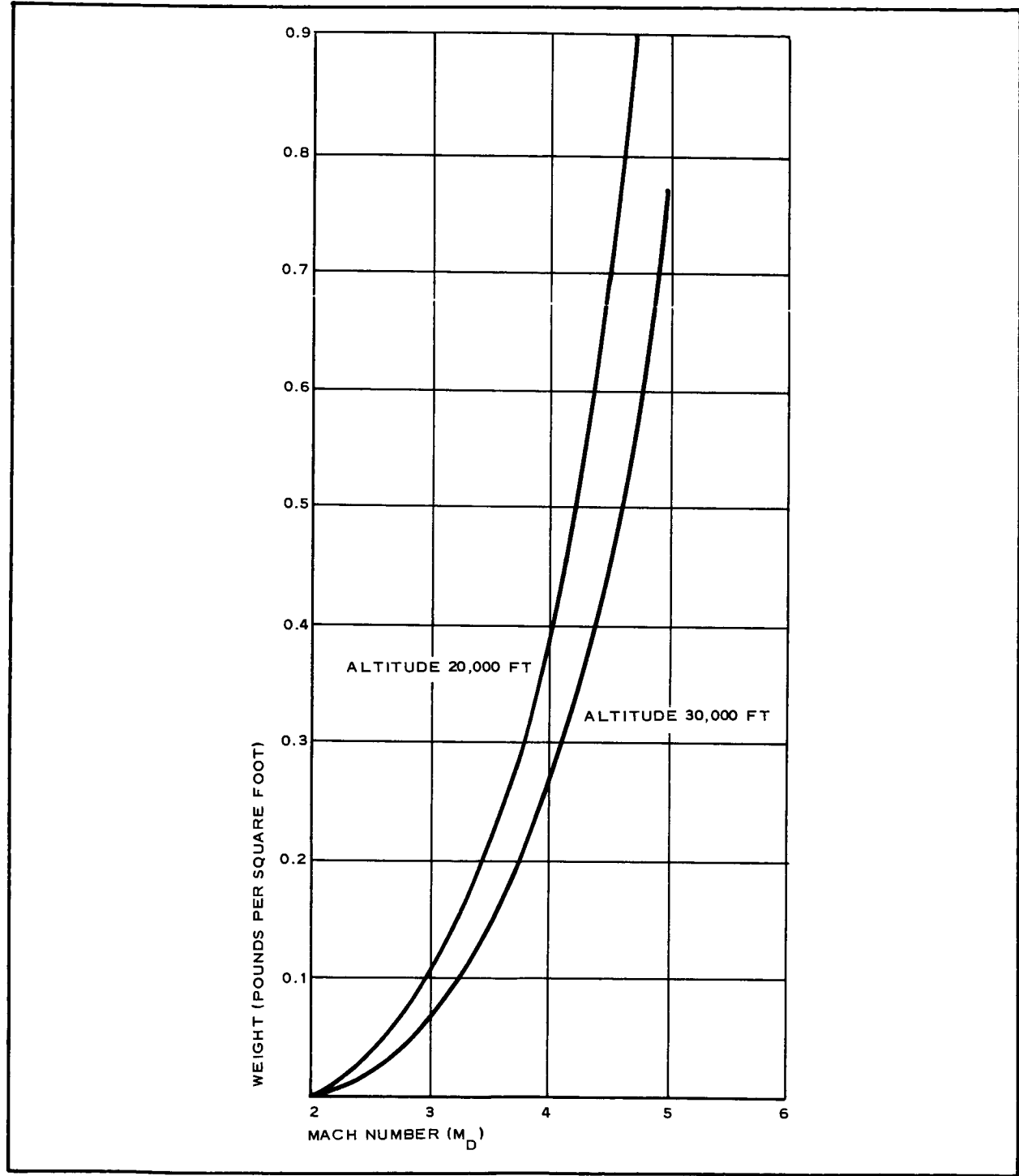


Figure 46 - Decelerator Fabric Envelope Weight Required versus Initial Mach Number, Trajectory B1

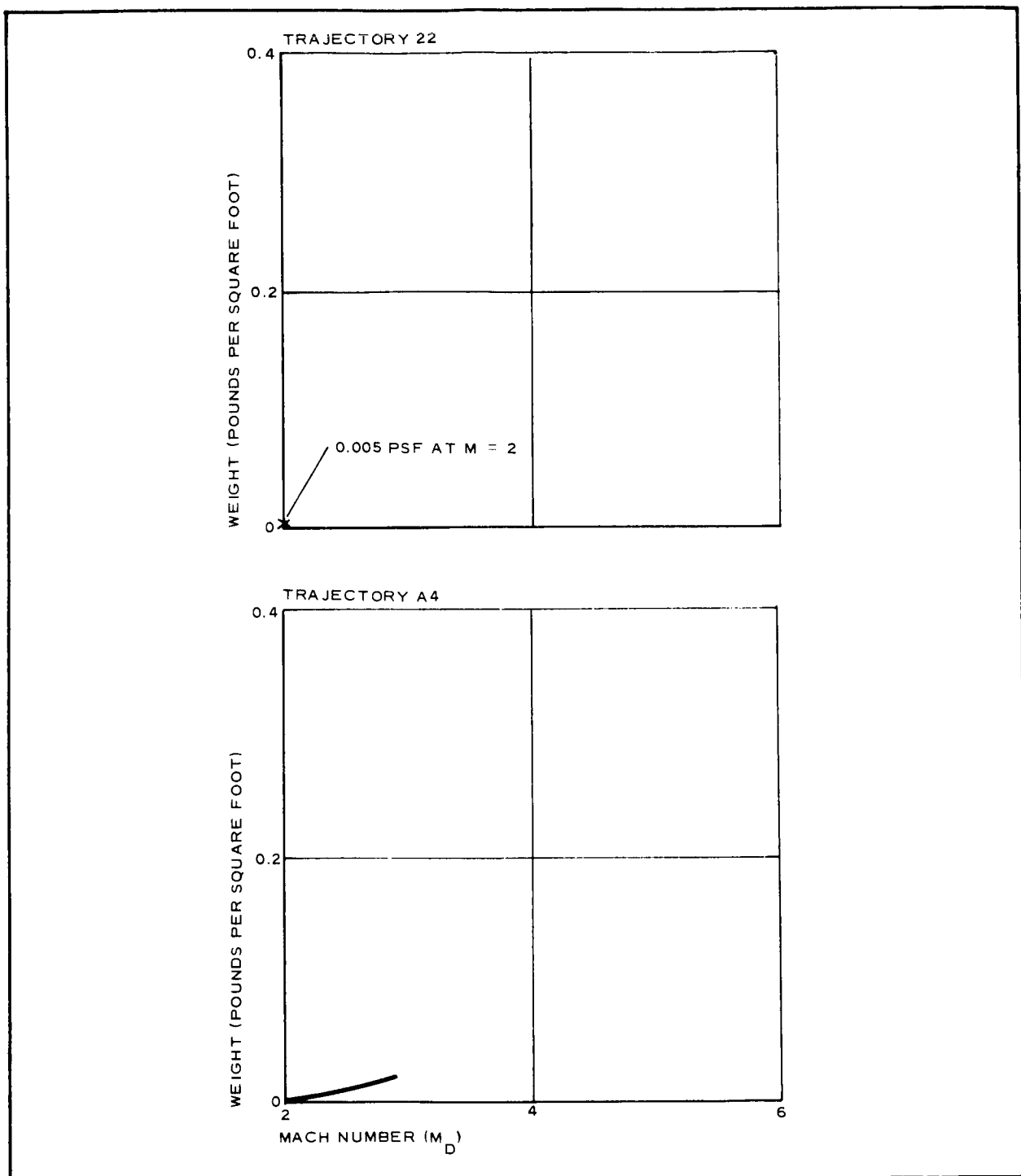


Figure 47 - Decelerator Fabric Envelope Weight Required versus Initial Mach Number, Trajectories A4 and 22

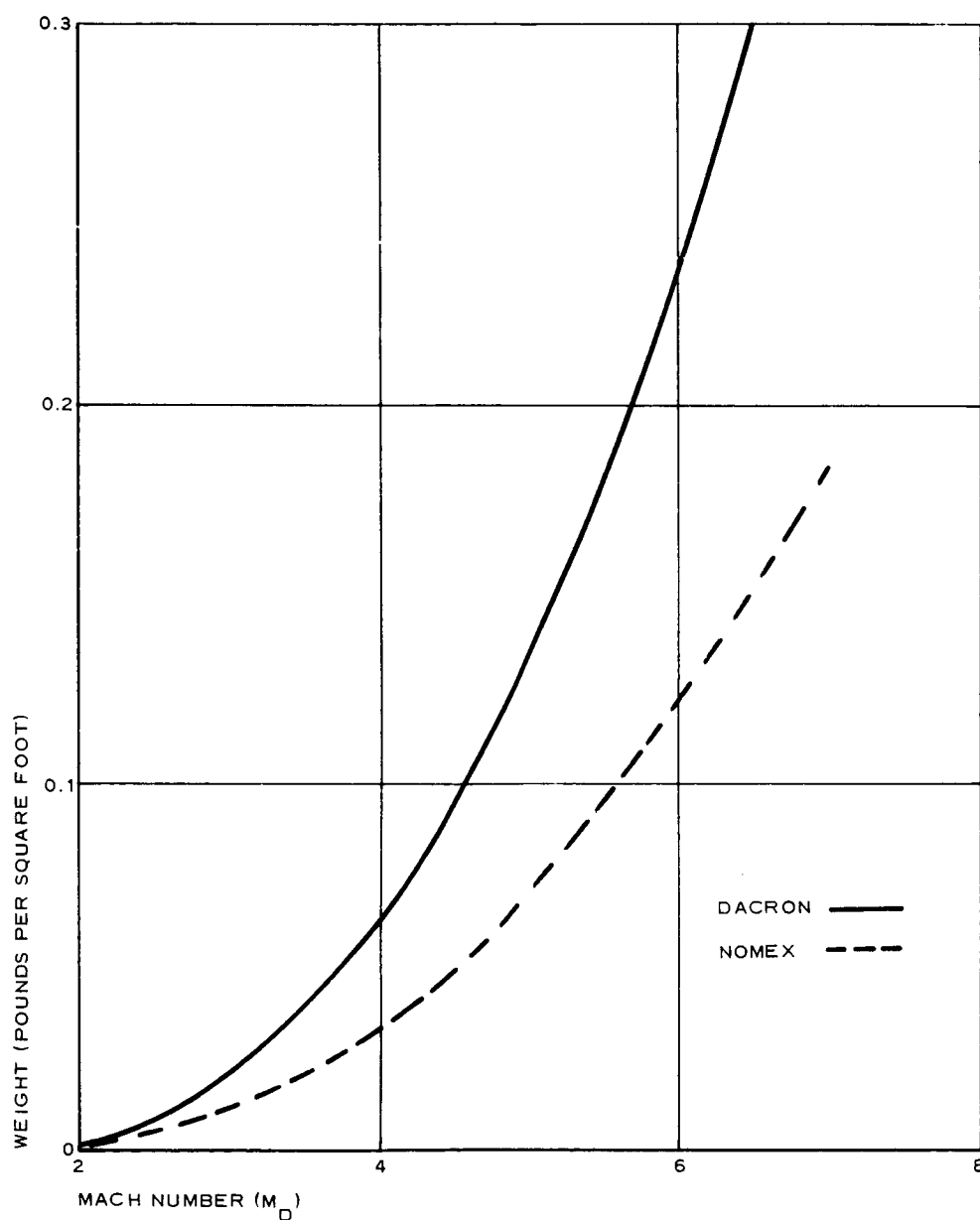


Figure 48 - Decelerator Fabric Envelope Weight Required versus Initial Mach Number, Trajectory 37

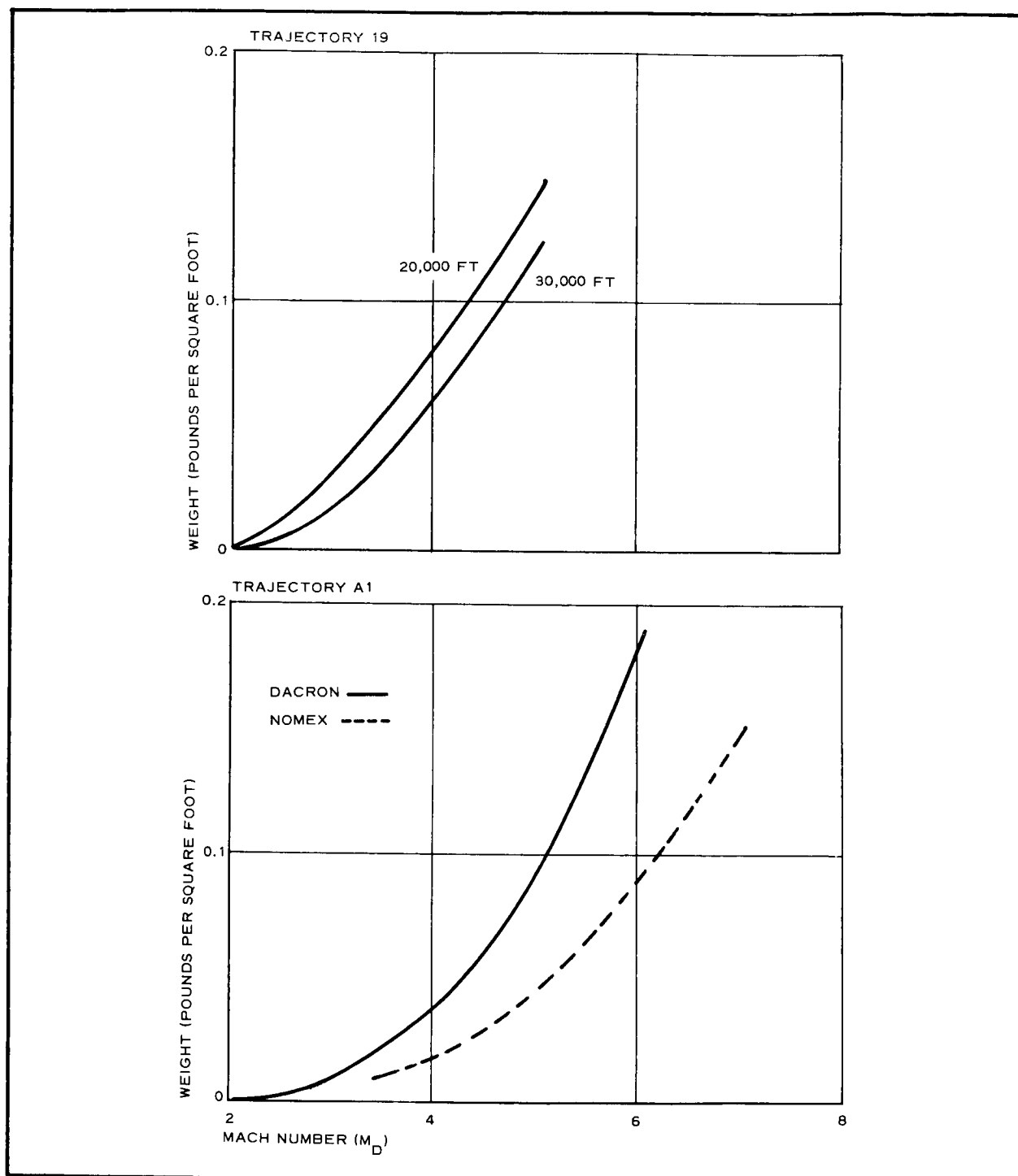


Figure 49 - Decelerator Fabric Envelope Weight Required versus Initial Mach Number, Trajectories A1 and 19

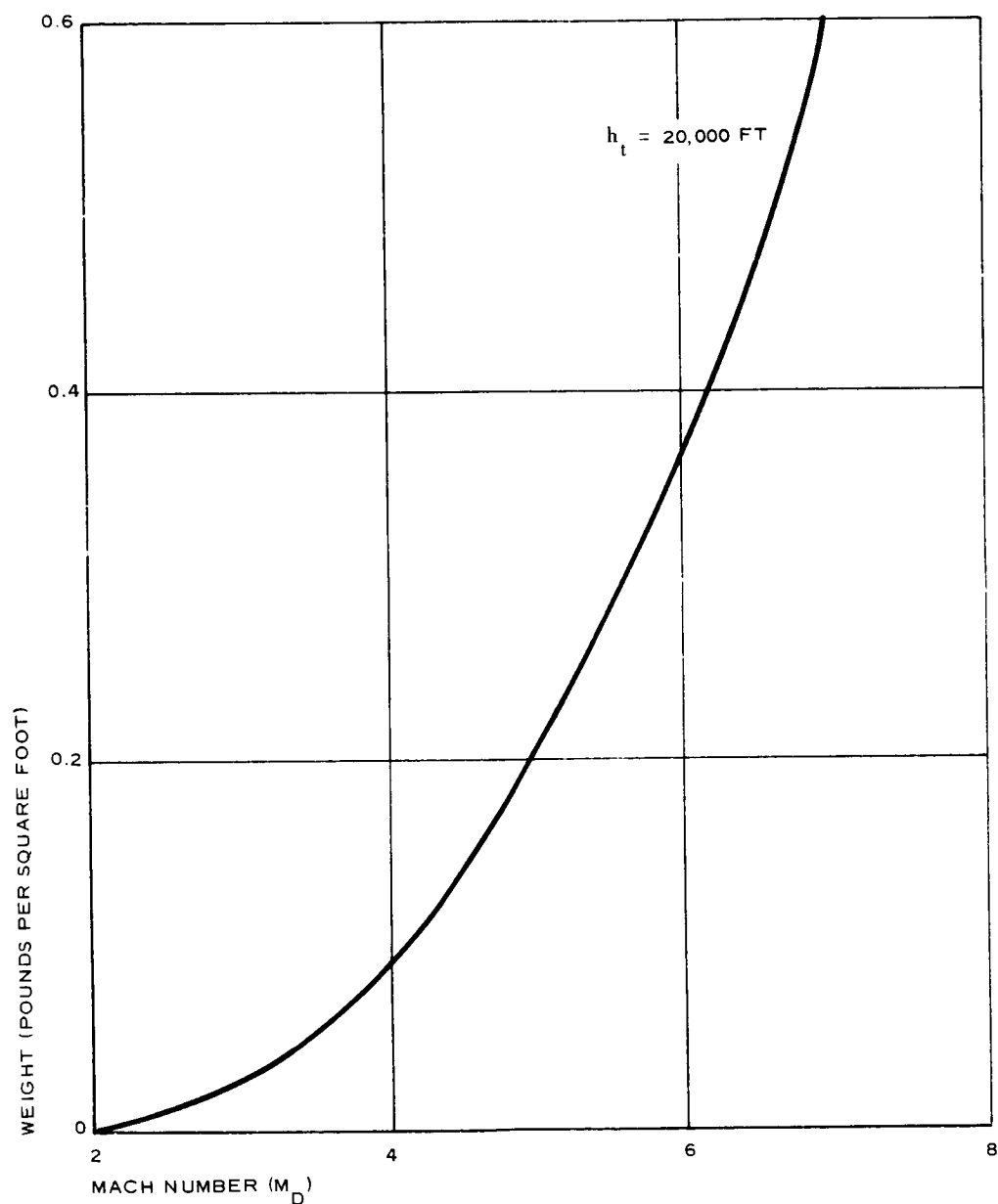
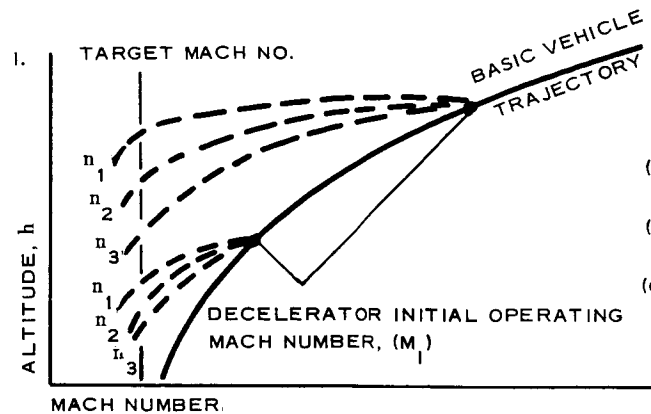


Figure 50 - Decelerator Fabric Envelope Weight Required versus Initial Mach Number, Trajectory B3

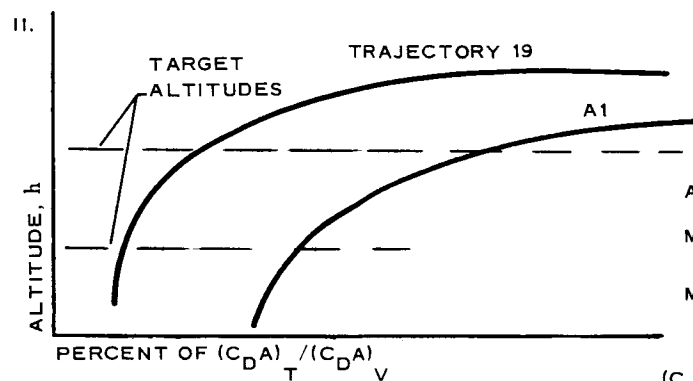


$$n = \text{PERCENT OF } \frac{(C_{DA})_T}{(C_{DA})_V} \times (C_{DA})_V$$

$(C_{DA})_V$ = VEHICLE DRAG AREA $\hat{=}$ 100 PERCENT VALUE

$(C_{DA})_D$ = DECELERATOR DRAG AREA

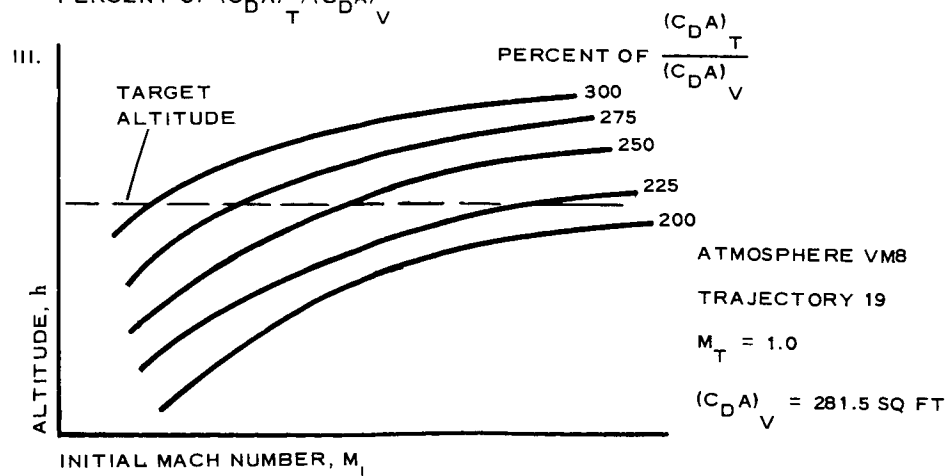
$$(C_{DA})_T = (C_{DA})_V + (C_{DA})_D$$



ATMOSPHERE VM8

$$M_T = 1.0$$

$$M_i = 3.0$$



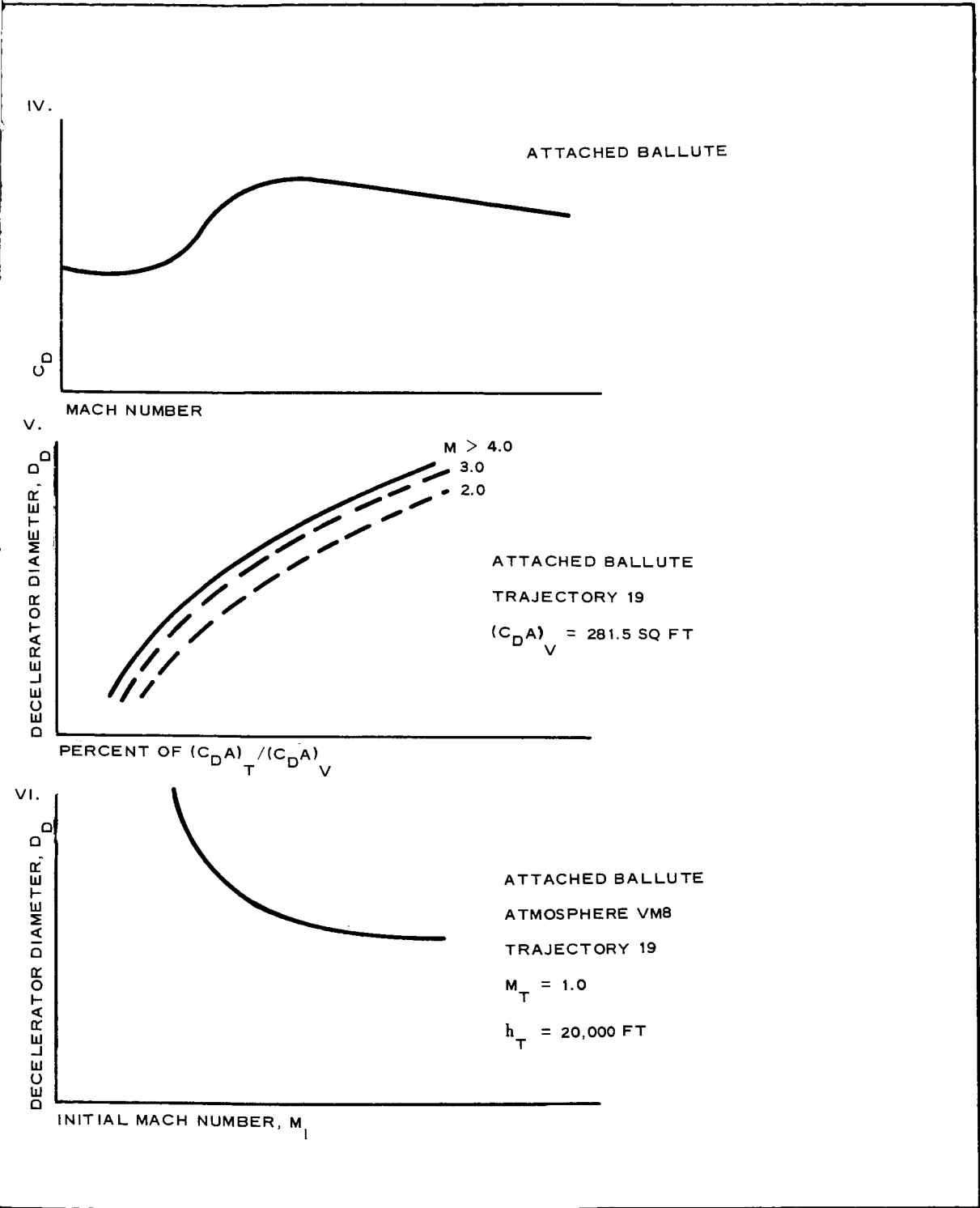


Figure 51 - Six Steps in Determining Decelerator Size

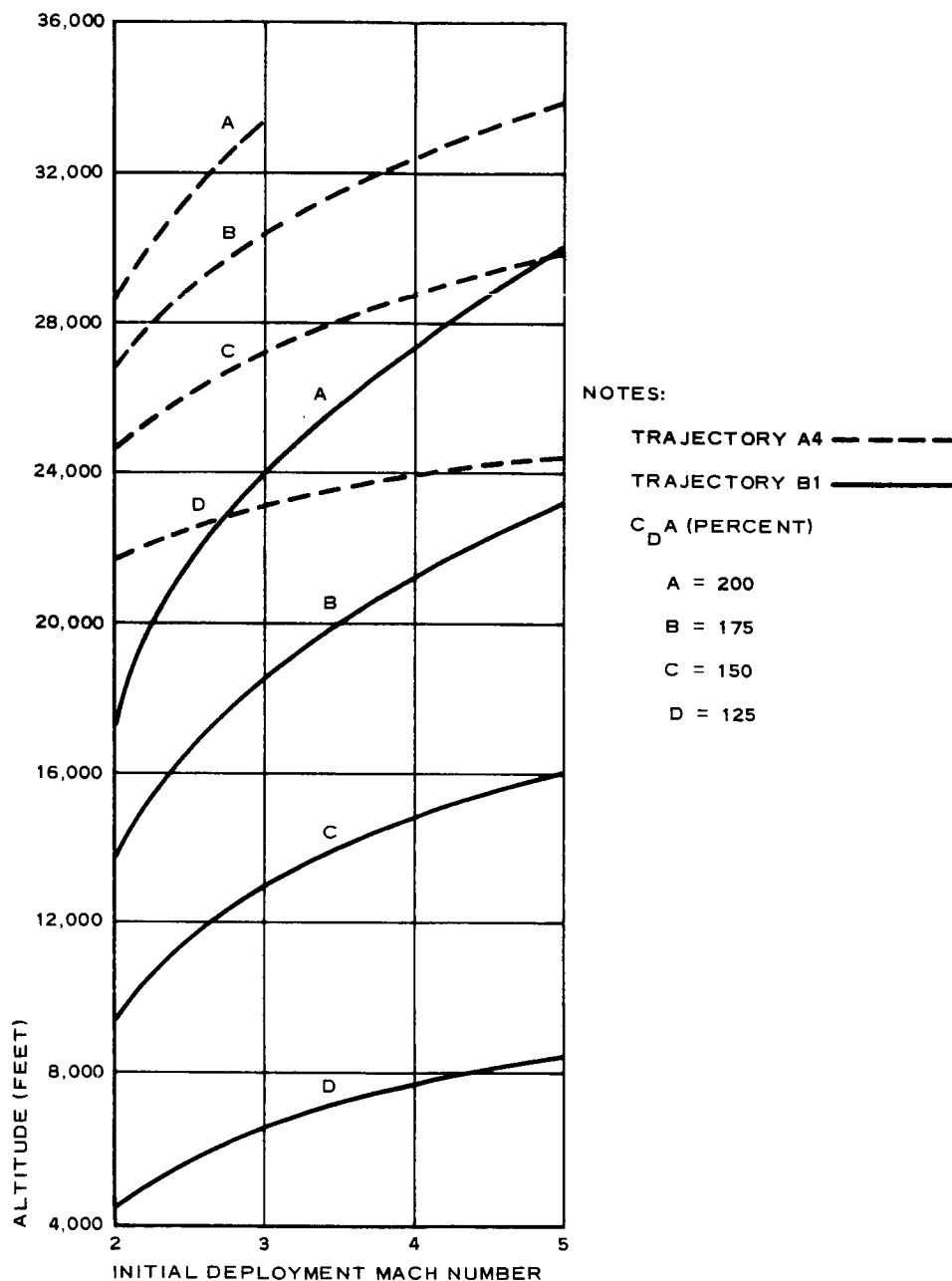


Figure 52 - Altitudes at which Various Decelerators Reach Mach Targets (M_t) as Functions of Initial Mach Numbers and Percent Initial $C_D A$ in VM7 Atmosphere

SECTION V - DECELERATOR SIZE
DETERMINATION

To determine the approximate sizes of expandable decelerators needed for specified target Mach numbers and altitudes, Goodyear Aerospace used graphic analysis of point-mass trajectory computations.

Figure 51 schematically illustrates six steps involved in this procedure. Figures 51 through 66 are curves used to determine decelerator sizes shown in Section VI.

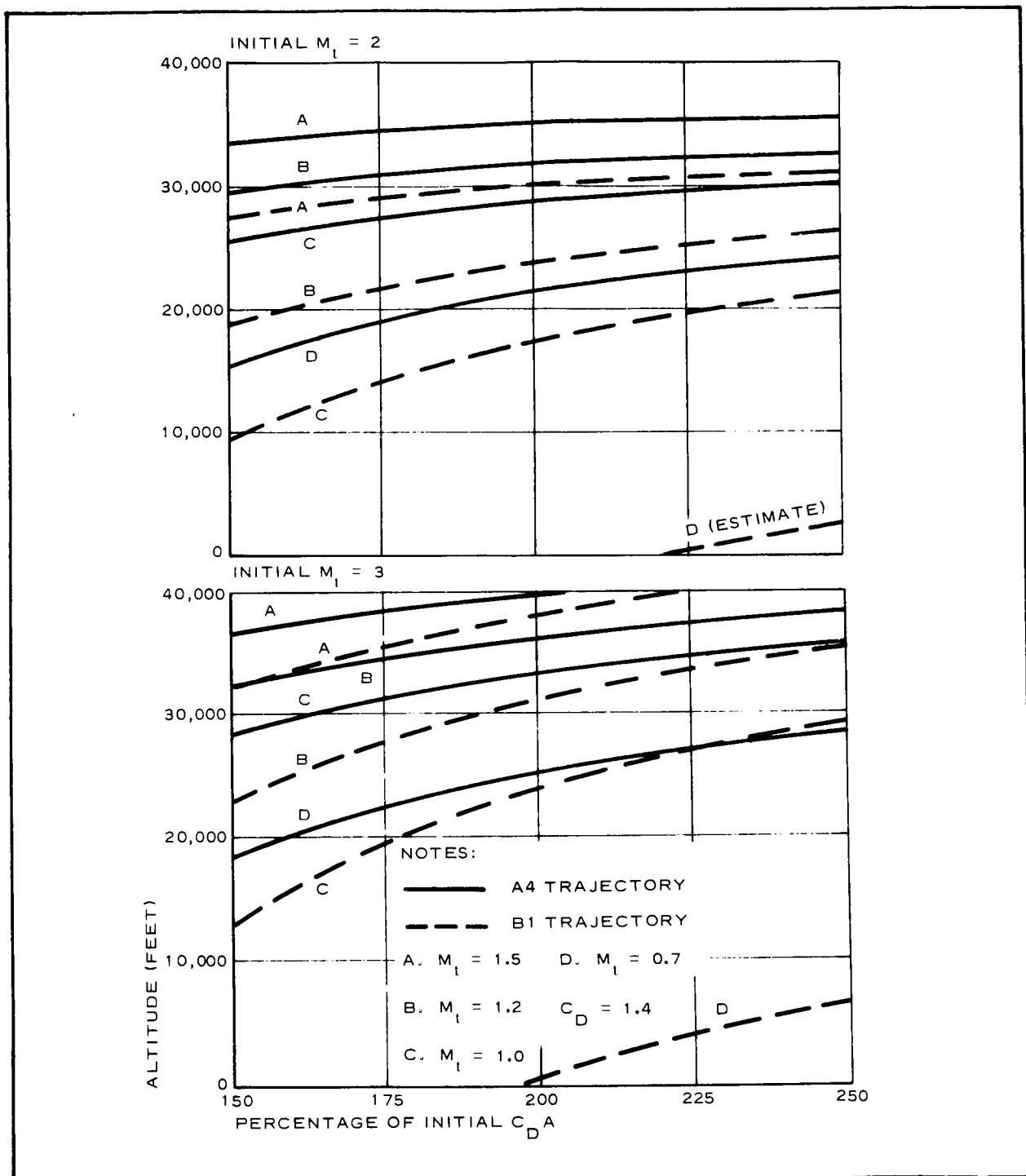


Figure 53 - Altitudes at which B1 and A4 Trajectory Decelerators Reach Mach Targets (M_t) (VM7 Atmosphere)

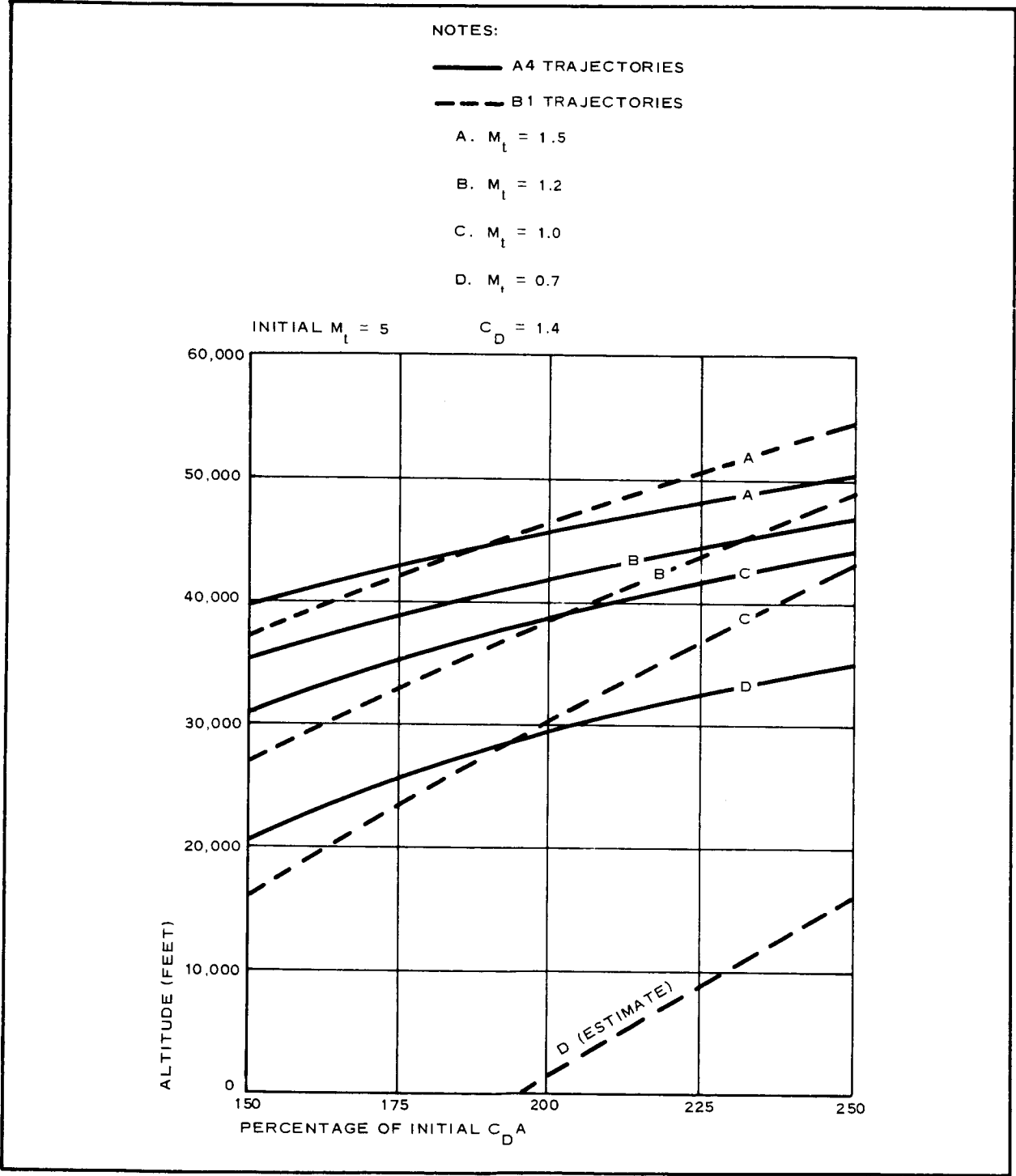


Figure 54 - Altitudes at which B1 and A4 Trajectory Decelerators Reach Mach Targets (M_t) in VM7 Atmosphere

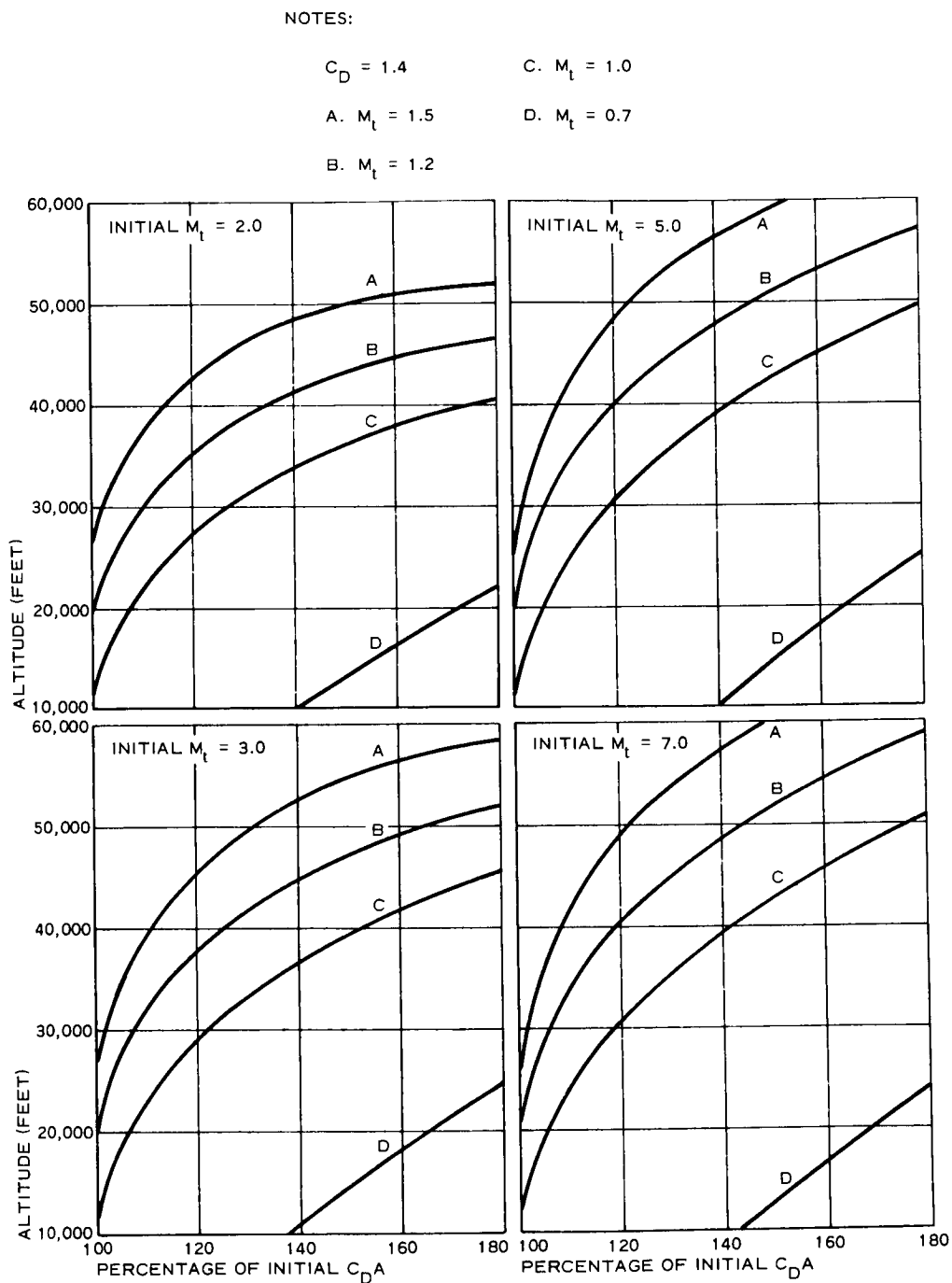


Figure 55 - Altitudes at which Trajectory 22 Decelerators Reach Mach Targets in VM7 Atmosphere

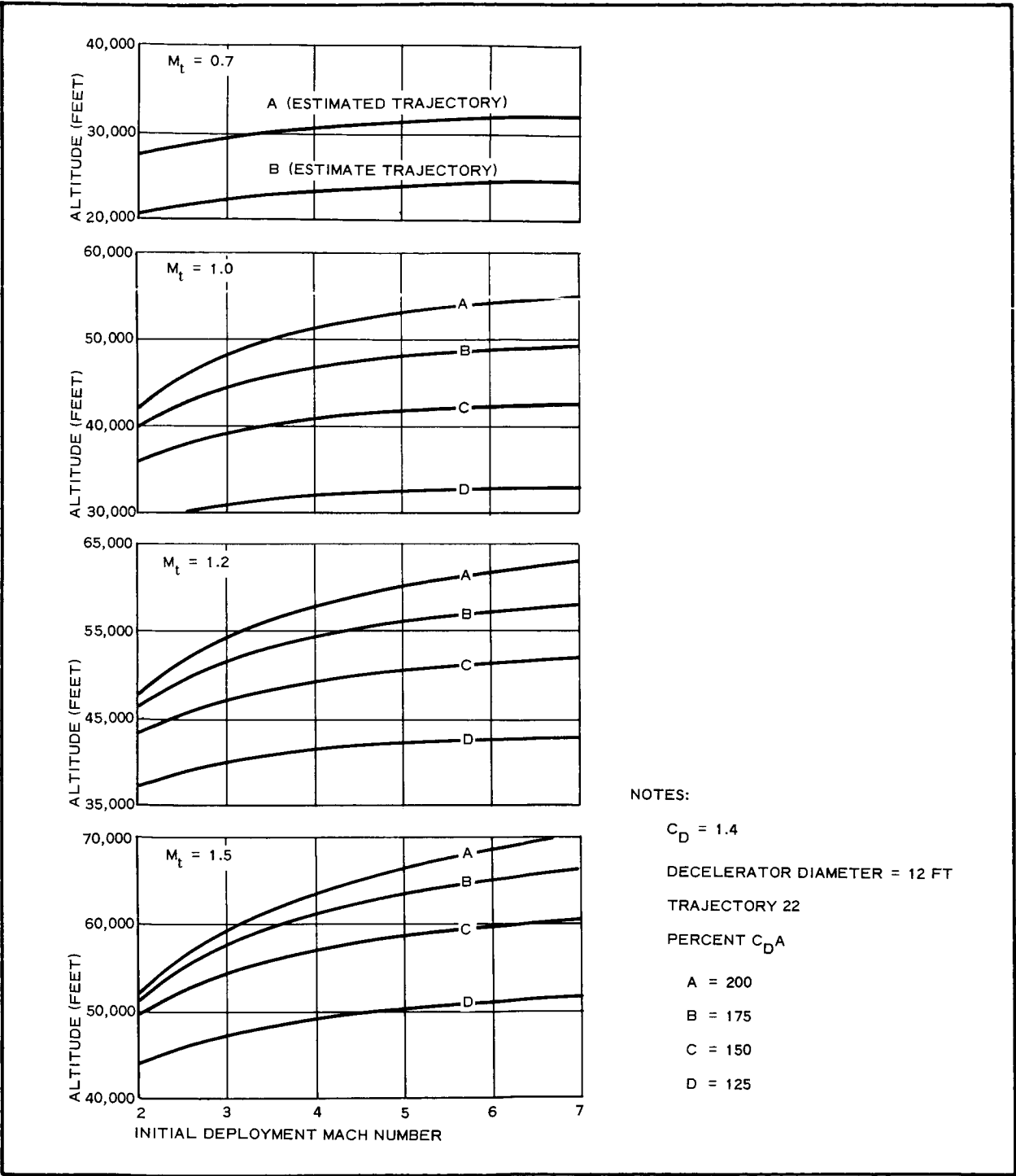


Figure 56 - Altitudes at which Trajectory 22 Decelerators Reach Mach Targets as Functions of Initial Mach Number and Percent Initial $C_D A$ in VM7 Atmosphere

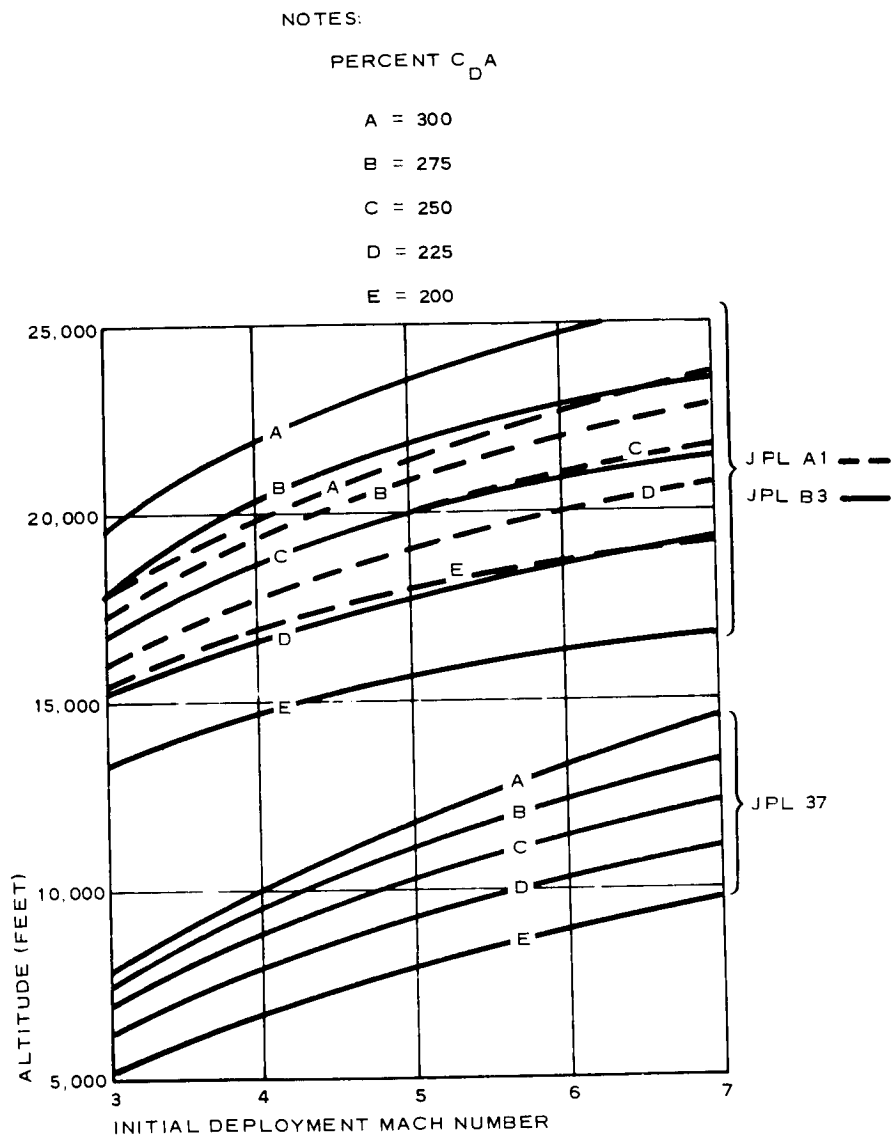


Figure 57 - Altitudes at which Various Decelerators Reach $M_t = 1.0$ as Functions of Original Mach Numbers and Percent of Initial $C_D A$ in VM8 Atmosphere

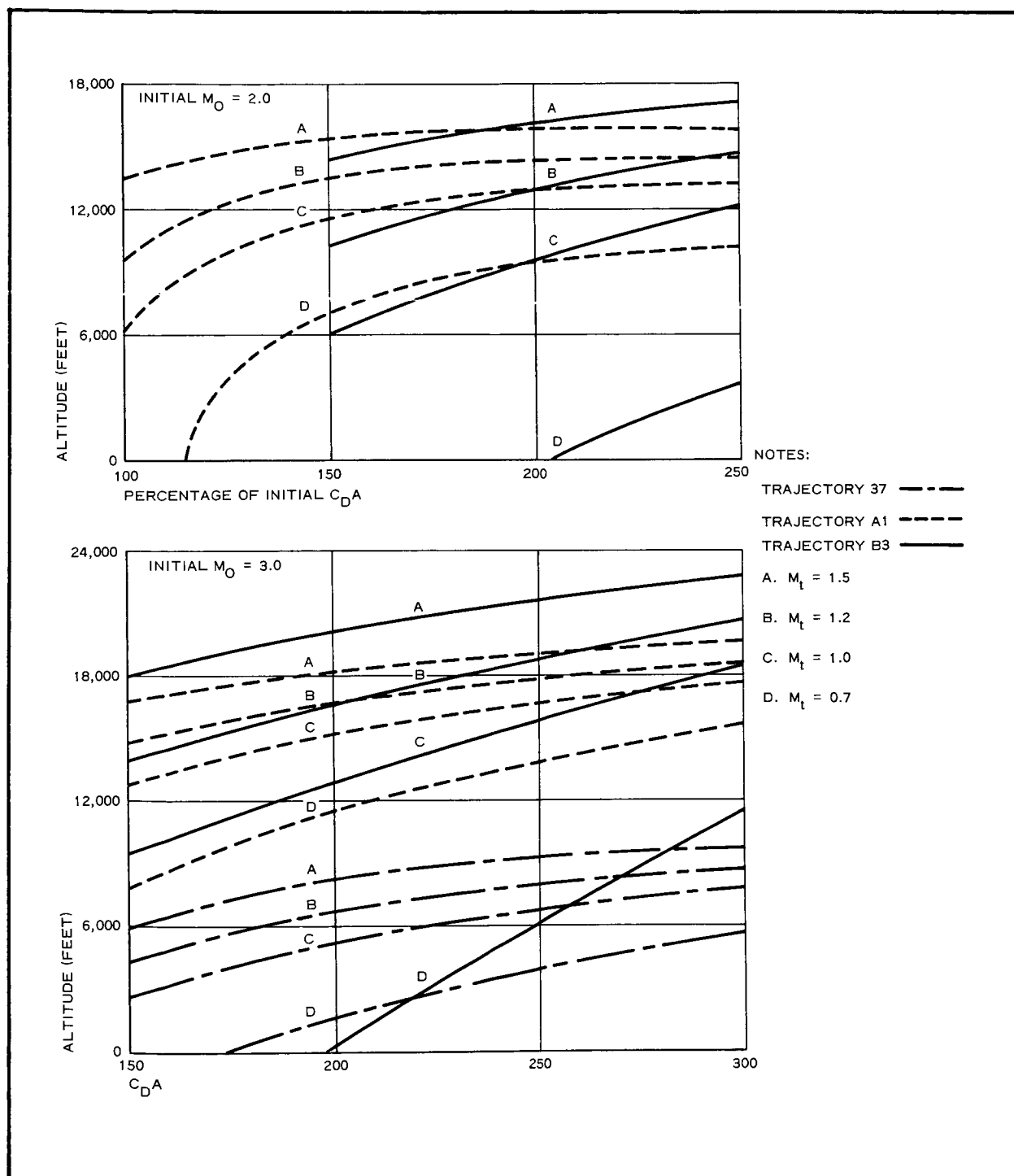


Figure 58 - Altitudes at which Decelerators Reach Mach Targets (M_t) in VM8 Atmosphere in A1, B3, and 37 Trajectories

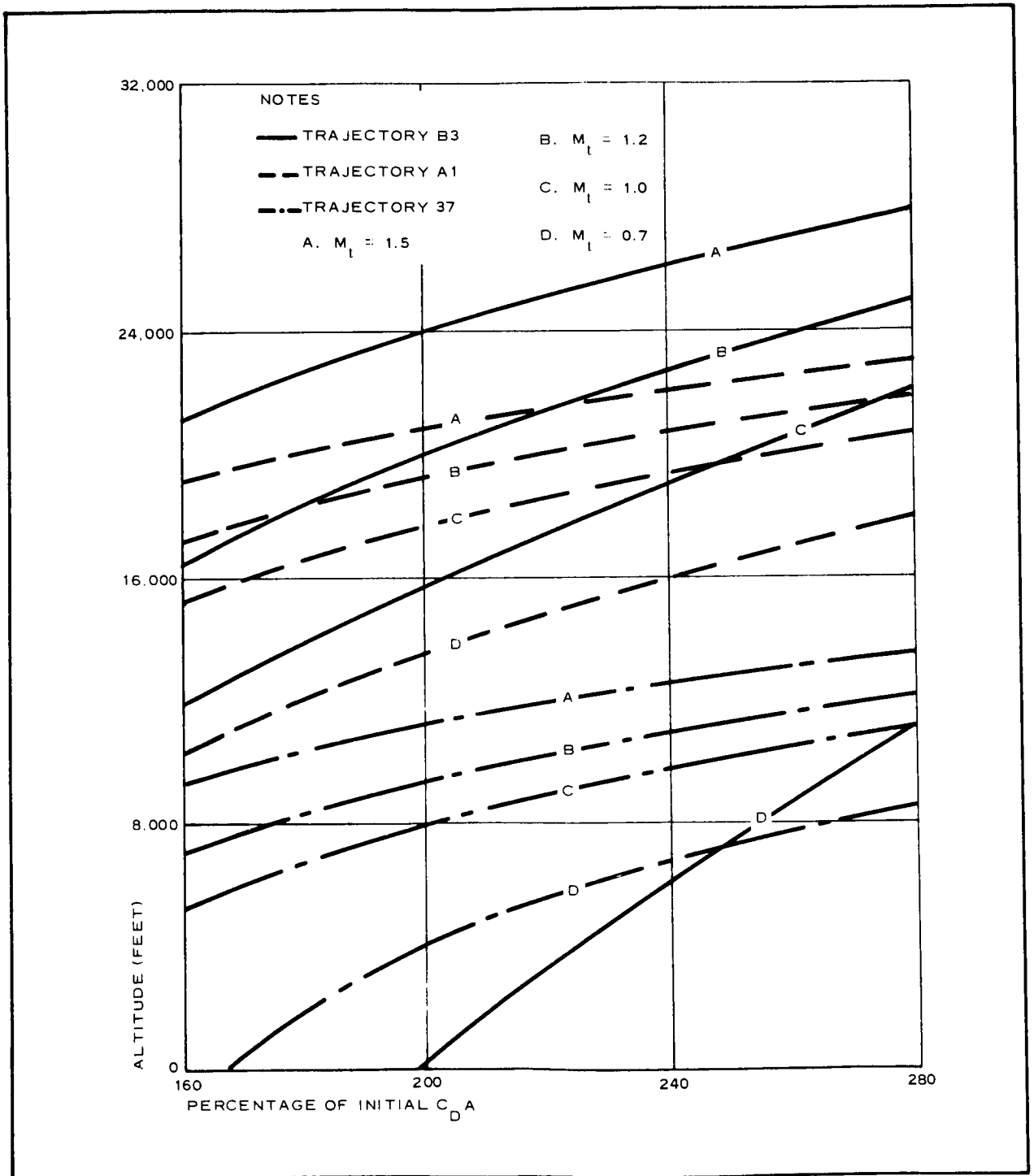


Figure 59 - Altitudes at which Decelerators Reach Mach Targets (M_t) in VM8 Atmosphere at Trajectories A1, B3, and 37 with Initial Mach 5.0

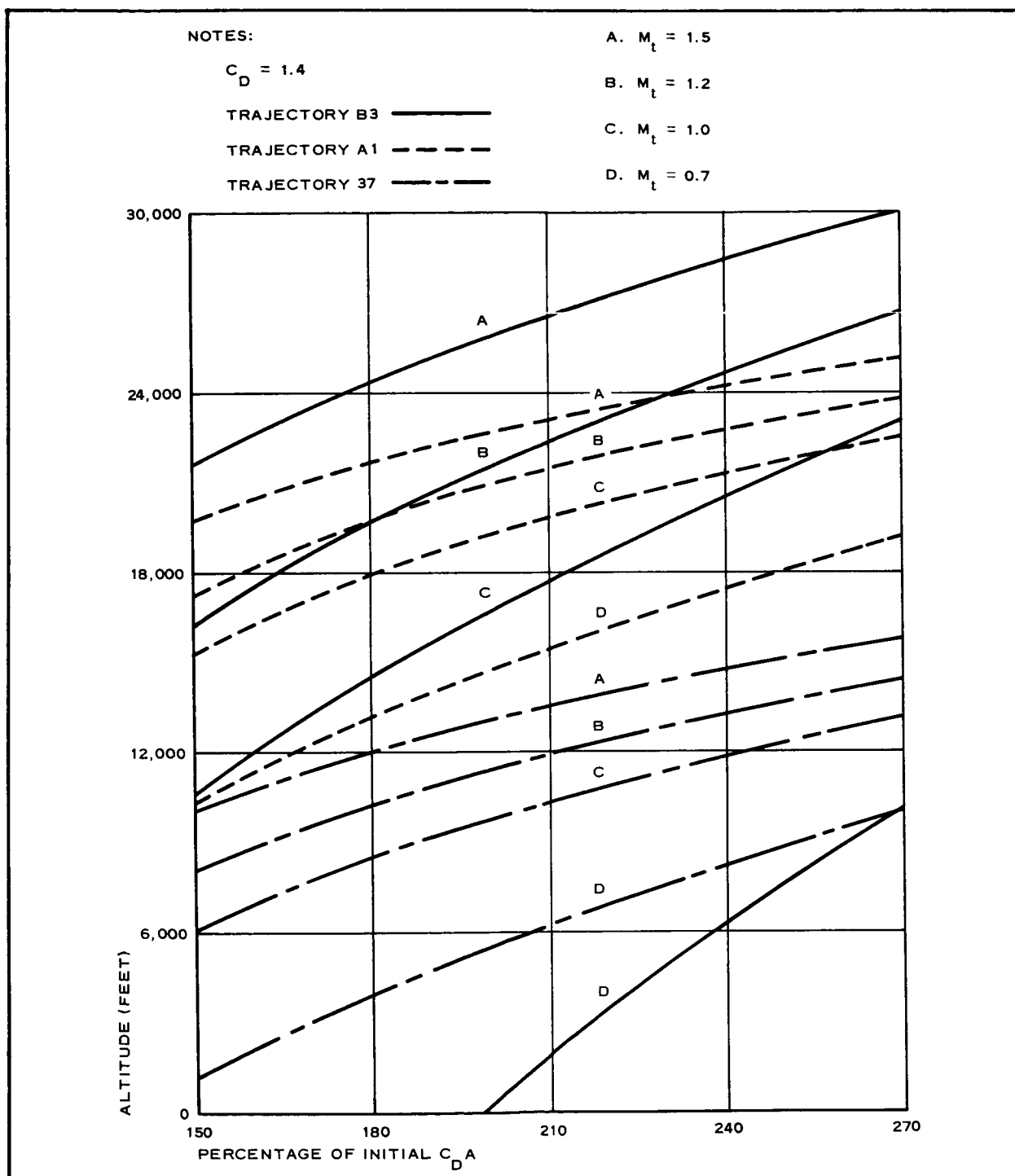


Figure 60 - Altitudes at which Decelerators Reach Mach Targets (M_t) in VM8 Atmosphere at Trajectories A1, B3, and 37 with Initial Mach 7.0

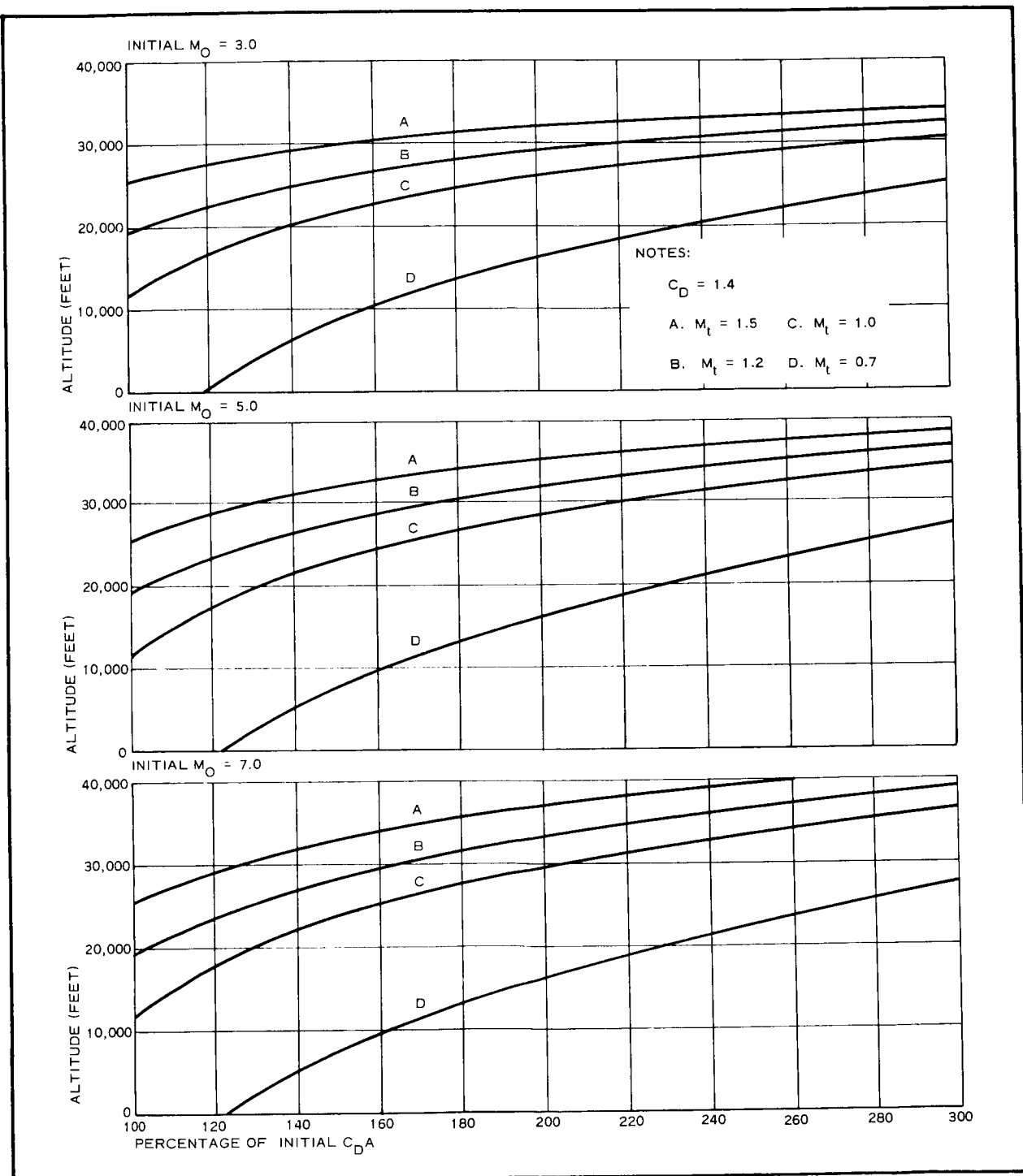


Figure 61 - Altitudes at which Decelerators Reach Mach Targets (M_t) in VM8 Atmosphere at Trajectory 19

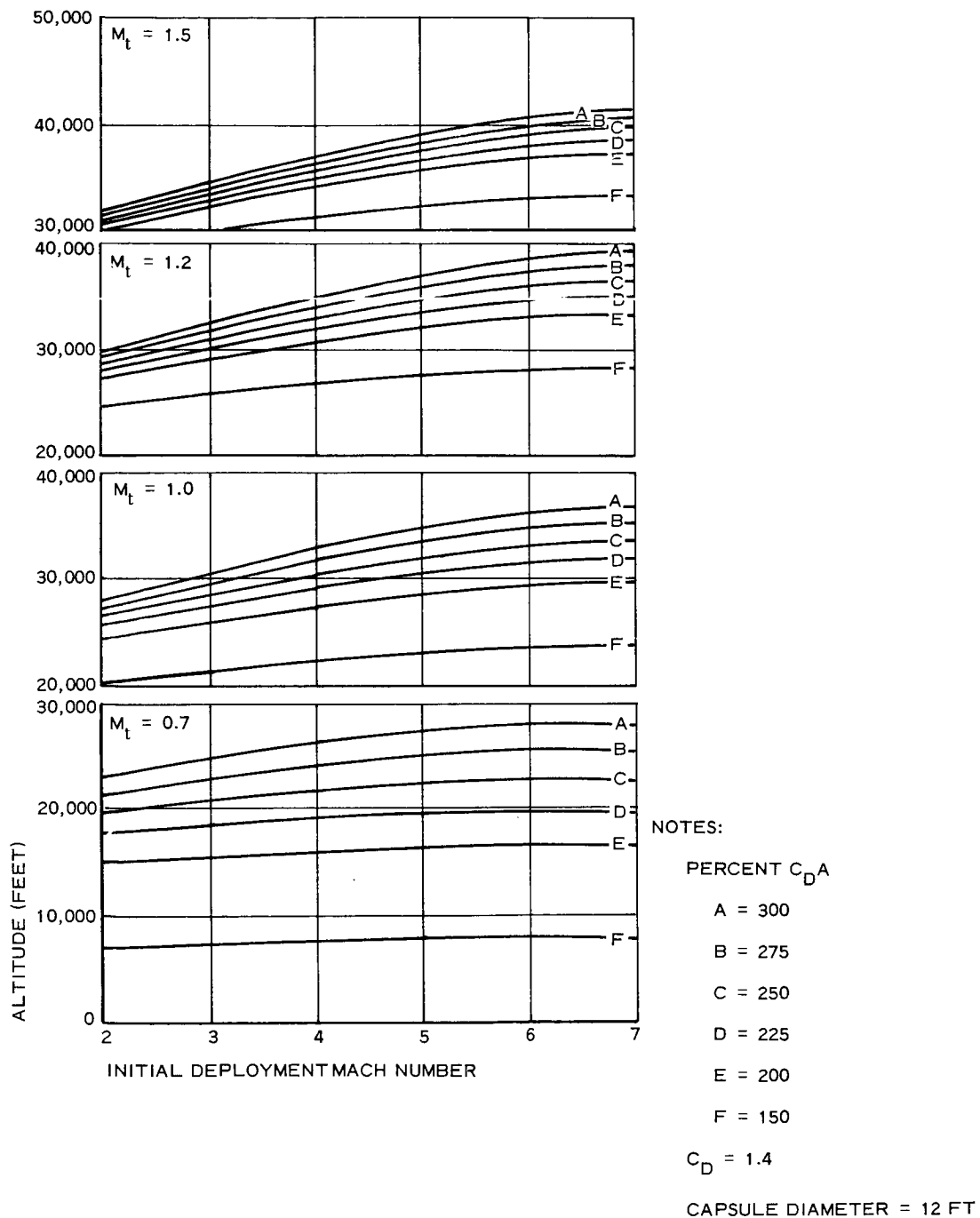


Figure 62 - Altitudes at which Decelerators Reach Mach Targets as Functions of Initial Mach Numbers and Percent of Initial $C_D A$ in VM8 Atmosphere with JPL-19 Trajectory

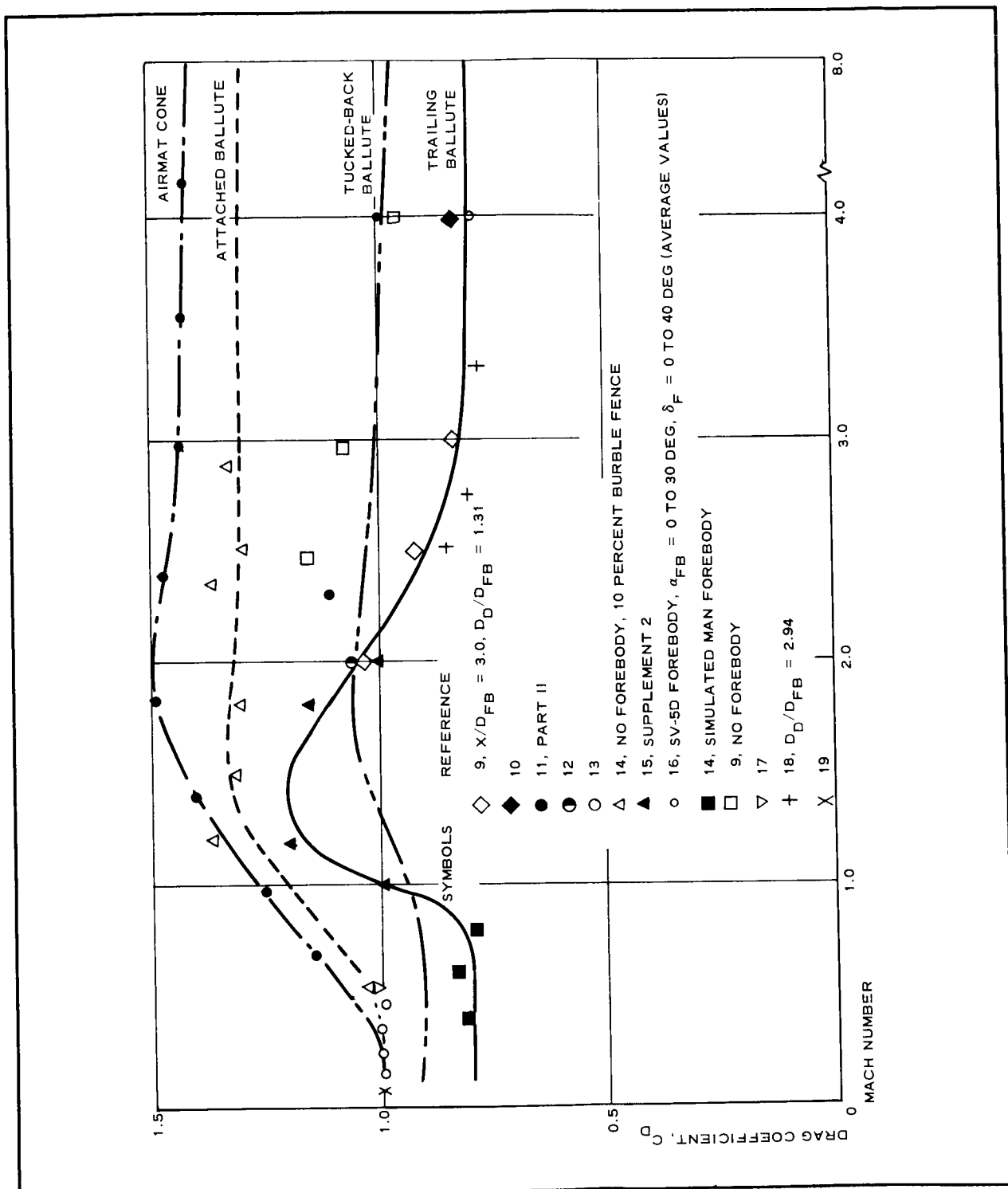


Figure 63 - Drag Coefficient Variation with Mach Number

CONFIGURATION NUMBER	DIAMETER (FEET)	MASS (SLUGS)	(C _D A) _{BASIC} (SQUARE FEET)
A	18.5	94.0	376.0
B	12.0	79.0	158.0
C	16.0	84.5	281.5

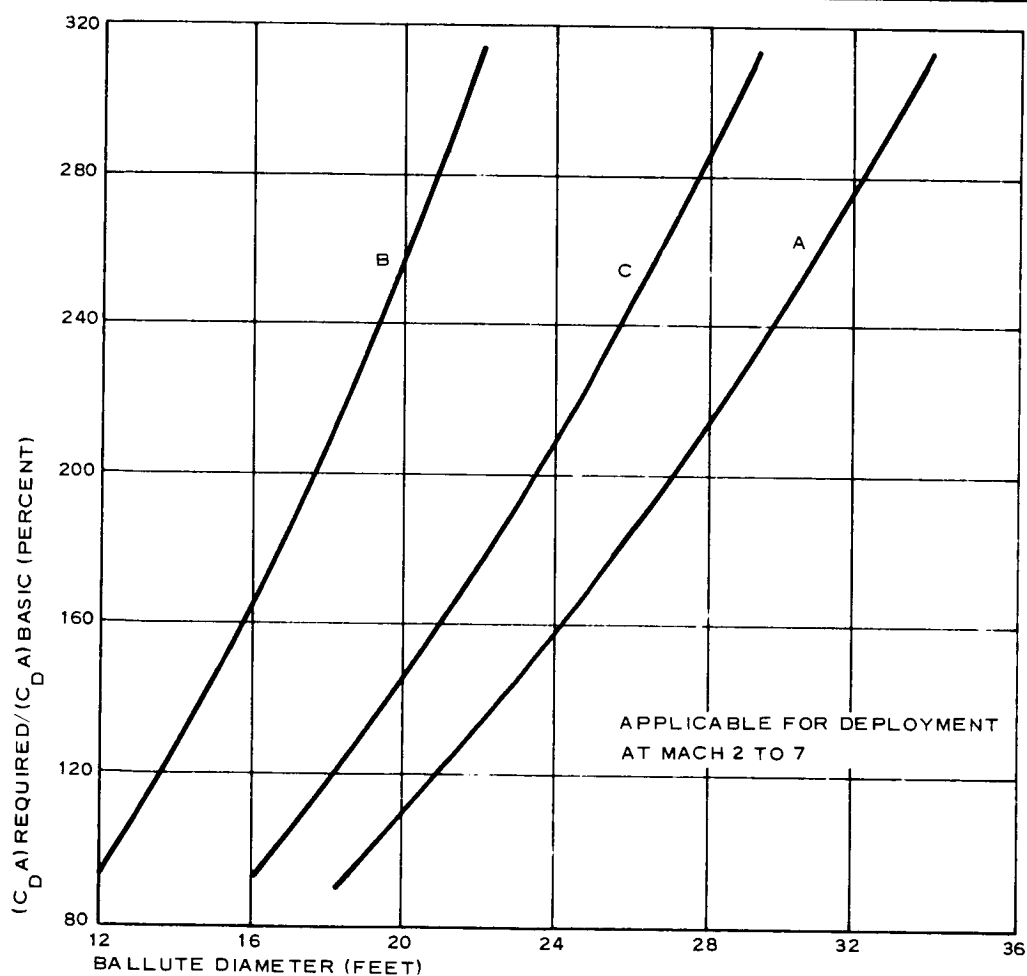


Figure 64 - Percent Drag Area versus Diameter for BALLUTE Decelerator Applied to Three Entry Configuration

CONFIGURATION NUMBER	DIAMETER (FEET)	MASS (SLUGS)	(C _D A) BASIC (SQARE FEET)
A	18.5	94.0	376.0
B	12.0	79.0	158.0
C	16.0	84.5	281.5

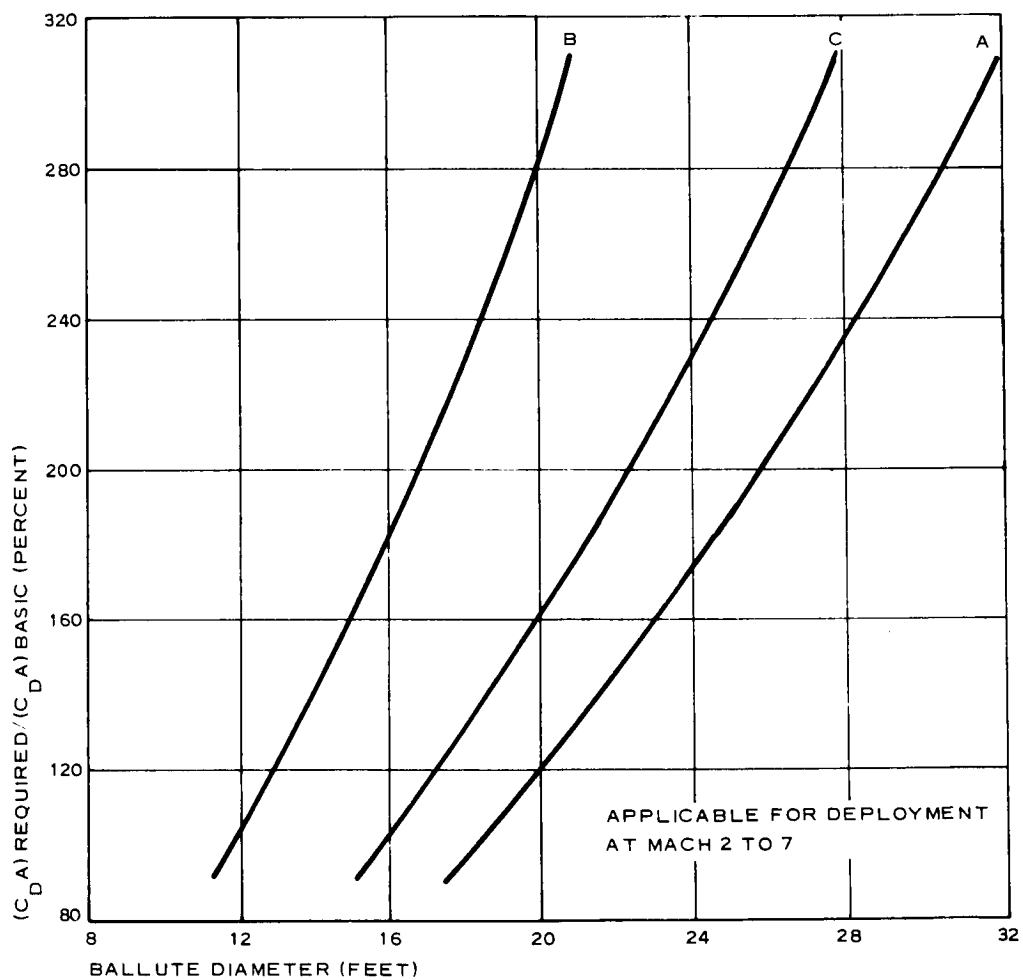


Figure 65 - Percent Drag Area versus Diameter for Inflatable Skirt Decelerator Applied to Three Entry Configuration

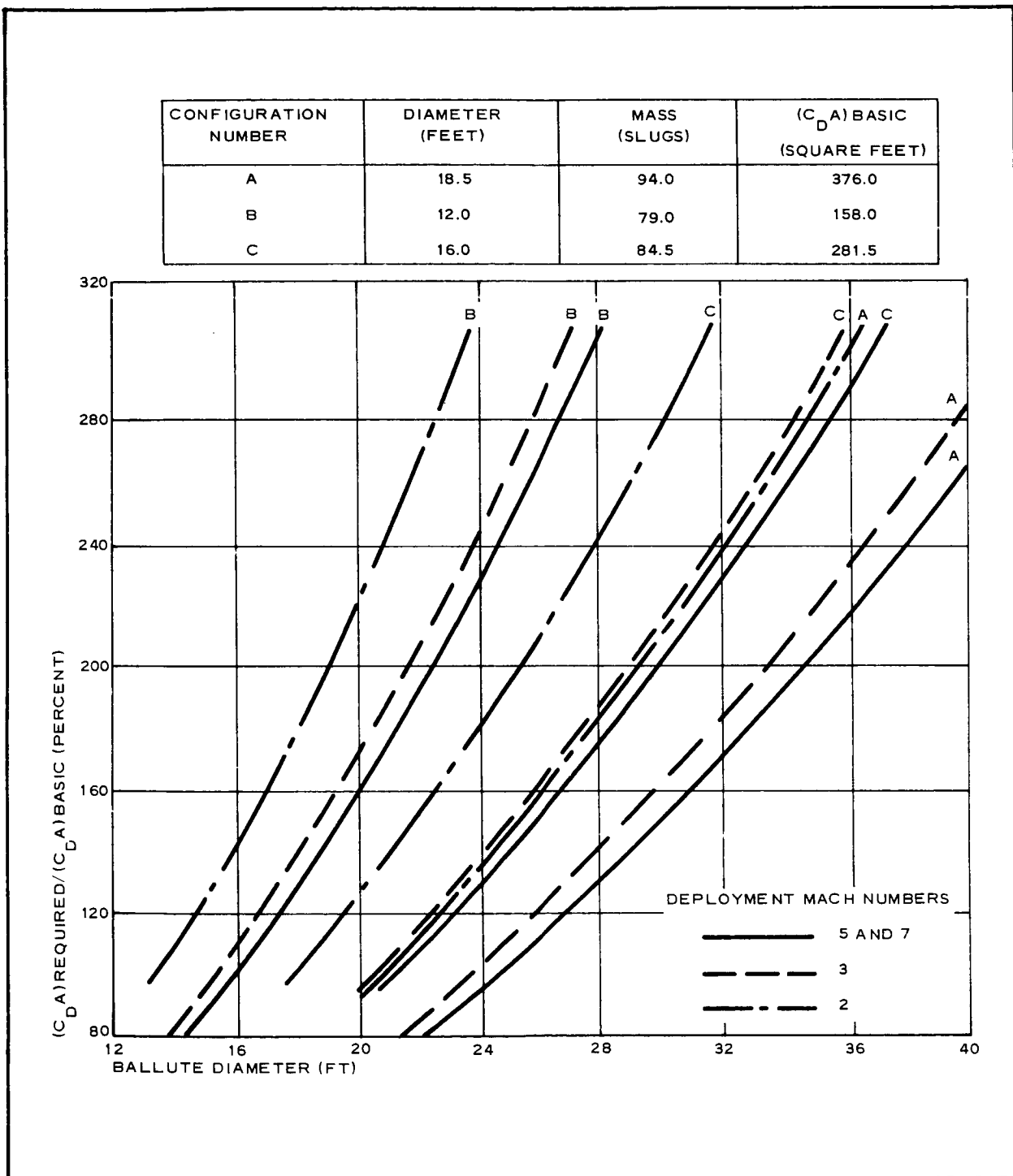


Figure 66 - Drag Area versus Diameter of Trailing BALLUTE for Three Entry Capsule Configuration

SECTION VI - ANALYSIS RESULTS

This section presents graphically the first approximations of decelerator size requirements determined by analyses described in Section V.

Percentage weight fractions are included for these decelerator sizes. These fractions were developed by analyses described in Appendix A of this volume as a function of the initial operating Mach number.

Figures 67 through 99 present curves that establish the minimum required decelerator envelope unit weight compatible simultaneously with aerodynamic heating and loading environments for several entry cases.

Each curve is associated with a decelerator configuration. These configurations decelerate the entry capsule to Mach 1 near the target altitude specified in the illustration. Indicated on the illustrations are optimum initial operating Mach numbers, which are associated with minimum percentage of decelerator to total entry vehicle weight.

Minimum practical envelope unit weight also is recorded on the curve illustrations for each decelerator type.

Thermal requirements are limited to a maximum temperature of 450 F for dacron and 700 F for Nomex. The minimum practical unit weight includes an 0.01-psf Neoprene or Vitron coating to provide the envelope with low porosity (approximately $0.02 \text{ cu ft/ft}^2/\text{sec}$). For this study, the coating was assumed to have the same specific heat as the envelope material.

NOTES:

TRAJECTORY: A1

ATMOSPHERIC PROFILE: VM8

TARGET MACH NUMBER: 1.0

TARGET ALTITUDE: 20,000 FT

 ϕ = OPTIMUM MACH NUMBER

ENTRY CAPSULE DATA

DIAMETER: 18.5 FT

MASS (SLUGS): 94

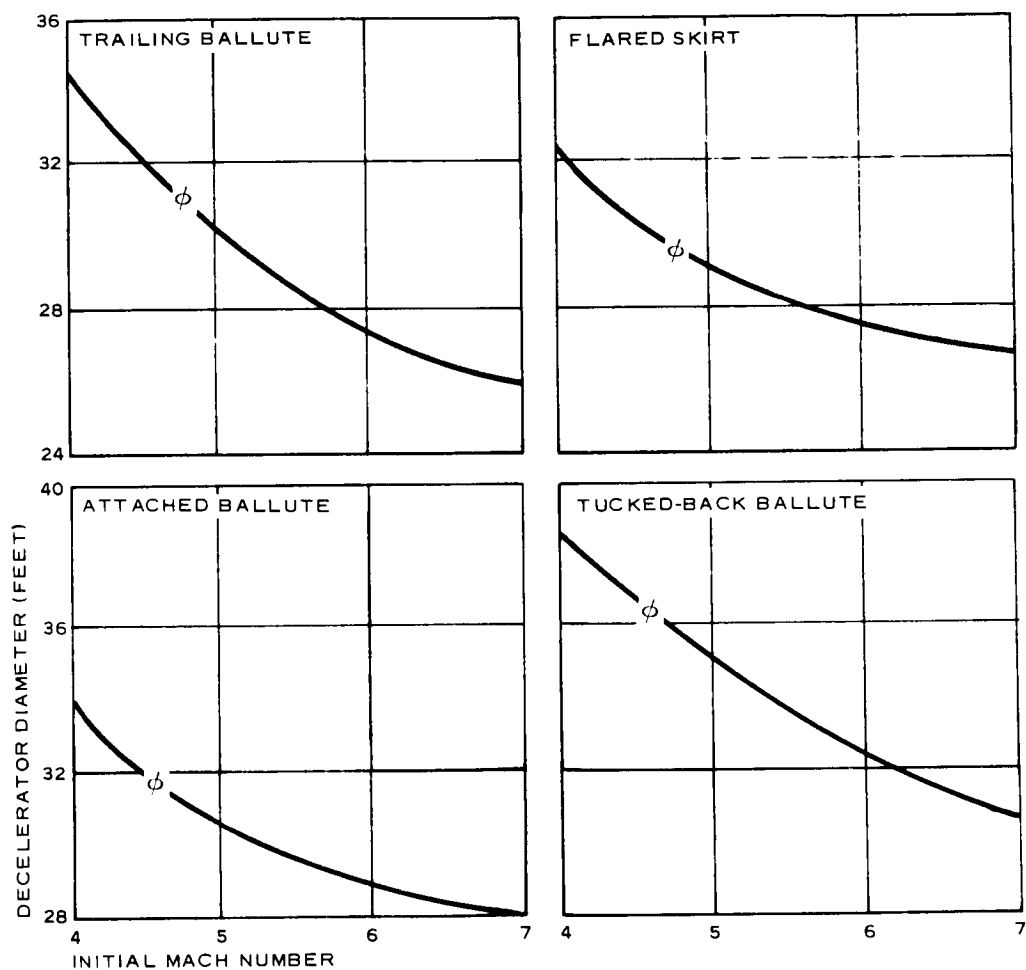
 $(C_D A)_V$: 376 SQ FT W_{EARTH} : 3025 LB

Figure 67 - Decelerator Diameter versus Deployment Mach Number for 18.5-Ft-Diameter Entry Capsule, Trajectory A1

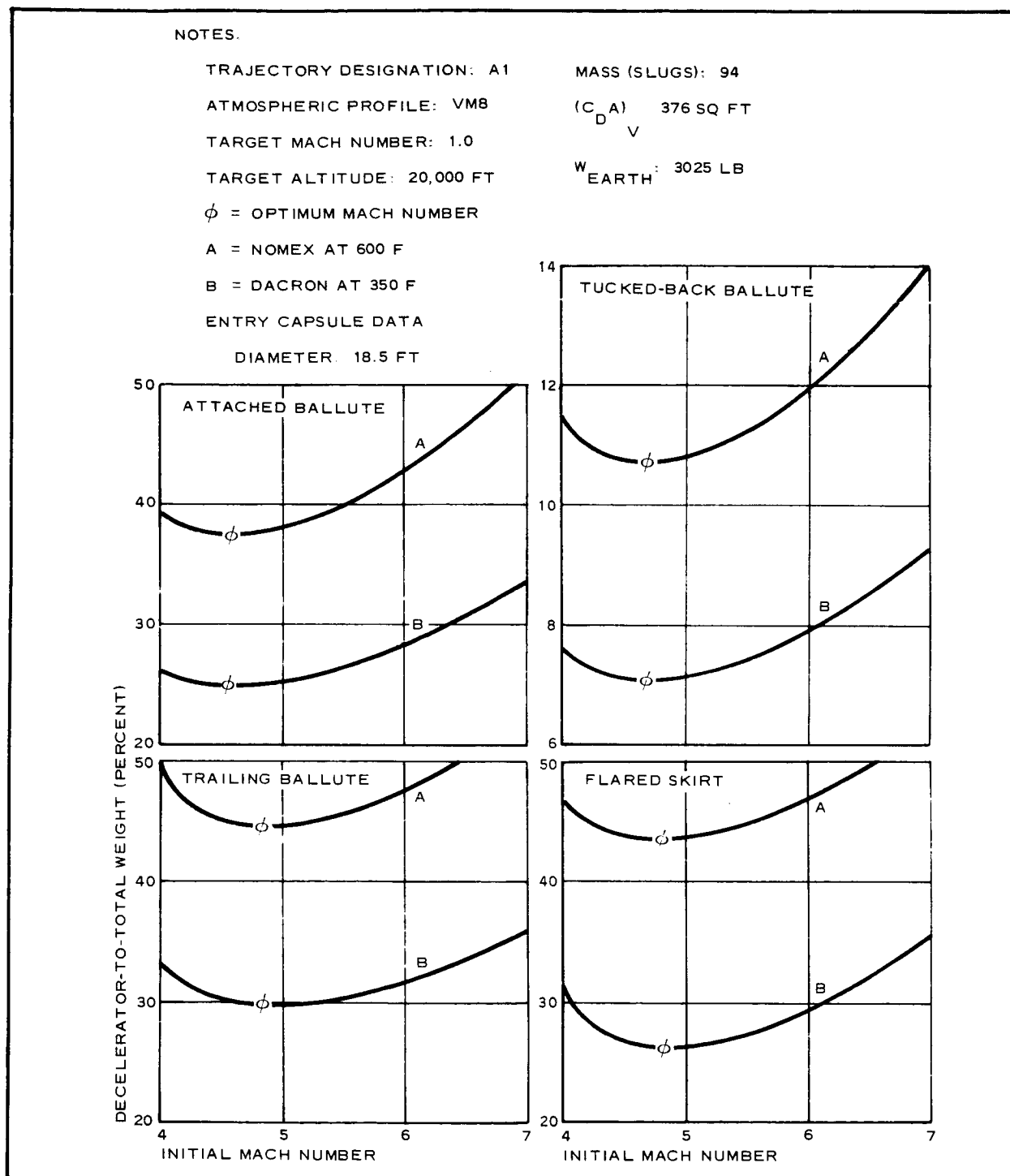


Figure 68 - Percent Decelerator to Total System Weight versus Deployment Mach Number for 18.5-Ft-Diameter Entry Capsule, Trajectory A1

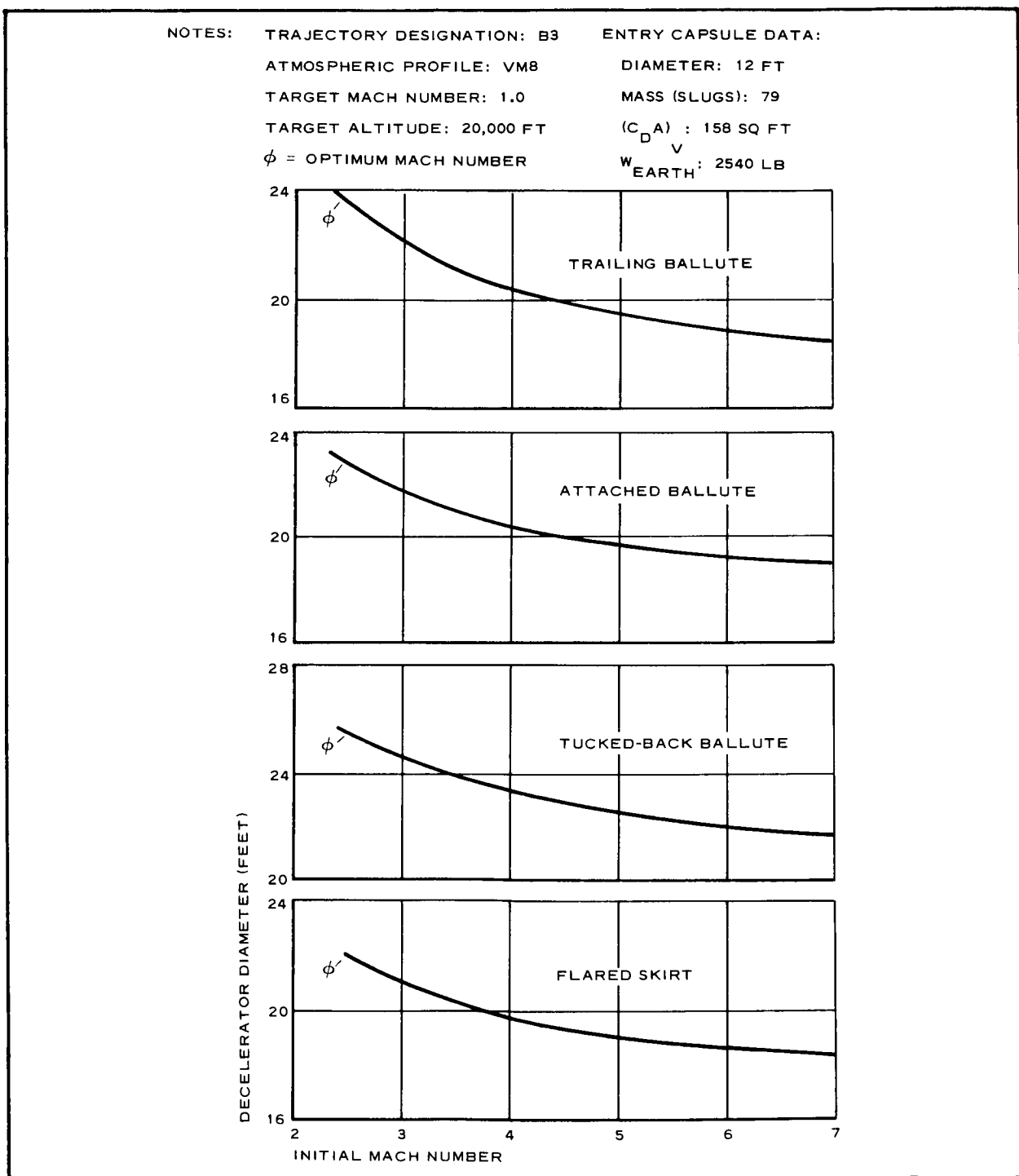
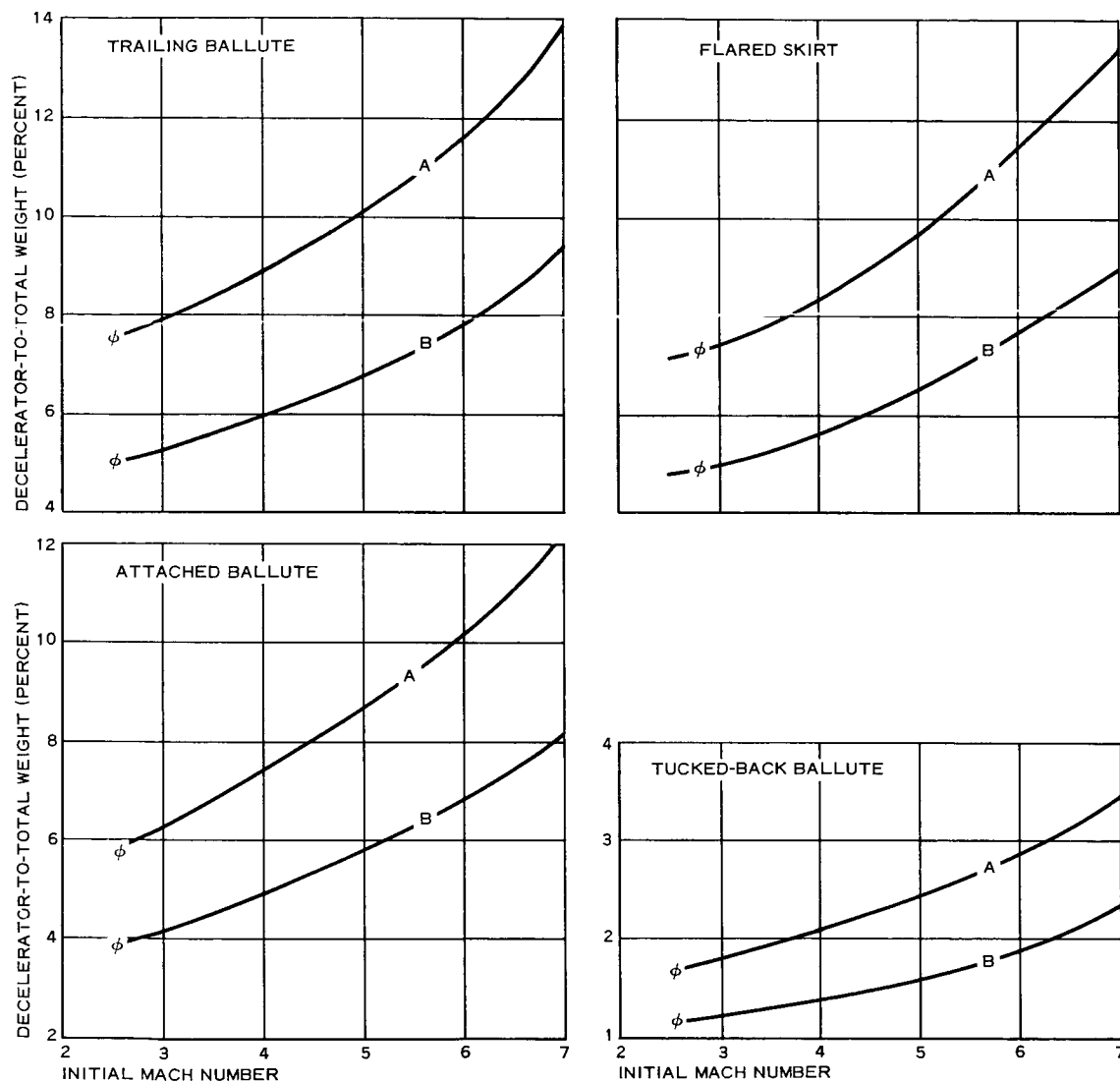


Figure 69 - Decelerator Diameter versus Deployment Mach Number for 12-Ft-Diameter Entry Capsule, Trajectory B3



NOTES:

TRAJECTORY DESIGNATION: B3
 ATMOSPHERIC PROFILE: VM8
 TARGET MACH NUMBER: 1.0
 TARGET ALTITUDE: 20,000 FT
 ϕ = OPTIMUM MACH NUMBER
 A = NOMEX AT 600 F
 B = DACRON AT 350 F

ENTRY CAPSULE DATA:
 DIAMETER: 12 FT
 MASS (SLUGS): 79
 $(C_D A)_V$: 158 SQ FT
 W_{EARTH} : 2540 LB

Figure 70 - Percent Decelerator to Total System Weight versus Deployment Mach Number for 12-Ft-Diameter Entry Capsule, Trajectory B3

NOTES:

TRAJECTORY DESIGNATION: 37

ATMOSPHERIC PROFILE: VM8

TARGET MACH NUMBER: 1.0

TARGET ALTITUDE: 10,000 FT

 ϕ = OPTIMUM MACH NUMBER

ENTRY CAPSULE DATA:

DIAMETER: 16 FT

MASS (SLUGS): 84.5

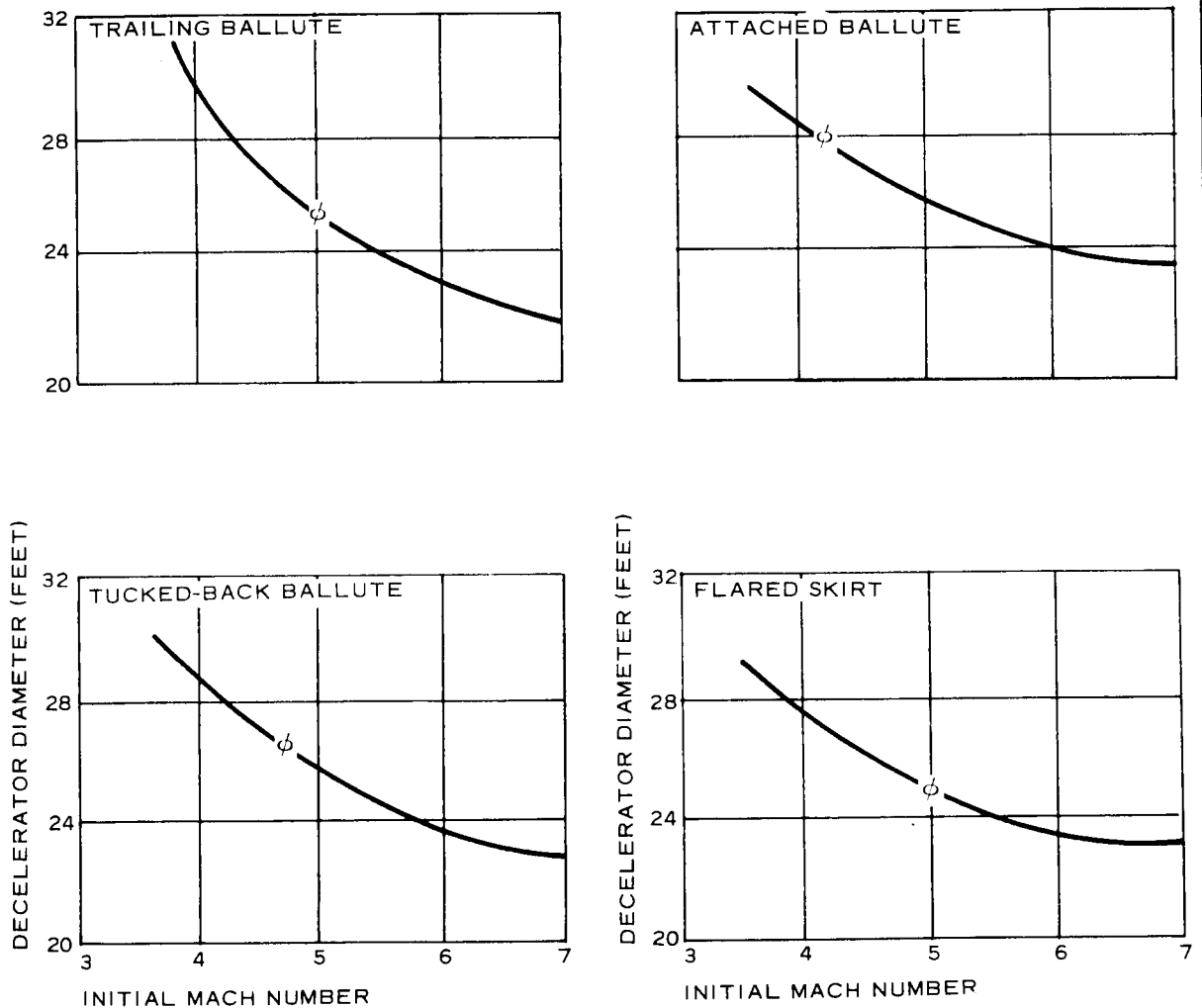
 $(C_D A)_V$: 281.5 SQ FT W_{EARTH} : 2720 LB

Figure 71 - Decelerator Diameter versus Deployment Mach Number for 16-Ft Entry Capsule Diameter, Trajectory 37

NOTES:

TRAJECTORY DESIGNATION: 37

ENTRY CAPSULE DATA

ATMOSPHERIC PROFILE: VM8

DIAMETER: 16 FT

TARGET MACH NUMBER: 1.0

MASS (SLUGS): 84.5

TARGET ALTITUDE: 10,000 FT

 $(C_D A) : 281.5 \text{ SQ FT}$
 V ϕ = OPTIMUM MACH NUMBER

A = NOMEX AT 600 F

 W_{EARTH} : 2720 LB

B = DACRON AT 350 F

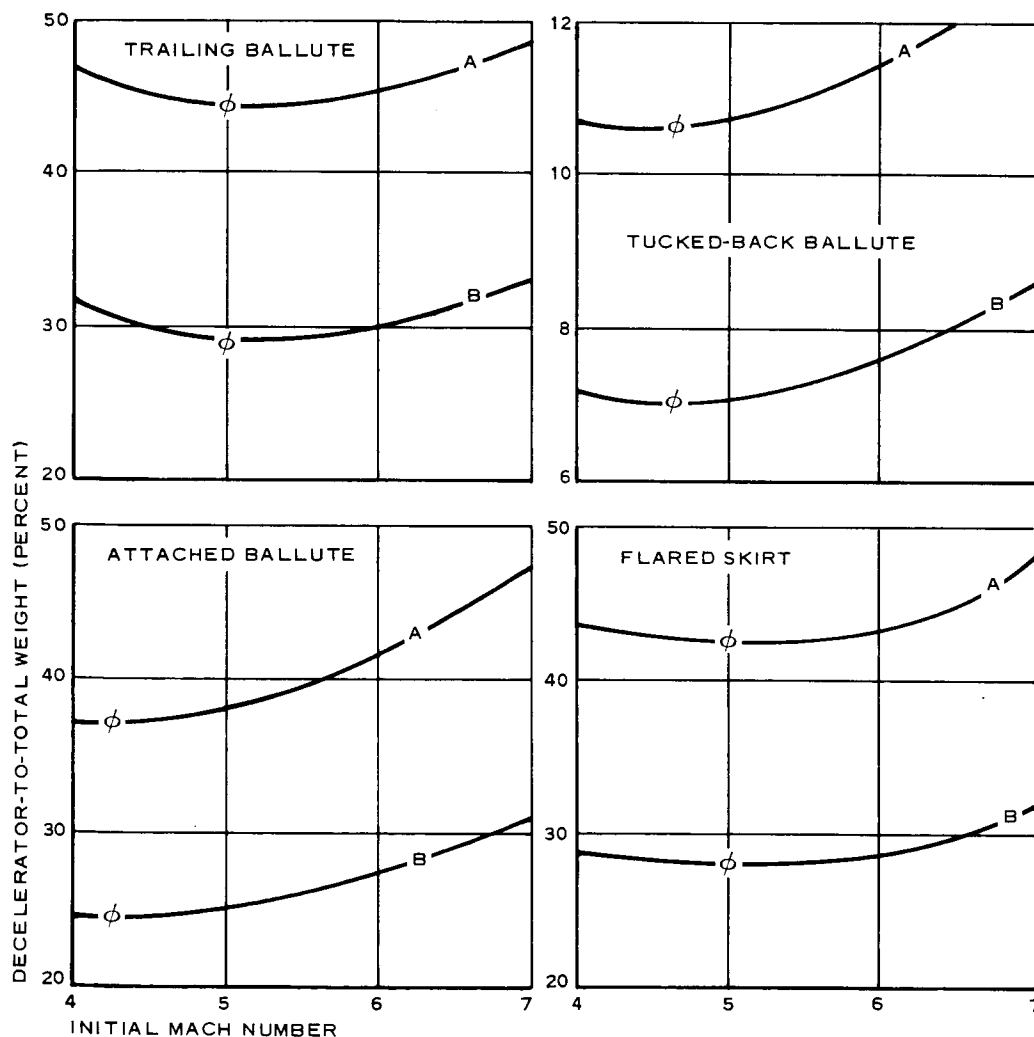


Figure 72 - Percent Decelerator to Total System Weight versus Deployment Mach Number for 16-Ft-Diameter Entry Capsule, Trajectory 37

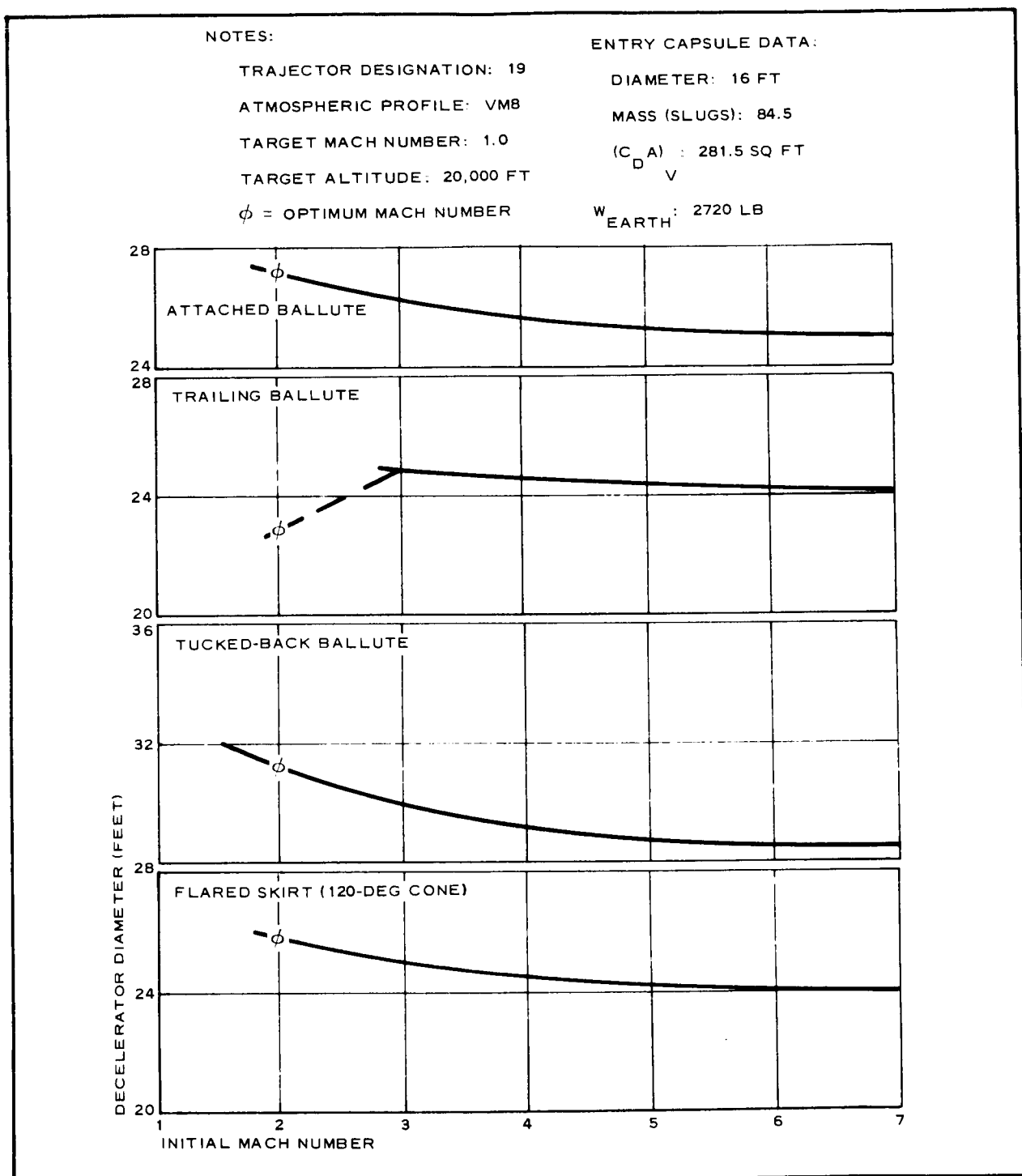


Figure 73 - Decelerator Diameter versus Deployment Mach Number for 16-Ft-Diameter Entry Capsule, Trajectory 19 at 20,000 Ft

NOTES:

TRAJECTORY DESIGNATION: 19
 ATMOSPHERIC PROFILE: VM8
 TARGET MACH NUMBER: 1.0
 TARGET ALTITUDE: 20,000 FT
 ϕ = SELECTED MACH NUMBER
 A = NOMEX 600 F
 B = DACRON 350 F

ENTRY CAPSULE DATA:

DIAMETER: 16 FT
 MASS (SLUGS): 84.5
 $(C_D A)_V$: 281.5 SQ FT
 W_{EARTH} : 2720 LB

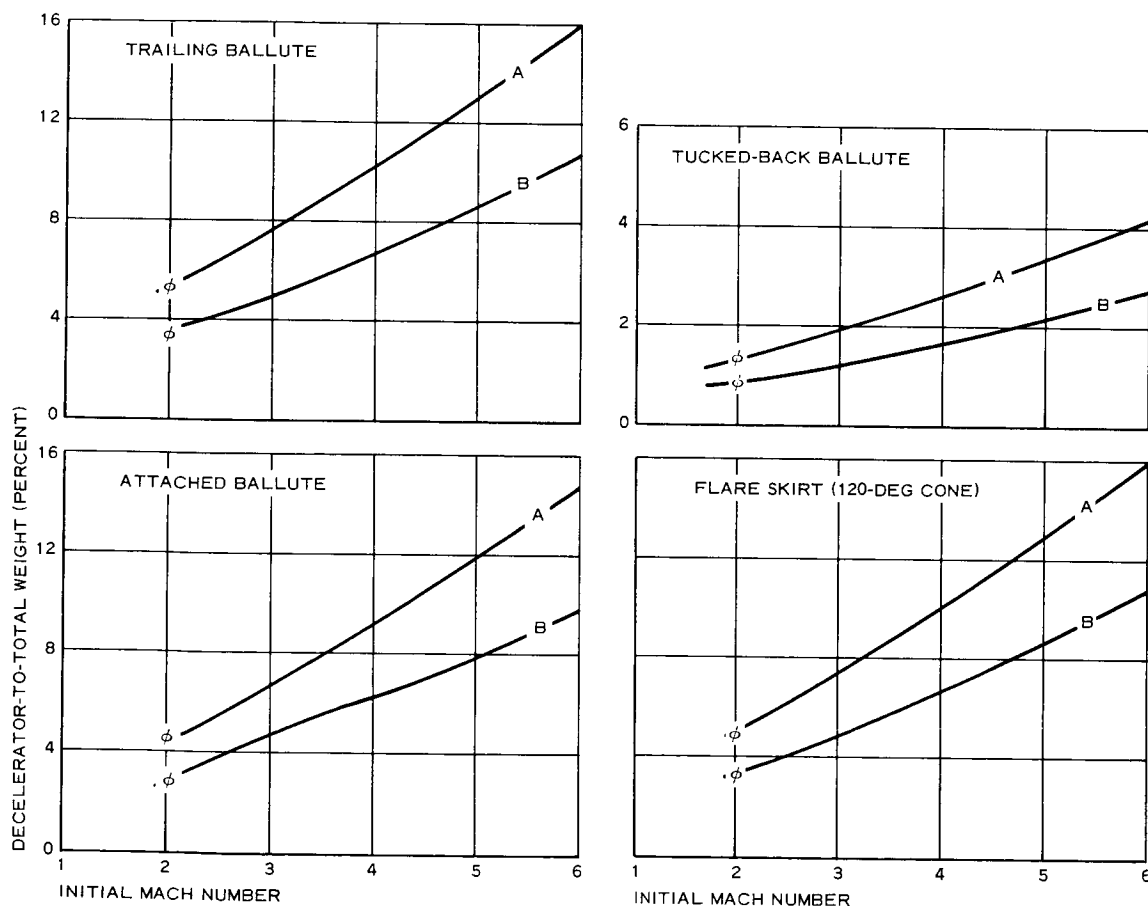
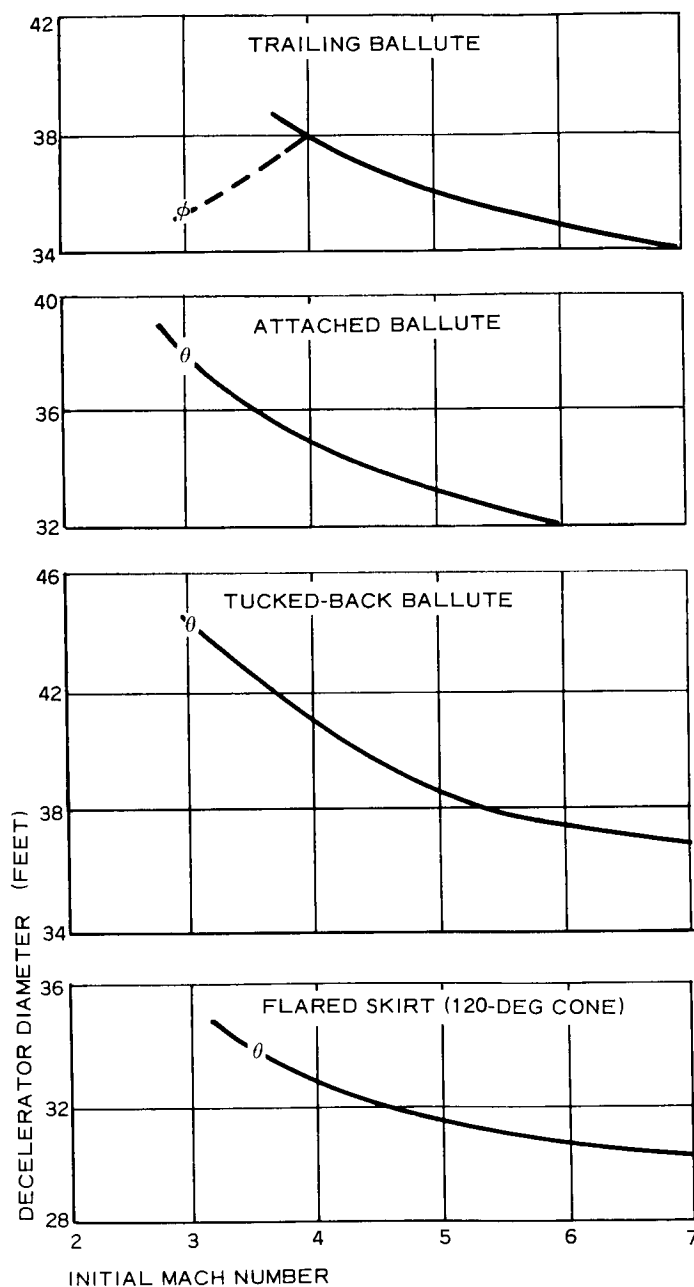


Figure 74 - Percent Decelerator to Total System Weight versus Deployment Mach Number for 16-Ft Entry Capsule, Trajectory 19 at 20,000 Ft



NOTES:

TRAJECTORY DESIGNATION: 19
 ATMOSPHERIC PROFILE: VM8
 TARGET MACH NUMBER: 1.0
 TARGET ALTITUDE: 30,000 FT
 θ = OPTIMUM MACH NUMBER
 ϕ = SELECTED MACH NUMBER

ENTRY CAPSULE DATA:

DIAMETER: 16 FT
 MASS (SLUGS): 84.5
 $(C_D A)_V$: 281.5 SQ FT
 W_{EARTH} : 2720 LB

Figure 75 - Decelerator Diameter versus Deployment, 16-Ft Diameter Entry Capsule, Trajectory 19 at 30,000 Ft

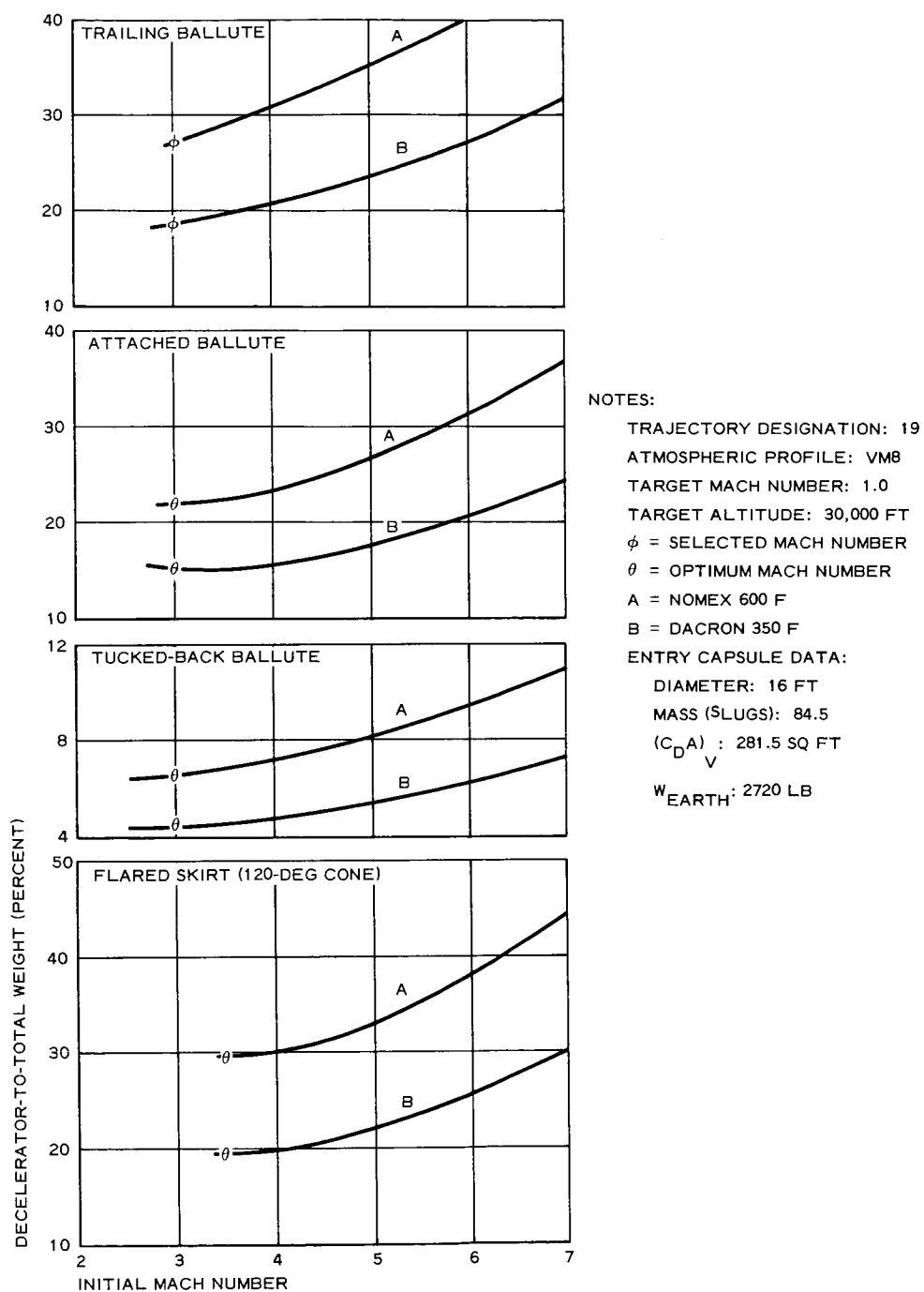


Figure 76 - Percent Decelerator to Total Weight versus Deployment Mach Number, 16-Ft-Diameter Entry Capsule Trajectory 19 at 30,000 Ft

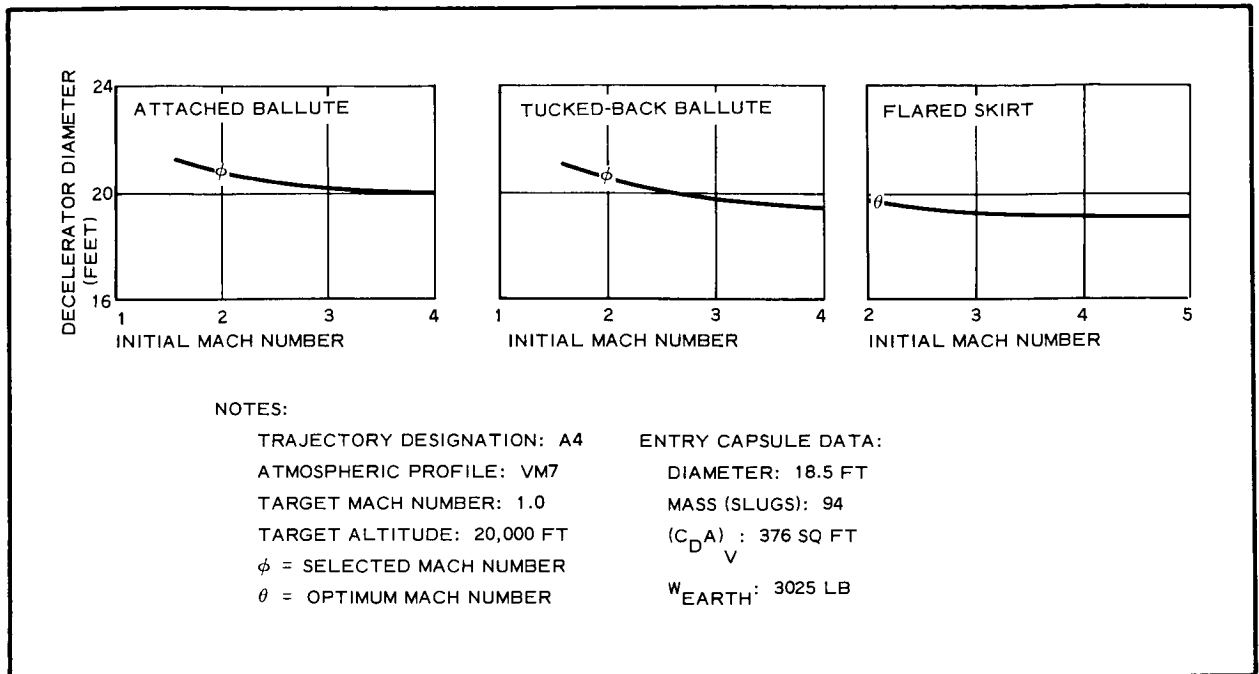


Figure 77 - Decelerator Diameter versus Deployment Mach Number for 18.5-Ft-Diameter Entry Capsule, Trajectory A4 at 20,000 Ft

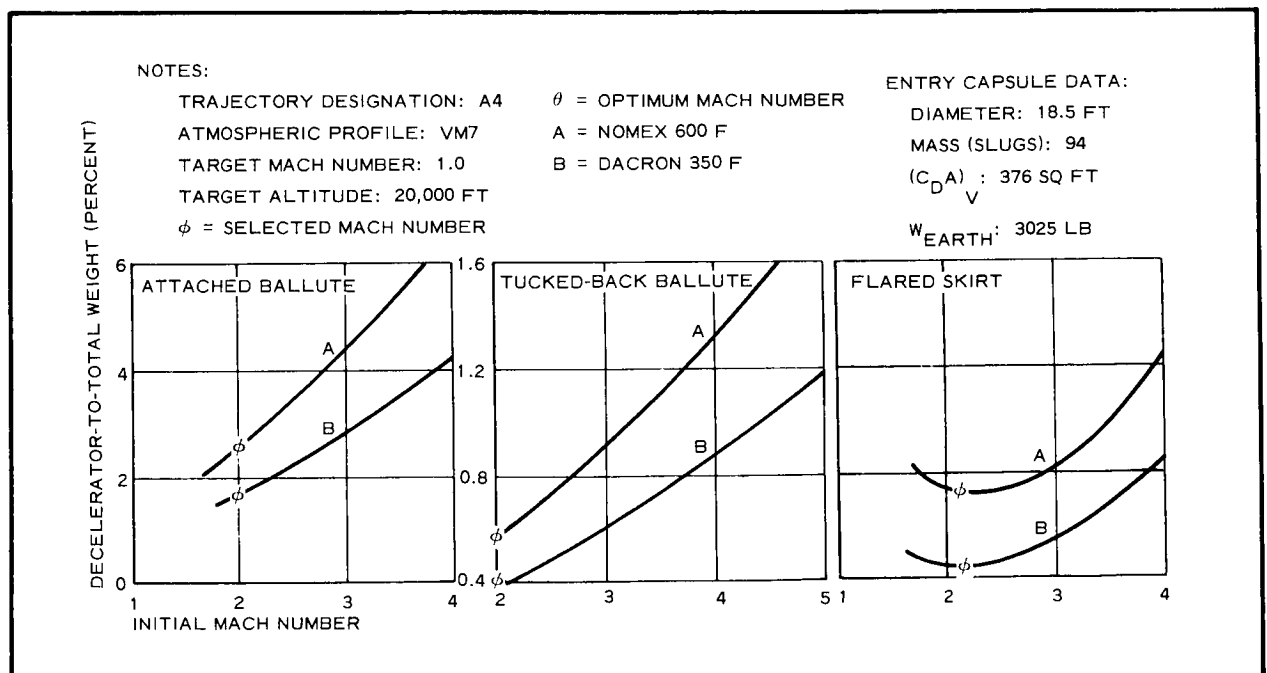


Figure 78 - Percent Decelerator to Total Weight versus Deployment Mach Number, 18.5-Ft-Diameter Entry Capsule, Trajectory A4 at 20,000 Ft

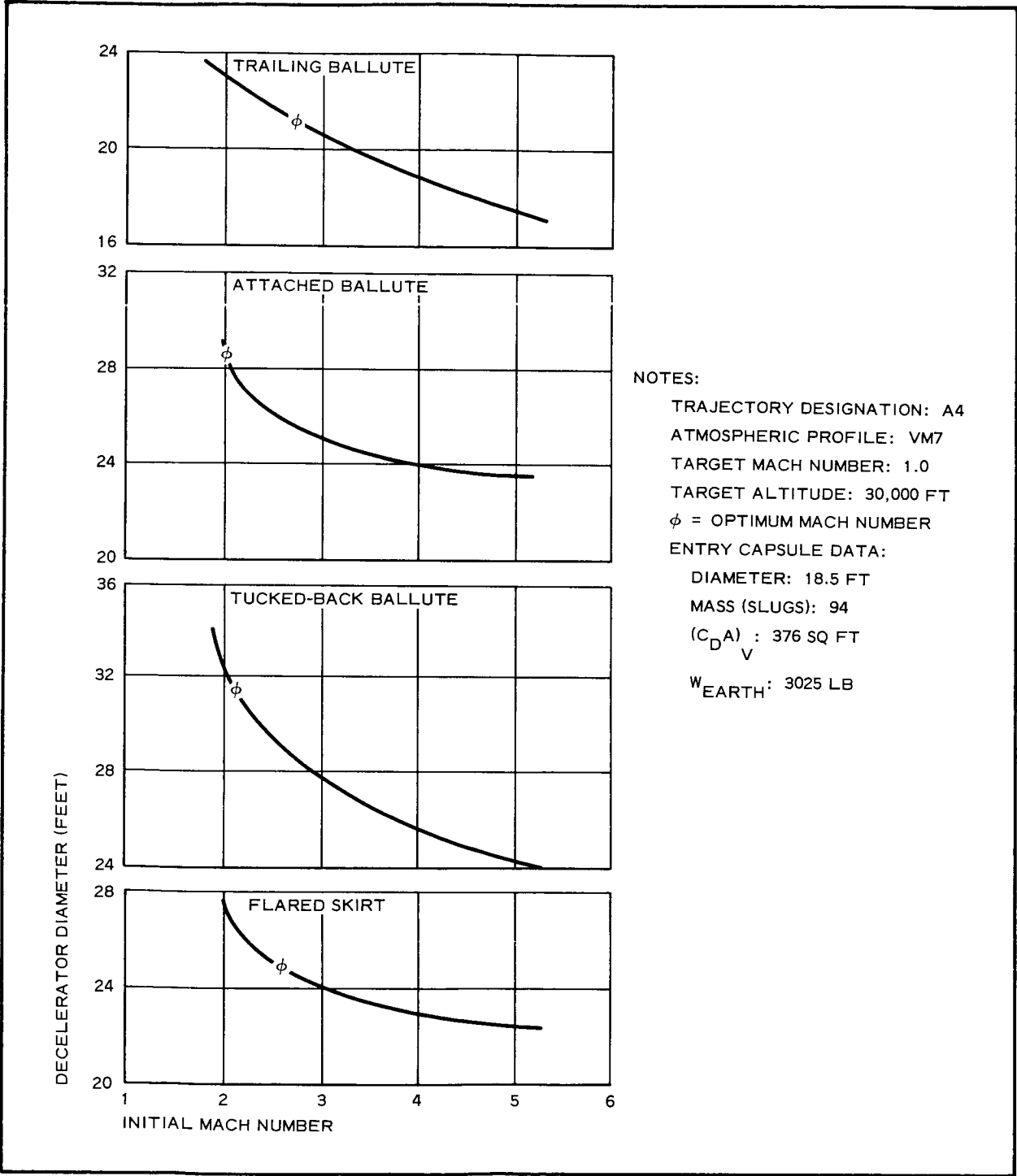


Figure 79 - Decelerator Diameter versus Deployment Mach Number, 18.5-Ft-Diameter Entry Capsule, Trajectory A4 at 30,000 Ft

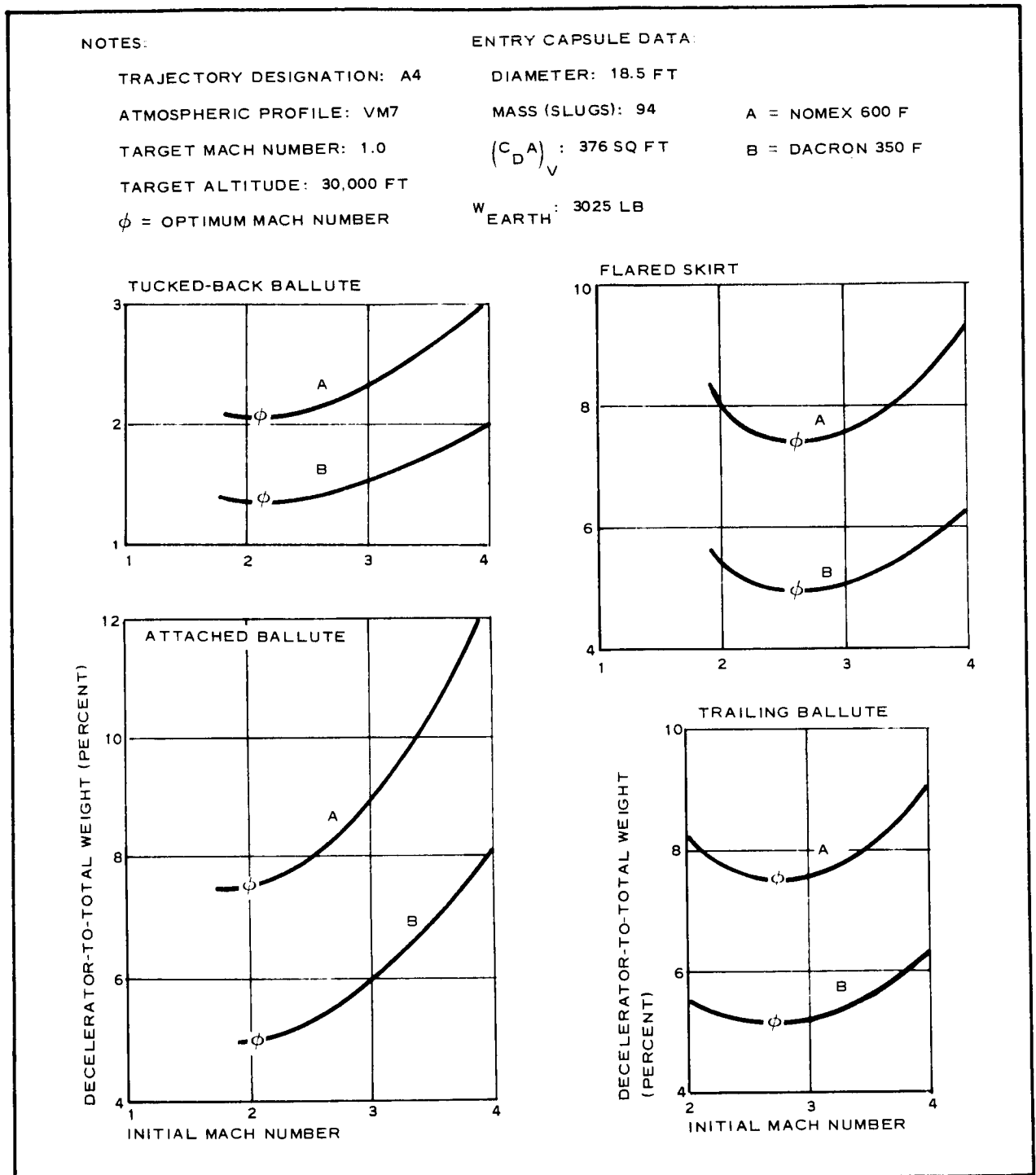


Figure 80 - Percent Decelerator to Total Weight versus Deployment Mach Number, 18.5-Ft Entry Capsule Diameter, Trajectory A4 at 30,000 Ft

NOTES:

TRAJECTORY DESIGNATION: B1

ATMOSPHERIC PROFILE: VM7

TARGET MACH NUMBER: 1.0

TARGET ALTITUDE: 20,000 FT

θ = OPTIMUM MACH NUMBER

ϕ = MACH NUMBER SELECTED

ENTRY CAPSULE DATA:

DIAMETER: 12 FT

MASS (SLUGS): 79

$(C_{D A})_V$: 158 SQ FT

W_{EARTH} : 2540 LB

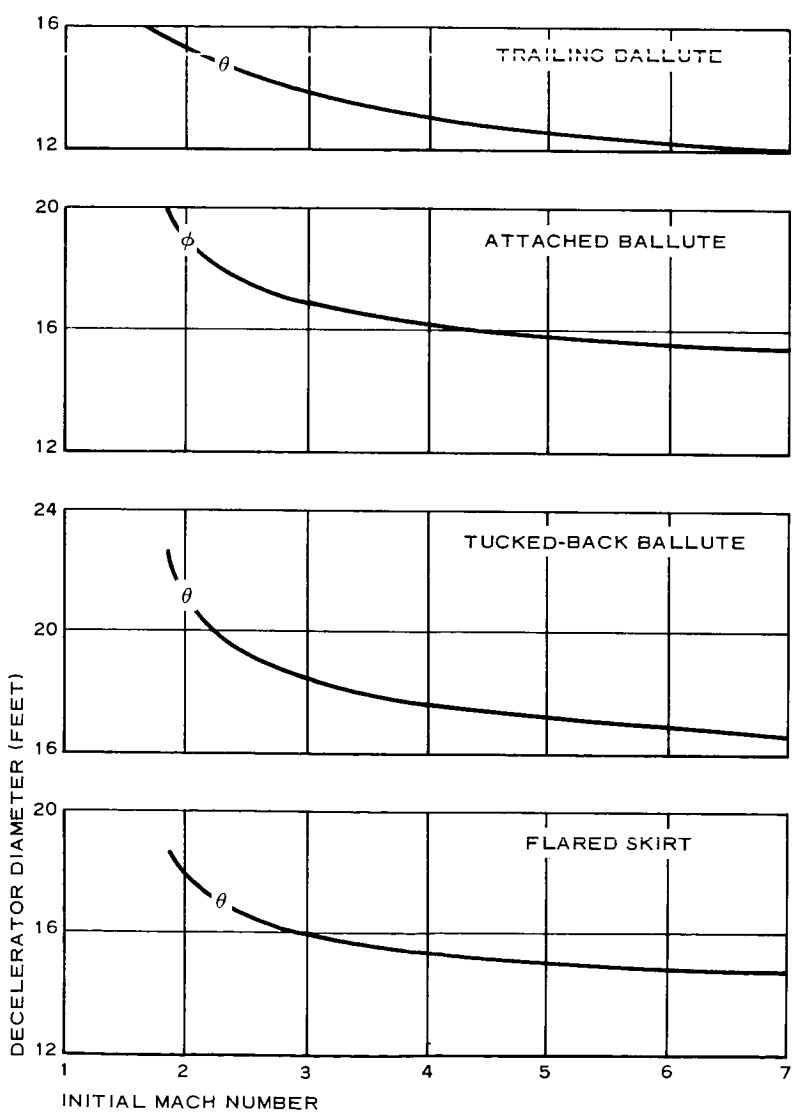


Figure 81 - Decelerator Diameter versus Deployment Mach Number, 12-Ft Entry Capsule Diameter, Trajectory B1 at 20,000 Ft

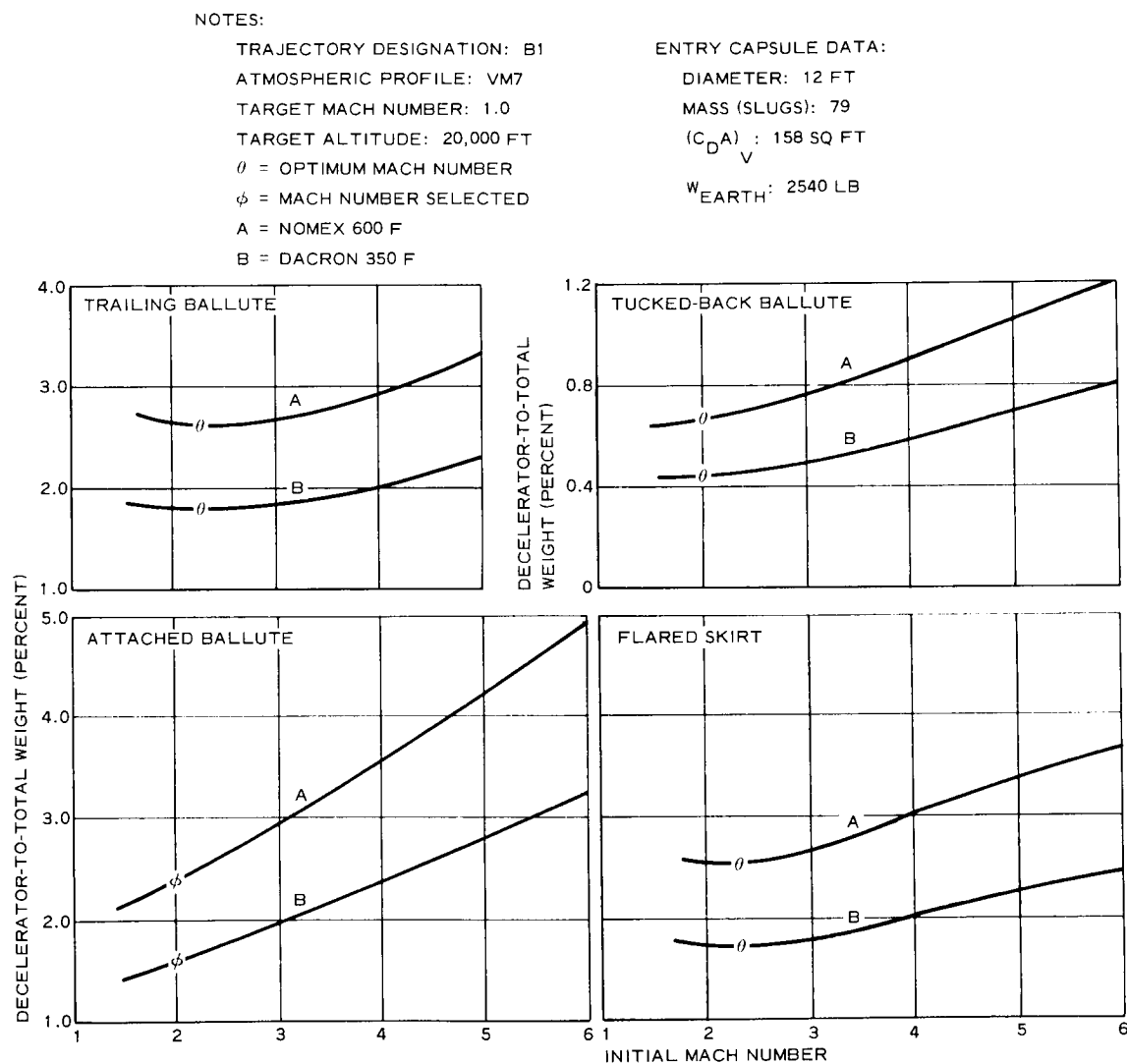


Figure 82 - Percent Decelerator to Total System Weight versus Deployment Mach Number, 12-Ft Diameter Entry Capsule, Trajectory B1 at 20,000 Ft

NOTES:

TRAJECTORY DESIGNATION: B1

ATMOSPHERIC PROFILE: VM7

TARGET MACH NUMBER: 1.0

TARGET ALTITUDE: 30,000 FT

 ϕ = SELECTED MACH NUMBER

ENTRY CAPSULE DATA:

DIAMETER: 12 FT

MASS (SLUGS): 79

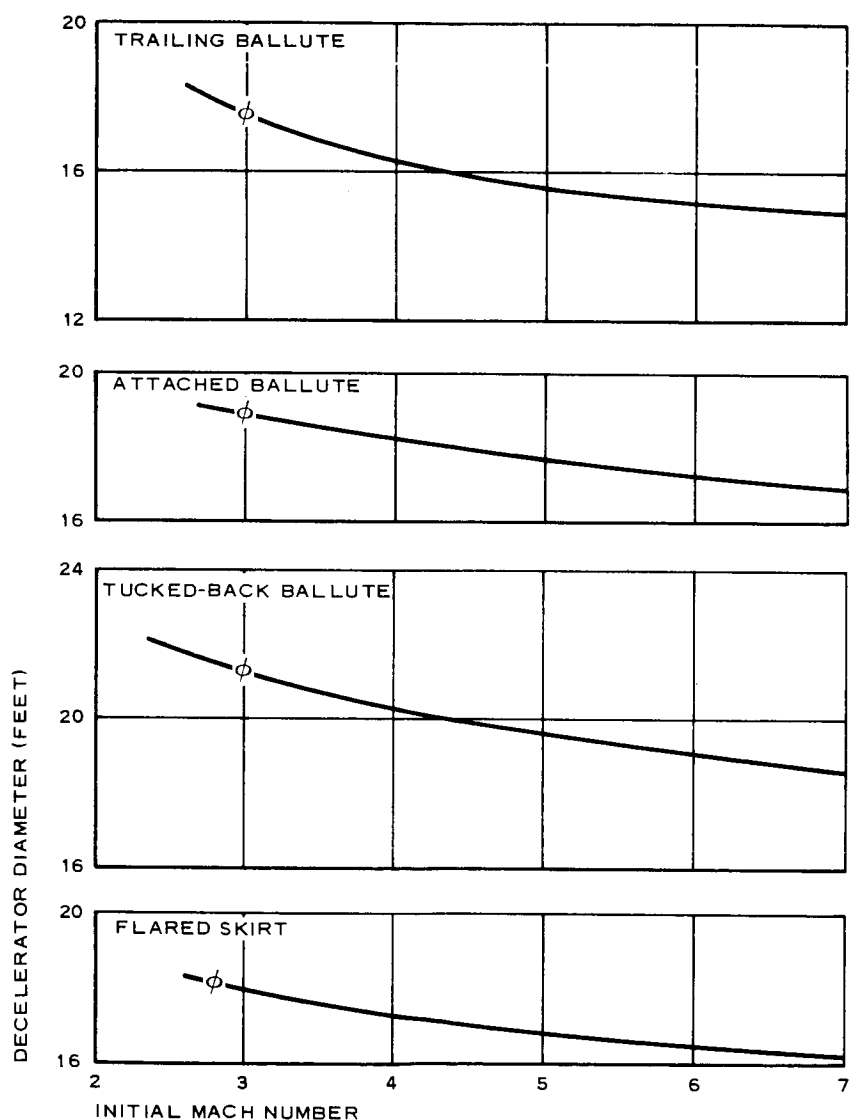
 $(C_D A) : 158 \text{ SQ FT}$
V $W_{\text{EARTH}} : 2540 \text{ LB}$ 

Figure 83 - Decelerator Diameter versus Deployment Mach Number for 12-Ft Diameter Entry Capsule, Trajectory B1 at 30,000 Ft

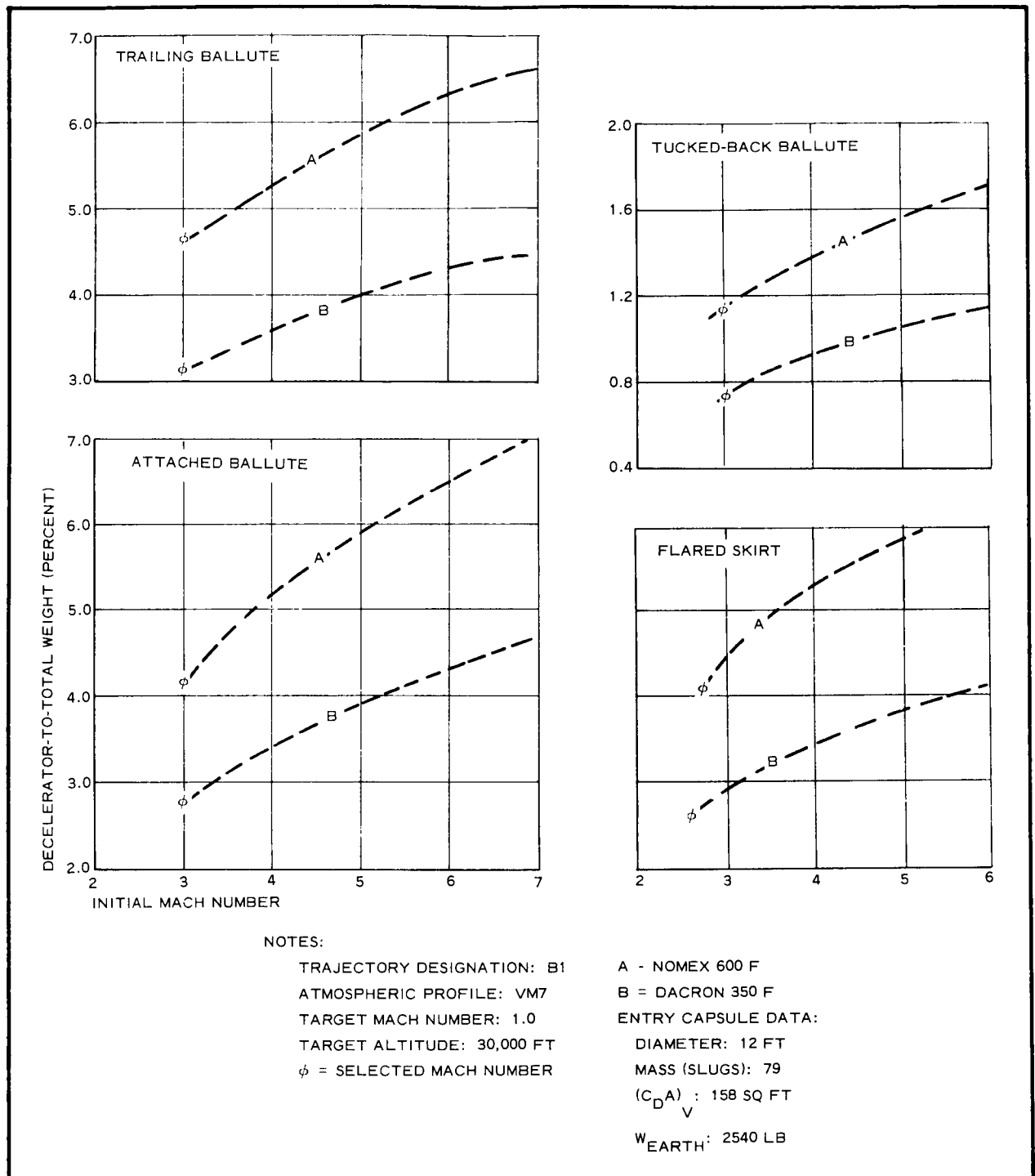


Figure 84 - Percent Decelerator to Total Weight versus Deployment Mach Number for 12-Ft Entry Capsule, Trajectory B1 at 30,000 Ft

NOTES:

TRAJECTORY DESIGNATION: 22

ATMOSPHERIC PROFILE: VM7

TARGET MACH NUMBER: 1.0

TARGET ALTITUDE: 20,000 FT

 ϕ = SELECTED MACH NUMBER

ENTRY CAPSULE DATA:

DIAMETER: 16 FT

MASS (SLUGS): 84.5

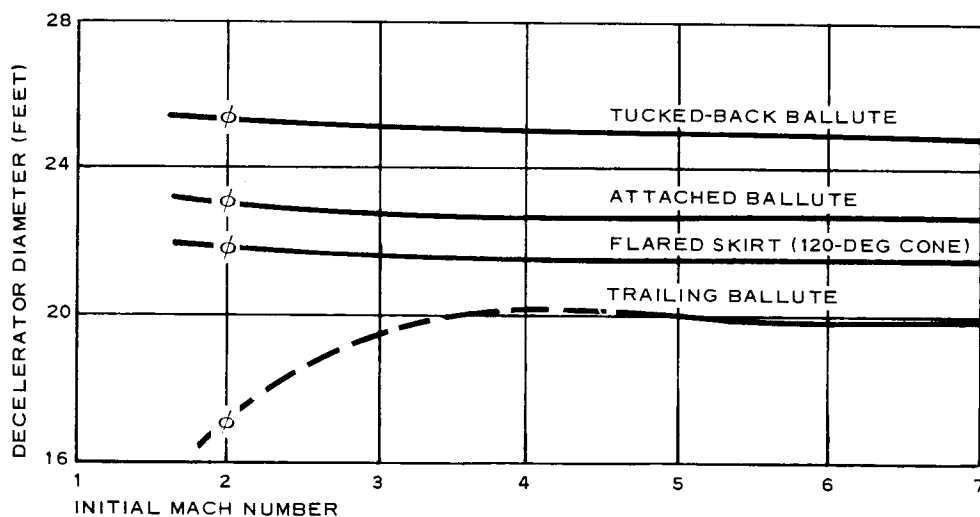
 $(C_D A)_V$: 281.5 SW FT W_{EARTH} : 2720 LB

Figure 85 - Decelerator Diameter versus Deployment Mach Number for 16-Ft Diameter Entry Capsule, Trajectory 22 at 20,000 Ft

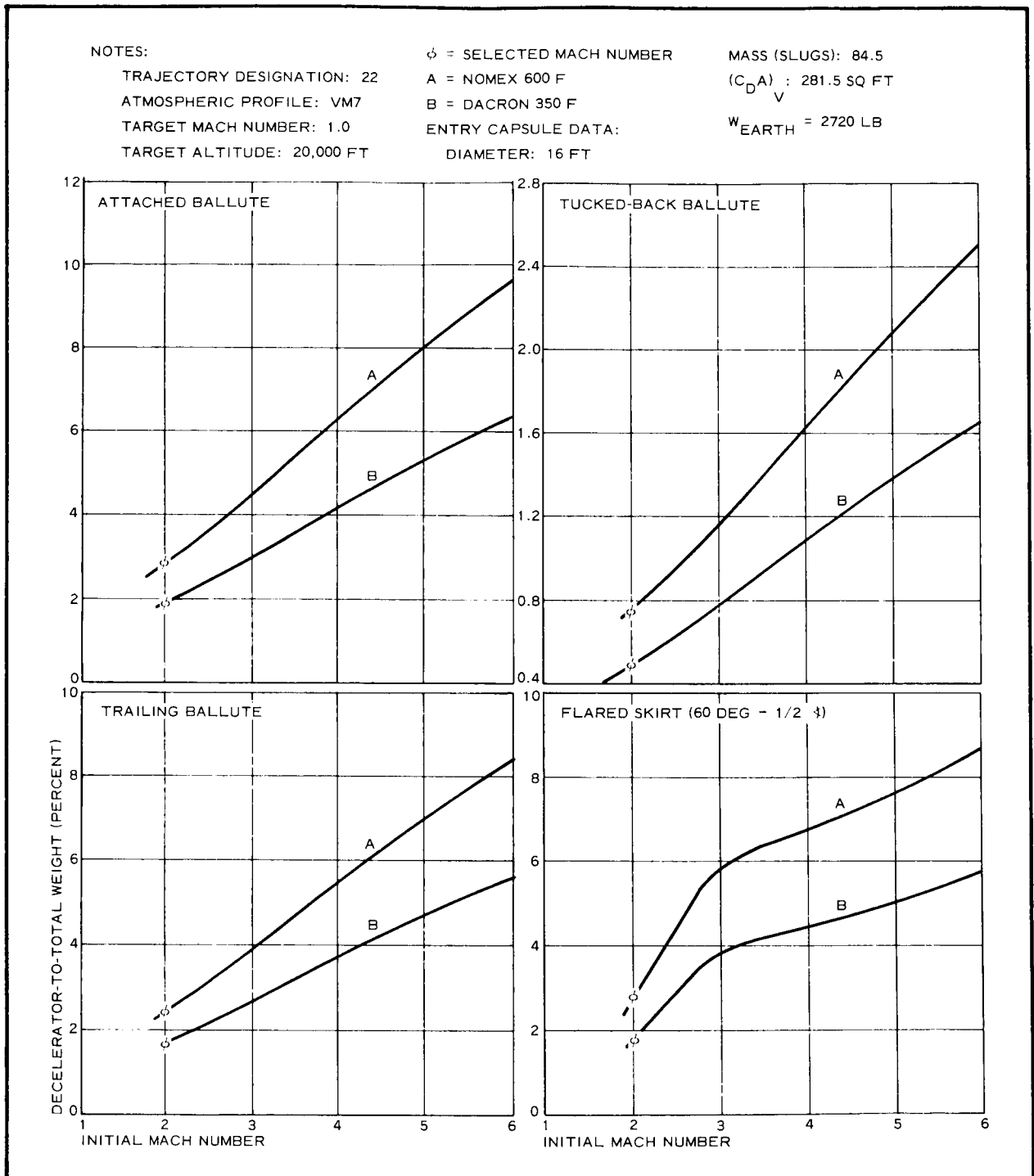


Figure 86 - Percent Decelerator to Total Weight versus Deployment Mach Number for 16-Ft Entry Capsule, Trajectory 22 at 20,000 Ft

NOTES:

TRAJECTORY DESIGNATION: 22

ATMOSPHERIC PROFILE: VM7

TARGET MACH NUMBER: 1.0

TARGET ALTITUDE: 30,000 FT

 ϕ = SELECTED MACH NUMBER

ENTRY CAPSULE DATA:

DIAMETER: 16 FT

MASS (SLUGS): 84.5

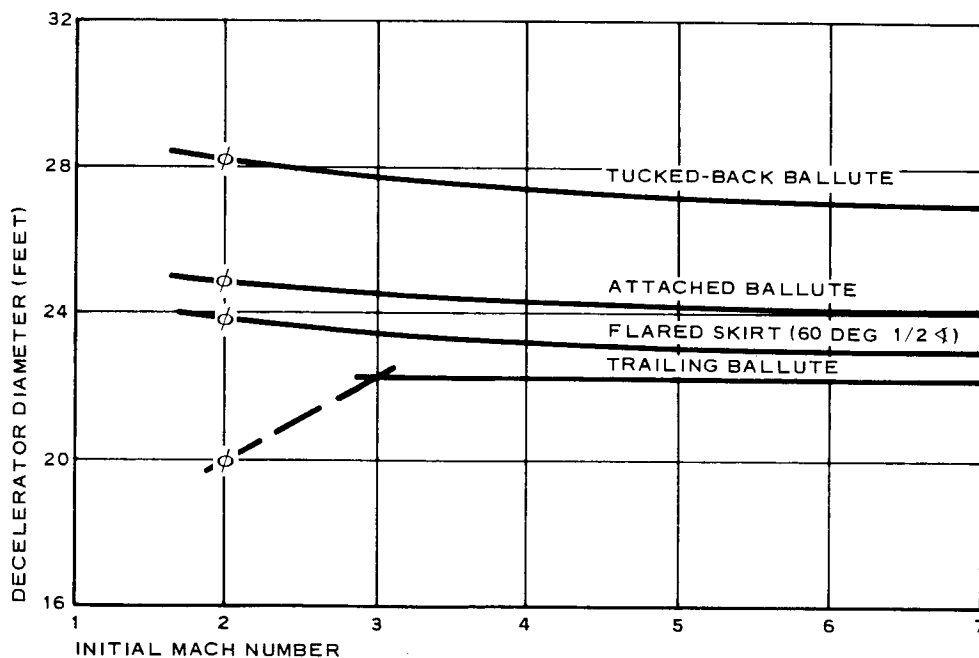
 $(C_D A)_V$: 281.5 SQ FT W_{EARTH} : 2720 LB

Figure 87 - Decelerator Diameter versus Deployment Mach Number for 16-Ft Diameter Entry Capsule, Trajectory 22 at 30,000 Ft

NOTES:

TRAJECTORY DESIGNATION: 22

ATMOSPHERIC PROFILE: VM7

TARGET MACH NUMBER: 1.0

TARGET ALTITUDE: 30,000 FT

 ϕ = SELECTED MACH NUMBER

A = NOMEX 600 F

B = DACRON 350 F

ENTRY CAPSULE DATA:

DIAMETER: 16 FT

MASS (SLUGS): 84.5

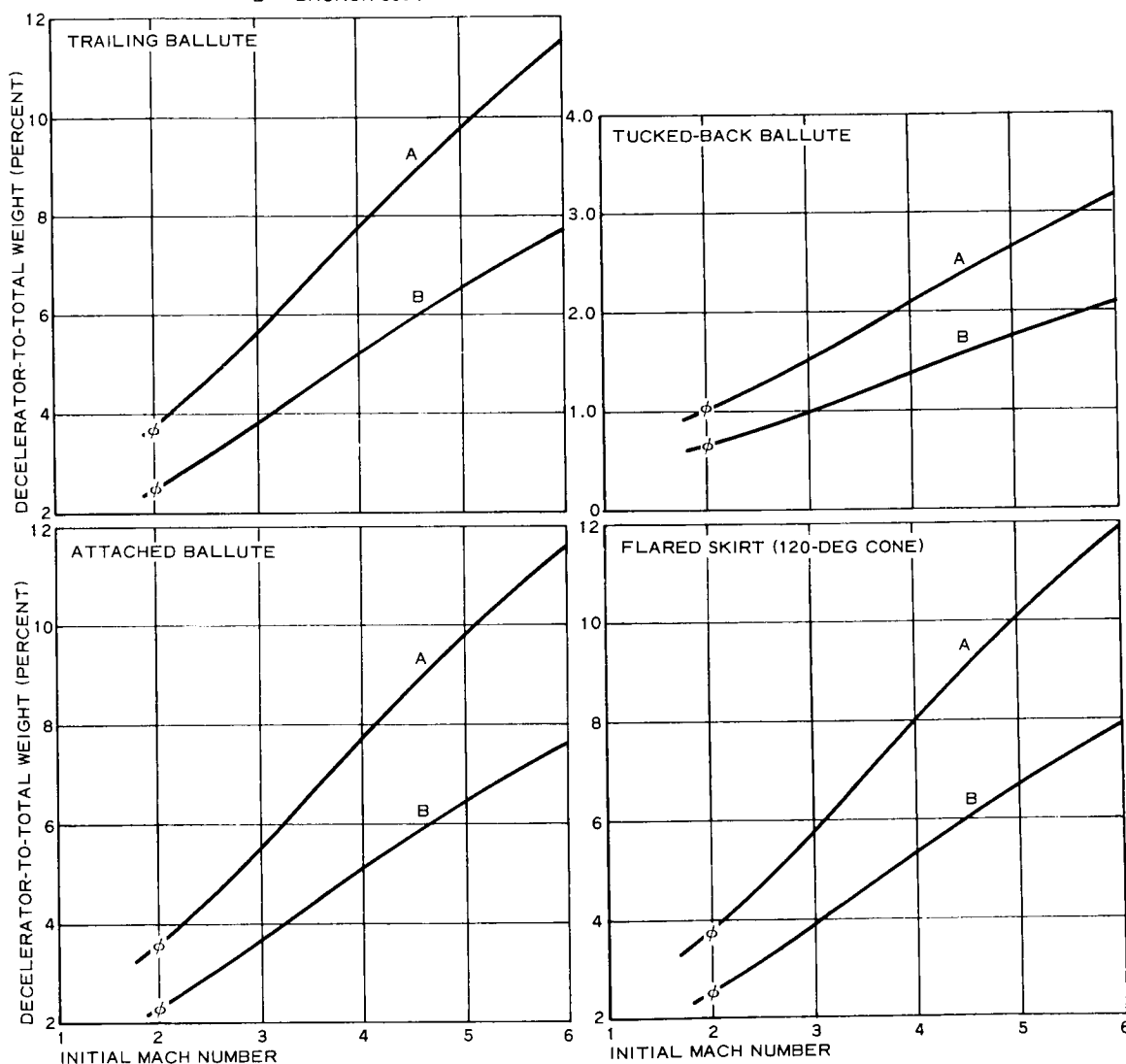
 $(C_D A)_V$: 281.5 SQ FT W_{EARTH} = 2720 LB

Figure 88 - Percent Decelerator to Total Weight versus Deployment Mach Number for 16-Ft Entry Capsule, Trajectory 22 at 30,000 Ft

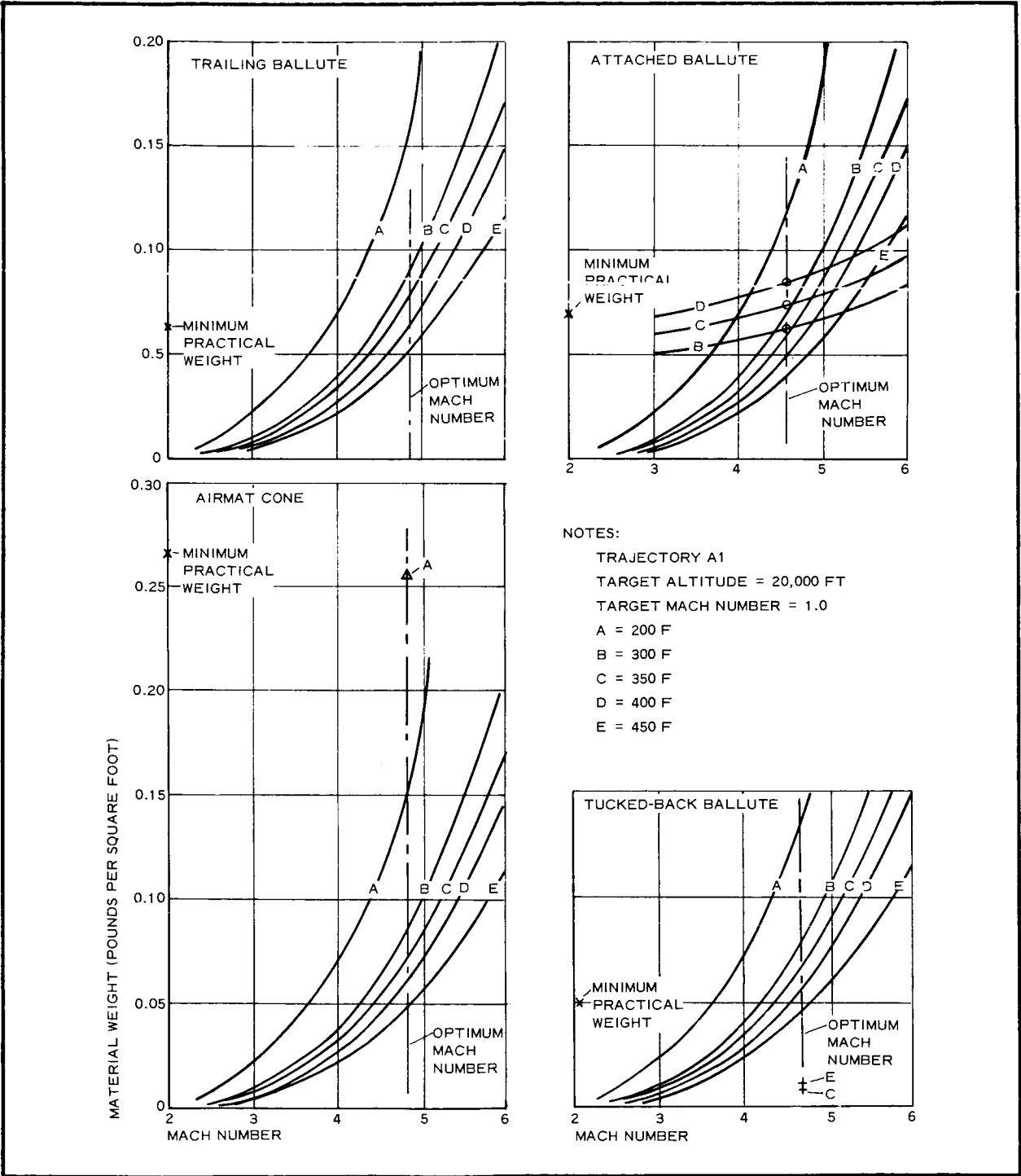


Figure 89 - Decelerator Envelope Unit Weight versus Deployment Mach Numbers at Trajectory A1 (Dacron)

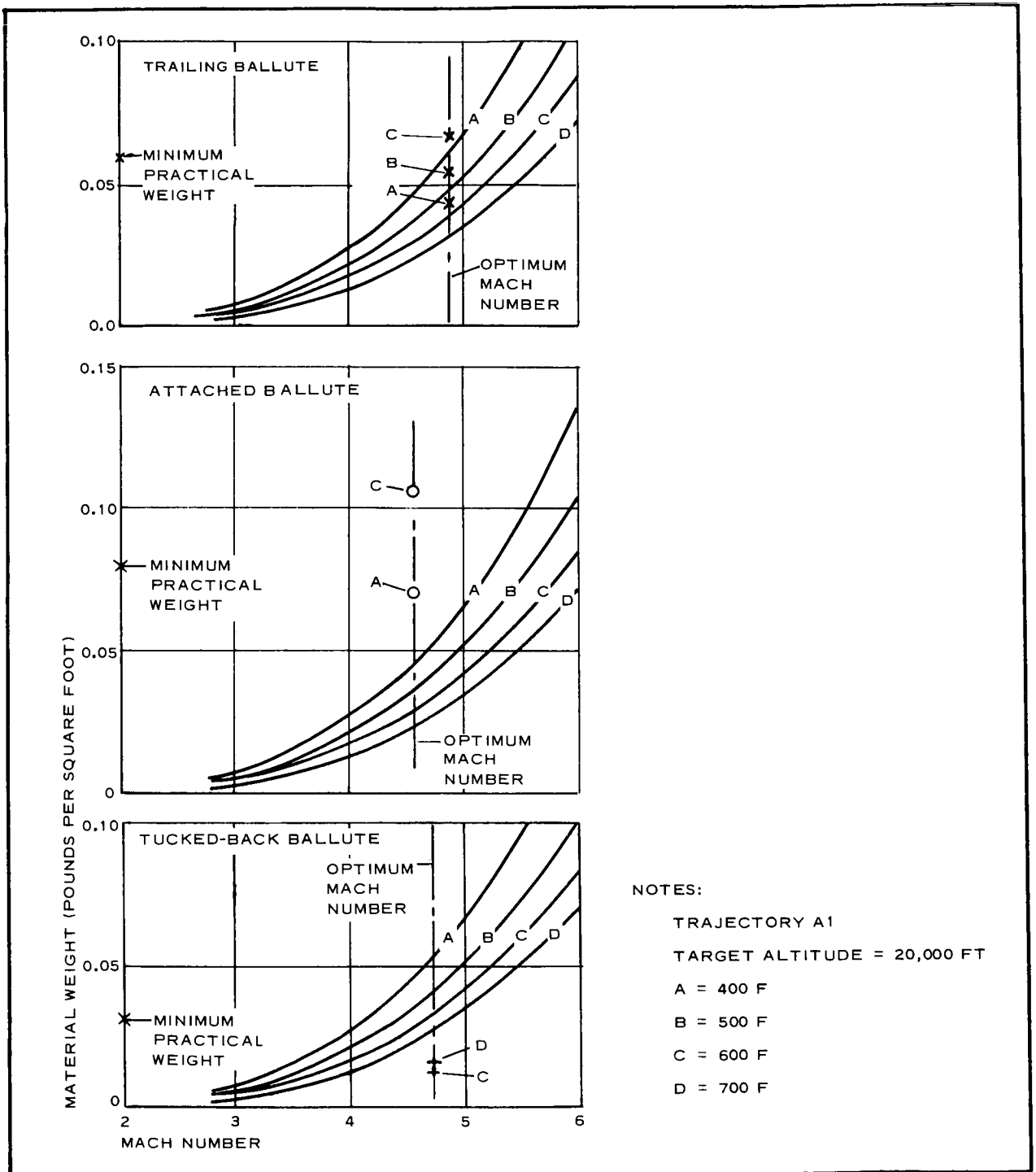


Figure 90 - Decelerator Envelope Unit Weight versus Deployment Mach Number, Trajectory A1 (Nomex)

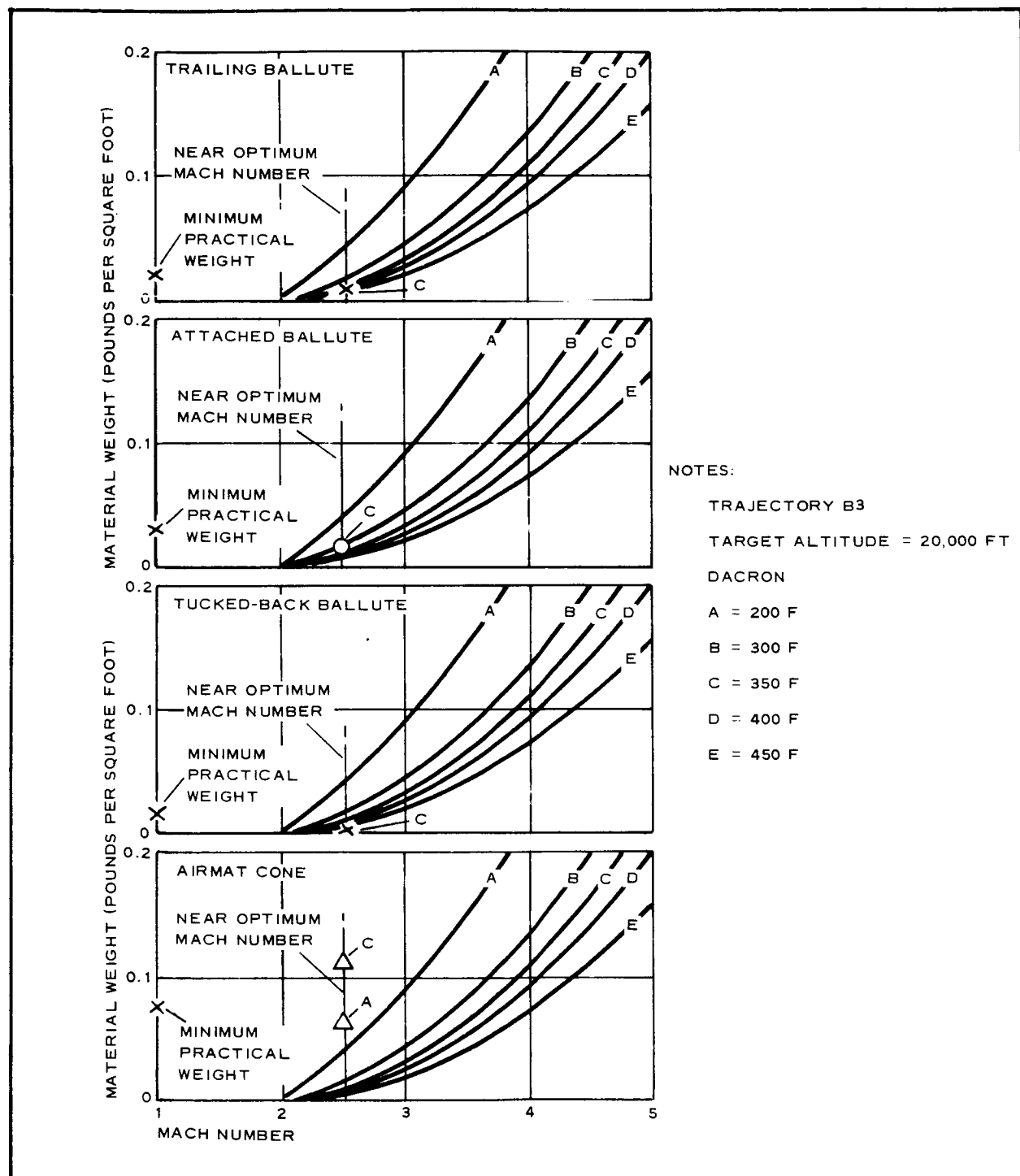


Figure 91 - Decelerator Envelope Unit Weight versus Deployment Mach Number, Trajectory B3

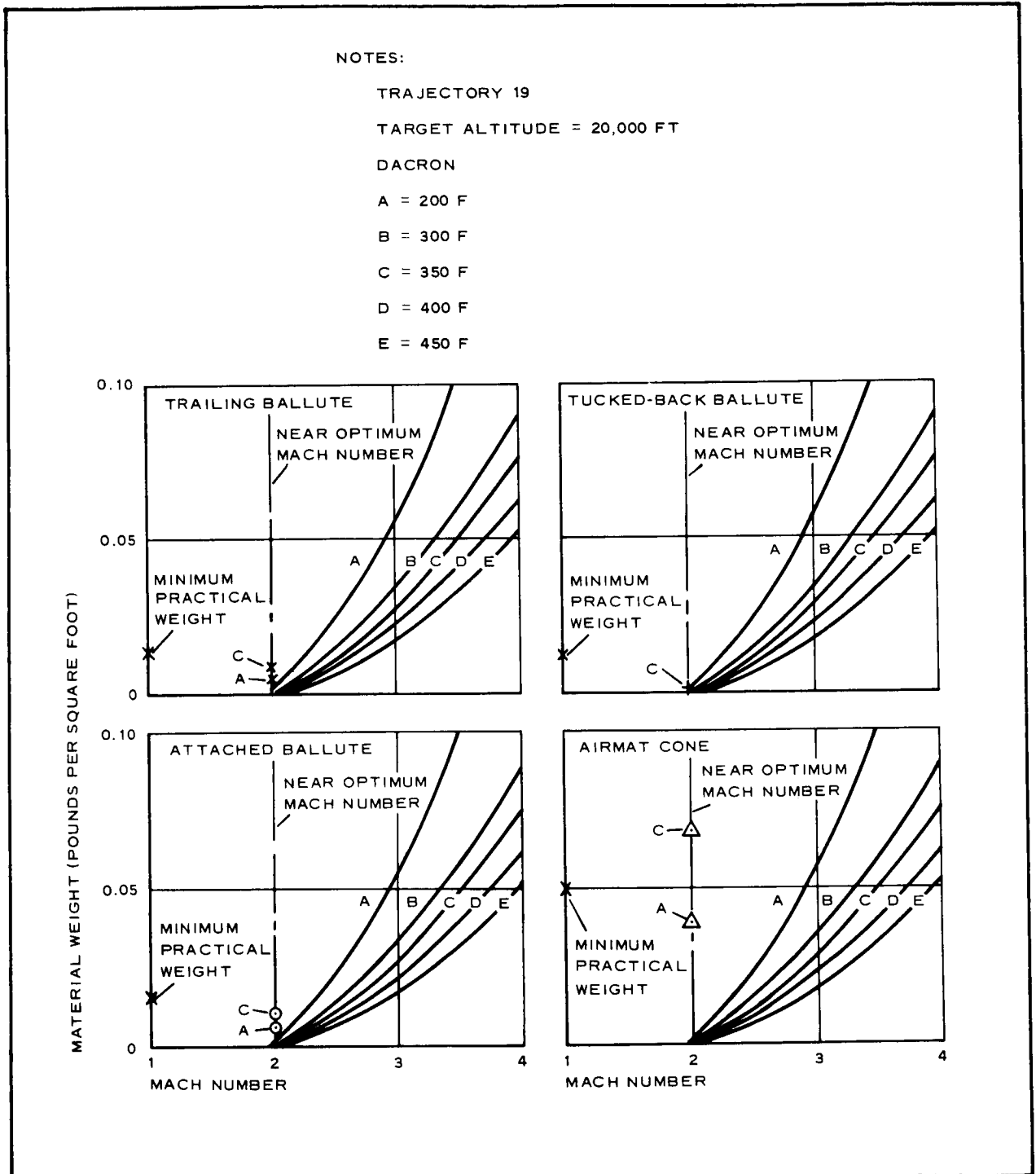


Figure 92 - Decelerator Envelope Unit Weight versus Deployment Mach Number, Trajectory 19 at 20,000 Ft

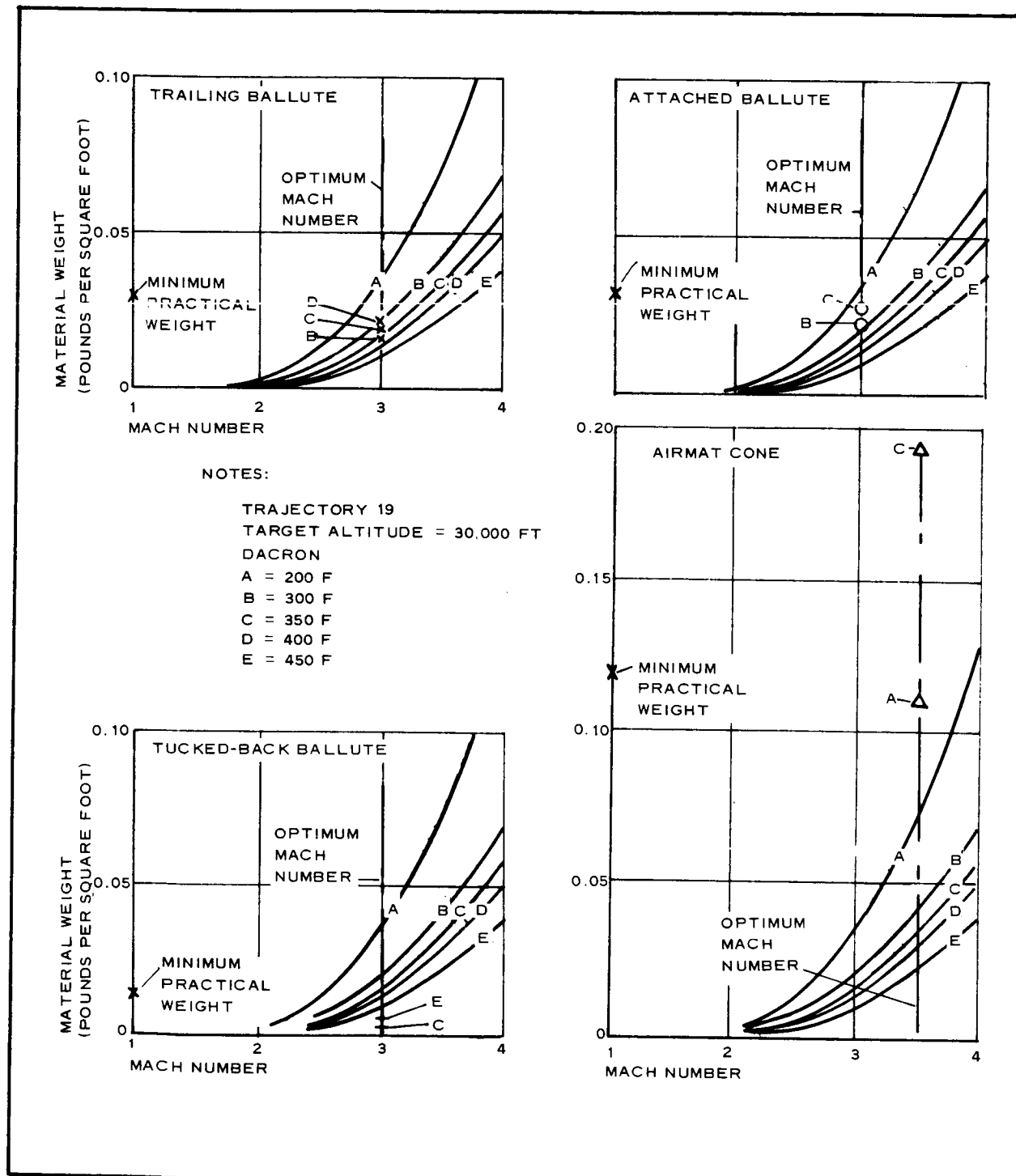


Figure 93 - Decelerator Envelope Unit Weight versus Initial Operating Mach Number, Trajectory 19 at 30,000 Ft

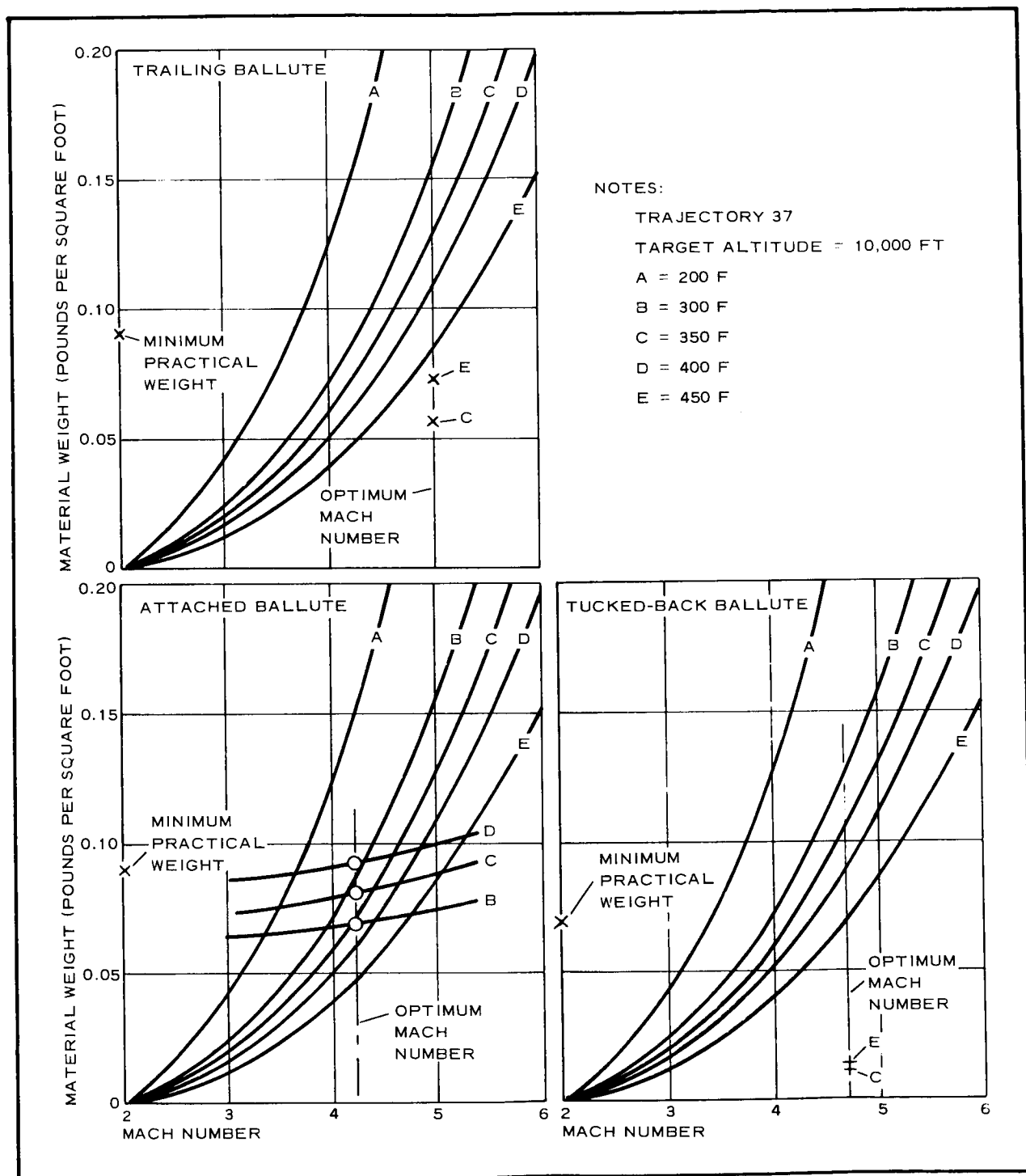


Figure 94 - Decelerator Envelope Unit Weight versus Deployment Mach Number, Trajectory 37 (Dacron)

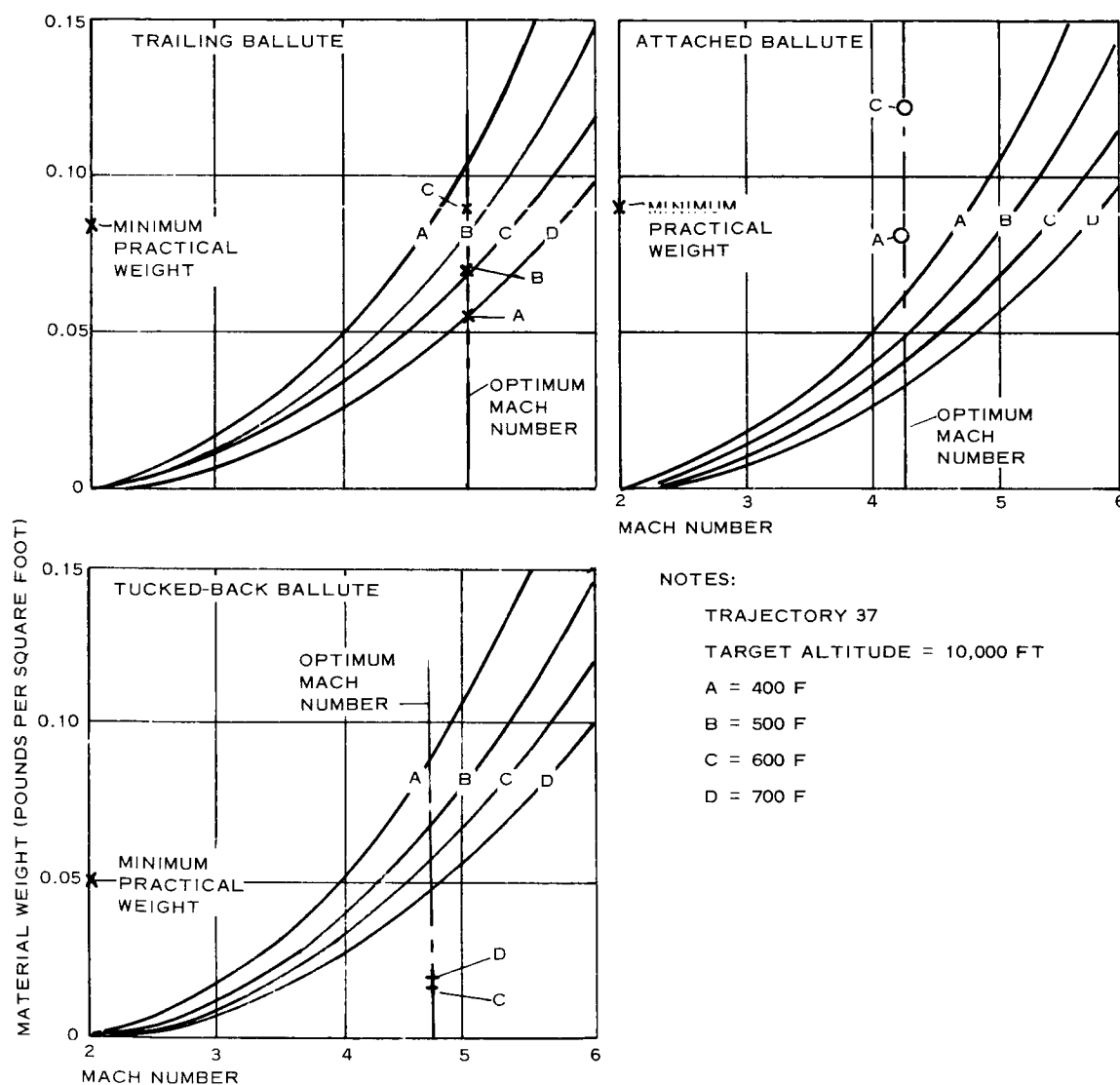


Figure 95 - Decelerator Unit Weight versus Deployment Mach Number, Trajectory 37 (Nomex)

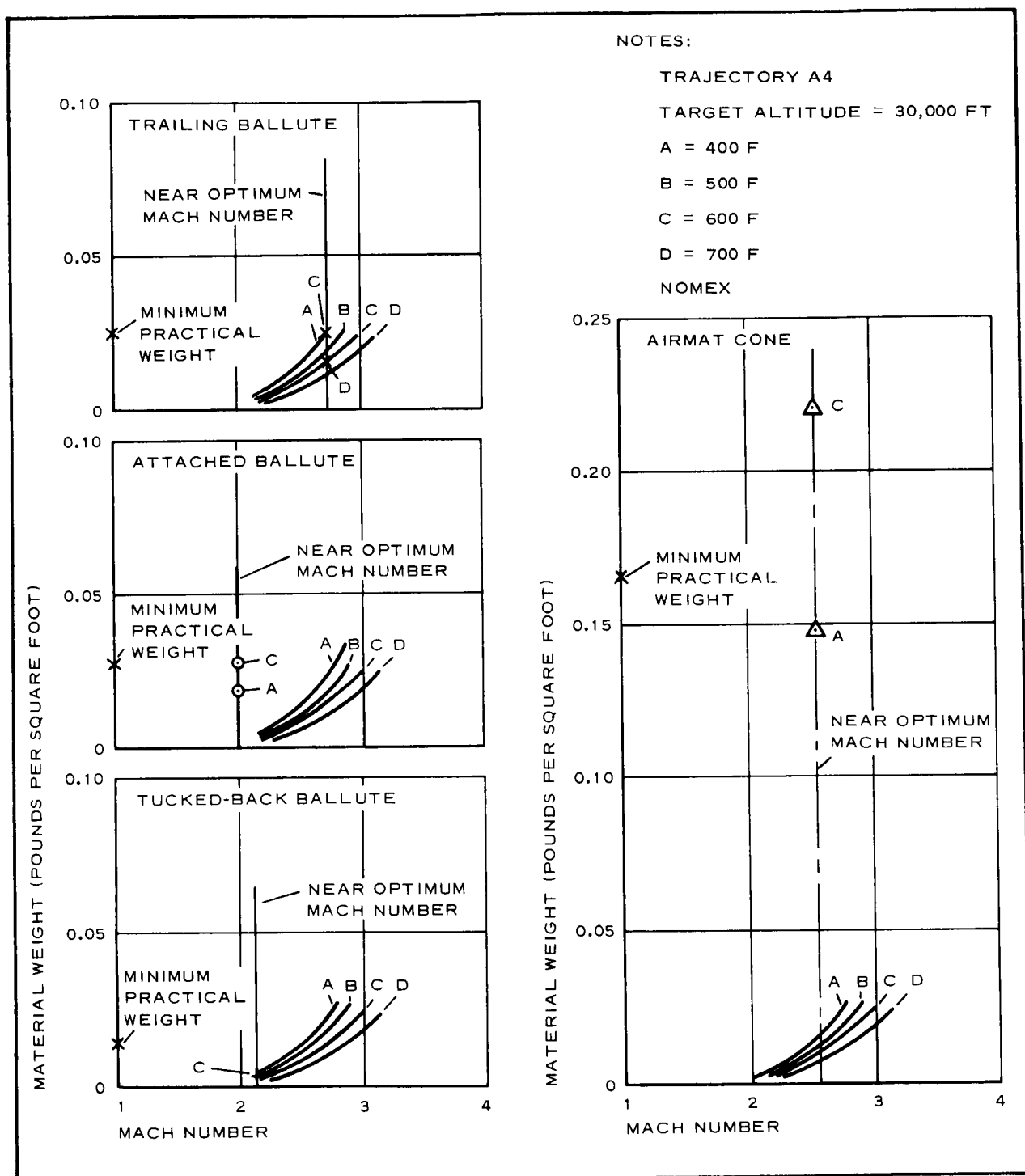


Figure 96 - Decelerator Envelope Unit Weight versus Deployment Mach Number, Trajectory A4

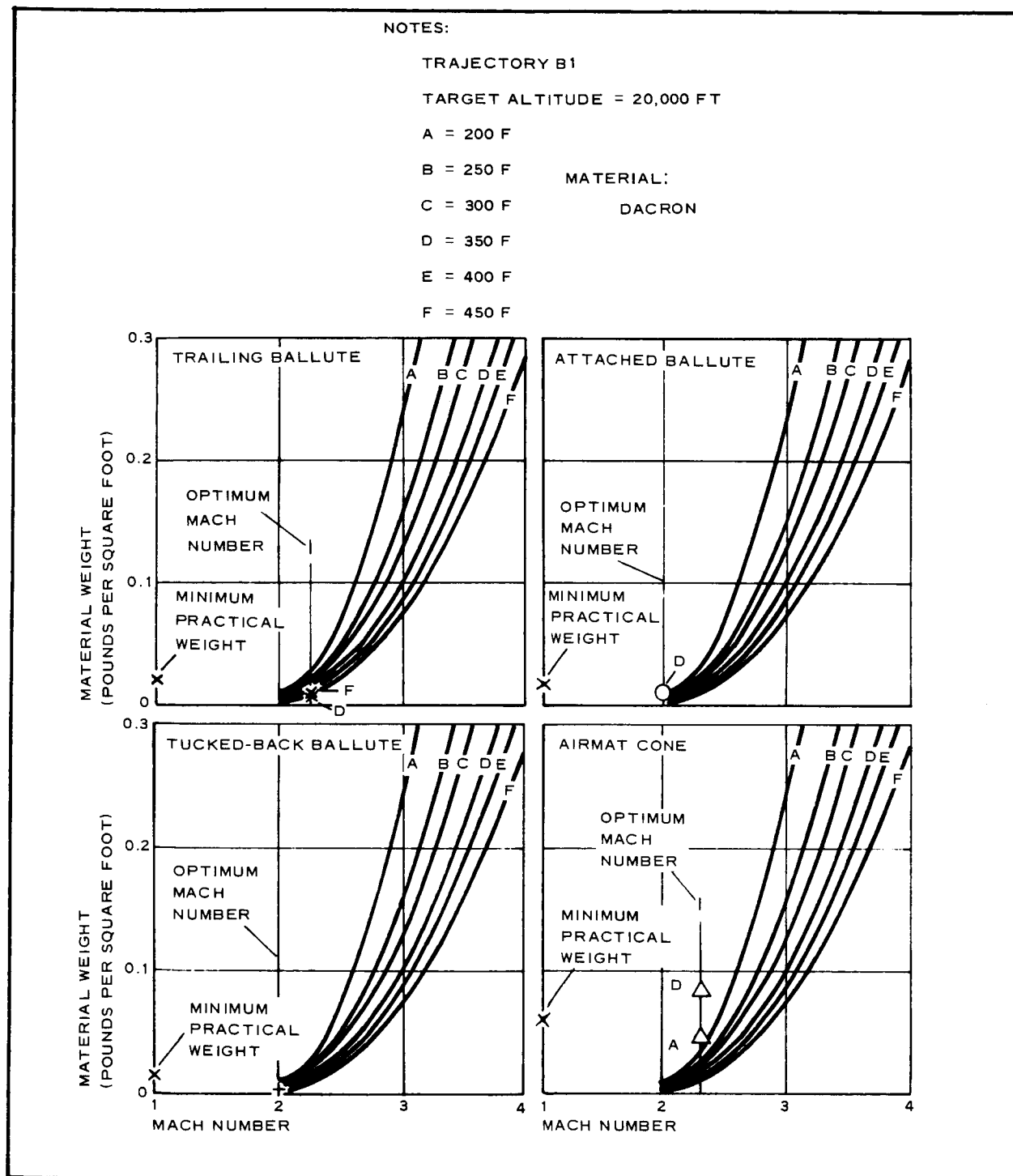
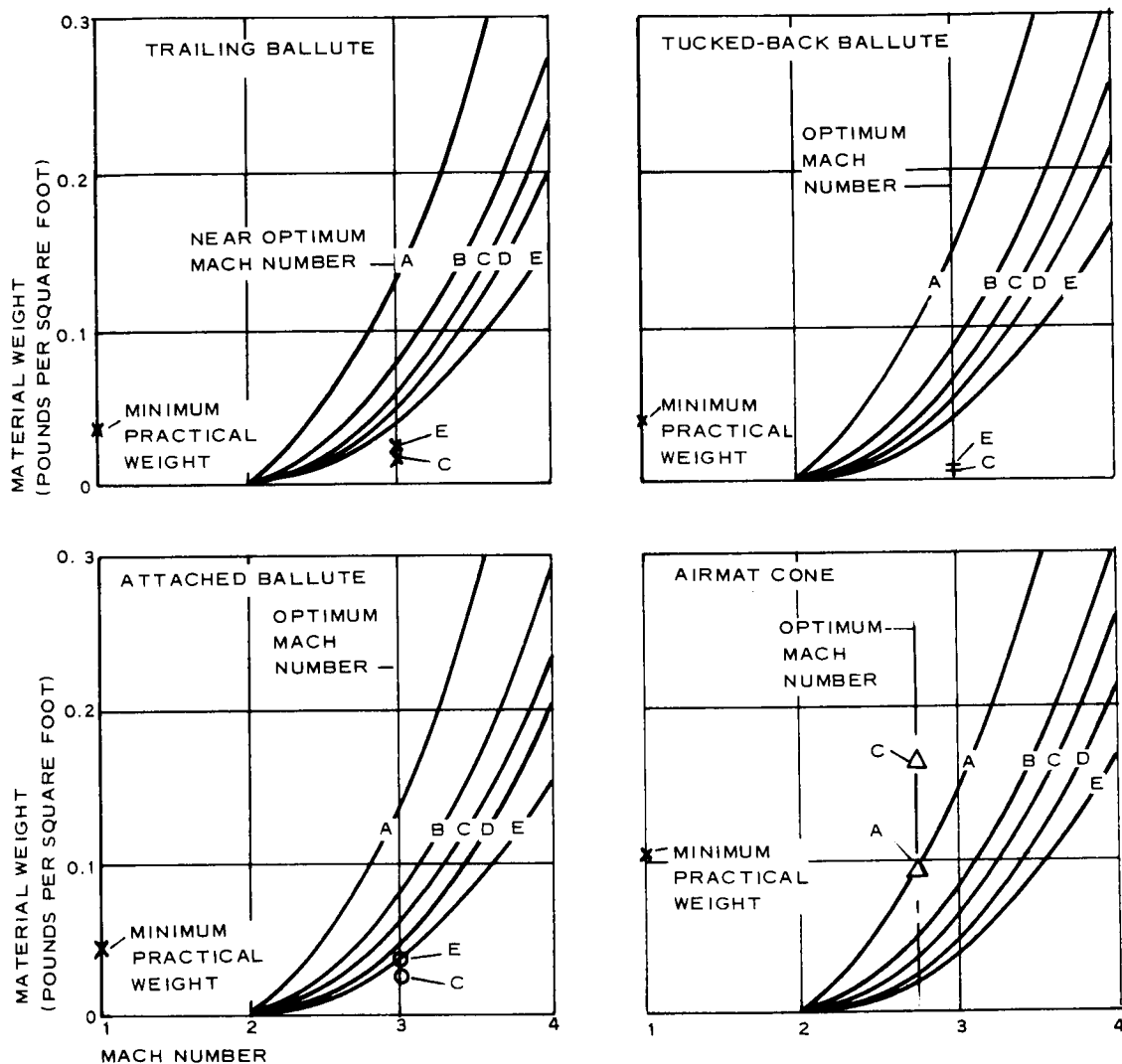


Figure 97 - Decelerator Envelope Unit Weight versus Deployment Mach Number at 20,000 Ft



NOTES:

TRAJECTORY B1

TARGET ALTITUDE = 30,000 FT

DACRON

A = 200 F

B = 300 F

C = 350 F

D = 400 F

E = 450 F

Figure 98 - Decelerator Envelope Unit Weight versus Deployment Mach Number, Trajectory B1 at 30,000 Ft

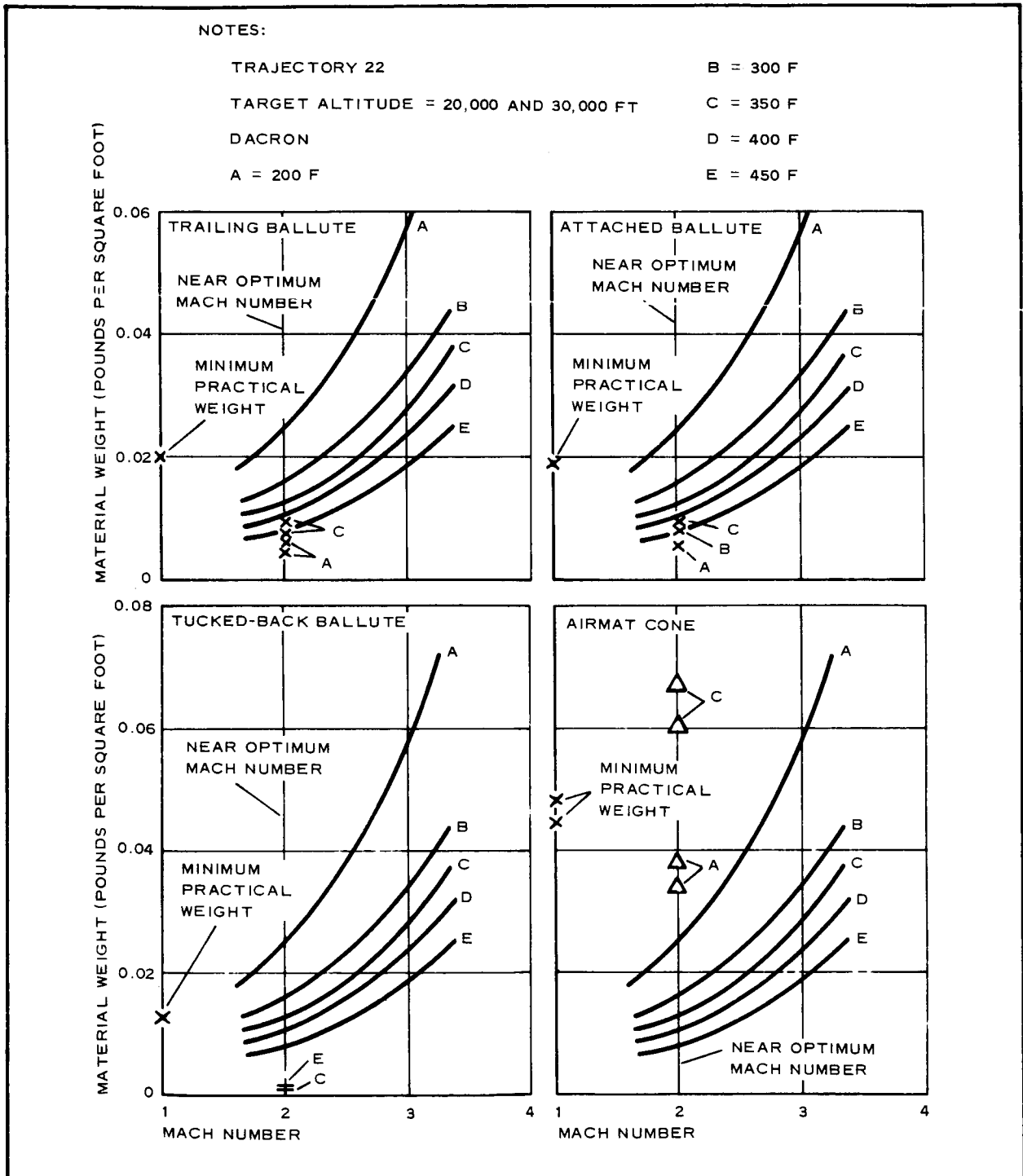


Figure 99 - Decelerator Envelope Unit Weight versus Deployment Mach Number, Trajectory 22

SECTION VII - AUXILIARY GAS-INFLATION MEANS FOR MARS ENTRY DECELERATORS

1. GENERAL

A gas-inflation system provides sufficient internal pressure to maintain a symmetrical rigid shape for an inflatable aerodynamic decelerator. Because decelerators can be applied in various stabilization and deceleration modes, each with peculiar thermal and structural considerations and a variety of altitude velocity regimes, inflation systems must be optimized separately.

Weight factors, prime considerations in determining acceptability of any design, are summarized in Figure 100 for more feasible methods of decelerator inflation. Systems considered were: (1) compressed gas in pressure vessels, (2) residual gas within the decelerator, (3) gas generation by burning fuel, (4) chemically generated gas, (5) auxiliary compressors, and (6) ram-air inflation.

2. COMPRESSED GAS IN PRESSURE VESSELS

Probably the most widely used method of delivering large volumes of gas at relatively low pressure is high-pressure release from relatively small-volume bottles made of steel, or fiberglass or bottles wound with wire.

The state-of-the-art in this area has progressed with development of metals and compression equipment with greater strength. Associated tubing, solenoids, and pyrotechnic valves have become off-the-shelf items. Inflation rates may be controlled easily with standard metering hardware.

Weight curves for steel-bottle and fiberglass-bottle systems in Figure 100 are based on catalog weights for commercially available bottles. Heat treated Ti-6A-4V alloy was selected and design conditions for the bottles

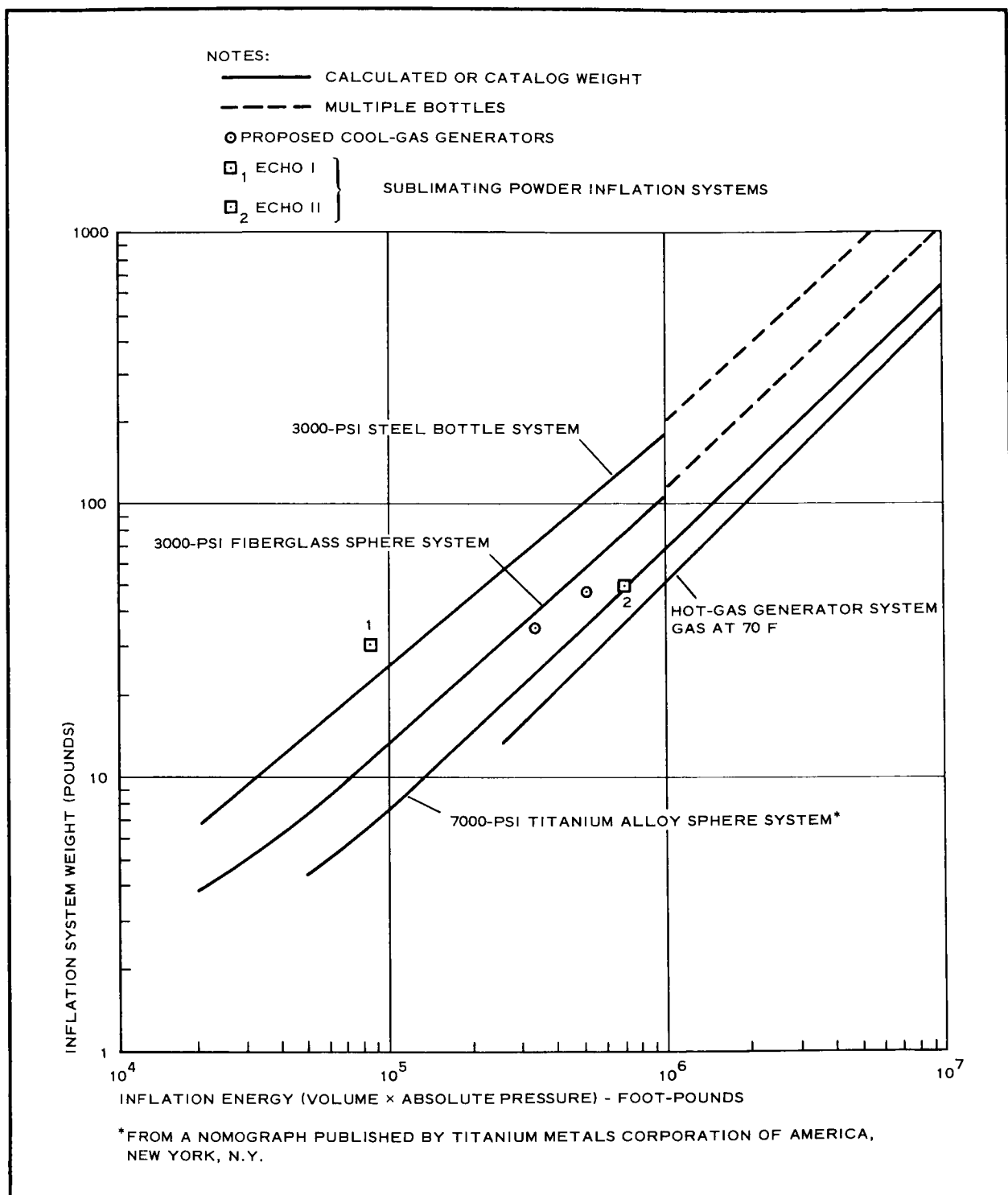


Figure 100 - Weights for Various Inflation Systems

were assumed to be 7000-psi pressure and 100,000-psi design stress. This stress level gives a safety factor of 1.6 at 70 F. At elevated temperatures corresponding to projected sterilization requirements for the entry capsule, the safety factor would be approximately 1.0.

Weight of each of the three gas-bottle systems included compressed air and the weight of the control valve. The control valve, assumed to be simple, was estimated to weigh from 1 to 3 lb over the range of bottle sizes.

3. RESIDUAL GAS WITHIN THE DECELERATOR

The extremely low density of the Mars atmosphere suggests the feasibility of using gas trapped inside the packaged decelerator for inflation. If necessary to eliminate predeployment stresses on the decelerator, the packaging canister may be sealed hermetically creating a zero pressure differential across the fabric. This system ensures rapid inflation and good reliability and eliminates need for a pressure vessel and valves.

4. GAS GENERATION BY BURNING SOLID FUEL

Generation of gas by burning "explosive" materials is reliable and being refined continually. Hot-gas and cool-gas generators are available in various sizes as off-the-shelf items.

Custom-made gas generators may be procured to fulfill most pressure volume requirements. These devices can be fired electrically or mechanically.

The gas generator curve in Figure 100 was calculated from the equation

$$P_v = w r T \quad (7)$$

where

P_v = energy (lb-ft),

w = propellant weight (lb),

T = gas temperature (F), and

r = energy constant (55 ft per deg R - a good average value for present-day ballistic generators).

Total weights of gas generator systems were determined arbitrarily by multiplying propellant weight by 1.5 to include weights of the case and hardware. The 1.5 factor, estimated from limited data on hot-gas generators, is based on an assumption that gas is generated hot and cooled to 70 F inside the decelerator envelope.

Two points in Figure 100 show the weights of two cool-gas generator systems proposed by McCormick-Selph Associates of Hollister, Calif. for specific inflatable devices.

5. CHEMICALLY GENERATED GAS

Applications to inflate decelerators at extremely low-density conditions can use subliming solids or vaporizing liquids as the gas source. Because this method can produce only very low pressures, its usefulness is limited to initial inflation of ram-air devices in low-density-altitude regimes.

Two examples of sublimating powder systems are shown in Figure 100. The points were calculated from data for Echo I and Echo II balloon inflation systems (see Table VII).

TABLE VII - ECHO I AND II INFLATION DATA

System	Sublimating solid	Weight (lb)	Density (psf)	Pressure (mm Hg)	Volume (cu ft)
Echo I	Benzoic acid Antraquinone	10	79	0.06	525,000
		20	89		
		30	84 (average)		
Echo II	Acetanide	50	72	0.20	1,290,000

6. AUXILIARY COMPRESSORS

A cursory feasibility examination of auxiliary compression equipment revealed several unfavorable characteristics. Compression of rarefied gases comparable to the Mars atmosphere imposes severe tolerance restrictions on the moving compressor parts. Time required is prohibitive for pumping large volumes of low-density gases into an inflatable device. Weights and volumes of airborne compressors compare unfavorably with other systems.

7. RAM-AIR INFLATION

Ram-air inflation has been proven practical in subsonic, supersonic, and hypersonic regimes. Basically, the ram-air concept converts kinetic energy of the external dynamic pressure to internal static pressure by presenting orifices normal to the airstream. The inflation aperture can be located in almost any area exposed to the airstream. Internal recovery pressures one to four times greater than dynamic external pressures have been noted in the supersonic range when side inlets were used with the BALLUTE. This pressure boost capacity indicates that configurations requiring inflation pressures greater than the free-stream dynamic pressure also may be ram-air inflated.

In contrast to closed inflation systems, the ram-air method operates in a wide range of dynamic pressure conditions without over-pressurizing the inflatable device. This flexibility avoids the need for programming inflation gas, thus reducing the structural requirements of the fabric.

Inflation rate and g loads imposed on the payload can be controlled by the size of the inflation orifice.

8. PACKAGE BULK FACTORS FOR THE VARIOUS INFLATION SYSTEMS

Package density, the ratio of weight to volume of the inflation system, was calculated for each method as follows:

<u>System</u>	<u>Density (pcf)</u>
Hot-gas generator ^a	60
Cool-gas generator ^b	95
Fiberglass sphere, air at 3000 psi	35
Titanium sphere, air at 7000 psi	59
Steel bottle, air at 3000 psi	63
Sublimating powders	
Echo I (benzoic acid and antraquinone)	85
Echo II (acetanide)	72

^aBased on data of Frankford Arsenal, Philadelphia, Pa.

^bBased on data of McCormick-Selph Associates, Hollister, Calif.

SECTION VIII - TESTING REQUIREMENTS, TECHNIQUES, AND FACILITIES

1. GENERAL

To evaluate accurately the performance of expandable decelerators, testing must be conducted under controlled or known conditions. These tests will determine important aeroballistic characteristics and structural integrity of the decelerator design and its effectiveness in decelerating and controlling Mars entry capsule systems. These tests must include specific areas of investigation described in Items 2 through 6 below.

2. STATIC AERODYNAMIC COEFFICIENTS AND AERODYNAMIC FLOW-FIELD EFFECTS

Static force and moment data must be obtained for the Mars entry capsule as functions of angle of attack, yaw, and roll for variations of expandable decelerator drag area related to operating Mach number ranges. In addition to measurements of static loads and moment, data must be obtained on the effects of shock-wave and effects of boundary-layer interaction, separation, and transition. These viscous flow phenomena will strongly influence the performance of entry capsule decelerator composites. Consequently, it is necessary in the experimental test program to control as closely as possible the correspondence and simulation of Mach number, Reynolds number, and flow conditions expected in the actual entry trajectory during decelerator operation.

Static aerodynamic derivatives can be obtained in transonic and supersonic wind-tunnel facilities with scale models supported by strain-gage instrumented sting balances. Aerodynamic flow-field effects can be determined with optical techniques such as Schlieren or shadowgraph photography or, preferably, with motion photography. Several configurations should be tested to study the effects of variations in decelerator geometry and arrangements.

These data are necessary to ensure desirable static stability margins for the decelerator composite and to determine decelerator effectiveness during deployment.

3. DECELERATOR LOADS AND LOAD DISTRIBUTION

Measurements to determine drag loading and load (pressure) distribution on decelerators must be made to estimate the induced moments and to determine the power requirements, bulk, and weight of the deployment and inflation mechanisms. In addition, the required structural integrity of the device itself will be determined by these measurements. A test program must determine unwanted rolling or yawing moments induced by flow asymmetries.

These data can be estimated from wind-tunnel tests by using a six-component sting balance and by providing known asymmetries.

4. DYNAMIC STABILITY

For symmetrical decelerators the variations of pitching moment coefficients with pitching velocities and rates of change in angle of attack must be measured to evaluate dynamic stability of the vehicle at critical points on the entry trajectory. Generally, the values for these derivatives are most important when the negative rate of change in dynamic pressure is maximum following initial deployment and inflation of the decelerator device.

These derivatives can be measured by model tests in high-speed wind tunnels with an oscillating balance, with free-flight tests on a ballistic range or with photographic measurements in a wind tunnel.

5. AERODYNAMIC HEATING

The decelerator must be tested in conditions of temperature and loading expected during entry into Mars atmosphere. These tests will determine the adequacy of materials and design integrity under these environmental conditions.

6. TESTING METHODS

a. General

Environmental conditions associated with Mars atmosphere entry flight pose difficult problems in devising experimental study techniques. These arise principally from the extremely low anticipated densities and pressures.

Figure 101 illustrates the range of Reynolds and Mach numbers that possibly may be encountered in Mars atmosphere flight entry simulated in the Earth's atmosphere.

Figure 102 shows the stagnation temperature levels encountered in the Earth's atmosphere as functions of Mach number. The solid portion of the curve represents temperature values for the assumption of equilibrium dissociation, and the dashed line is for no dissociation. Dissociation is encountered as Mach number exceeds approximately seven. The temperature at which complete ionization of air occurs is approximately 20,000 R and will not be reached for most contemplated recoverable Mars entry vehicles.

Much progress has been made in testing techniques and procedures for study of the aerodynamics of high-speed flows. However, at present, no single laboratory technique is adequate to study all problems simultaneously. Problems must be separated into parts that can be studied with the laboratory techniques now available. The separate results then must be synthesized.

b. Testing Facilities

Shock tubes, shock tunnels, and ballistic range facilities have been significant contributions to gaining understanding of problems in the flow regime of present interest. These facilities include flow processes behind normal shock waves ahead of blunt bodies, boundary-layer transition phenomena, skin friction and drag, and heat transfer as inferred from skin friction.

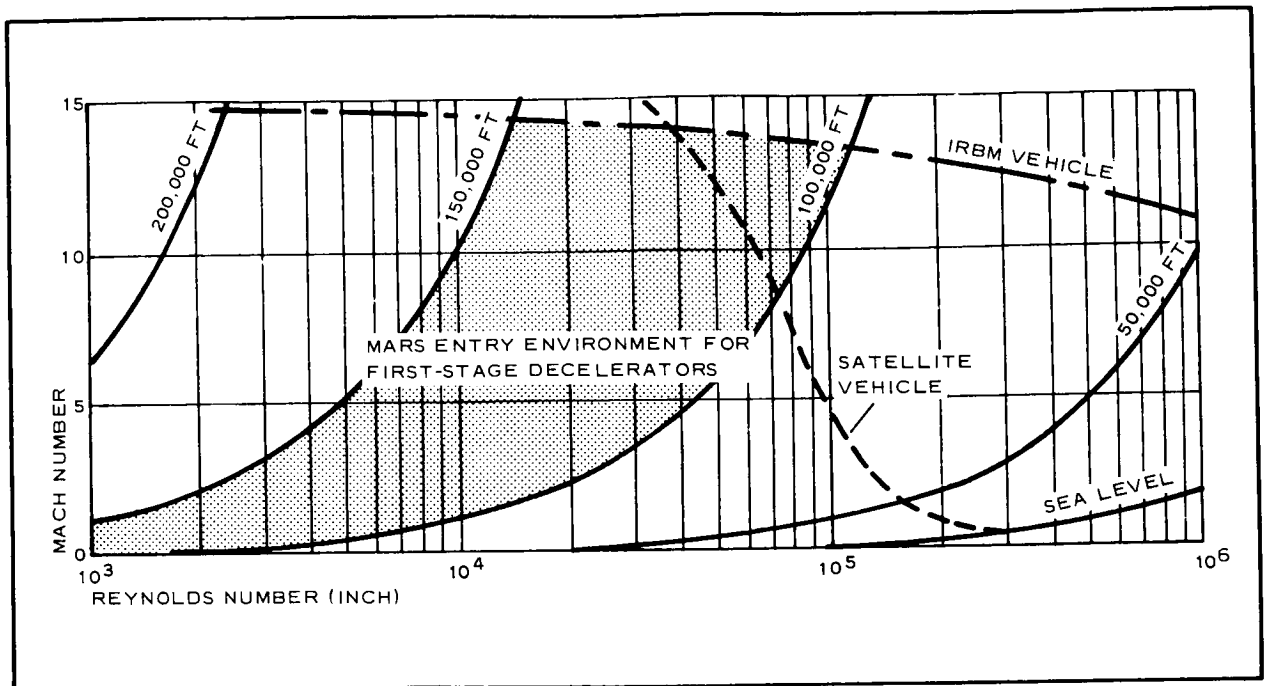


Figure 101 - Mach and Reynolds Numbers for Simulating Mars Flight in the Earth's Atmosphere

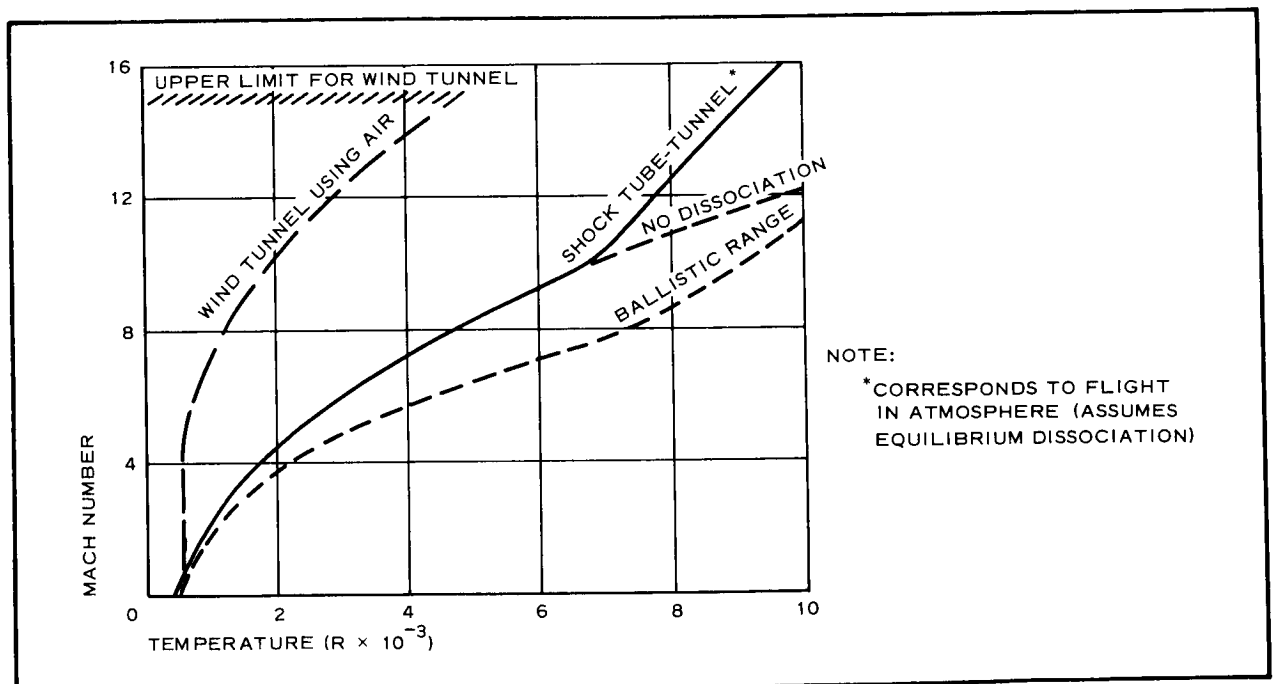


Figure 102 - Mach Number and Temperature for Atmospheric Flight and for Various Laboratory Testing Methods

Figure 103 shows the range of Mach and Reynolds numbers and the temperature level obtainable in wind tunnels using air superimposed on the flight regions of Figure 101. The wind tunnel only allows coverage of a portion of the region of interest. In addition, at the low values of Reynolds number required for simulation, accuracy of most wind-tunnel data is limited.

Ballistic range facilities and free-flight model testing in wind tunnels also can determine static aerodynamic force and moment coefficients in addition to dynamic stability derivatives. Pressurized ballistic ranges and wind tunnels make possible a reasonable flight Reynolds number of the actual Mars entry capsule over the entire Mach number range of interest for expandable decelerators shown in Figure 103. Ballistic range facilities use light gas guns to propel the models to test velocities and can accommodate models to 3 or 4 in. in diameter. The required mass scaling to preserve dynamic similarity is somewhat difficult from the standpoint of size. However, the scaling is

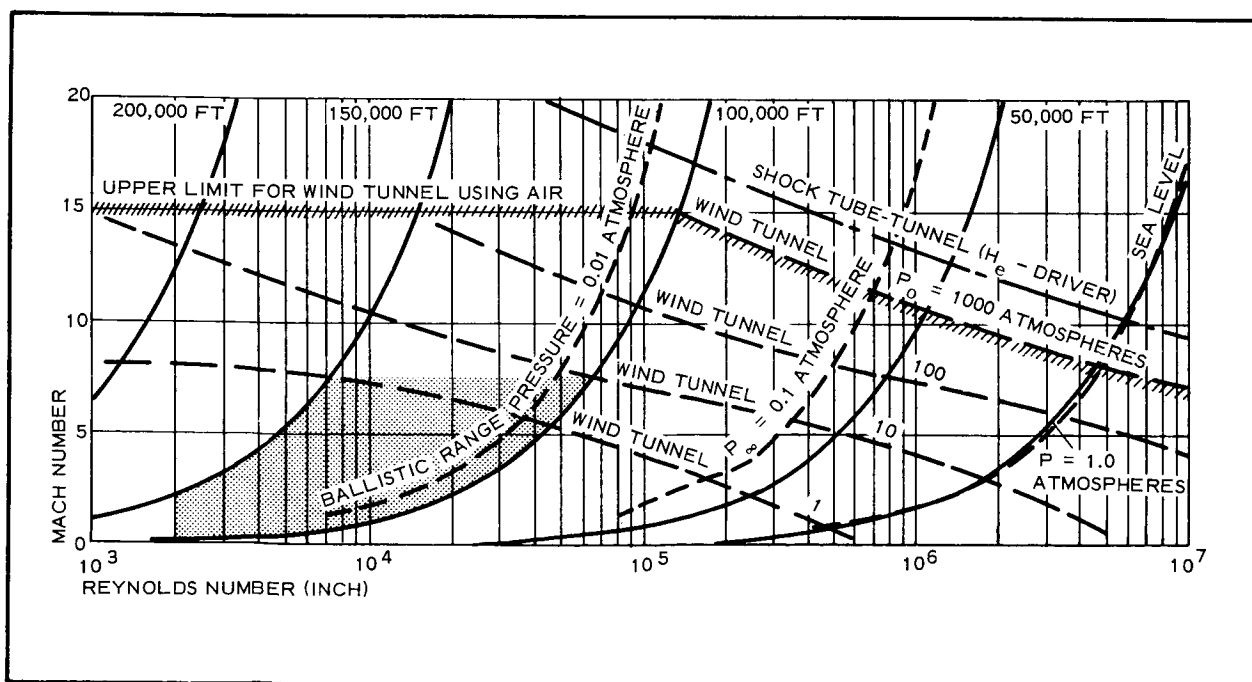


Figure 103 - Mach and Reynolds Numbers for Various Laboratory Testing Methods

usually within the capabilities of the model propelling equipment for rotationally symmetric configurations of the type being considered. Thus, motion of the actual decelerator composite can be duplicated closely by the scaled model. In addition, all realistic interactions will be inherent in this testing method whereas unforeseen interactions of different effects may go undiscovered in wind-tunnel tests.

Ballistic range facilities also are turbulence-free and homogeneous, features desirable for the study of viscous effects such as boundary-layer transition and shock-wave boundary-layer interaction.

A disadvantage is that model sizes do not allow for extensive instrumentation. However, measurements can be made with photographs, shadowgraphs, and spectrographs of the model in flight and by observing the recovered model after test.

Free-flight model tests in wind-tunnels and ballistic ranges are limited by short testing times. Design study of expandable decelerators for Mars entry requires duplication of expected flight temperatures and rates of heating to determine how structures and structural materials react at high temperatures. Short running times of wind-tunnel and ballistic-range tests force the use of other tests for detailed investigations of such problems as aerothermo-elastic phenomena, cooling methods and surface chemistry with hot surfaces.

Heating rates experienced by Mars entry capsules could vary widely, depending on atmosphere, drag area, weight, velocity, altitude, and entry angle. For expandable decelerator applications considered in this study, the heat flux could range from 1 to 8 Btu/ft²/sec.

Except for actual free-flight testing, the power required to generate such heat fluxes over the large configurations required precludes simulation of aerodynamic heating on the full-scale body of the entry capsule.

c. Heating Techniques

(1) General

Techniques developed for research in the fields of decelerator materials and structures at temperatures that correspond to the anticipated Mars entry environment include: (1) electrical resistance heating, (2) electric blankets, (3) radio frequency heating, (4) hot body radiation, (5) wind-tunnel testing, (6) heating with hot gas jets, and (7) free flight testing.

These techniques are described in Items (2) through (8) below.

(2) Electrical Resistance Heating

Electrical resistance heating, with current passed directly through the conducting part, is confined generally to testing of small-area specimens with uniform cross section; otherwise, the current requirements become excessive. Theoretically, the rate of temperature rise obtainable is almost limitless, depending only on the internal resistance of the material and the voltage applied.

(3) Electric Blankets

An electric blanket relies on conduction for heating. Flexible and adaptable to irregular shapes, its use is confined to applications requiring slow heating, although large areas may be covered. Practical heating rates with this technique range from 0.1 to 4.0 Btu/ft²/sec.

(4) Radio Frequency Heating

Radio-frequency induction heating lends itself to rapid heating of reasonable size structural components of uniform material. This method closely approximates heating because the outer surface is heated. A disadvantage of this technique is that dissimilar materials will heat at different rates, causing problems in mounting test specimens. If rapid heating is desired, power requirements limit this method to testing of small sizes.

(5) Hot Body Radiation

Several methods using hot-body radiation have been devised to simulate aerodynamic heating. One method uses a large electrically heated graphite plate. Electrical current through the plate generates the heat by self-resistance. A refractory oven is used. When the plate is withdrawn from the oven, it faces and heats the test specimen by radiation. Relatively large specimens can be heated by this method with rapid temperature rises possible. Longer heating periods are used, however, to reduce power requirements. Test specimens can be heated on both sides of the plate simultaneously. A similar, more flexible method uses graphite rods heated to incandescence by a large electrical current passed through them.

Another similar device is a tubular quartz lamp with tungsten filaments. Filament temperatures to 3500 F can be attained with acceptable life. Such lamps are satisfactory in terms of flexibility and control. By control of filament current, the heat flux can be controlled and programmed.

(6) Wind Tunnel Testing

Some research on structures has been done in wind tunnels using air; however, this testing does not lend itself well to existing facilities, primarily because structural failure could cause severe wind-tunnel damage and delay the use of an expensive installation. High-speed wind tunnel facilities have been developed for structural testing that incorporate some heating techniques discussed in this section.

(7) Heating with Hot Gas Jets

Hot gas jets for simulation of aerodynamic heating can heat the material and simulate the effects of oxidation and erosion. Oxidation and erosion simulation require that the oxygen content be proportional to the atmosphere and that the gas move at high

velocity. Among these devices are ram-jet configurations supplied with air from a preheated auxiliary air supply. The supply can be augmented with pure oxygen to maintain atmospheric oxygen content at the nozzle exit. Tests at temperatures to 2000 F at $M = 2$ can be obtained. By injecting and burning fuel such as ethylene gas, jet stagnation temperatures corresponding to $M \approx 6$ can be obtained.

Similar devices, modified rocket motors burning kerosene with hydrogen peroxide or red fuming nitric acid with anhydrous ammonia, have been useful for preliminary materials evaluation and for research on insulation and cooling schemes. Although the above methods provide simplicity and utility, the gas streams are not real air. Work has been conducted at the NASA Langley Laboratories to provide an uncontaminated air jet with stagnation temperatures of approximately 4000 F. This device consists of heating ceramic pebbles in a chamber. When the desired temperature is reached, the heater is turned off and uncontaminated air pumped into the chamber and through a supersonic water-cooled nozzle into a test chamber.

(8) Free-Flight Testing

Free-flight testing is the one feasible way of attaining accurate heat flux associated with flight at higher Mach numbers. This technique would use high-performance rocket units in progressive stages to which the test vehicle with decelerator is attached. By varying trajectories or flight paths of these rocket-powered test vehicles, a wide variety of test conditions can be attained. Trajectories are varied by changing the number of stages and the time-delays between stages. Firing all stages during the ascending phase produces a straightaway trajectory. This trajectory yields information on high-speed behavior at high altitudes. An over-the-top trajectory is achieved by firing the latter

stages after the test vehicle has started to descend. This flight path yields information at lower altitudes and can simulate closely a Mars entry trajectory. -

This method of testing, although relatively expensive and requiring extensive instrumentation, has been successful. Section XI contains a comprehensive description of the free-flight test techniques.

Table VIII summarizes various experimental techniques that may be employed for the study and evaluation of expandable decelerator devices for Mars atmospheric entry.

TABLE VIII - EXPERIMENTAL TECHNIQUES FOR STUD

Experimental technique	Suitable areas of study	
Rocket-propelled models	Heat-transfer and skin friction; boundary-layer transition; cooling methods; characteristics of materials and structures at high temperatures and heating rates; and vehicle lift, drag, and stability including dynamic behavior.	Cor num
Ballistic ranges and free-flight, wind-tunnels	Skin friction and drag; boundary-layer transition; flow characteristics, including shock-wave, boundary-layer interaction; and heat-transfer and dynamic flight behavior (requires improved techniques and instrumentation for accurate measurements).	Cor num
Shock tubes and shock tube wind tunnels	Properties of air at high temperatures; relaxation effects; heat-transfer and boundary-layer phenomena for some conditions; and flow configurations, pressure distribution.	Cor num or num ber
Intermittent tunnels of "hotshot" type	Similar to those suitable for shock-tube study.	Cor num abo
"Hot" supersonic tunnels with long testing times and heating by: <ol style="list-style-type: none"> 1. Combustion of fuels 2. Air compression 3. Ceramic storage heaters 4. Combinations of (2) and (3) 5. Electric arcs. 	Heat transfer to moderately high Mach numbers; study of cooling methods; behavior and development of materials and structures, including aerothermoelastic problems; and aerodynamic problems to Mach numbers approaching 15.	Cor num aro pra
"Cold" supersonic tunnels	Aerodynamics of perfect gas flows; model configuration studies; exploratory aerodynamic research to high Mach numbers.	Ma usi

Y OF EXPANDABLE DECELERATORS

Simulation capabilities	Limitations
irect flight enthalpy, Mach number, and Reynolds number.	Relatively high cost, inability to observe phenomena at close range, complexity of over-all system operation degrading reliability of data acquisition
irect flight enthalpy, Mach number, and Reynolds number.	Model size is small and short testing time makes difficult the accurate measurements of more than a few relatively simple quantities
irect enthalpy and Reynolds number with low Mach number correct enthalpy and Mach number with low Reynolds number.	Millisecond testing times
irect enthalpy and Reynolds numbers to Mach numbers of up to 15.	Short testing times
irect enthalpy and Reynolds number to Mach numbers of up to 7. Continuous flow for practical purposes.	Short testing time
ch numbers to about 9 or 10 ng air.	Incorrect enthalpies

152

SECTION IX - FREE-FLIGHT TEST SIMULATION

1. GENERAL

This section discusses an earth atmosphere, free-flight test technique for acquisition of data to evaluate deployment, inflation, performance, and structural integrity of expandable terminal decelerators for a Mars entry capsule. Concepts of this system are dictated primarily by reliability, performance, and economic factors. The system will require reduced range and ground-support facilities compared with those used for long-range ballistic missile or satellite systems. Complexity of program operations is minimized and reliability is increased.

The functional performance evaluation of expandable decelerators for a Mars entry capsule requires that consideration be given to free-flight simulation in the Earth's atmosphere of all possible combinations of loads and stresses anticipated for a range of nominal entry trajectories to the Mars surface.

Experimental techniques available for controlled laboratory and captive testing are limited in capability of simulating simultaneously the range of environmental effects that could be encountered. Consequently, the requirement for approximately full-scale, free-flight, proof testing under conditions approaching environments anticipated during passage through the Mars atmosphere.

Function and performance can be evaluated feasibly for expandable decelerators with existing range and ground-support requirements, for example, those available at Wallops Island, Va., White Sands Missile Range, N. M., or Kennedy Space Center.

A proven approach consists of launching a rocket-powered vehicle controlled for near-vertical ascent ($\gamma_0 \approx 80$ deg). Inherent aerodynamic

stability would be provided to control the launch vehicle and some spin would minimize dispersion caused by errors of thrust alignment, for example, lateral offset and unknown wind errors. The test vehicle is propelled to attain desired velocity and altitude in ascent or descent.

During descent tests, impact-point dispersion can be reduced by firing the last stage during re-entry. This firing will achieve necessary test velocity and altitude without the need for extreme summit altitudes.

Various government-sponsored programs have shown that this technique makes possible a wide range of velocity-altitude test combinations. Magnitude and time of impact pressures, deceleration loads, and heating are disadvantages. These will be higher than those for normally shallower entry angles anticipated for Mars entry unless more precise control of the vehicle flight path is provided. However, the aerodynamic effects anticipated for currently projected Mars entry flight paths for the most part can be simulated realistically by this technique.

2. DESCRIPTION OF LAUNCH VEHICLE SYSTEM

a. General

Selection of the propulsion units and staging for a rocket-boosted decelerator test vehicle must be based on analysis of such considerations as performance, range safety, aerodynamics, reliability, construction, and thermal effects. In determining motor staging, the ability to attain the desired test velocity and altitude is a primary consideration. Solid-propellant rocket motors have been developed to support rocket-propelled free-flight tests. Combinations of these motors can produce desired test velocity and altitude.

b. Booster Selection

Booster sizes should be chosen for near-optimum mass ratios for the stages. Selection of the initial stage is influenced by thermal and inertial loading. To minimize aerodynamic heating and g load effects

during boost, a relatively long burning time for the initial stage is desirable. Related also to booster selection are lead time required for delivery and associated standardized hardware such as interstage connections, stabilizing fin assemblies, ground service equipment, launchers, and erectors. The current Aerodynamic Deployable Decelerator Performance Evaluation Program (ADDPEP) program conducted under Contract AF33(615)-1513 by Goodyear Aerospace has integrated these selection considerations and has established and proved in 16 rocket-boostered free-flight deployable decelerator tests the reliability and performance of the selection method. For free-flight entry simulation testing of the entry capsule, required summit altitudes of 50 to 100 mi can be attained at launch angles near 80 deg with a typical combination of XM33-Recruit and Lance boosters in sequential stages. Firing the final stage may be desirable during descent in an over-the-top trajectory to reduce summit altitudes and impact-point dispersions. Whether firing all stages in ascent or reserving the last for re-entry, motor staging energy needs comparatively are almost equal.

3. LAUNCH VEHICLE FLIGHT CHARACTERISTICS

To establish adequately the performance of expandable terminal decelerators for the entry capsule, requirements must be determined for static and dynamic stability of the launch vehicle. Required stabilizing surfaces must be established for stability at the Mach range applicable at each stage. Dispersion studies should determine effects of perturbations from such influences as thrust malalignments, wind measurement or prediction errors, launching inaccuracies.

Two conflicting requirements relate to aerodynamic stability of the launch vehicle. High stability is desirable to minimize dispersion caused by malalignments. Conversely, minimum stability will achieve minimum dispersion from lateral winds. For an unguided vehicle, changing launcher position for known winds can compensate to a great extent for in-flight

wind effects. Changing launcher position restricts wind dispersion to errors in measurement or changes in the wind.

Center of pressure for the typical booster (without fins) is usually at an unstable location. Thus, additional stabilization is needed for moderate aerodynamic stability; too much, however will cause the vehicle to become extremely sensitive to disturbance inputs. Initial static stability of 5 to 6 percent of total vehicle length usually is adopted for a preliminary design. A cruciform fin arrangement secures this margin. Delta-shaped stabilizing fins might be selected for structurally efficient load-carrying capability. The static margin desired, combined with increased fin effectiveness caused by fin-body interference, indicates that required fin sizes do not cause excessive performance reduction from aerodynamic drag. First-stage static stability improves as fuel is consumed because the forward center of gravity shifts. With increasing supersonic Mach numbers, the moment arm of a delta-shaped configuration generally will increase at a faster rate than the fin effectiveness decreases. The moment arm is that distance from fin center of pressure to vehicle center of gravity. Thus, the static margin of stability is usually least for a short interval just after launching.

Subsequent stages are designed for substantially greater static stability than the first stage because lateral winds are less forceful as vehicle velocity increases. Flared skirts or fins at the base of the succeeding stage can provide a stability margin of approximately 15 percent of body length. The stability margin for these stages also will increase during burning. However, aerodynamic surfaces must be designed for stability despite possible reduction of body flare or fin effectiveness as higher supersonic Mach numbers are attained.

4. DISPERSION CONTROLS

Dispersion of the decelerator test vehicle from its nominal trajectory can be caused by winds, aerodynamic asymmetries, thrust malalignments, variations in total rocket motor impulse, and reduced

aerodynamic damping caused by decreasing air density during ascent. Because of the relatively steep initial launch angle normally used in rocket-launched decelerator test programs to minimize range and tracking requirements, peak altitude will not be greatly affected by small dispersive influences. However, the steep launch attitude will increase range dispersion.

Dispersion caused by malalignments, asymmetries, and winds is greatly reduced when spin is used in staging. Low-altitude winds will have the greatest effect on the vehicle trajectory because vehicle velocity is low. Usually, greatest stability demands occur shortly after launch.

Rotating and tipping the launcher to account for changes in launch angle caused by the wind can compensate for wind dispersion. The actual wind dispersion then is associated with errors in wind measurement or wind changes between measurement and launch.

For test missions to be conducted, ranges of approximately 500 naut mi can be anticipated. Although severe dispersions may be considered, missions of this type could be conducted at Wallops Island or at KSC.

Experience with ADDPEP has shown that dispersion from thrust malalignment may be reduced by employing larger fins to increase stability. This approach, however, increases vehicle wind sensitivity. Higher spin rates also may be employed to reduce dispersion from thrust malalignment. At a certain value, determined for each launch configuration, increasing the spin rate will not reduce dispersion further. However, dispersion can be reduced further by rail launching techniques.

Wind effects on dispersion when all motors function properly are found to be virtually linear with variations in wind structure. This linearity is the dispersion in path angle at burnout. Typically, the total range for a 2σ wind is twice that of a 1σ wind. In assessing errors caused by winds, the degree to which winds can be measured must be considered.

For test conditions at Mach 3 to 5 and 140,000 to 150,000 ft, experience has shown launch-vehicle performance must be examined carefully. Such

tests require close attention to the vehicle design. Dynamic characteristics of the vehicle must be considered; for example, balancing the vehicle and precisely controlling launching.

5. HEAT TRANSFER

In establishing decelerator criteria for a Mars entry capsule, heat transfer calculations delineate design and trajectory programming requirements. Critical test-vehicle components and booster must be guarded from excessive aerodynamic heating. Velocities of the various stages in significant atmospheric regions should be programmed to prevent excessive heating periods, thus minimizing the heat-protection requirements. Frequently, minimum coasting periods between stages in multiple-stage configurations can reduce heating, particularly since higher Mach numbers will be encountered during ascent. Adequate heat-protection materials must be provided for various exposed components of the launch vehicle. The maximum skin temperature allowable for most solid propellant motors is determined by the temperature limits of propellant-to-case bonding. Fortunately, booster side area heating is reduced by the relatively large distances from the nose. Analyses and tests have shown that wide ranges of skin temperatures are possible by varying coasting times between stages. These ranges can vary by as much as a factor of four for large variations in coast times. Mach number usually is not significantly reduced by increasing the coast period; hence, coast optimization to limit heating will not affect seriously overall performance. However, substantial altitude variation can be expected with variations of the coast time.

Heating on inclined surfaces and at stagnation points also must be considered. Heating at these points is more severe than side heating, and appropriate selections must be made of leading-edge and nose radii, material types, and material thicknesses. Heat sink weight many times is not practical and lightweight insulation must be provided for critical areas.

6. TEST VEHICLE CONCEPT

a. General

The test-vehicle concept consists of an aerodynamically "clean" payload-carrier forebody carrying the expandable decelerator test item in a container mounted in the after part of the carrier. A deployable inflatable AIRMAT^a cone envelopes the test item and, just prior to the test, gives the forebody its increased size, simulating the configuration and performance characteristics of the Mars Voyager entry capsule. A few seconds before reaching the test point, the AIRMAT cone is inflated.

Figure 104 shows the basic suggested operational sequence of events on the mission trajectory. The launch vehicle combines an XM-33 booster and two Recruit boosters for the first stage and a Lance booster for the second stage.

b. AIRMAT in Simulation

An inflatable AIRMAT cone simulates the basic entry capsule. A multisided regular pyramid is selected for money-saving simplicity of fabrication and because it forms a reasonable approximation of a 120-deg blunt cone currently considered for the Mars entry capsule. Analysis shows that for a 12-ft diameter decagonal base, the maximum deviation from a true circular base is three inches. For low inflation pressures required at desired Mach number and altitude test conditions, operational loadings cause structural deflections of much less than an inch.

The design is based on a cone to be deployed at approximately 150,000 ft, in a dynamic pressure field ranging to about 60 psf.

The AIRMAT cone deployment Mach number, dynamic pressure, and altitude are anticipated to have the following ranges for two conditions:

^aTM, Goodyear Aerospace Corporation, Akron, Ohio.

1. $M \approx 4.0$; $q \approx 25$ psf; $h \approx 150,000$ ft
2. $M \approx 6.0$; $q \approx 60$ psf; $h \approx 155,000$ ft

Typical selection of materials for the AIRMAT cone is based on a flat-plate wall temperature of 500 to 600 F for an emissivity of 0.8. Consequently, Nomex or Dacron or both with heat protective coating are required.

The suggested skirt configuration is a regular 18-sided pyramid with ribs and flat sides. Both ribs and sides will have AIRMAT construction.

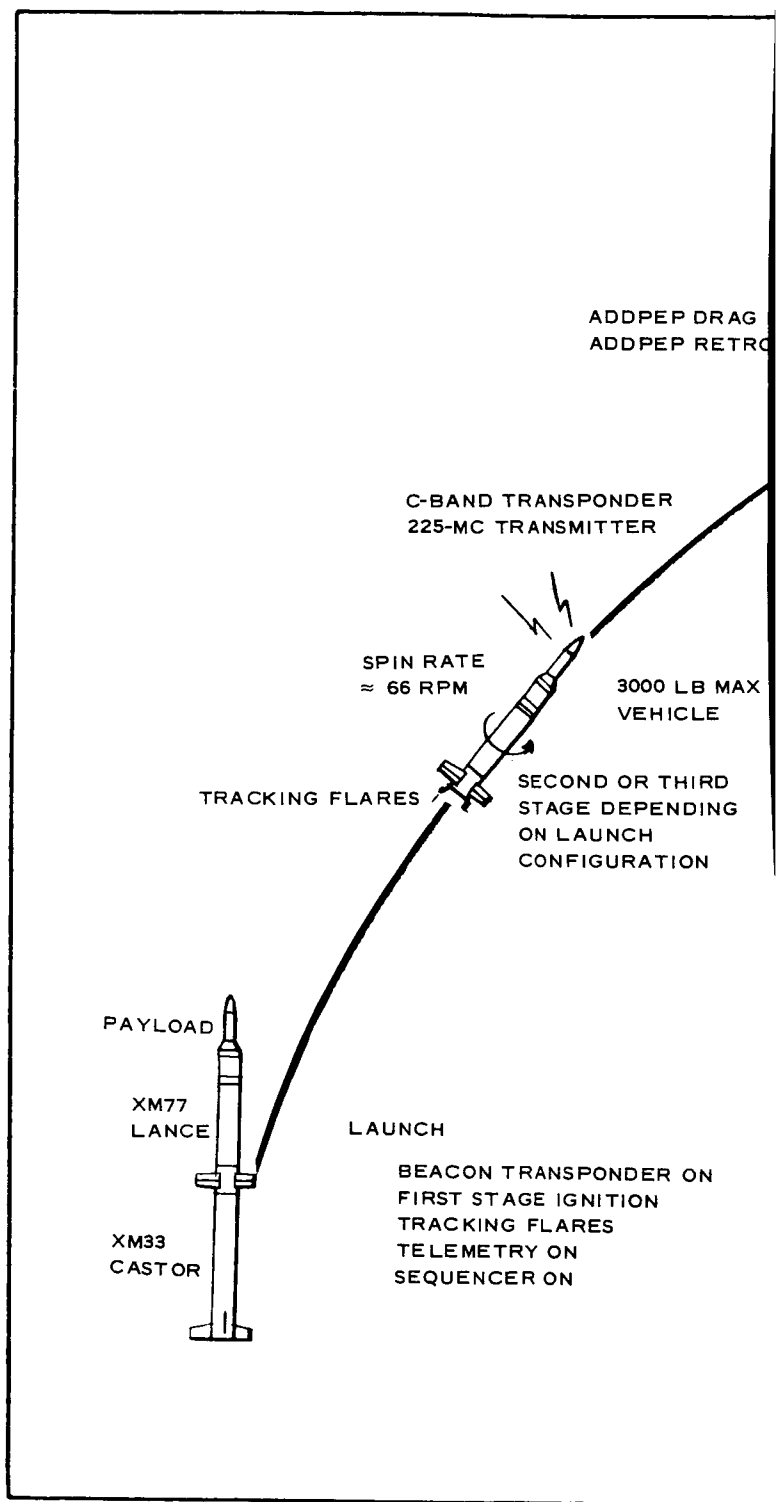
With asymmetric external aerodynamic loading, webs acting as spokes prevent distortion of the near-circular cross section of the skirt. The webs also prevent lateral displacement of the skirt with respect to the major longitudinal axis of symmetry.

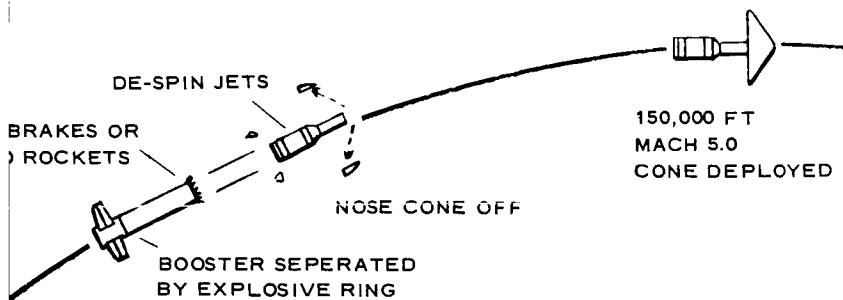
The inner and outer skins forming the exterior skirt surfaces terminate in a welt clamped in place by a retainer ring. The ring eliminates the need for fastener holes through the fabric and permits uniform transfer of tensile loads. Pressure scaling of these interfaces can be accomplished easily during assembly.

c. Design Considerations

Preliminary calculations indicate that, for an inflation pressure of 20 psi maintained to retain the shape of the AIRMAT cone with nominal deflection, the total weight is about 45 lb. To account for heat insulation coating and structural design, the total weight is estimated to be 100 lb with a deflection of about 2 in. The deflection can be decreased by increasing inflation pressure, an action that will increase weight and decrease the factor of safety.

This general design arrangement can be optimized easily for a specific set of design requirements. The important design variables are (1) number of ribs, (2) face sheet material, (3) number of drop threads, and (4) AIRMAT thickness.





IN-FLIGHT (ELECTROMECHANICAL TIMER) - AD

LAST STAGE BOOSTER IGNITION
 LAST STAGE BOOSTER SEPARATION, DRAG
 TELEMETRY CALIBRATE
 DE-SPIN JETS (RATE GYRO)
 ON-BOARD CAMERAS (2)
 STATIC AND DYNAMIC PRESSURE PORTS O
 CANISTER EJECTION

DATA TRANSMISSION - ADDPEP TELEMETRY

STATIC PRESSURE
 DYNAMIC PRESSURE
 DECELERATOR SHOCK
 DECELERATOR DRAG
 ACCELERATION
 TEMPERATURES
 BALLUTE INTERNAL PRESSURE
 FM/FM PAM EVENT MONITORING

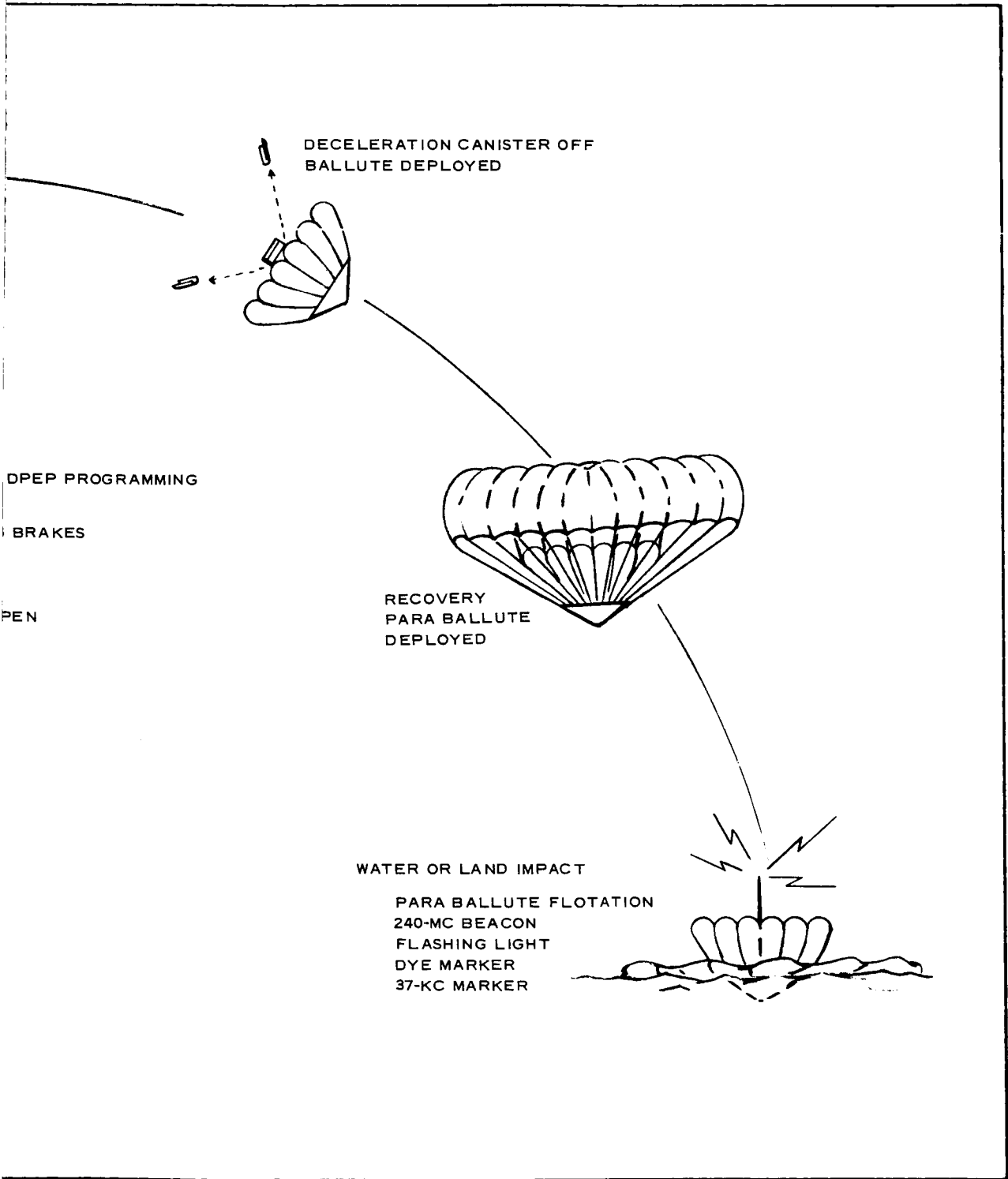


Figure 104 - Rocket Boost Techniques for Simulation Tests

If a conical shape is mandatory, the same basic arrangement can be used except that, instead of being flat the faces would be curved by tucking the inner-face in "pinch-pleats" or by slitting the outer face and masking the slits.

The most sophisticated and expensive alternate approach would entail actually weaving symmetrical, curved, tapered AIRMAT sections of the flare.

Again referring to the Air Launched, Air Recoverable Rocket (ALARR) flared skirt discussed above, design and development produced these conclusions and recommendations:

1. Functional testing must be conducted to solidly support and validate the analyses made in determining the design.
2. The conical shape, cantilevered extension beyond hard superstructure, and the sharp-cornered after termination at the base combine to provide a good aerodynamic configuration.
3. Inflation tests and asymmetric loading of the skirt indicate that the flare could be considered a rigid body under dynamic pressure and angle of attack environment.
4. Altitude-chamber inflation tests have demonstrated gas storage bottles, manifold, and valving are adequate for completely inflating a decelerator in a fraction of a second.
5. Structural integrity of fabric intersections of low and high-temperature skirts has been demonstrated under test conditions duplicating mission environments.

6. Skirt packaging in a annular container similar to that suggested in this section has been demonstrated satisfactorily by Goodyear Aerospace at Holloman Air Force Base, N. M.
7. A demonstration test at the Holloman AFB solid-track facility resulted in successful deployment, inflation, and erection of the skirt system.

7. INSTRUMENTATION SYSTEM

The major areas of consideration for instrumentation of the Mars entry capsule decelerator test vehicle include (1) requirements, (2) environments, (3) unique conditions, and (4) survey.

In government programs for expandable aerodynamic decelerator development, free-flight test data have led to development and selection of instrument systems appropriate to the Mars entry problem. Selection and optimization of components and systems usually was contingent upon results in each of the four areas. Various inputs were integrated to establish specific selections. These inputs became guidelines to support required compromise.

Major areas of investigation are outlined below to depict more directly the specific efforts of concentration that should be studied.

1. Requirements

- a. Programming - data acquisition and recovery sensing and sequence
- b. Data acquisition

(1) Electronic

Sensors - opening shock force, drag force, acceleration, test vehicle motion (inertial measuring technique), static pressure, density (ionization techniques), impact pressure, and temperature

Data recording and transmission - telemetry, magnetic tape, stored and delayed telemetry, and direct

Photographic - a separate discussion

- c. Timing and time synchronization
- d. Radar tracking
- e. Destruct systems
- f. Search and location
- g. Power
- 2. Environments
 - a. Altitude
 - b. Acceleration
 - c. Temperature
 - d. Aerodynamic heating
- 3. Unique conditions
 - a. Measurement by decelerator attachment influence on shock and drag force
 - (1) Strain gage sensors - wire and semiconductor
 - (2) Capacity, inductance, and displacement sensors
 - b. Temperature and thermal effects
 - (1) Decelerator integrity - surface temperature, temperature gradients, and thermal energy absorption
 - (2) Structural integrity - aerodynamic heating
 - c. Altitude, density, pressure, and temperature
 - d. Search beacons - pulsed and CW systems
- 4. Surveys
 - a. Evaluation of past and current systems, subsystems, and components
 - (1) ADDPEP
 - (2) NASA free-flight tests
 - (3) Other government-sponsored FFT programs

- b. Item a devices indicating performance characteristics
 - (1) Environmental conditions encountered
 - (2) Accumulated statistical and tested reliability
 - (3) Operational history
- c. Determination of prior concepts extended to present test objectives
 - (1) Direct integration
 - (2) Modification
 - (3) Radical change
- d. Probability prediction for all suggested approaches and configurations
- e. Reliability analysis
 - (1) Component selection
 - (2) System integration
 - (3) Redundancy
- f. Probability prediction for given reliability versus economy

SECTION X - PRELIMINARY DESIGN, DEVELOPMENT, AND TESTING

1. OBJECTIVES

This section delineates work that must be accomplished for aerodynamic deceleration, stabilization, and terminal descent for a Mars entry capsule that ultimately will reach the planet's surface.

Such a deceleration system must slow the entry capsule and lower its effective ballistic coefficient to permit deployment of the terminal descent stage at a sufficiently high altitude.

Program objectives should include the following guidelines:

1. To establish engineering design details for the range of entry conditions specified and to determine the most effective means for reconfiguring and staging to achieve terminal velocity compatible with the capsule's surface-impacting subsystem
2. To establish engineering design details compatible with flight conditions
3. To establish analyses and tests

2. PRELIMINARY DESIGN

Point-mass trajectories should be computed for the vehicle deceleration system from primary decelerator deployment to surface impact. Initially, these computations should be selected from the specified entry trajectory furnished by the customer. Such combinations of initial point and decelerator ballistic coefficient must be chosen to achieve the velocity at altitude target specified by the customer. Histories of all significant flight and configuration variables for computed trajectories must be

included. Results should be analyzed for vehicle and decelerator configurations, sets of initial conditions, atmospheric model, and velocity-at-altitude targets as are requested initially in the customer's Request for Quotation (RFQ).

3. PRELIMINARY DECELERATOR ANALYSIS

Selection of the most promising decelerator should be based on preliminary aerodynamic, dynamic, structural, and design investigations. These investigations must be supported by examination of previous analyses. Shapes and dimensions then would be determined to produce the required ballistic coefficients determined in Item 2 of this section. The calculations and references used in selection must be reported and documented.

Transient thermal analysis must be conducted on primary decelerator fabrics before choices are made of fabrics and coatings that can withstand maximum calculated temperatures and heating conditions.

Pressure distribution over the primary decelerator must be determined for the operating range of Mach numbers. Results would be used to establish an optimum fabricated shape after strength analysis described in this section.

Deployment force history, including shock loading, must be computed with gas-flow rates, reference areas, and drag characteristics. The deployment sequence must be established, including time increments and limits.

The dynamic motion of the composite vehicle and decelerator be determined. Acceleration and angular motions must be determined through evaluation similar in scope to that described for the point-mass trajectories.

Detailed preliminary engineering design drawings showing the decelerator, packaged and deployed, must be provided to the customer. These

would include detailed construction features. The equipment required for deployment sequence also must be presented.

Dynamic loads on the decelerator must be determined. The snatch load of the vehicle and decelerator connector would be based on prior testing of similar decelerators. After all loads are determined, critical or significant components must be analyzed structurally.

Decelerator weight must be determined according to structural analysis and geometric arrangement.

4. DEVELOPMENT PROGRAM

a. Five Phases

A development program could be divided into five phases: (1) analysis of preliminary design, (2) scale-model design and fabrication, (3) model testing, (4) full-scale system design, and (5) fabrication and flight testing of a full-scale system.

Work should be organized to provide maximum design data and to permit interphase branching.

Scheduled progress reporting during each phase with final reporting at the conclusions of each phase would provide suitable documentation.

After Phase V, a complete program report must be provided.

b. Phase I - Test Evaluation of Decelerator Models

Wind tunnel tests should be conducted on a solid model of the decelerator shape established in preliminary design. Tests should provide pressure distribution, drag coefficient, and moment analysis of the models at simulated Martian dynamic pressure and at atmospheric density. A solid, small-scale model should be fabricated and instrumented for measurement of moment and pressure distribution in wind-tunnel tests. Tests should duplicate dynamic loading and

density extremes of the projected Martian atmosphere as closely as possible.

c. Phase II - Test Evaluation of Larger-Scale Model

A model of approximately four-foot overall diameter should be designed and fabricated reflecting Phase I results and analytical studies of the preliminary design. Wind-tunnel tests, at simulated Martian dynamic and atmospheric pressures, should be conducted to evaluate deployment, stability, drag-time history, and general design.

d. Phase III - System Design and Mockup Testing

A decelerator system incorporating recommended modification of the Phase II configuration should be engineered and designed.

System engineering analysis must ensure decelerator system compatibility with the entry capsule and spacecraft bus. All flight environments including sterilization cycling will be included in these analyses. After analysis, a complete decelerator system design should be made and complete working drawings prepared.

A full-scale functional mockup of this design then should be fabricated, with sufficient detail and durability to be used for design aid, for evaluating packaging and deployment, and for drop testing in Phase IV.

The mockup should be tested in a laboratory to determine the best packaging and deployment techniques. Mockup dimensions should be checked to verify fabrication procedures.

A report should delineate the work performed and solutions to problems encountered in Phase III.

e. Phase IV - Air-Drop Test

The functional mockup, incorporating the best packaging and deployment design determined in Phase III, should be dropped from a C-130

aircraft. Decelerator deployment staging should be accomplished at preset dynamic pressure.

Instrumentation, checkout, and ground-handling equipment should be fabricated and the functional mockup tested for operational readiness before shipment to the test site. Controls should be provided for deploying each decelerator stage at the desired velocity.

The mockup should be dropped from an aircraft to examine deployment, inflation, and correlation with model test data. Data on deployment, deceleration, and stability should be recorded and evaluated and a report prepared encompassing work conducted in Phase IV.

f. Phase V - Flight Test

A flight test plan should establish full-scale balloon-launch testing and reduced-scale rocket-launch testing of the decelerator system at earth altitudes where the atmospheric density closely approximates that of the anticipated Mars entry environment.

Spacecraft and AGE must be fabricated to support the flight test plan.

A field-test crew must be assigned for assembly, checkout, and launch of the spacecraft.

Flight tests should be conducted according to the initial plan. Flight test data must be recorded and evaluated.

A final report should be made of all program phases and final design for follow-on qualification and flight acceptance tests.

5. SCHEDULE

A schedule for preliminary design and development (Figure 105) shows total work area in each phase with a number of stations for complete review of decelerator performance. The schedule also provides firm checkpoints for control of schedule and expenditures.

The schedule permits complete program performance within 24 months,

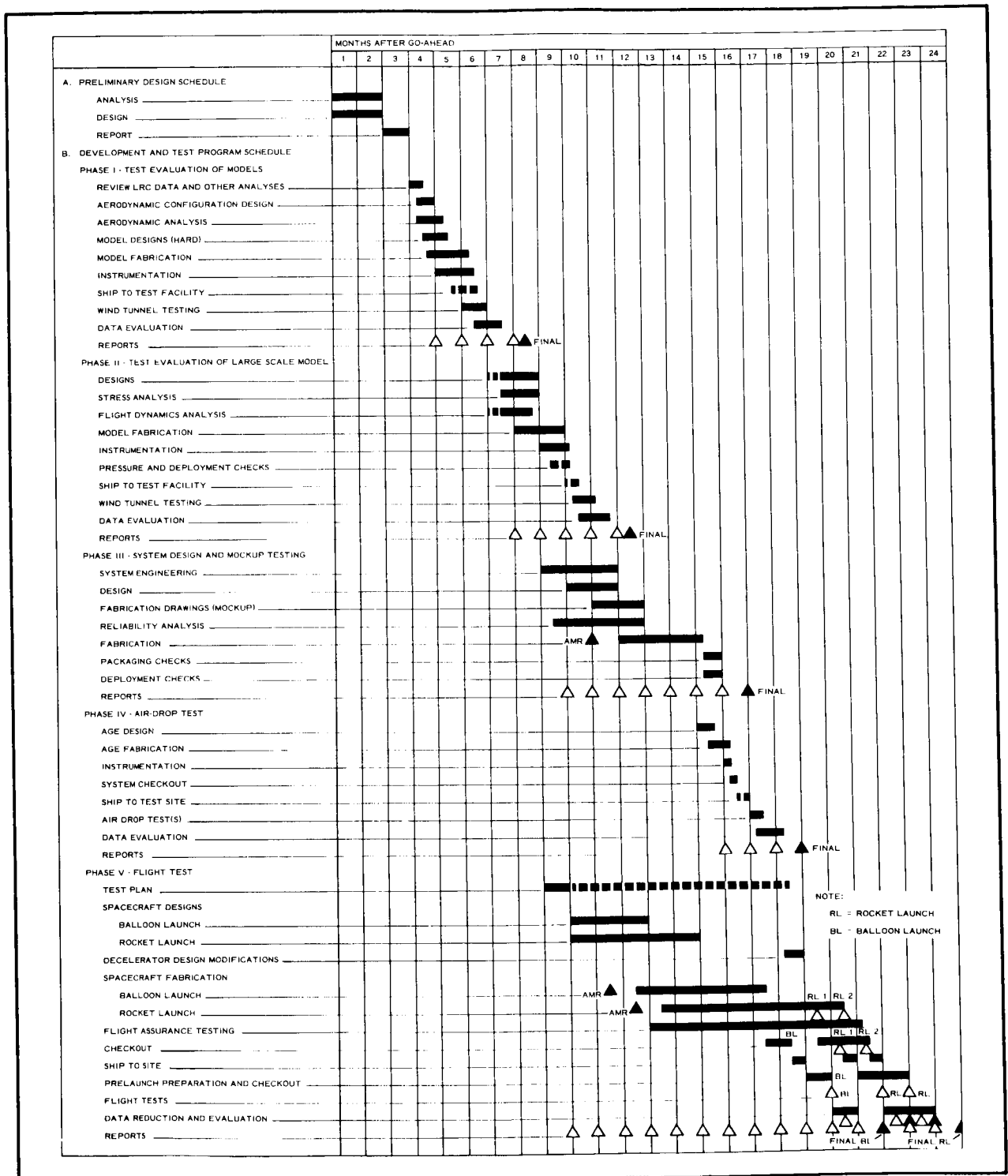


Figure 105 - Preliminary Program Schedule

making it compatible with the Voyager program freeze date for selection of configuration and subsystems.

PERT/time and PERT/cost controls should begin with Phase III. The PERT controls then would include the remainder of Phase II.

Technical briefings are scheduled at major technical decision points. More briefings could be added.

Field operations for the program include three distinct testing operations: wind-tunnel, air-drop, and flight.

Wind-tunnel testing could be performed at either NASA or Air Force facilities. An engineer associated with decelerator analysis should be assigned to supervise these tests, assisted by test technicians in setup and data recording.

Air-drop testing could be conducted with C-130 aircraft flown from Air Force Missile Test and Development Center, Holloman AFB, N. M. Radar and optical tracking and telemetry would record data. A decelerator systems test engineer as supervisor, an instrumentation and electrical engineer, and two test technicians should make up the field crew.

Flight testing could be conducted at the White Sands Missile Range. Because of the small number of flights, the same crew should conduct rocket and balloon launches. A field test manager, a rocket-launch program engineer, a balloon launch program engineer, an instrumentation and electrical engineer, three technicians, and a reliability and quality-assurance engineer should make up the crew.

6. DOCUMENTATION

Informal technical status reports should be submitted monthly, reporting activities from the first of the preceding month through the first of the current month. These reports should include but not be limited to (1) a brief summary of work status at the start of the current period and (2) a

description of work performed during the preceeding month, including positive or negative results.

Formal technical reports should be submitted within 30 days after completion of each phase. These reports should contain such items as calculations, graphs, sketches, data, and photographs.

A final report, documenting and relating the results of the entire proposed program, should be submitted within 30 days after the end of the flight test phase. Operation and maintenance manuals should be written for all AGE equipment used in the flight test program. Test plans should be submitted for approval 45 days prior to the air-drop and flight-test programs.

Financial status reports should be submitted monthly by the contract administrator for the contractor.

7. CUSTOMER RESPONSIBILITIES

a. Preliminary Design Phase

It would be required that the customer furnish to the contractor the following constraints and parameters:

1. Physical profile characteristic of the Mars atmosphere
2. Entry vehicle shape, dimensions, and sub-assembly arrangements
3. Maximum allowable deceleration during deployment of auxiliary aerodynamic device
4. Ballistic Mars-atmosphere entry trajectory, to impact, of the specified entry vehicle in specified atmosphere or atmospheres, at the specified initial entry path angle
5. Initial trajectory conditions at deployment (including dynamic amplitudes and frequencies)

6. Target velocity-at-altitude combinations for significant sequencing events: secondary decelerator deployment, impact, for example. Items 5 and 6 might be determined jointly by the contractor and the customer

b. Development Program

During the development program, use of the following or similar government-owned facilities would be required:

1. Phase I - four-foot Arnold-Von Karman facility wind tunnel A
2. Phase II - sixteen-foot transonic PWT wind tunnel
3. Phase III - building space at Holloman MTDS for assembly and checkout of mockup, C-130 aircraft, and range services of radar and optical tracking, telemetry recording, and data reduction
4. Phase IV - building space at Holloman MTDS and Walker AFB for assembly and checkout of spacecraft; launch balloon, adapter, and balloon launch services at Walker AFB; launch rockets and adapter sections; rocket launcher and related equipment; and range services of radar tracking, telemetry recording, and data reduction

LIST OF SYMBOLS

- A = area
- a = acceleration (g)
- $A'_{s(1)}$ = area of any of three parts of BALLUTE
- C = coefficient
- c = specific heat of material (Btu/lb-deg F)
- \bar{c} = constant depending on gas composition
- C_{dB} = BALLUTE drag coefficient
- C_{dC} = cone drag coefficient
- C_{do} = reference drag coefficient
- C_D = drag coefficient
- CGS = center of gravity of surface
- C_{IS} =
- C_{L_α} = lift coefficient slope
- C_{M_α} = moment coefficient slope
- C_m = pitching moment coefficient
- C_{m_q} = damping derivative due to pitch rate
- $C_{m_{\dot{\alpha}}}$ = damping derivative due to angle of attack rate

C_{N_α} = normal force coefficient slope

C_n = yawing moment coefficient

C_p = pressure coefficient

C_{Pq} = pressure coefficient times dynamic pressure

d = diameter

D_B = BALLUTE drag

d_B = BALLUTE diameter

d_C = cone diameter

D_o = reference diameter

D_T = total drag

F = pole load

FS = factor of safety

f_f = fabric stress

h = altitude

I = inertia

I_{CGS} = moment of inertia about system cg

I_{vYYi} = volume mass moment of inertia about Y-Y

I_{YYi} = surface mass moment of inertia about the Y-Y axis

$$K = \frac{nT_m}{p\pi R_B^2}$$

K_c = meridian strength to weight ratio (working)

- K_f = fabric strength to weight ratio (working)
- K_m = material strength to weight ratio (ultimate)
- L = length
- m = riser length forebody diameter ratio
- M_D = deployment mach number
- N = total drag to JPL drag ratio
- N = exponent depending on gas composition
- n = number of meridians
- P, p = pressure (gage)
- P_L = local static pressure on surface
- P_I = internal pressure
- P_ℓ = surface pressure
- P_o = stagnation pressure behind normal shock (atmospheres)
- P_v = pressure energy (ft-lb)
- P_∞ = free-stream static pressure
- q = dynamic pressure; heat flux (Btu/ft^2)
- \dot{q} = heat flux rate ($\text{Btu}/\text{ft}^2\text{-sec}$)
- \dot{q}_o = stagnation point heat flux rate, ($\text{Btu}/\text{ft}^2\text{-sec}$)
- q_W = ratio of wall to total enthalpy
- R = radius
- R_B = BALLUTE radius

R_C	= cone radius
R_N	= nose radius
R_O	= reference radius
R_v	= forebody base radius
r	= energy constant
T	= gas temperature (F)
T_f	= final maximum temperature (F)
T_i	= initial temperature
T_{ℓ}	= surface temperature
T_m	= load in one meridian
T_{∞}	= ambient temperature
U_{∞}	= free-stream velocity divided by 10,000 pfs
V, v	= volume
V_B	= volume of BALLUTE
W	= weight
W_B	= weight of BALLUTE
W_C	= cone weight
W_f	= fabric weight
W_R	= weight of riser
W_T	= total system weight

w = propellant weight (lb)

$\bar{X}_{\textcircled{1}}$ = centroidal distance of any of three BALLUTE parts

x_o = distance

\bar{X}_s = BALLUTE center of gravity

\bar{X}_v = center of gravity of complete BALLUTE volume

$\bar{Y}_{\textcircled{1}}$ = centroidal distance of any of three BALLUTE parts

y_w = viscous wake half-width

γ = average weight per equal foot of BALLUTE surface

ρ_h = density at altitude

ρ = surface density

θ_s = body surface inclination

α = angle of attack

$$\rho = \frac{F}{p\pi R_B^2}$$

γ = unit weight

Δ = increment

γ = specific heat ratio

Γ = adiabatic lapse rate (K^+ /km and R /1000 ft)

θ = local surface inclination angle

δ = thickness of material (ft)

τ = time (sec)

ρ = density of material (pcf)

σ = standard deviation

LIST OF REFERENCES

1. Marvin, J. G.; and Deiwert, G. S.: Convective Heat Transfer in Planetary Gases. NASA TR R-224, July 1965.
2. Lees, L.: "Laminar Heat Transfer Over Blunt-Nosed Bodies at Hypersonic Flight Speeds," Jet Propulsion, April 1956; 259-268.
3. Champney, W. B.; Athans, J. B; and Mayerson, C. D.: A Study of Hypersonic Aerodynamic Drag Devices. WADC TR 59-324, Part II. Wright-Patterson Air Force Base, Ohio. December 1960.
4. Alexander, W. C.: Investigation to Determine the Feasibility of Using Inflatable Balloon Type Drag Devices for Recovery Applications in the Transonic, Supersonic and Hypersonic Flight Regime. ASD-TDR-62-702, Part II. Wright-Patterson Air Force Base, Ohio. October 1962.
5. JPL Voyager Capsule Flight Equipment TA and FA Test Procedures For Heat Sterilization and ETO Decontamination Compatibility, Vol - 50503-ETS. Pasadena, Calif., Jet Propulsion Laboratory, California Institute of Technology.
6. Anderson, A. R.: Effect of Biological Sterilization and Vacuum on Certain Parachute Retardation System Components. Final Rep 4324. Pasadena, Calif., Jet Propulsion Laboratory, California Institute of Technology. August 1963.
7. Chernowitz, G.; and DeWeese, J. H.: Performance of and Design Criteria for Deployable Aerodynamic Decelerators. Second major revision of USAF Parachute Handbook, ASD-TR-61-579, AD-429971, December 1963.
8. ASD-TDR-62-542: New and Improved Materials for Expandable Structures. Pasadena, Calif., Jet Propulsion Laboratories, California Institute of Technology. June 1962.
9. AEDC TR-65-218: Drag Characteristics of Three BALLUTE Decelerators in the Wake of the ALARR Payload at Mach Numbers 2 to 4. Arnold Air Force Station, Tenn. Arnold Engineering Development Center. 1965.

10. AEDC TDR-63-119: Performance of Flexible Aerodynamic Decelerators at Mach Numbers from 1.5 to 6. Arnold Air Station, Tenn. Arnold Engineering Development Center. 1963.
11. Alexander, W. C.: Investigation to Determine the Feasibility of Using Inflatable Balloon Type Drag Devices for Recovery Applications in the Transonic, Supersonic, and Hypersonic Flight Regime. Part II. Mach 4 to Mach 10 Feasibility Investigation. Akron, Ohio. Goodyear Aircraft Corp. ASD TDR-62-704. December 1965.
12. Charczenko, N.: Aerodynamic Characteristics of Towed Spheres, Conical Rings and Cones Used as Decelerators at Mach Numbers from 1.57 to 4.65. TND-1789. NASA, April 1963.
13. Charczenko, N.; and McShera, J. T.: Aerodynamic Characteristics of Towed Cones Used as Decelerators at Mach Numbers from 1.57 to 4.65. TND-994. NASA, December 1965.
14. Altgelt, R.: Gemini BALLUTE System Development. GER-11538 Akron, Ohio. Goodyear Aerospace Corporation. January 1965.
15. GER-11665: Aerodynamic Deployable Decelerator Performance Evaluation Program. Akron, Ohio. Goodyear Aerospace Corporation.
16. AEDC-TR-65-266: The Characteristics of a BALLUTE in the Wake of the Martin Fullscale SV-5D Vehicle at Mach Numbers from 0.6 to 2.9. Arnold Air Station, Tenn. Arnold Engineering Development Center. 1965.
17. AEDC-TR-64-131: Gemini BALLUTE Structural Test at Mach Numbers 0.55 and 1.92. Arnold Air Station, Tenn. Arnold Engineering Development Center. 1964.
18. McShera, J. T.: Aerodynamic Drag and Stability Characteristics of Towed Inflatable Decelerators at Supersonic Speeds. TND-1601. NASA.
19. GER-11762: BALLUTE Evaluation Program for Project Sleigh Ride. Akron, Ohio. Goodyear Aerospace Corporation.

APPENDIX A - DETAILED ANALYSIS OF DECELERATORS

1. STRUCTURAL AND WEIGHT ANALYSES

a. General

Weight calculations for several fabric decelerators for a Mars entry capsule are contained in this appendix. Decelerators described are: trailing BALLUTES; enveloping BALLUTES, plain and tucked back; attached skirts; and AIRMAT cone. This work was done to assist in evaluation of these configurations and to assist in selection of designs to be studied in more detail.

The weights of the fabric decelerators are functions of the drag increase, the deployment conditions, the vehicle size and weight, and the strength of the selected materials. No allowances are included for the container weights, ejection systems, construction details, and inflation system if used. The effects of these omitted items are to be included in the analysis of the selected designs.

b. Trailing BALLUTES

The weight equation^a for a plain-back BALLUTE is

$$W_B = P \frac{\pi}{8} d_B^3 \left[\frac{4(1 - K)}{K_f} + \frac{2\pi K}{K_c} \right], \quad (A-1)$$

where

$$P = C_p q, \quad (A-2)$$

^aAlexander, W. C.: Investigation to Determine the Feasibility of Using Inflatable Balloon-Type Drag Devices for Recovery Applications in the Transonic, Supersonic, and Hypersonic Flight Regimes, Part II, Mach 4 to Mach 10 Feasibility Investigation. ASD-TDR-62-702, December 1962, p 140.

$$q = \frac{aW_T}{C_{do} \pi \frac{(d_o)^2}{4}} \quad (A-3)$$

$$D_o = C_{do} q \pi \frac{(d_o)^2}{4}, \text{ and} \quad (A-4)$$

$$aW_T = C_{do} q \pi \frac{(d_o)^2}{4}. \quad (A-5)$$

In these equations,

P = pressure (gage),

C_p = pressure coefficient,

q = dynamic pressure,

a = acceleration (g's),

W_T = total system weight,

C_{do} = reference drag coefficient,

D_o = reference drag, and

d_o = reference diameter.

The equation for vehicle drag with decelerator deployed, as a function of the basic vehicle drag, is

$$D_T = ND_o \quad (A-6)$$

or

$$D_T = D_o + D_B, \quad (A-7)$$

when

D_T = total drag,

N = total drag to JPL capsule drag ratio,

D_B = BALLUTE drag load, and

D_o = reference drag;

then

$$D_B = (N - 1)D_o . \quad (A-8)$$

BALLUTE drag is expressed as

$$D_B = C_{dB} \pi q \frac{(d_B)^2}{4} \quad (A-9)$$

when

(d_B) = BALLUTE diameter, and

C_{dB} = BALLUTE drag coefficient.

With C_{dC} = coefficient of cone drag, let

$$C = \frac{C_{dB}}{C_{do}} \quad (A-10)$$

or

$$C = \frac{C_{dC}}{C_{do}} ; \quad (A-11)$$

then, substitution in Equation A-9 and Equations A-4, A-8, and A-10 produces

$$(N - 1) \left[C_{do} \pi q \frac{(d_o)^2}{4} \right] = C \left(C_{do} \pi q \frac{d_B^2}{4} \right) ,$$

and

$$d_B = \sqrt{\frac{N - 1}{C}} d_o . \quad (A-12)$$

Substitution in Equation A-1 the values from Equations A-2, A-5, and A-12 produces the equations:

$$W_B = \frac{C_p a W_T}{C_{do} \pi \frac{(d_o)^2}{4}} \left(\sqrt{\frac{N-1}{C}} d_o \right)^3 \frac{\pi}{8} \left[\frac{4(1-K)}{K_f} + \frac{2\pi K}{K_c} \right],$$

and

$$\frac{W_B}{a W_T} = \frac{C_p d_o}{2 C_{do}} \sqrt{\left(\frac{N-1}{C} \right)^3 \left[\frac{4(1-K)}{K_f} + \frac{2\pi K}{K_c} \right]}, \quad (A-13)$$

when

$$K = \frac{n T_m}{p \pi (R_B)^2},$$

n = number of meridians,

T_m = load on one meridian,

R_B = BALLUTE radius,

K_c = meridian strength-weight ratio (working), and

K_f = fabric strength-weight ratio (working).

With an additional factor of safety (FS) on the riser and assuming the riser to be made of the same material as the meridians with a riser length of "m" JPL diameters, a weight equation for the riser becomes:

$$W_R = \frac{D_B m d_o (FS)}{K_c}. \quad (A-14)$$

From Equations A-4, A-5, and A-8, where m = riser length fore-body diameter ratio,

$$D_B = a W_T (N-1), \quad (A-15)$$

$$W_R = \frac{aW_T(FS)md_o}{K_c} (N - 1) ,$$

and

$$\frac{W_R}{aW_T} = \frac{(FS)(m)(d_o)}{K_c} (N - 1) . \quad (A-16)$$

The total weight of the BALLUTE and riser is found by adding Equations A-13 and A-16.

$$\frac{W_B + W_R}{aW_T} = d_o(N - 1) \left\{ \frac{C_p}{2C_{do}} \sqrt{\frac{N - 1}{C^3}} \left[\frac{4(1 - K)}{K_f} + \frac{2\pi K}{K_c} \right] + \frac{FSm}{K_c} \right\} . \quad (A-17)$$

Equation A-17 gives the weight of a trailing BALLUTE and riser line as a function of the deployment conditions, basic body diameter and weight, the desired drag increase, and BALLUTE material.

c. Enveloping BALLUTES

(1) Plain-Back BALLUTE

The weight of a plain-back BALLUTE is given by Equation A-1. Equations A-2 through A-8 also are applicable to plain-back enveloping BALLUTES. The additional drag from the BALLUTE is given by the following equation,

$$D_B = C_{dB}\pi q \frac{(d_B)^2 - (d_o)^2}{4} . \quad (A-18)$$

Substitution of Equations A-4, A-10, and A-16 into A-8 yields

$$C(C_{do}\pi q) \frac{(d_B)^2 - d_o^2}{4} = (N - 1)C_{do}q\pi \frac{d_o^2}{4} ,$$

$$C(d_B^2 - d_o^2) = (N - 1)d_o^2 ,$$

and

$$d_B = \sqrt{\frac{(N + C - 1)}{C}} d_o . \quad (A-19)$$

Substitution from Equations A-2, A-5, and A-19 into Equation A-8 produces:

$$W_B = \frac{C_p a W_T}{C_d \pi \frac{d_o^2}{4}} d_o^3 \sqrt{\left(\frac{N + C - 1}{C}\right)^3} \frac{\pi}{8} \left[\frac{4(1 - K)}{K_f} + \frac{2\pi K}{K_c} \right]$$

and

$$\frac{W_B}{a W_T} = \frac{C_p d_o}{2 C_{do}} \sqrt{\left(\frac{N - 1}{C} + 1\right)^3} \left[\frac{4(1 - K)}{K_f} + \frac{2\pi K}{K_c} \right] . \quad (A-20)$$

(2) Tucked-Back BALLUTES

The weight equation for a tucked-back BALLUTE, whose configuration fits the JPL capsule sketched in JPL Drawing J-141989, is developed in Item 2 of this appendix.

The equation is

$$W_B = P \pi \frac{(d_B)^3}{8} \left[\frac{1.29(0.537 - K)}{K_f} + \frac{2.15 K}{K_c} \right] . \quad (A-21)$$

Substitution of Equations A-2, A-5, and A-19 into Equation A-21 gives:

$$W_B = \frac{C_p a W_T}{C_{do} \pi \frac{d_o^2}{4}} d_o^3 \sqrt{\left(\frac{N - 1}{C} + 1\right)^3} \frac{\pi}{8} \left[\frac{1.29(0.537 - K)}{K_f} + \frac{2.15 K}{K_c} \right] ,$$

and

$$\frac{W_B}{a W_T} = \frac{C_p d_o}{2 C_{do}} \sqrt{\left(\frac{N - 1}{C} + 1\right)^3} \left[\frac{1.29(0.537 - K)}{K_f} + \frac{2.15 K}{K_c} \right] . \quad (A-22)$$

BALLUTE weight is a function of deployment conditions, material properties, total capsule weight, and drag ratio; that is, total drag to JPL drag.

d. AIRMAT Cone Decelerator

A weight equation for an AIRMAT cone decelerator with a half-cone angle of θ and a half-taper angle of ϕ is developed in Item 2.

The equation is:

$$W_C = \frac{6(FS)P}{K_M} \frac{\pi}{8} \left(\frac{\cos \phi}{\sin \theta} \right)^2 \cos \phi (\tan \theta - \tan \phi) (d_C^3 - d_o^3), \quad (A-23)$$

where

K_M = material strength-weight ratio (ultimate), and

d_C = cone diameter.

Substitution from Equations A-2, A-5, and A-19 into Equation A-23 gives the weight of the cone as a function of deployment conditions, material properties, total weight of the capsule, and drag ratio; that is, total drag to JPL drag. The equation becomes

$$\frac{W_C}{aW_T} = \frac{3(FS)C_{p_o}d_o}{K_M C_{d_o}} \left(\frac{\cos \phi}{\sin \theta} \right)^2 \cos \phi (\tan \theta - \tan \phi) \left[\sqrt{\left(\frac{N-1}{C} + 1 \right)^3} - 1 \right]. \quad (A-24)$$

e. Decelerator Comparison

Equation A-17 is evaluated for two cases of trailing BALLUTES. Numerical values are listed below:

For a riser four diameters in length, values are:

$$C = 0.8,$$

$$C_{d_o} = 1.45,$$

$$C_p = 2.75,$$

$$d_o = 12 \text{ ft},$$

$$FS = 2.0,$$

$$K = 0.6,$$

$$\left. \begin{array}{l} K_c = 24,900 \text{ ft} \\ K_f = 17,700 \text{ ft} \end{array} \right\} \begin{array}{l} 37,500 \text{ ft} \\ 26,700 \text{ ft} \end{array} \left. \begin{array}{l} 600 \text{ F Nomex} \\ 350 \text{ F Dacron, and} \end{array} \right\}$$

$$m = 4.0.$$

For a riser eight diameters in length, values are

$$C = 0.9,$$

$$C_{do} = 1.45,$$

$$C_p = 2.75,$$

$$d_o = 12 \text{ ft},$$

$$FS = 2.0,$$

$$K = 0.6,$$

$$\left. \begin{array}{l} K_c = 24,900 \text{ ft} \\ K_f = 17,700 \text{ ft} \end{array} \right\} \begin{array}{l} 37,500 \text{ ft} \\ 26,700 \text{ ft} \end{array} \left. \begin{array}{l} 600 \text{ F Nomex} \\ 350 \text{ F Dacron, and} \end{array} \right\}$$

$$m = 8.0.$$

Solving Equation A-17 for BALLUTE fabric weight as a function of total BALLUTE weight produces the equation,

$$\frac{W_f}{W_B + W_R} = \frac{\left[\sqrt{\frac{N-1}{C^3}} \frac{4(1-K)}{K_f} \right] \frac{C_o}{2C_{do}}}{\frac{C_p}{2C_{do}} \left[\sqrt{\frac{N-1}{C^3}} \left[\frac{4(1-K)}{K_c} + \frac{2\pi K}{K_c} \right] + \frac{(FS)m}{L_c} \right]}. \quad (A-25)$$

Equation A-12 in nondimensional form becomes

$$\frac{d_B}{d_o} = \sqrt{\left(\frac{N-1}{C}\right)} . \quad (A-26)$$

Equations A-25 and A-26 also can be evaluated for two types of trailing BALLUTES (see Figures A-1 and A-2).

Equation A-20 can be evaluated for a plain-back BALLUTE using the following data:

$$\begin{aligned} C &= 0.90, \\ C_{do} &= 1.45, \\ C_p &= 2.75, \\ d_o &= 12 \text{ ft}, \\ K &= 0.6, \text{ and} \\ \left. \begin{array}{l} K_c = 24,900 \text{ ft} \\ K_f = 17,700 \text{ ft} \end{array} \right\} &\left. \begin{array}{l} 37,500 \text{ ft} \\ 26,700 \text{ ft} \end{array} \right\} \begin{array}{l} 600 \text{ F Nomex} \\ 350 \text{ F Dacron.} \end{array} \end{aligned}$$

Equation A-19 becomes, in nondimensional form:

$$\frac{d_B}{d_o} = \sqrt{\frac{N-1}{C} + 1} . \quad (A-27)$$

Solving Equation A-20 for BALLUTE fabric weight as a function of total BALLUTE weight produces the following equation (see Figure A-3),

$$\begin{aligned} \frac{W_f}{W_B} &= \frac{\frac{4(1-K)}{K_f}}{\frac{4(1-K)}{K_f} + \frac{2\pi K}{K_c}} \\ &= 0.38 . \end{aligned}$$

Equation A-22 for a tucked-back BALLUTE is evaluated using the following data:

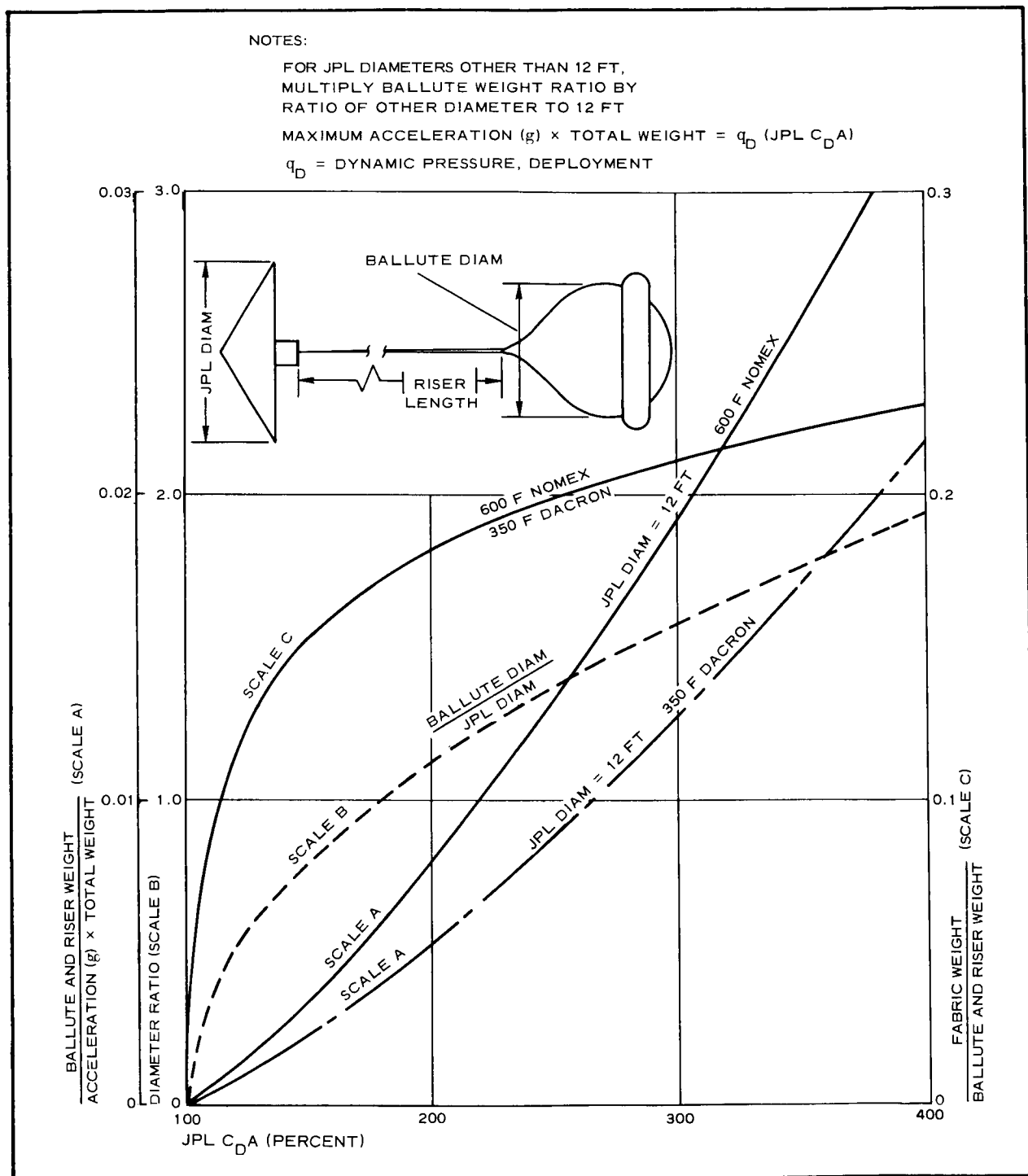


Figure A-1 - Trailing BALLUTE Weight, Ram-Air Inflation, Riser Length of Four JPL Diameters

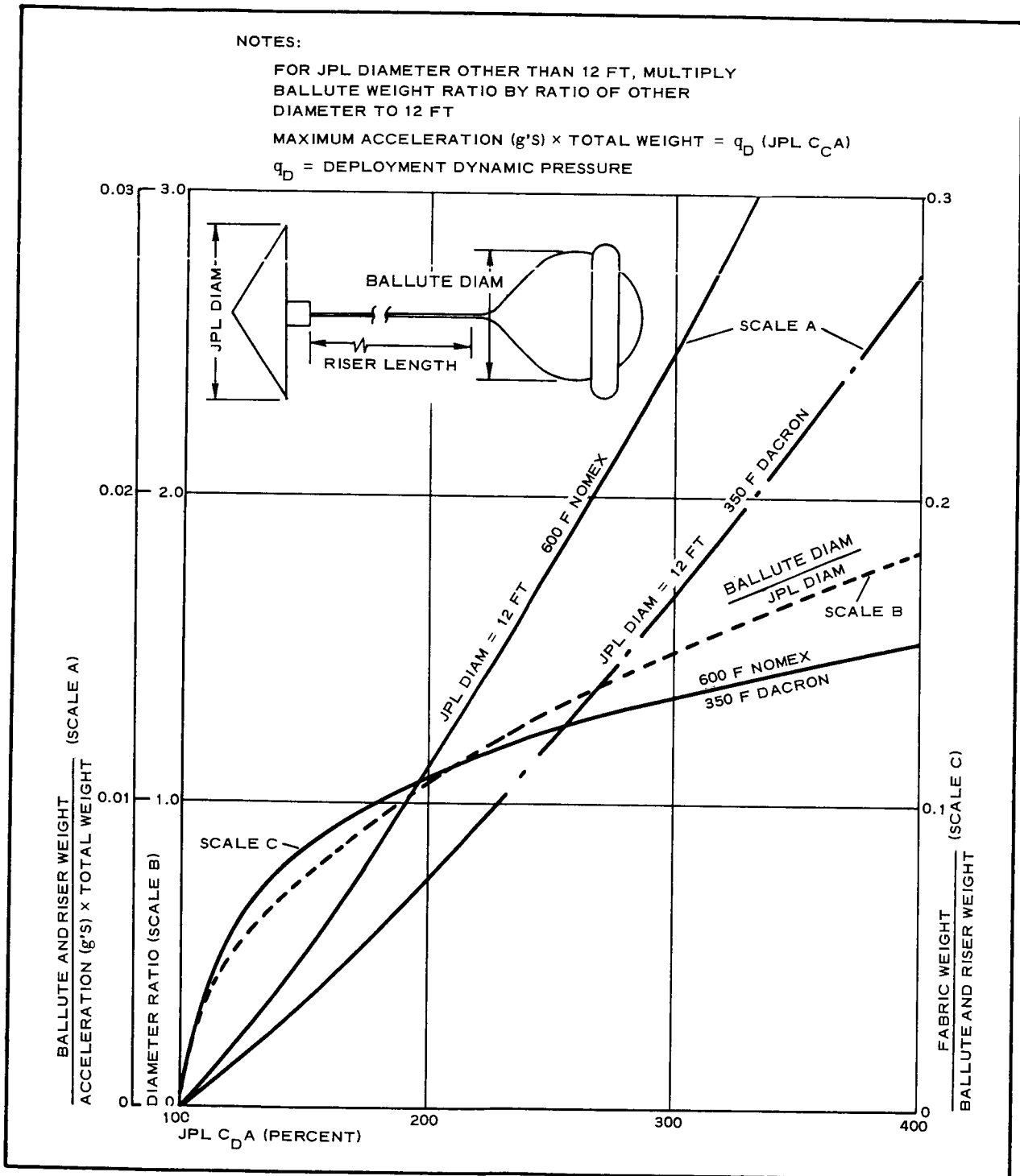


Figure A-2 - Trailing BALLUTE Weight Ram-Air Inflation, Riser Length of Eight JPL Diameters

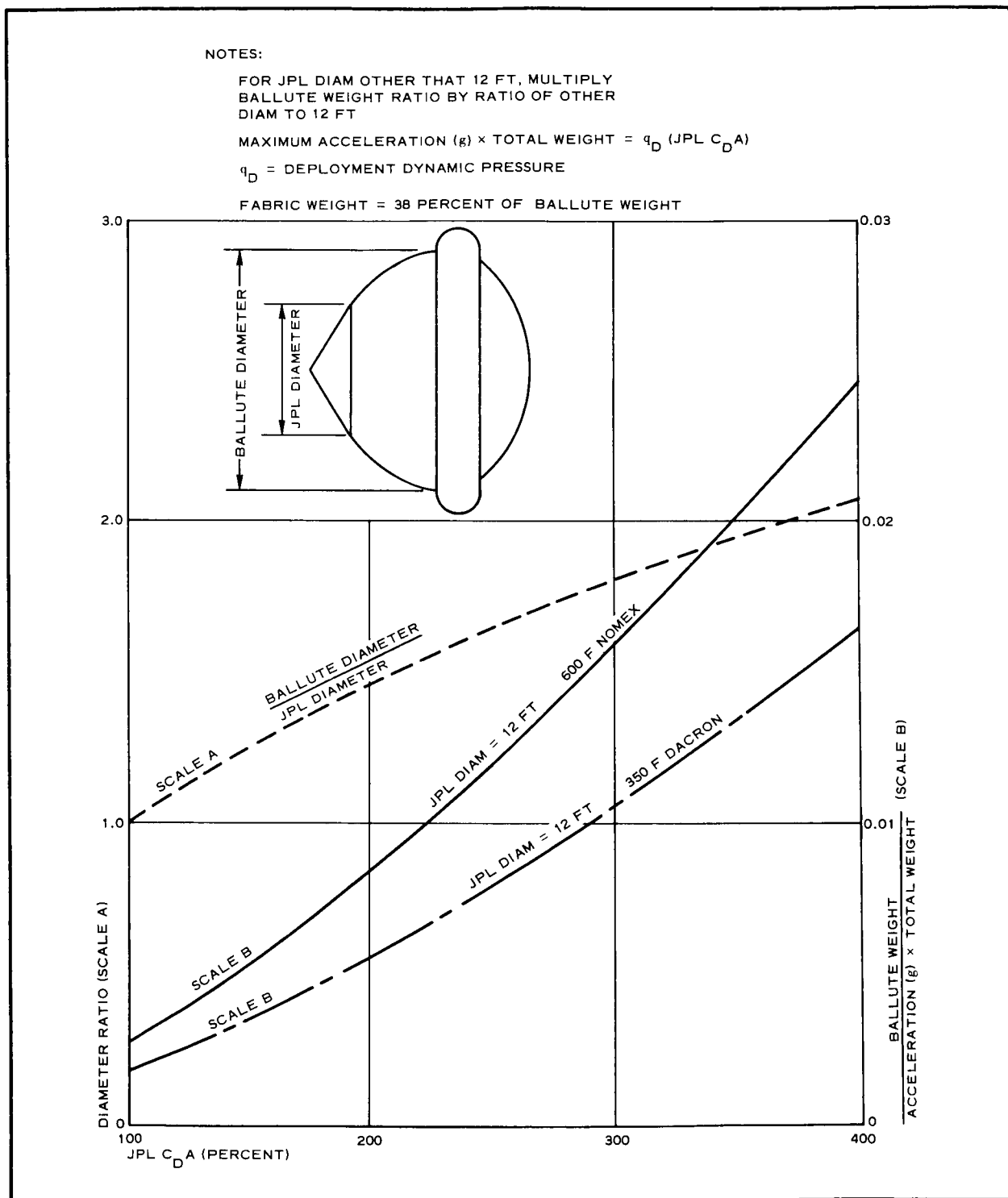


Figure A-3 - Enveloping BALLUTE Weight with Ram-Air Inflation

$$C = 0.61,$$

$$C_{do} = 1.45,$$

$$C_p = 2.75.$$

$$d_o = 12 \text{ ft},$$

$$K = \rho = 0.475. \text{ and}$$

$$\left. \begin{array}{l} K_c = 24,900 \text{ ft} \\ K_f = 17,700 \text{ ft} \end{array} \right\} \begin{array}{l} 37,500 \text{ ft} \\ 26,700 \text{ ft} \end{array} \left. \begin{array}{l} 600 \text{ F Nomex} \\ 350 \text{ F Dacron,} \end{array} \right\}$$

where

$$\rho = \frac{F}{P\pi R_B^2}.$$

When Equation A-27 is used for the diameter ratio, solving Equation A-22 for BALLUTE fabric weight as a function of total BALLUTE weight produces the equation (see Figure A-4),

$$\frac{W_f}{W_B} = \frac{\frac{1.29(0.537 - K)}{K_f}}{\frac{1.29(0.537 - K)}{K_f} + \frac{2.15 K}{K_c}} \approx 0.10.$$

Equation A-24 for the AIRMAT cone decelerator can be evaluated using the following data (see Figure A-5),

$$C = 1.0,$$

$$C_{do} = 1.45,$$

$$C_p = 1.45,$$

$$d_o = 12 \text{ ft},$$

$$FS = 2.0,$$

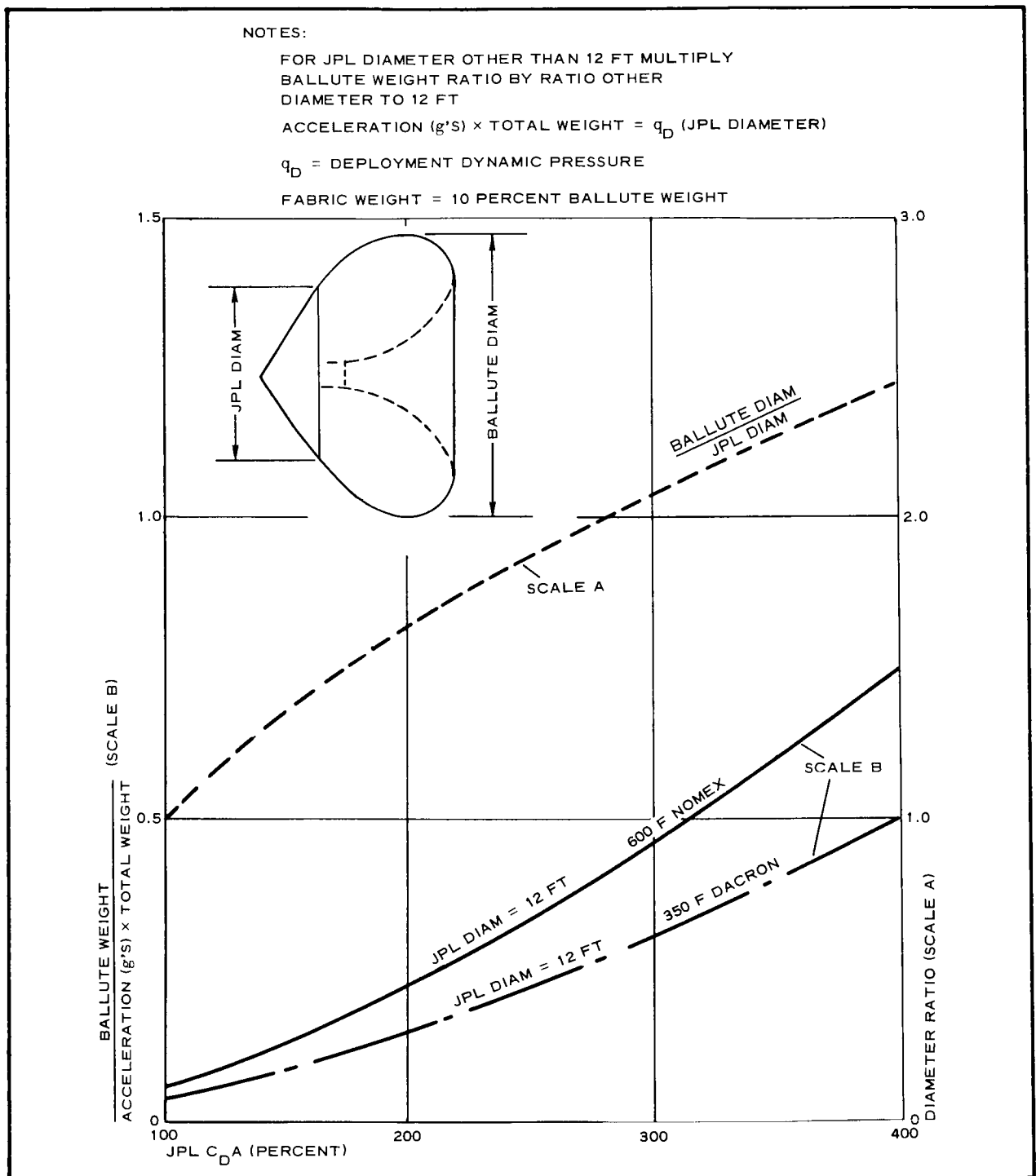


Figure A-4 - Enveloping BALLUTE Weight, Ram-Air Inflation,
Tucked-Back Without Burble Fence

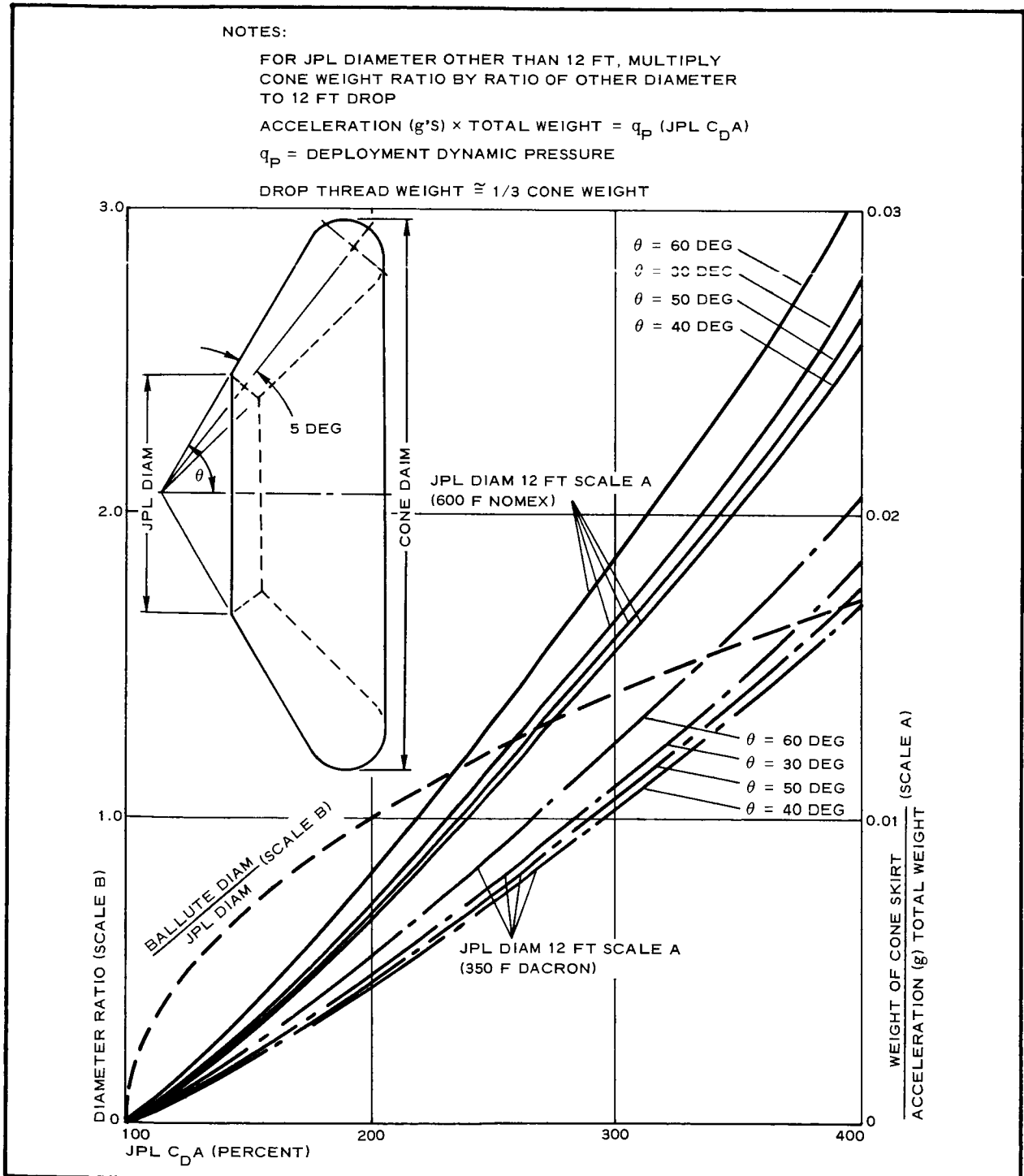


Figure A-5 - Conical AIRMAT Skirt Weight Analysis
(without Inflation-System Weight)

$$K_M = 35,000 \text{ ft (600 F Nomex), } 52,800 \text{ ft (350 F Dacron),}$$

$$\phi = 5 \text{ deg, and}$$

$$\theta = 60, 50, 40, \text{ and } 30 \text{ deg.}$$

2. WEIGHT EQUATIONS

a. Tucked-Back BALLUTE

The weight equations for the tucked-back BALLUTE, whose configuration fits the sketched shape of the JPL capsule, have been calculated by selecting isotenoid curves that fit a small-scale layout of the capsule back.^a The resulting shape has a drag ratio of about 2.25. Although the weight equations are for this specific design, the drag ratio is near the middle of the range of interest. Therefore, these weight equations are considered general weight equations for this decelerator. The profile used in developing the equations is presented to scale in Figure A-6. In this illustration;

$$\rho = \frac{F}{P\pi(R_B)^2},$$

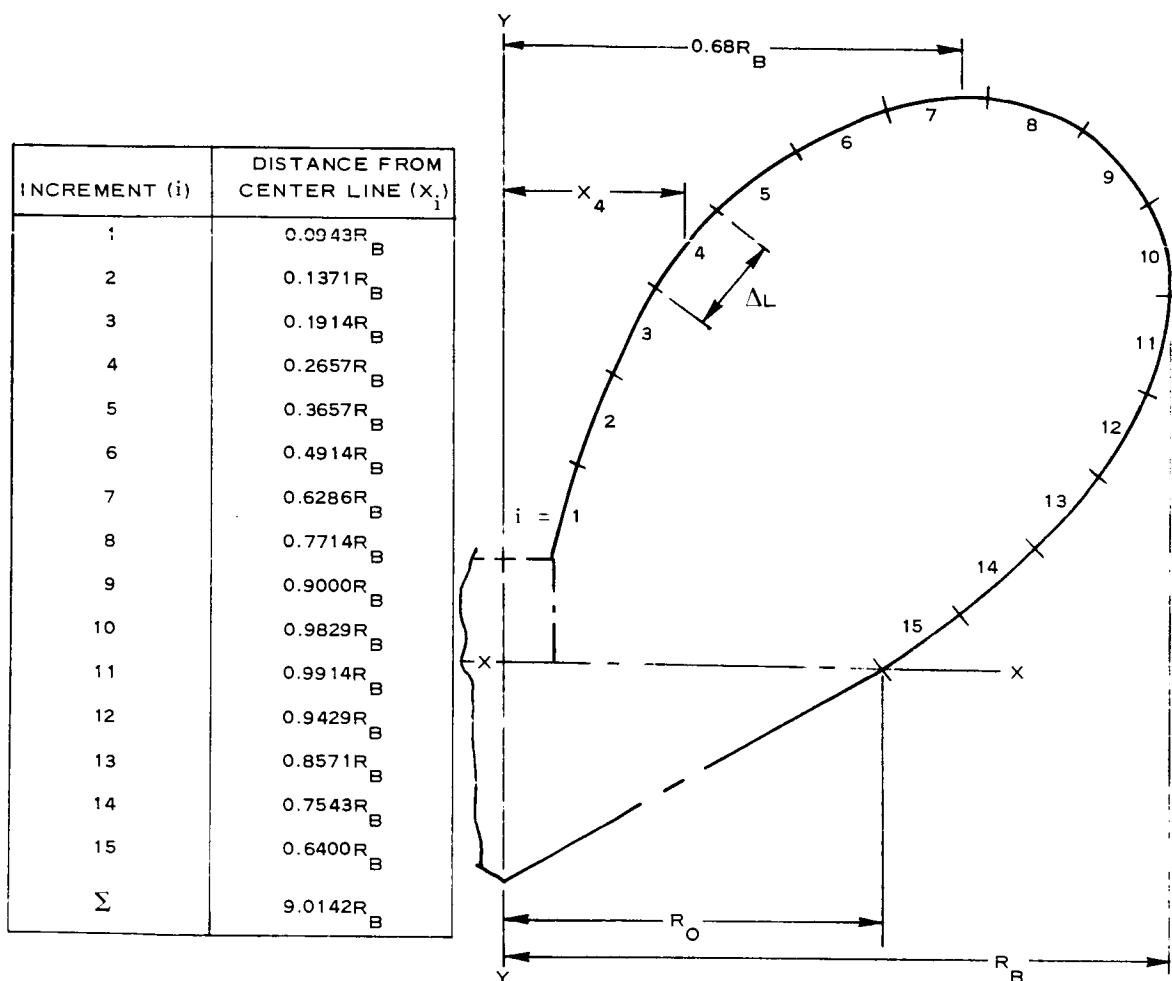
F = pole load, and

L_M = meridian length.

Thus, the centroid of meridian length becomes

$$\begin{aligned} X_L &= \frac{(0.143R_B)(9.0142R_B)}{2.145R} \\ &= 0.601R_B. \end{aligned} \tag{A-28}$$

^aHoutz, N. E.: "Optimization of Inflatable Drag Devices by Isotenoid Design," AIAA Paper 64-437.



REAR HALF

$$K = 0.95$$

$$\frac{\rho}{K} = 1.0$$

$$K = \rho = 0.475$$

FRONT HALF

$$K = 0.475$$

$$\Delta L = 0.143R_B$$

$$L_M = 15 (0.143R_B)$$

$$= 2.14R_B$$

$$\text{USE } L_M = 2.15 R_B$$

Figure A-6 - Tucked-Back BALLUTE Profile

The surface area of a body of revolution is equal to the product of meridian length and centroidal perimeter. This can be expressed as

$$\begin{aligned} A_s &= 2\pi(0.601R)(2.15R) \\ &= 8.112R^2 . \end{aligned} \quad (A-29)$$

The fabric stress is calculated at radius R_B by noting that the rear half of the BALLUTE curve is tangent to a line parallel to the X axis at a value of $X = 0.68R_B$.

Summing forces in the Y direction produces

$$2f_f\pi R_B + nTm = \pi P \left[R_B^2 - (0.68R_B)^2 \right]$$

or

$$2f_f + \frac{nTm}{\pi R_B} = R_B P (1 - 0.68^2) ,$$

when f_f = fabric stress.

Thus, with

$$K = \frac{nTm}{P\pi R_B^2}$$

and

$$PKR_B = \frac{nTm}{\pi R_B} ,$$

fabric stress can be expressed as

$$f_f = \frac{PKR_B}{2} (0.537 - K) . \quad (A-30)$$

Fabric weight is

$$\begin{aligned}
 W_f &= \frac{f_f A_s}{K_f} \\
 &= \frac{8.12(R_B)^2 \left(\frac{PR_B}{2} \right) (0.537 - K)}{K_f} \\
 &= \frac{4.06R_B^3 P(0.537 - K)}{K_f} \quad . \quad (A-31)
 \end{aligned}$$

Tension in a meridian is

$$T_m = \frac{K\pi R_B^2 P}{n}$$

and weight of the meridians is

$$\begin{aligned}
 W_c &= \frac{nT_m L_m}{K_c} \\
 &= \frac{K\pi R_B^3 P 2.15}{K_c} \quad . \quad (A-32)
 \end{aligned}$$

Thus, BALLUTE weight is

$$\begin{aligned}
 W_B &= W_f + W_c \\
 &= P\pi R_B^3 \left[\frac{1.29(0.537 - K)}{K_f} + \frac{2.15K}{K_c} \right] \\
 &= P\pi \frac{(d_B)^3}{8} \left[\frac{1.29(0.537 - K)}{K_f} + \frac{2.15K}{K_c} \right] \quad . \quad (A-33)
 \end{aligned}$$

b. AIRMAT Cone Decelerator

Weight equations for the AIRMAT cone decelerator are given below, based on geometry shown in Figure A-7.

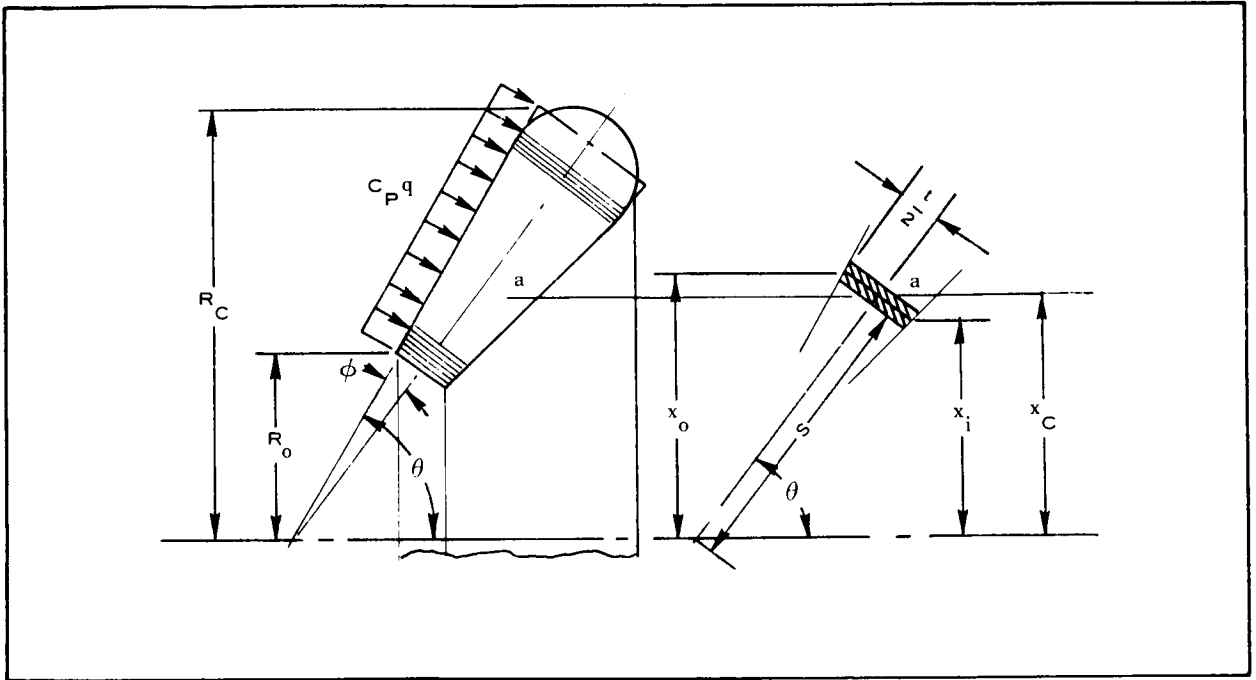


Figure A-7 - AIRMAT Cone Geometry

The weight of a pressurized isotenoid AIRMAT is given by the equation

$$W = \frac{3 \, p \, v \, F S}{K_m} \quad (A-34)$$

Expressions v and p for the AIRMAT cone (see Figure A-7) are developed in the following manner:

$$\frac{t}{2} = S \tan \phi, \quad (A-35)$$

$$S = \frac{x_c}{\sin(\theta - \phi)}, \quad (A-36)$$

$$\frac{t}{2} = \frac{x_c \tan \phi}{\sin(\theta - \phi)}, \quad (A-37)$$

$$\begin{aligned}
 x_o &= x_c + \frac{t}{2} \cos (\theta - \phi) \\
 &= x_c \left[1 + \frac{\tan \phi}{\tan (\theta - \phi)} \right],
 \end{aligned}
 \tag{A-38}$$

and

$$\begin{aligned}
 x_i &= x_c - \frac{t}{2} \cos (\theta - \phi) \\
 &= x_c \left[1 - \frac{\tan \phi}{\tan (\theta - \phi)} \right].
 \end{aligned}
 \tag{A-39}$$

The volume increment (dv) (see Figure A-8) can be expressed in the terms,

$$dv = 2\pi x_c t dS,$$

$$dS = \frac{dx_c}{\sin (\theta - \phi)},$$

$$dv = \frac{4\pi x_c^2 \tan \phi dx_c}{\sin^2 (\theta - \phi)},$$

and

$$v = \int_B^A \frac{4\pi x_c^2 \tan \phi dx_c}{\sin^2 (\theta - \phi)},$$

when

$$A = \frac{R_c}{1 + \frac{\tan \phi}{\tan (\theta - \phi)}}$$

and

$$B = \frac{R_o}{1 + \frac{\tan \phi}{\tan (\theta - \phi)}}.$$

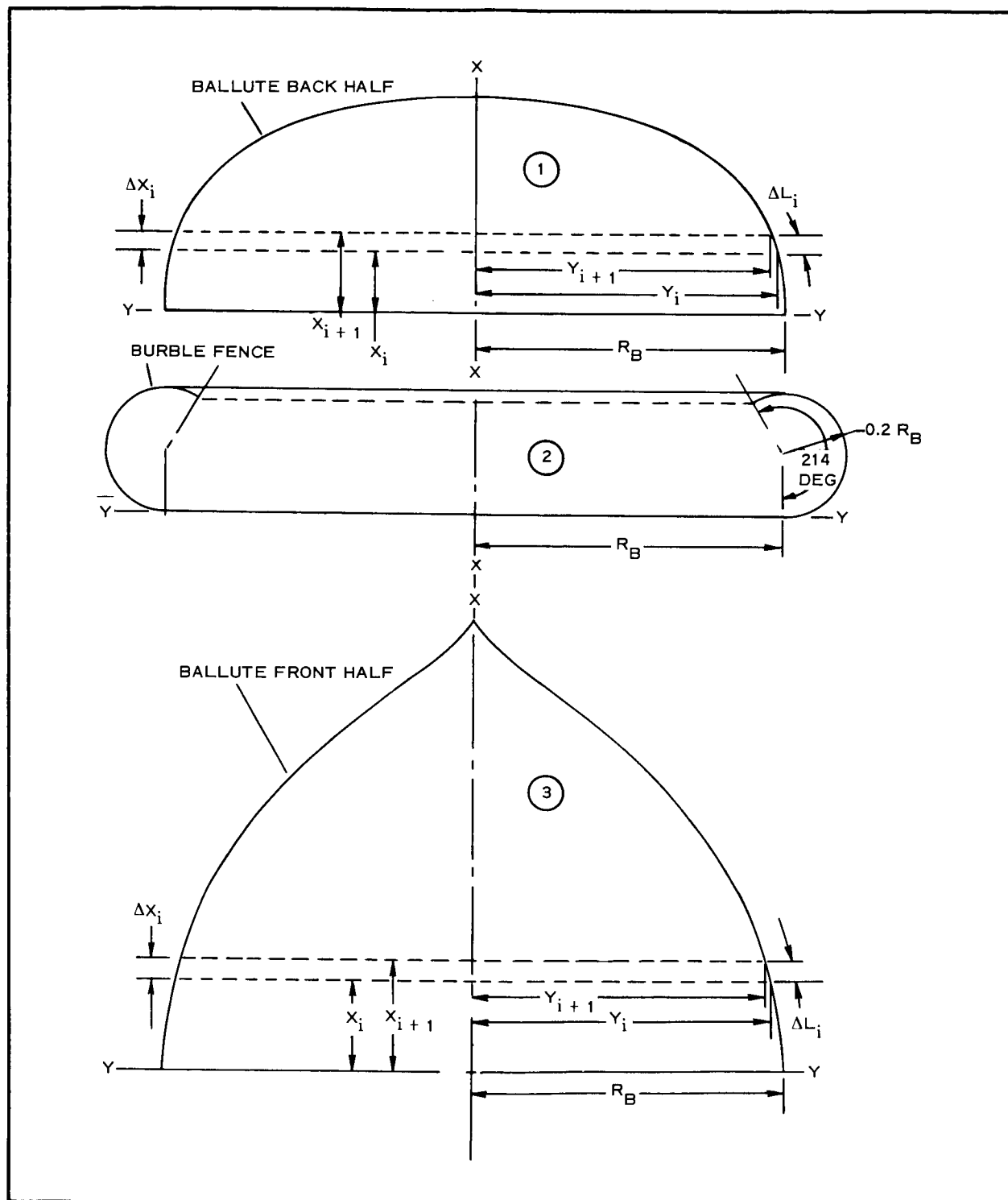


Figure A-8 - Typical BALLUTE

Thus,

$$v = \frac{4}{3} \frac{\pi \tan \phi}{\sin^2 (\theta - \phi)} \left[\frac{\tan (\theta - \phi)}{\tan (\theta - \phi) + \tan \phi} \right]^3 (R_c^3 - R_o^3) . \quad (A-40)$$

Inflating to a pressure three times that required to support the external pressure and considering equilibrium of circumferential forces results in the following equations (see Figure A-7),

$$\begin{aligned} p_I^t &= \frac{3.0 C_p q x_o}{\cos \theta} , \\ p_I &= \frac{1.5 C_p q \left[1 + \frac{\tan \phi}{\tan (\theta - \phi)} \right] \sin (\theta - \phi)}{\tan \phi \cos \theta} \\ &= 1.5 C_p q \frac{\left(\tan (\theta - \phi) + \tan \phi \right) \cos (\theta - \phi)}{\tan \phi \cos \phi} , \end{aligned} \quad (A-41)$$

and

$$\begin{aligned} p_I^v &= \frac{6\pi C_p q}{3} \frac{\sin \theta \cos \phi - \cos \theta \sin \phi}{\cos \theta \left(\frac{\sin \theta}{\cos \theta} \right)^2} (R_c^3 - R_o^3) \\ &= 2\pi C_p q \left(\frac{\cos \phi}{\sin \theta} \right)^2 \cos \phi (\tan \theta - \tan \phi) (R_c^3 - R_o^3) , \end{aligned} \quad (A-42)$$

when

p_I = internal pressure, and

R_o = reference radius.

Substituting Equation A-42 into A-34 produces

$$W_C = \frac{6\pi C_p q}{K_m} \left(\frac{\cos \phi}{\sin \theta} \right)^2 \cos \phi (\tan \theta - \tan \phi) (R_c^3 - R_o^3) (FS) .$$

To permit examination of cone weight in the same terms as BALLUTES, let

$$P = C_p q ,$$

$$R = \frac{d}{2} ,$$

and

$$W_C = \frac{3\pi FSP}{4K_m} \left(\frac{\cos \phi}{\sin \theta} \right)^2 \cos \phi (\tan \theta - \tan \phi) (d_c^3 - d_o^3) . \quad (A-43)$$

3. PHYSICAL CHARACTERISTICS ANALYSIS

a. General

Physical characteristics of decelerators are defined as surface area, contained volume, centers of gravity of the surface and volume, and the inertias of the surface and volume. Typical configurations for the BALLUTE and tucked-back BALLUTE are used to calculate their physical characteristics. The shapes of typical bodies depend on some design parameters but generally will not differ enough from the typical profiles to affect analysis of characteristics significantly.

BALLUTE characteristics are functions of the ratio of a front cutoff radius to the maximum BALLUTE radius. For a radius ratio of zero, a complete BALLUTE usually is used as a trailing BALLUTE. BALLUTE inertias are about the corresponding centers of gravity.

A BALLUTE profile has three parts or curves, the rear half, the front half, and the burble fence (see Figure A-8). The Y-Y axis is common to all three, but the front half is rotated 180 deg about the Y-Y axis to join the three segments into a BALLUTE shape.

b. BALLUTE Surface

The surface areas of the front and rear section are found by dividing profile arc lengths into equal lengths (ΔL) (see Figure A-8). The radius to the centroid of the length increment is \bar{Y}_i . The surface areas are given by the equation: when A'_{s1} = any BALLUTE part area.

$$A'_{s(i)} = 2\pi\Delta L \sum_1^n \bar{Y}_i, \quad (A-44)$$

using the nondimensional forms: $\Delta L/R_B$ and Y_i/R_B ,

$$A'_{s(i)} = 2\pi R_B^2 \frac{\Delta L}{R_B} \sum_1^n Y_i.$$

In the front half, n is the increment where the value of $Y_{(i+1)}/R_B$ is R_o/R_B .

The burble-fence surface is

$$A'_{s(2)} = 2\pi L_{(2)} \bar{Y}_{(2)}.$$

For Figure A-8 proportions:

$$L_{(2)} = 0.748R_B,$$

$$\bar{Y}_{(2)} = 1.097R_B,$$

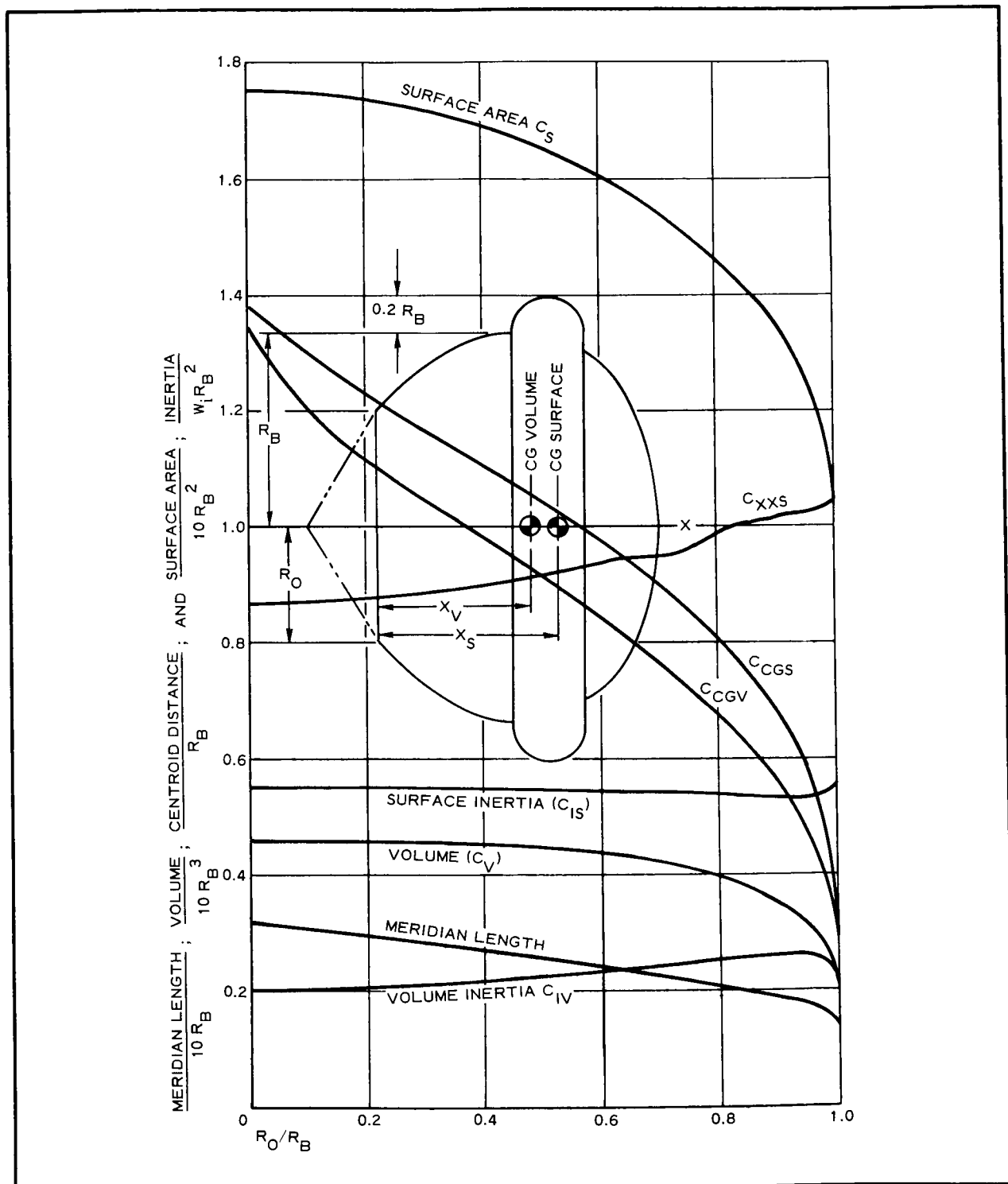
$$\begin{aligned} A'_{s(2)} &= (1.097)(2\pi)(0.748)R_B^2 \\ &= 5.156R_B^2, \text{ and} \end{aligned}$$

$$A_s = A'_{s(1)} + A'_{s(2)} + A'_{s(3)}.$$

The equation for the surface area is evaluated and may be written in the form

$$A_s = 10C_S R_B^2, \quad (A-46)$$

where C_S is a function of R_o/R_B of the BALLUTE front half. C_S is presented in Figure A-9. Surface centers of gravity of the rear and front halves of the BALLUTE are obtained from the equation for any of the three major elements of the BALLUTE,

Figure A-9 - BALLUTE with $0.20 R_B$ Burble Fence

$$\bar{X}_{\textcircled{i}} = \frac{\sum_{l=1}^n \bar{Y}_i \bar{X}_i}{\sum_{l=1}^n \bar{Y}_i} . \quad (\text{A-47})$$

Again for the front half n is the increment where the value of Y_{i+1}/R_B is R_O/R_B .

The burble fence surface center of gravity of Figure A-8 is

$$X_{\textcircled{2}} = 0.230R_B . \quad (\text{A-48})$$

The center of gravity of the complete BALLUTE is

$$X_s = \frac{A'_{s\textcircled{1}} \bar{X}_{\textcircled{1}} + A'_{s\textcircled{2}} \bar{X}_{\textcircled{2}} + A'_{s\textcircled{3}} \bar{X}_{\textcircled{3}}}{A_s} .$$

Then

$$\bar{X}_s = \bar{X}_{M\textcircled{3}} - \bar{X}_s , \quad (\text{A-49})$$

where $\bar{X}_{M\textcircled{3}}$ is \bar{X}_{i+1} of the front half corresponding to the value of n used in the equation for $A'_{s\textcircled{3}}$.

The equation for \bar{X}_s may be written in the form

$$\bar{X}_s = C_{CGS} R_B , \quad (\text{A-50})$$

where C_{CGS} is center of gravity of surface, a function of R_O/R_B of the front half. C_{CGS} is presented in Figure A-9.

The BALLUTE front and rear surface mass moments of inertia are calculated by treating each section ΔL as a thin hollow cylinder with radius equal to the average of \bar{Y}_i and \bar{Y}_{i+1} , a length of $\Delta \bar{X}_i$ and being an average of \bar{X}_i and \bar{X}_{i+1} distance from the Y-Y axis. The surface mass moment of inertia about the Y-Y axis for any of the three elements is;

$$I_{YY①} = \pi \gamma_s R_B^4 \frac{\Delta L}{R_B} \sum_1^n \left(\frac{\bar{Y}_{i \text{ avg}}}{R_B} \right)^3 + \left(\frac{\bar{Y}_{i \text{ avg}}}{6R_B} \right) \left(\frac{\Delta X_i}{R_B} \right) + 2 \left(\frac{\bar{Y}_i}{R_B} \right) \left(\frac{\bar{X}_{i \text{ avg}}}{R_B} \right)^2, \quad (\text{A-51})$$

where γ is the average weight per square foot of the BALLUTE surface.

The burble fence of Figure A-8 surface mass moment of inertia about the Y-Y axis is:

$$I_{YY②} = 3.854 \gamma R_B^4. \quad (\text{A-52})$$

The inertias of the three parts about the Y-Y axis are added and transferred to the surface center of gravity by standard inertia transfer equations. The surface mass moment of inertia may be written in the form

$$I_{CGS} = C_{IS} W_S R_B^2, \quad (\text{A-53})$$

where W_S is the BALLUTE weight and C_{IS} is a function of R_o/R_B of the front half. C_{IS} is also presented in Figure A-9.

The mass moment of inertia of the BALLUTE surface about the X-X axis is

$$I_{XXs} = \gamma_s R_B^2 \times \left\{ \sum_1^{n_1} \Delta A'_{s①} \left(\frac{Y_{\text{avg}①}}{R_B} \right)^2 + \sum_1^{n_③} \Delta A'_{s③} \left(\frac{\bar{Y}_{\text{avg}③}}{R_B} \right)^2 + A'_{s②} \left(\frac{\bar{Y}_{s②}}{R_B} \right)^2 \right\}.$$

The value of $n_③$ is the increment where the value of R_o/R_B is identical to \bar{Y}_{i+1}/R_B . This equation may be written in the form

$$I_{XXS} = C_{XXS} R_B^2 W_S .$$

where C_{XXS} is a function of R_o/R_B of the front half of the BALLUTE. C_{XXS} is presented in Figure A-9.

c. BALLUTE Volume

The volumes of the front and rear halves are found by dividing the profile x ordinates into a number of equal length increments, ΔX .

The average radii of the lengths, $\bar{Y}_{avg i}$, are calculated. The volumes are given by the equation:

$$V_i = \pi \Delta \bar{X}_i \sum_1^n (\bar{Y}_{avg i})^2 . \quad (A-54)$$

Using nondimensional forms, $\Delta \bar{X}/R_B$ and $\bar{Y}_{avg i}/R_B$,

$$V_i = \pi R_B^3 \frac{\Delta X}{R_B} \sum_1^n \left(\frac{\bar{Y}_{avg}}{R_B} \right)^2 .$$

For the front half of the BALLUTE, n is the increment where the value of \bar{Y}_{i+1}/R_B is R_o/R_B .

The burble fence volume is:

$$V_{\textcircled{2}} = 2\pi \bar{Y}_V A . \quad (A-55)$$

For Figure A-8 proportions,

$$\bar{Y}_V = 1.065 R_B ,$$

$$A = 0.07487 R_B^2 ,$$

$$V_{\textcircled{2}} = 0.501 R_B^3 ,$$

and

$$\bar{X}_{V_{\textcircled{2}}} = 0.220 R_B . \quad (A-56)$$

The volume of the BALLUTE in Figure A-8 is

$$V_B = V_{\textcircled{1}} + V_{\textcircled{2}} + V_{\textcircled{3}} .$$

The equation for the volume may be written in the form

$$V = 10C_v R_B^3 , \quad (\text{A-57})$$

where C_v is a function of R_o/R_B of the BALLUTE front half. C_v is presented in Figure A-9. Volume centers of gravity of the rear and front halves of the BALLUTE are obtained from the equation,

$$\bar{X}_{v\textcircled{1}} = \frac{\sum_{i=1}^n \bar{Y}_{\text{avg } i}^2 \bar{X}_i}{\sum_{i=1}^n \bar{Y}_{\text{avg } i}^2} , \quad (\text{A-58})$$

where \bar{X}_i is the \bar{X} distance to the centroid of the $\Delta\bar{X}$ length increments. Again, for the front half n is an increment where the value of Y_{i+1}/R_B is R_o/R_B . The burble fence volume center of gravity of Figure A-8 is given in Equation A-56.

The center of gravity of the complete BALLUTE volume is

$$X_v = \frac{V_{\textcircled{1}}\bar{X}_{v\textcircled{1}} + V_{\textcircled{2}}\bar{X}_{v\textcircled{2}} - V_{\textcircled{3}}\bar{X}_{v\textcircled{3}}}{V} . \quad (\text{A-59})$$

Then

$$\bar{X}_v = \bar{X}_{M\textcircled{3}} - \bar{X}_v ,$$

where $X_{M\textcircled{3}}$ is the X_{i+1} value of the front half which corresponds to the value of n used in the equation for $V_{\textcircled{3}}$.

The equation for X_v may be written in the form:

$$X_v = C_{CGv} R_B , \quad (\text{A-60})$$

where C_{CGv} is a function of R_o/R_B of the front half. C_{CGv} is presented in Figure A-9.

The BALLUTE front and rear half volumes mass moment of inertia are calculated by considering each section ΔX as a cylinder with radius equal to the average of \bar{Y}_i and \bar{Y}_{i+1} , a height of $\Delta \bar{X}$ and a distance of \bar{X}_{vi} from the Y-Y axis. The volume mass moment of inertia about the Y-Y axis is:

$$I_{vYY(1)} = \frac{\pi}{12} \gamma_G R_B^5 \frac{\Delta X}{R_B} \sum_1^n \left(\frac{Y_{avg i}}{R_B} \right)^2 \left\{ 3 \left(\frac{Y_{avg i}}{R_B} \right)^2 + \left(\frac{\Delta X}{R_B} \right)^2 + \left(\frac{\bar{X}_{vi}}{R_B} \right)^2 \right\}, \quad (A-61)$$

where γ_G is the gas weight.

For the burble fence of Figure A-8, the volume mass moment of inertia about the Y-Y axis is

$$I_{vYY(2)} = 0.616 \gamma_G V_{(2)} R_B^2. \quad (A-62)$$

The inertias of the three parts of volume about the Y-Y axis are added and transferred to the volume center of gravity by standard inertia transfer equations. The volume mass moment of inertia may be written in the form:

$$I_{CGv} = C_{Iv} W_G R_B^2, \quad (A-63)$$

where W_G is the weight of the contained gas and C_{Iv} is a function of R_o/R_B of the front half. C_{Iv} is presented in Figure A-9.

The mass moment of inertia of the contained gas is:

$$I_{XXv} = \gamma_G R_B^2 \left\{ \sum_1^n \frac{\Delta V_{(1)}}{2} \left(\frac{Y_{avg(1)}}{R_B} \right)^2 + \sum_1^n \frac{\Delta V_{(3)}}{2} \left(\frac{Y_{avg(3)}}{R_B} \right)^2 + V_{(2)} \left(\frac{\bar{Y}_{v(2)}}{R_B} \right)^2 \right\}. \quad (A-64)$$

This equation may be written in the reduced form

$$I_{XXv} = C_{XXv} W_G R_B^2 ,$$

where C_{XXv} is a function of R_o/R_B of the front half. C_{XXv} is presented in Figure A-9. Physical characteristics of the tucked-back BALLUTE are obtained from the same equations used for the conventional BALLUTES. These constants are:

$$C_S = 0.81 ,$$

$$C_{CGS} = 0.524 ,$$

$$C_{IS} = 0.384 ,$$

$$C_{XXS} = 0.630 ,$$

$$C_v = 0.1835 ,$$

$$C_{CGv} = 0.402 ,$$

$$C_{Iv} = 0.045 , \text{ and}$$

$$C_{XXv} = 0.443 .$$

Inertia properties of the AIRMAT cone shown in Figure A-7 are developed in the following manner, using Equation A-34 for weight and the derivation for Equation A-40 for volume.

The center of gravity of the AIRMAT cone is found by noting that

$$dW = \frac{3P_{Iv} dV_{FS}}{K_m} ;$$

$$W_c Y = \int y_c dW ;$$

$$y_c = \frac{x_i}{\tan(\theta - \phi)} ;$$

$$\begin{aligned}
 W_{cY} &= \frac{3P_I FS}{K_M} 4\pi \int_B^A \frac{x_c^2 \tan \theta dx_c}{\sin^2(\theta - \phi)} \frac{x_c}{\tan(\theta - \phi)} \\
 &= \frac{12P_I FS\pi}{K_M} \frac{\tan \phi}{\tan(\theta - \phi) \sin^2(\theta - \phi)} \int_B^A x_c^3 dx_c \\
 &= \frac{12P_I FS\pi}{K_M} \frac{\tan \phi}{\tan(\theta - \phi) \sin^2(\theta - \phi)} \left(\frac{x_c^4}{4} \right) \Big|_B^A, \quad (A-65)
 \end{aligned}$$

when

$$A = \frac{R_c}{1 + \frac{\tan \phi}{\tan(\theta - \phi)}}$$

and

$$B = \frac{R_o}{1 + \frac{\tan \phi}{\tan(\theta - \phi)}}$$

and

$$W\bar{Y} = \frac{3\pi P_I FS}{K_M} \frac{\tan \phi}{\tan(\theta - \phi) \sin^2(\theta - \phi)} \left[\frac{\tan(\theta - \phi)}{\tan(\theta - \phi) + \tan \phi} \right]^4 \left[R_c^4 - R_o^4 \right].$$

Because

$$W = \frac{4\pi P_I \tan \phi FS}{K_M \sin^2(\theta - \phi)} \left[\frac{\tan(\theta - \phi)}{\tan(\theta - \phi) + \tan \phi} \right]^3 \left[R_c^3 - R_o^3 \right],$$

$$\bar{Y} = \frac{3}{4 \tan(\theta - \phi) + \tan \phi} \left(\frac{R_c^4 - R_o^4}{R_c^3 - R_o^3} \right). \quad (A-66)$$

The mass moment of inertia about a diameter of a ring dS long having the volume dv and a weight dw is:

$$dI_{oRing} = \frac{dwR^2}{2} . \quad (A-67)$$

The inertia of the AIRMAT core about its center of gravity becomes

$$\begin{aligned} I_o &= \int \frac{dwR^2}{2} + \int dwy^2 - W\bar{Y}^2 \\ &= \frac{12P_I\pi FS}{K_M} \frac{\tan \phi}{\sin^2 (\theta - \phi)} \left\{ \int_B^A \left[\frac{x_c^4}{4} + \frac{x_c^4}{\tan^2 (\theta - \phi)} \right] dx_c \right\} - W\bar{Y}^2 . \end{aligned} \quad (A-68)$$

Thus,

$$\begin{aligned} \frac{I_o}{W} &= \frac{3}{\left[\frac{\tan (\theta - \phi)}{\tan (\theta - \phi) + \tan \phi} \right]^3 (R_c^3 - R_o^3)} \left[\frac{x_c^5}{10} + \frac{x_o^5}{5 \tan^2 (\theta - \phi)} \right] \Bigg|_B^A - \\ &\quad \left\{ \left[\frac{3}{4 \tan (\theta - \phi) + \tan \phi} \right] \left[\frac{R_c^4 - R_o^4}{R_c^3 - R_o^3} \right] \right\}^2 \\ &= \frac{3}{\left[\tan (\theta - \phi) \tan \phi \right]^2} \left\{ \left[\frac{R_c^5 - R_o^5}{R_c^3 - R_o^3} \right] \left[\frac{\tan^2 (\theta - \phi)}{10} + \frac{1}{5} \right] - \right. \\ &\quad \left. \left[\frac{3}{16} \left(\frac{R_c^4 - R_o^4}{R_c^3 - R_o^3} \right)^2 \right] \right\} . \end{aligned} \quad (A-69)$$

The polar moment of inertia of a ring dS long having a volume dv and a weight dW is

$$dI_{\text{xring}} = dwR^2. \quad (\text{A-70})$$

Thus,

$$I_x = \frac{12\pi P_{IFS}}{K_M} \frac{\tan \phi}{\sin^2 (\theta - \phi)} \int_B^A x_c^2 dx_c x_c^2,$$

and

$$\begin{aligned} \frac{I_x}{W} &= \frac{3}{\left[\frac{\tan (\theta - \phi)}{\tan (\theta - \phi) + \tan \phi} \right]^2 \left[R_c^3 - R_o^3 \right]} \frac{x_c^5}{5} \Big|_B^A \\ &= \frac{3}{5} \left[\frac{\tan (\theta - \phi)}{\tan (\theta - \phi) + \tan \phi} \right]^2 \left(\frac{R_c^5 - R_o^5}{R_c^3 - R_o^3} \right). \end{aligned} \quad (\text{A-71})$$

The weight may include the weight of the contained gas and the weight of the AIRMAT material.

APPENDIX B - DYNAMIC ANALYSIS

This appendix describes a digital computer program for simulating the motion of re-entry vehicles with either rigidly erected or tethered decelerator systems. Eight degrees-of-freedom equations of motion are developed from basic principles. A Fortran IV program listing and a computational flow chart are included.

SECTION IINTRODUCTION

The primary objective of this computer program is to satisfy the need for a trajectory program which meets the following requirement:

1. Capable of simulating re-entry flight with both rigid and tethered decelerator systems.
2. Capable of simulating the decelerator erection or inflation sequence.
3. Capable of simulating entry into any planet; i.e. Earth, Mars, Venus, etc., with either spherical or oblate spheroidal shapes.
4. Reasonable running time.
5. Programmed in a computer language (Fortran IV) which is applicable to any scientific computer facility.

The differential equations of motion are based on an inertial rectangular coordinate system with origin at the center of the earth. The numerical integrations of these equations are performed with the fourth order Runge Kutta method using automatic step size control.

The aerodynamics include both body (re-entry vehicle) and tethered decelerator effects separately. The aerodynamic force and moment coefficients appear as linear table look-up functions of Mach number and angle of attack.

SECTION IINTRODUCTION
(Continued)

Matrix algebra is used almost exclusively. The various matrix notations are defined in Section III.

SECTION IIREFERENCE FRAMES AND TRANSFORMATIONS

The reference frames are right handed orthogonal sets. They are designated by X, Y, Z with corresponding unit vectors i, j, k .

The reference frames and their definitions are itemized below and shown in Figures I and II.

Inertial Reference Frame (X_I, Y_I, Z_I)

1. The origin O_I coincides with the center of the earth.*
2. Z_I is parallel to the earth's rotational axis and is positive north.
3. X_I and Y_I lie in the earth's equatorial plane with the $X_I Z_I$ plane initially intersecting Greenwich, England.

Earth Reference Frame (X_E, Y_E, Z_E)

1. The origin O_E coincides with the center of the earth.
2. Z_E is parallel to the earth's rotational axis and is positive north.
3. X_E and Y_E lie in the earth's equatorial plane with X_E passing through the Greenwich meridian.

Geocentric Reference Frame (X_G, Y_G, Z_G)

1. The origin O_G coincides with the center of the earth.

*Earth reference as used here implies any planet.

SECTION IIREFERENCE FRAMES AND TRANSFORMATIONS
(Continued)Geocentric Reference Frame (Continued)

2. X_G passes through the body centroid.
3. $X_G Z_G$ plane contains the polar axis and Z_G is positive north of the equatorial plane.

Body Geocentric Reference Frame (X_v, Y_v, Z_v)

1. The origin O_v is at the body centroid.
2. The Z_v axis passes through the earth's center.
3. The $X_v Z_v$ plane contains the earth polar axis, X_v is positive north and Y_v is positive east.

Body Reference Frame (X_b, Y_b, Z_b)

1. The origin O_b is at the body centroid.
2. The X_b axis is colinear with the body centerline and is positive forward.
3. Y_b is positive out the right side and Z_b is positive downward.

Tethered Decelerator Reference Frame (X_o, Y_o, Z_o)

1. The origin O_o is at the tether harness point.
2. The X_o axis lies along the tether line, positive toward body.
3. Y_o is positive out the right side and Z_o is positive downward.

SECTION IIREFERENCE FRAMES AND TRANSFORMATIONS
(Continued)

A set of Euler angles ψ , ϕ and θ establish the orientation of the body frame relative to the body geocentric reference frame. The sequential rotation starting from the inertial axis frame is:

1. The earth's sidereal rotation $\Omega_e t$ about the Z_I axis to X_E, Y_E, Z_E .

$$\begin{bmatrix} \Omega_e t \end{bmatrix} = \begin{bmatrix} \cos \Omega_e t & \sin \Omega_e t & 0 \\ -\sin \Omega_e t & \cos \Omega_e t & 0 \\ 0 & 0 & 1 \end{bmatrix}$$

2. The longitudinal rotation ψ about the Z_E axis to X_I, Y_I, Z_I .

$$\begin{bmatrix} \psi \end{bmatrix} = \begin{bmatrix} \cos \psi & \sin \psi & 0 \\ -\sin \psi & \cos \psi & 0 \\ 0 & 0 & 1 \end{bmatrix}$$

3. The geocentric latitude rotation $-\phi$ about the Y_I axis to X_G, Y_G, Z_G .

$$\begin{bmatrix} -\phi \end{bmatrix} = \begin{bmatrix} \cos \phi & 0 & \sin \phi \\ 0 & 1 & 0 \\ -\sin \phi & 0 & \cos \phi \end{bmatrix}$$

SECTION IIREFERENCE FRAMES AND TRANSFORMATIONS
(Continued)

4. A -90° rotation about the Y_c axis to X_v, Y_v, Z_v .

$$\begin{bmatrix} -90 \end{bmatrix} = \begin{bmatrix} 0 & 0 & 1 \\ 0 & 1 & 0 \\ -1 & 0 & 0 \end{bmatrix}$$

5. The Euler rotation ψ about the Z_v axis to X_2, Y_2, Z_2 .

$$\begin{bmatrix} \psi \end{bmatrix} = \begin{bmatrix} \cos \psi & \sin \psi & 0 \\ -\sin \psi & \cos \psi & 0 \\ 0 & 0 & 1 \end{bmatrix}$$

6. The Euler rotation θ about the Y_2 axis to X_3, Y_3, Z_3 .

$$\begin{bmatrix} \theta \end{bmatrix} = \begin{bmatrix} \cos \theta & 0 & -\sin \theta \\ 0 & 1 & 0 \\ \sin \theta & 0 & \cos \theta \end{bmatrix}$$

7. The Euler rotation ϕ about the X_3 axis to X_B, Y_B, Z_B .

$$\begin{bmatrix} \phi \end{bmatrix} = \begin{bmatrix} 1 & 0 & 0 \\ 0 & \cos \phi & \sin \phi \\ 0 & -\sin \phi & \cos \phi \end{bmatrix}$$

SECTION IIREFERENCE FRAMES AND TRANSFORMATIONS
(Continued)

8. The decelerator rotation ζ about the Y_4 axis to X_4, Y_4, Z_4 .

$$\begin{bmatrix} \zeta \end{bmatrix} = \begin{bmatrix} \cos \zeta & 0 & -\sin \zeta \\ 0 & 1 & 0 \\ \sin \zeta & 0 & \cos \zeta \end{bmatrix}$$

9. The decelerator rotation $-\eta$ about the Z_4 axis to X_0, Y_0, Z_0 .

$$\begin{bmatrix} -\eta \end{bmatrix} = \begin{bmatrix} \cos \eta & -\sin \eta & 0 \\ \sin \eta & \cos \eta & 0 \\ 0 & 0 & 1 \end{bmatrix}$$

The matrix transformation between the reference frames are indicated by $[T]$. Subscripts are employed to indicate the two frames involved and the direction in which the transformation takes place. Thus, $[T_{E \rightarrow I}]$ indicates a transformation from the earth frame to the inertial frame. The inverse transformation is indicated by a -1 superscript and the transpose by a tilde (\sim).

The transformations employed between the various reference frames in terms of single rotation matrices are,

SECTION IIREFERENCE FRAMES AND TRANSFORMATIONS
(Continued)

1. Body geocentric to body reference:

$$[T_{V \rightarrow B}] = [\theta][\phi][\psi]$$

and

$$[T_{B \rightarrow V}] = [-\psi][-\phi][-\theta] = [\tilde{T}_{V \rightarrow B}]$$

2. Geocentric to body reference:

$$[T_{G \rightarrow B}] = [T_{V \rightarrow B}][-90]$$

and

$$[T_{B \rightarrow G}] = [90][\tilde{T}_{V \rightarrow B}] = [\tilde{T}_{G \rightarrow B}]$$

where

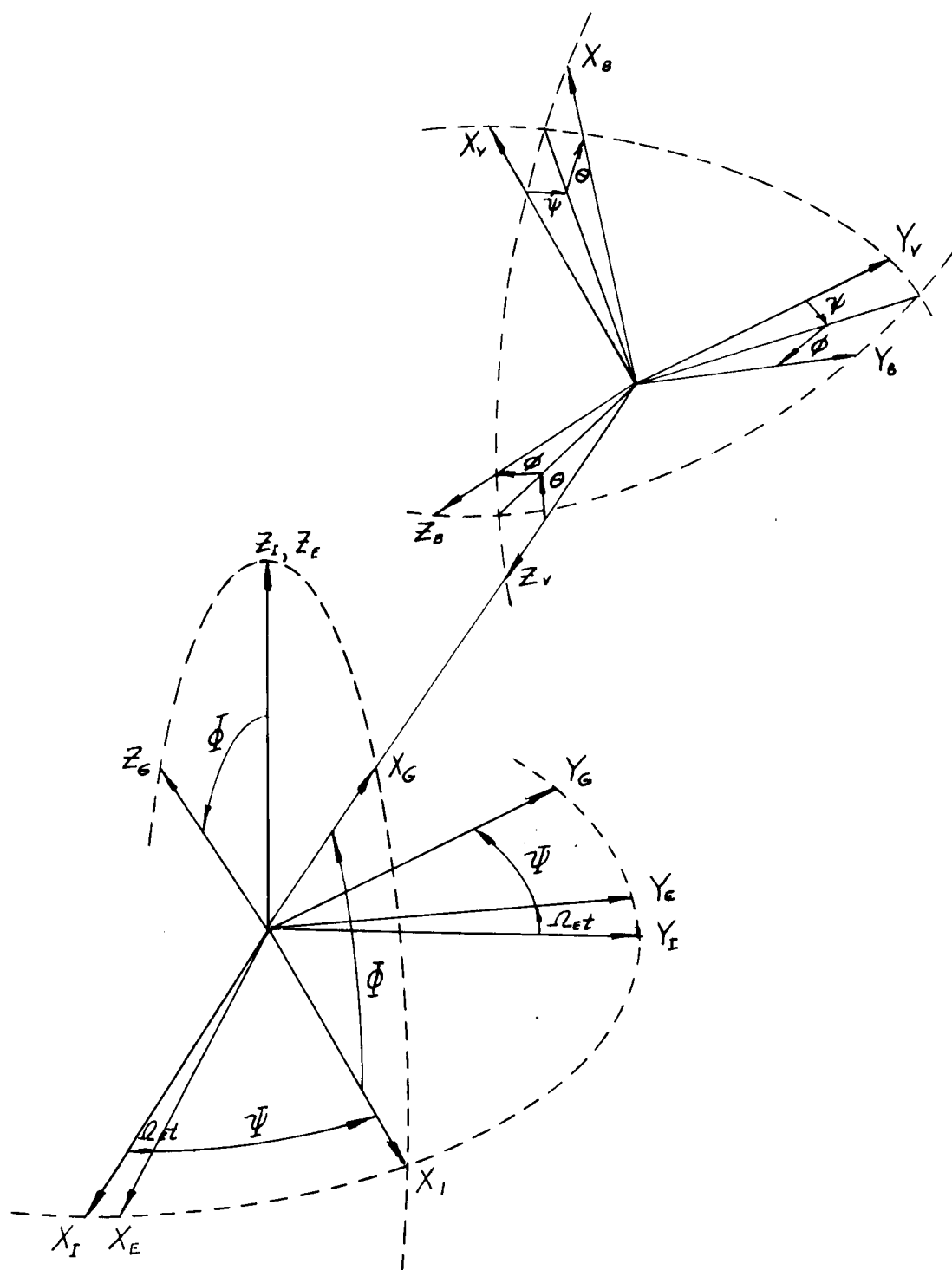
$$[90] = \begin{bmatrix} 0 & 0 & -1 \\ 0 & 1 & 0 \\ 1 & 0 & 0 \end{bmatrix}$$

3. Body to decelerator reference:

$$[T_{B \rightarrow D}] = [-\eta][\zeta]$$

and

$$[T_{D \rightarrow B}] = [-\zeta][\eta] = [\tilde{T}_{B \rightarrow D}]$$



Reference Frames

Figure 1

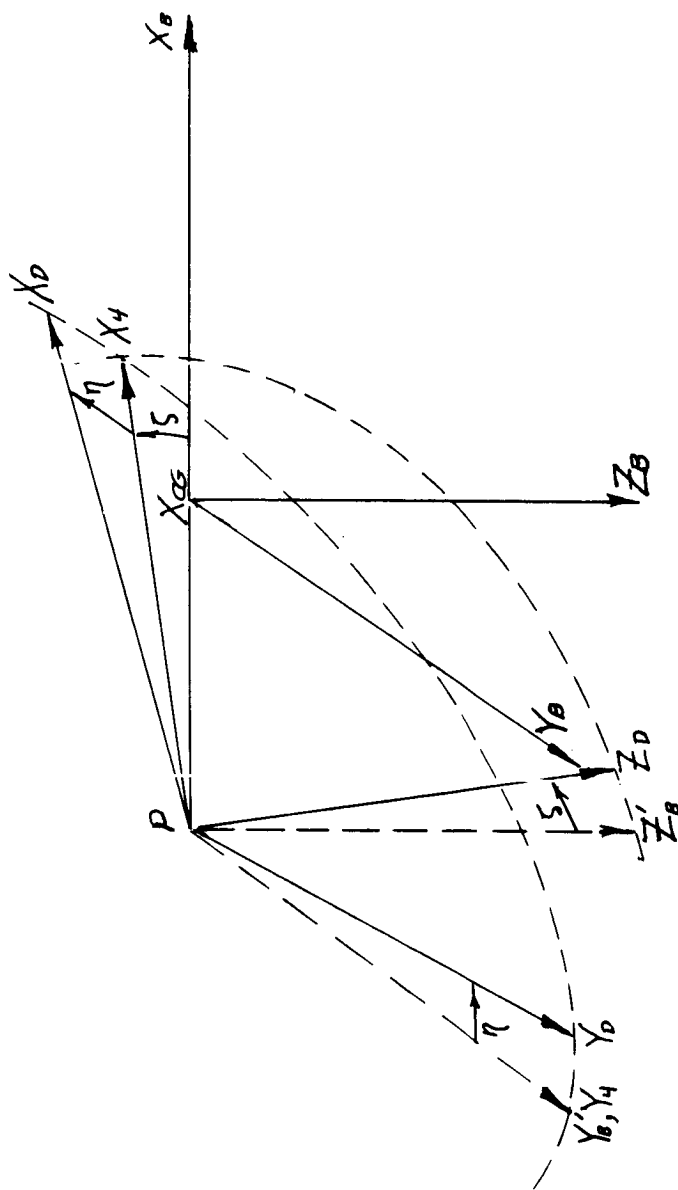


FIGURE II
BODY AND TETHERED DECELERATOR REFERENCE FRAMES

SECTION III
EQUATIONS OF MOTION

The equations of motion are derived from momentum considerations (Newton's Second Law). The basic vector equations of motion for a mass particle $\int m_p$ are:

$$\int \vec{F}_I(0)_B = \int m_p \frac{d \vec{v}_I(P)_B}{dt} \quad (1)$$

$$\int \vec{M}_I(P)_B = \frac{d}{dt} \int \vec{h}_I(P)_B \quad (2)$$

Where $\vec{v}_I(P)_B$ is the velocity vector and $\int \vec{h}_I(P)_B$ the momentum moment vector of the mass particle.

The notation adopted is best explained by considering a general column matrix $X_I(P)_B$: X indicates a coordinate matrix; P indicates the point the coordinate describes; the first subscript, in this case I , indicates the coordinates are taken relative to the inertial frame and the second subscript, in this case B , indicates that the matrix components are expressed in the body reference frame. The coordinate matrix $X_I(P)_B$ is written:

$$X_I(P)_B = \begin{bmatrix} X_I(P)_i_B \\ X_I(P)_j_B \\ X_I(P)_k_B \end{bmatrix}$$

SECTION III
EQUATIONS OF MOTION
 (Continued)

The velocity and force matrices are similarly designated $V_I(P)_B$ and $F_I(P)_B$ which are the velocity and force of P relative to the inertial frame with components in the body frame. $V_I(P)_B$ and $F_I(P)_B$ are written:

$$V_I(P)_B = \begin{bmatrix} V_I(P)_{iB} \\ V_I(P)_{jB} \\ V_I(P)_{kB} \end{bmatrix} ; \quad F_I(P)_B = \begin{bmatrix} F_I(P)_{iB} \\ F_I(P)_{jB} \\ F_I(P)_{kB} \end{bmatrix}$$

An arrow is used to indicate a vector. Thus, $\vec{V}_I(P)_B$ is the inertial velocity vector of P with components in the body system.

A. Body Translational Equations

Summing equation (1) over all the mass particles \mathcal{S}_m of the body yields,

$$\sum \mathcal{S} \vec{F}_I(P)_B \triangleq F_I(O)_B = \frac{d}{dt} \sum \vec{v}_I(P)_B \mathcal{S}_m \quad (3)$$

where $F_I(O)_B$ is the external force matrix. Assuming body rigidity cancels the effects of internal forces since every particle (P) exhibits equal and opposite forces in accordance with Newton's Third Law.

The velocity of a mass particle \mathcal{S}_m may be expressed as,

$$\vec{v}_I(P)_B = V_I(O)_B + \frac{d}{dt} \vec{X}_B(P)_B \quad (4)$$

SECTION IIIEQUATIONS OF MOTION
(Continued)A. Body Translational Equations (Continued)

where, $V_I(0)_B$ is the velocity vector matrix of the body centroid and $\vec{X}_B(P)_B$ is the radius vector from the centroid to the particle. Substituting this velocity relationship into the linear momentum term of equation (3) and treating the body as a constant mass gives,

$$\begin{aligned}\sum \vec{v}_I(P)_B \Delta m_P &= \sum (V_I(0)_B + \frac{d}{dt} \vec{X}_B(P)_B) \Delta m_P \\ &= m V_I(0)_B + \frac{d}{dt} \vec{X}_B(P)_B \sum \Delta m_P \\ &= m V_I(0)_B\end{aligned}\quad (5)$$

where m is the total mass of the system of particles. The summation of $\vec{X}_B(P)_B \Delta m_P$ vanishes since it represents the mass moment about the centroid which by definition is zero. Thus, equation (1) relates the external forces to the motion of the center of mass.

$$F_I(0)_B = m \frac{d}{dt} V_I(0)_B = m \left\{ \dot{V}_I(0)_B + [\omega_I(0)_B \times] V_I(0)_B \right\}^{(6)}$$

where $\dot{V}_I(0)_B$, as used here, is a scalar differentiation since general vector integration is not definable. The cross product term $[\omega_I(0)_B \times] V_I(0)_B$ constitutes the motion of the body frame in inertial space. This combined operation is vector differentiation

SECTION IIIEQUATIONS OF MOTION
(Continued)A. Body Translational Equations (Continued)

and must be interpreted with care. Vector differentiation is further explained in Appendix A of Reference 1.

The above equation can be expressed in a form suitable for integration as follows:

$$\dot{V}_I(o)_B = \frac{1}{m} F_I(o)_B - [\omega_I(o)_B \times] V_I(o)_B \quad (7)$$

The velocity relative to the inertial reference frame with components in the body frame is found by integrating,

$$V_I(o)_B = \int_0^t \dot{V}_I(o)_B dt + V_I(o)_B_0 \quad (8)$$

B. Body Rotational Equations

The angular momentum of a particle ($\int h_I(P)_B$) is the moment of its linear momentum about a space fixed point. By locating this point at the body centroid such that it is simultaneously a space fixed and body fixed point, the summation of particle angular momentums over the body results in,

$$\sum \int h_I(P)_B \triangleq H_I(o)_B = \sum (\vec{X}_I(P)_B \times \vec{U}_I(P)_B) \sum m_p \quad (9)$$

SECTION III
EQUATIONS OF MOTION
(Continued)

B. Body Rotational Equations (Continued)

Where $\vec{X}_I(P)_B$ is the radius vector from the centroid to the particle mass δm_p .

The particle velocity vector may be expanded to,

$$\vec{v}_I(P)_B = V_I(0)_B + [\omega_I(0)_B \times] \vec{X}_I(P)_B \quad (10)$$

substituting for $\vec{v}_I(P)_B$ in equation (9).

$$\begin{aligned} H_I(0)_B &= \sum \vec{X}_I(P)_B \times (V_I(0)_B + [\omega_I(0)_B \times] \vec{X}_I(P)_B) \delta m_p \\ &= \sum \vec{X}_I(P)_B \times V_I(0)_B \delta m_p + \sum \vec{X}_I(P)_B \times [\omega_I(0)_B \times] \vec{X}_I(P)_B \delta m_p \quad (11) \end{aligned}$$

Since $V_I(0)_B$ is constant with respect to the summation and $\sum \vec{X}_I(P)_B \delta m_p \triangleq 0$ again by definition, the angular momentum matrix becomes,

$$\begin{aligned} H_I(0)_B &= \sum \vec{X}_I(P)_B \times \omega_I(0)_B \times \vec{X}_I(P)_B \delta m_p \\ &= \sum \left\{ \omega_I(0)_B (\vec{X}_I(P)_B \cdot \vec{X}_I(P)_B) - \dot{X}_I(P)_B (\omega_I(0)_B \cdot \vec{X}_I(P)_B) \right\} \delta m_p \quad (12) \end{aligned}$$

since $\vec{X}_I(P)_B$ has body components X , Y and Z equation (12) may

SECTION IIIEQUATIONS OF MOTION
(Continued)B. Body Rotational Equations (Continued)

also be written,

$$H_I(0)_B = \omega_I(0)_B \sum (X^2 + Y^2 + Z^2) \Delta m_p - \sum X_I(P)_B (PX + QY + RZ) \Delta m_p$$

where

$$\omega_I(0)_B \triangleq \begin{bmatrix} P \\ Q \\ R \end{bmatrix} ; \quad X_I(P)_B \triangleq \begin{bmatrix} X \\ Y \\ Z \end{bmatrix}$$

The components of $H_I(0)_B$ are,

$$H_I(0)_{iB} = P \sum (Y^2 + Z^2) \Delta m_p - Q \sum XY \Delta m_p - R \sum XZ \Delta m_p$$

$$H_I(0)_{jB} = -P \sum XY \Delta m_p + Q \sum (X^2 + Z^2) \Delta m_p - R \sum YZ \Delta m_p \quad (13)$$

$$H_I(0)_{kB} = -P \sum XZ \Delta m_p - Q \sum YZ \Delta m_p + R \sum (X^2 + Y^2) \Delta m_p$$

The summation $\sum (Y^2 + Z^2)$ is defined as the moment inertia I_x of the body mass about the X axis. Similarly, the summation $\sum XY \Delta m_p$ is defined as the product of inertia I_{xy} . The remaining summations are similarly defined and equations (13) takes the form,

$$H_I(0)_B = \begin{bmatrix} I_x & -I_{xy} & -I_{xz} \\ -I_{yx} & I_y & -I_{yz} \\ -I_{zx} & -I_{zy} & I_z \end{bmatrix} \begin{bmatrix} P \\ Q \\ R \end{bmatrix} = [I] \omega_I(0)_B \quad (14)$$

SECTION IIIEQUATIONS OF MOTION
(Continued)B. Body Rotational Equations (Continued)

The angular momentum equation (equation 2) when summed over the mass of the body may be written as,

$$M_I(o)_B = \frac{d}{dt} H_I(o)_B = \dot{H}_I(o)_B + [\omega_I(o)_B \times] H_I(o)_B \quad (15)$$

where the dot indicates a scalar differentiation. A more suitable form for integration using the moment of inertia relationship of expression (14) is,

$$M_I(o)_B = [I] \dot{\omega}_I(o)_B + [\omega_I(o)_B \times] [I] \omega_I(o)_B \quad (16)$$

In terms of the angular velocity in the body reference frame,

$$\dot{\omega}_I(o)_B = [I]^{-1} \left\{ M_I(o)_B - [\omega_I(o)_B \times] [I] \omega_I(o)_B \right\} \quad (17)$$

Integrating,

$$\omega_I(o)_B = \int_0^t \dot{\omega}_I(o)_B dt + \omega_I(o)_B_0 \quad (18)$$

The inverse moment of inertia matrix $[I]^{-1}$ presents a formidable problem, not only above, but also in solving for the tension force in the tether cable. By simplifying the body shape to one which has

SECTION III
EQUATIONS OF MOTION
(Continued)

B. Body Rotational Equations (Continued)

longitudinal symmetry the moment of inertia matrices are,

$$\begin{bmatrix} I \end{bmatrix} = \begin{bmatrix} I_x & 0 & 0 \\ 0 & I_y & 0 \\ 0 & 0 & I_z \end{bmatrix}; \quad \begin{bmatrix} I \end{bmatrix}^{-1} = \begin{bmatrix} 1/I_x & 0 & 0 \\ 0 & 1/I_y & 0 \\ 0 & 0 & 1/I_z \end{bmatrix} \quad (19)$$

C. Euler Angle Equations

The body angular orientation is described by the Euler angles ψ , θ and ϕ (see Figure 1). These angles specify the ordered rotation between the body geocentric (V) and the body (B) reference frames and are obtained from angular rate relationships.

$$\omega_I(\omega)_B = \dot{\psi} + \dot{\theta} + \dot{\phi} + \dot{\phi} + (\dot{\psi} + \dot{\theta}) \mathbf{e}_3$$

In the matrix notation of Section I this relationship is,

$$\begin{aligned} \omega_I(\omega)_B &= \begin{bmatrix} \dot{\phi} \\ 0 \\ 0 \end{bmatrix} + \begin{bmatrix} \phi \end{bmatrix} \begin{bmatrix} 0 \\ \dot{\theta} \\ 0 \end{bmatrix} + \begin{bmatrix} \phi \end{bmatrix} \begin{bmatrix} \theta \end{bmatrix} \begin{bmatrix} 0 \\ 0 \\ \dot{\psi} \end{bmatrix} + \begin{bmatrix} T_{B \rightarrow V} \end{bmatrix} \begin{bmatrix} 0 \\ -\dot{\phi} \\ 0 \end{bmatrix} + \begin{bmatrix} T_{B \rightarrow V} \end{bmatrix} \begin{bmatrix} 0 \\ 0 \\ \dot{\psi} \end{bmatrix} \begin{bmatrix} 0 \\ 0 \\ \dot{\psi} \end{bmatrix} \\ &= \begin{bmatrix} 1 & 0 & -\sin \theta \\ 0 & \cos \phi & \cos \theta \sin \phi \\ 0 & -\sin \phi & \cos \theta \cos \phi \end{bmatrix} \begin{bmatrix} \dot{\phi} \\ \dot{\theta} \\ \dot{\psi} \end{bmatrix} + \begin{bmatrix} T_{V \rightarrow B} \end{bmatrix} \begin{bmatrix} 0 \\ -\dot{\phi} \\ 0 \end{bmatrix} + \begin{bmatrix} -90 \end{bmatrix} \begin{bmatrix} \phi \end{bmatrix} \begin{bmatrix} 0 \\ 0 \\ \dot{\psi} \end{bmatrix} \\ &= \begin{bmatrix} A \end{bmatrix} \begin{bmatrix} \dot{E} \end{bmatrix} + \begin{bmatrix} T_{V \rightarrow B} \end{bmatrix} \begin{bmatrix} (\dot{\psi} + \dot{\theta}) \cos \phi \\ -\dot{\phi} \\ -(\dot{\psi} + \dot{\theta}) \sin \phi \end{bmatrix} \end{aligned} \quad (20)$$

SECTION III
EQUATIONS OF MOTION
 (Continued)

C. Euler Angle Equations (Continued)

The above relationship can be used in solving for the rates of change of the Euler angles.

$$\begin{bmatrix} \dot{E} \end{bmatrix} = \begin{bmatrix} A \end{bmatrix}^{-1} \begin{bmatrix} \omega_1(\phi)_B \end{bmatrix} - \begin{bmatrix} A \end{bmatrix}^{-1} \begin{bmatrix} T_{V \rightarrow B} \end{bmatrix} \begin{bmatrix} (\dot{\psi} + \Omega_e) \cos \phi \\ -\dot{\phi} \\ -(\dot{\psi} + \Omega_e) \sin \phi \end{bmatrix} \quad (21)$$

where,

$$\begin{bmatrix} A \end{bmatrix}^{-1} = \begin{bmatrix} 1 & \frac{\sin \theta \sin \phi}{\cos \theta} & \frac{\sin \theta \cos \phi}{\cos \theta} \\ 0 & \cos \phi & -\sin \phi \\ 0 & \frac{\sin \phi}{\cos \theta} & \frac{\cos \phi}{\cos \theta} \end{bmatrix}$$

The Euler angles are obtained by integrating

$$\begin{bmatrix} E \end{bmatrix} = \begin{bmatrix} \phi \\ \theta \\ \psi \end{bmatrix} = \int_0^t \begin{bmatrix} \dot{E} \end{bmatrix} dt + \begin{bmatrix} E \end{bmatrix}_0 \quad (22)$$

D. Tethered Decelerator Equations

The predominant motions of a tethered decelerator (Ballute type) are represented by translational motion in spherical coordinates with origin at the tether harness point (P). Assuming direct transmittal of body spin through the tether, the spin motions of

SECTION III
EQUATIONS OF MOTION
 (Continued)

D. Tethered Decelerator Equations (Continued)

both body and decelerator may be combined in the body rotational motion. Under this assumption, the tethered decelerator only adds two degrees-of-freedom to the system. The added freedoms consist of an angular pitch displacement (ζ) and a yaw displacement (η), (see Figure III).

The translational equation of motion (equation 6) yields an expression for the decelerator motion.

$$\begin{aligned} F_I(d)_D &= m_D \frac{d}{dt} V_I(d)_D \\ &= m_D \left\{ \dot{V}_I(d)_D + \omega_I(o)_D \times V_I(d)_D \right\} \end{aligned} \quad (23)$$

Where,

$$\begin{aligned} V_I(d)_D &= [T_{B \rightarrow D}] \left\{ V_I(o)_B + \omega_I(o)_B \times X_B(p)_B \right\} \\ &\quad + \omega_I(o)_D \times X_D(d)_D \\ \dot{V}_I(d)_D &= [\dot{T}_{B \rightarrow D}] \left\{ V_I(o)_B + \omega_I(o)_B \times X_B(p)_B \right\} \\ &\quad + [T_{B \rightarrow D}] \left\{ \dot{V}_I(o)_B + \dot{\omega}_I(o)_B \times X_B(p)_B \right\} \\ &\quad + \dot{\omega}_I(o)_D \times X_D(d)_D \\ \omega_I(o)_D &= [T_{B \rightarrow D}] \omega_I(o)_B + \omega_B(o)_D \\ \dot{\omega}_I(o)_D &= [\dot{T}_{B \rightarrow D}] \omega_I(o)_B + [T_{B \rightarrow D}] \dot{\omega}_I(o)_B + \dot{\omega}_B(o)_D \end{aligned}$$

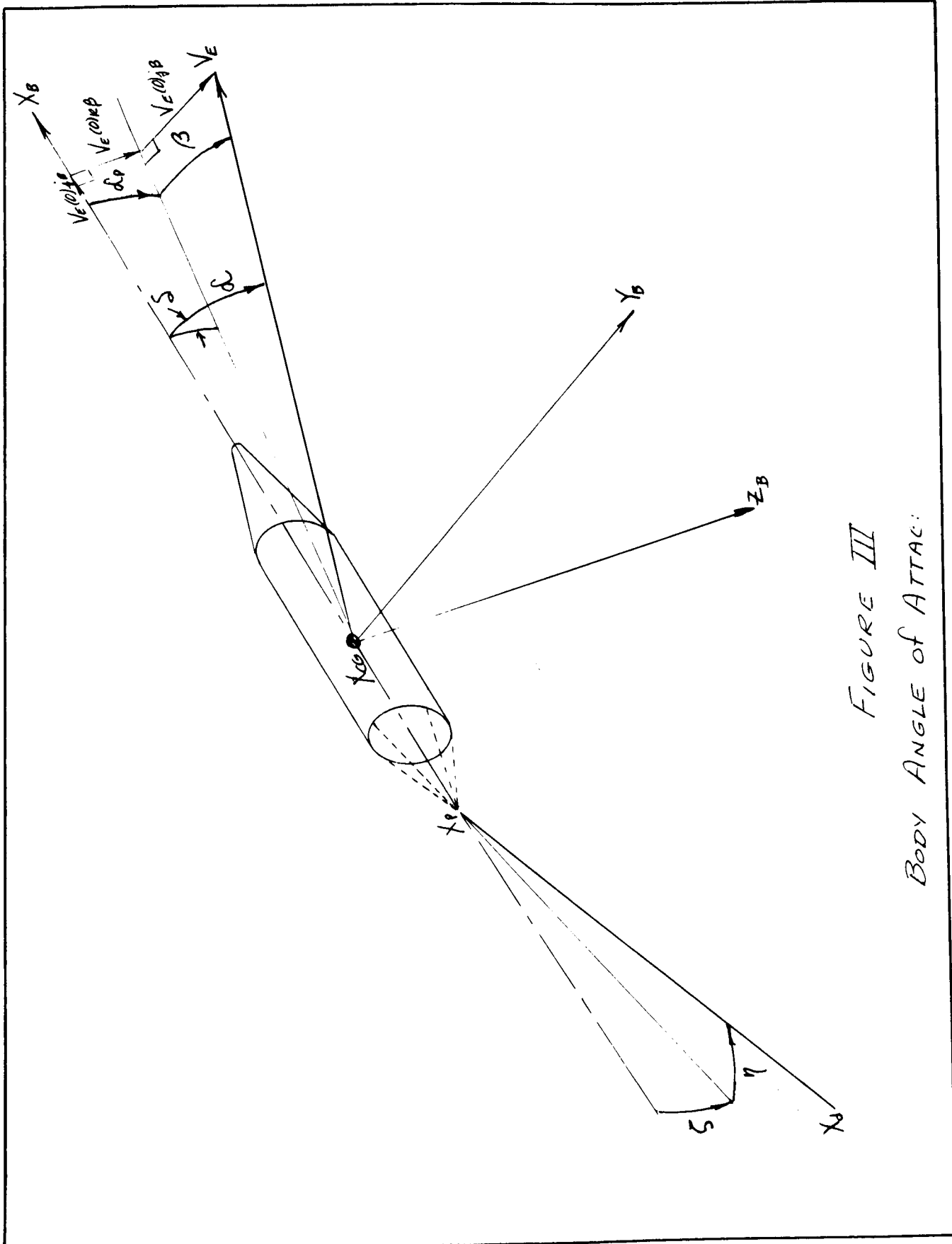


FIGURE III
BODY ANGLE OF ATTACK:

SECTION III

EQUATIONS OF MOTION
(Continued)D. Tethered Decelerator Equations (Continued)

$$X_B(P)_B = \begin{bmatrix} -X_{\text{harness point}} \\ 0 \\ 0 \end{bmatrix} ; \quad X_D(d)_D = \begin{bmatrix} -X_{\text{decelerator centroid}} \\ 0 \\ 0 \end{bmatrix}$$

$$[\dot{T}_{B \rightarrow D}] = \begin{bmatrix} -(\dot{\eta} \sin \eta \cos \zeta + \dot{\zeta} \cos \eta \sin \zeta) & -\dot{\eta} \cos \eta & \dot{\eta} \sin \eta \sin \zeta - \dot{\zeta} \cos \eta \cos \zeta \\ \dot{\eta} \cos \eta \cos \zeta - \dot{\zeta} \sin \eta \sin \zeta & -\dot{\eta} \sin \eta & -(\dot{\eta} \cos \eta \sin \zeta + \dot{\zeta} \sin \eta \cos \zeta) \\ \dot{\zeta} \cos \zeta & 0 & -\dot{\zeta} \sin \zeta \end{bmatrix}$$

substituting inertial and dynamic relationships for the acceleration expressions $\dot{\omega}_I(0)_B$ and $\dot{V}_I(0)_B$ (See Section V) and expanding $\dot{\omega}_B(0)_D \times X_D(d)_D$ in terms of $\ddot{\eta}$ and $\ddot{\zeta}$ the desired second order differential parameters of the decelerator relative motion gives,

$$\begin{aligned} & \frac{F_I^A(d)_D + F_I^T(0)_D + [T_{G \rightarrow D}] F_I^G(d)_G}{m_D} = [\dot{T}_{B \rightarrow D}] \left\{ V_I(0)_B + \omega_I(0)_B \times X_B(P)_B \right\} \\ & + [\dot{T}_{B \rightarrow D}] \left\{ \frac{F_I^A(0)_B - [T_{D \rightarrow B}] F_I^T(0)_D + [T_{G \rightarrow B}] F_I^G(0)_G}{m} - \omega_I(0)_B \times V_I(0)_B \right. \\ & \left. + [I]^{-1} \left[M_I^A(0)_B + [T_{D \rightarrow B}] F_I^T(0)_D \times X_B(P)_B - \omega_I(0)_B \times [I] \omega_I(0)_B \right] \times X_D(d)_D \right\} \\ & + X_D \begin{bmatrix} 0 \\ \ddot{\eta} \\ \ddot{\zeta} \cos \eta - \dot{\zeta} \dot{\eta} \sin \eta \end{bmatrix} + [\dot{T}_{B \rightarrow D}] \omega_I(0)_B \times X_D(d)_D + [T_{B \rightarrow D}] \dot{\omega}_I(0)_B \times X_D(d)_D \\ & + \omega_I(0)_D \times V_I(d)_D \end{aligned}$$

SECTION III

EQUATIONS OF MOTION
(Continued)D. Tethered Decelerator Equations (Continued)

Letting

$$\begin{aligned}
[C] = & - \left(\frac{F_I^A(d)_D + [T_{G \rightarrow D}] F_I^G(d)_G}{m_D} + [T_{B \rightarrow D}] \left\{ V_I(d)_B + \omega_I(d)_B \times X_B(P)_B \right\} \right. \\
& + [T_{B \rightarrow D}] \omega_I(d)_B \times X_D(d)_D + [T_{B \rightarrow D}] \left\{ \frac{F_I^A(d)_B + [T_{G \rightarrow B}] F_I^G(d)_G}{m} - \omega_I(d)_B \times V_I(d)_B \right. \\
& + [I]^{-1} \left\{ M_I^A(d)_B - \omega_I(d)_B \times [I] \omega_I(d)_B \right\} \times X_B(P)_B \left. \right\} + [T_{B \rightarrow D}] \left\{ [I]^{-1} \left[M_I^A(d)_B \right. \right. \\
& \left. \left. - \omega_I(d)_B \times [I] \omega_I(d)_B \right] \right\} \times X_D(d)_D + \omega_I(d)_D \times V_I(d)_D \quad (25)
\end{aligned}$$

and,

$$\begin{aligned}
[B] = & \frac{F_I^T(d)_D}{m_D} + \frac{F_I^T(d)_D}{m} - [T_{B \rightarrow D}] \left\{ [I]^{-1} \left([T_{D \rightarrow B}] F_I^T(d)_D \times X_B(P)_B \right) \times X_B(P)_B \right\} \\
& - [T_{B \rightarrow D}] \left\{ [I]^{-1} \left([T_{D \rightarrow B}] F_I^T(d)_D \times X_B(P)_B \right) \right\} \times X_D(d)_D
\end{aligned}$$

equation (24) may be written as,

$$[B] = [C] + X_D \begin{bmatrix} 0 \\ \ddot{\eta} \\ \ddot{\zeta} \cos \eta - \dot{\zeta} \dot{\eta} \sin \eta \end{bmatrix} \quad (26)$$

The tension force magnitude may be isolated by employing the following relationship:

$$F_I^T(d)_D = \begin{bmatrix} T \\ 0 \\ 0 \end{bmatrix} = T \begin{bmatrix} 1 \\ 0 \\ 0 \end{bmatrix} = T \left\{ F_I^T(d)_D \right\}$$

SECTION IIIEQUATIONS OF MOTION
(Continued)D. Tethered Decelerator Equations (Continued)

Thus, if $[B] = F_r^{Tr}(0)_D + F_r^{Tr}(0)_D - [T_{B \rightarrow D}] \{ [I]^{-1} [T_{D \rightarrow B}] F_r^{Tr}(0)_D \times X_B(P)_B \} \times X_B(P)_B \}$
 $\times X_D(d)_D - [T_{B \rightarrow D}] \{ [I]^{-1} [T_{D \rightarrow B}] F_r^{Tr}(0)_D \times X_B(P)_B \} \times X_D(d)_D$
 then,

$$T[B] = [C] + X_D \begin{bmatrix} 0 \\ \ddot{\eta} \\ \ddot{\zeta} \cos \eta - \dot{\zeta} \dot{\eta} \sin \eta \end{bmatrix} \quad (27)$$

The tensile force magnitude (T) is given by,

$$T = \frac{[C]_i}{[B]_i} \quad (28)$$

The differential equations of relative decelerator motion are,

$$\ddot{\eta} = \frac{1}{X_D} \{ T[B]_j - [C]_j \} \quad (29)$$

$$\ddot{\zeta} = \frac{\dot{\zeta} \dot{\eta} \sin \eta}{\cos \eta} + \frac{1}{X_D \cos \eta} \{ T[B]_k - [C]_k \} \quad (30)$$

The following integrations define the motion.

$$\dot{\eta} = \int_0^t \ddot{\eta} dt + \dot{\eta}_0 \quad ; \quad \eta = \int_0^t \dot{\eta} dt + \eta_0 \quad (31)$$

$$\dot{\zeta} = \int_0^t \ddot{\zeta} dt + \dot{\zeta}_0 \quad ; \quad \zeta = \int_0^t \dot{\zeta} dt + \zeta_0 \quad (32)$$

SECTION IV
TRAJECTORY KINEMATICS

A. Velocity and Positions

The motion of the body relative to the earth is measured in the geocentric, G , reference frame. The relative earth velocity is obtained from,

$$V_E(0)_G = [T_{B \rightarrow G}] V_I(0)_B - \Omega_E(r)_G \quad (33)$$

where,

$$\Omega_E(r)_G = \begin{bmatrix} 0 \\ \Omega_E r \cos \bar{\phi} \\ 0 \end{bmatrix} ; r \text{ and } \bar{\phi} \text{ are given by equation (37).}$$

The flight path is described by both an elevation angle (γ') and an azimuth angle (λ). The magnitudes of these angles are,

$$\gamma' = \tan^{-1} \left\{ \frac{V_E(0)_{iG}}{\sqrt{V_E(0)_{iG}^2 + V_E(0)_{rG}^2}} \right\} \quad (34)$$

and

$$\lambda = \tan^{-1} \left\{ \frac{V_E(0)_{iG}}{V_E(0)_{rG}} \right\} \quad (35)$$

The position of the body is described in the geometric terms of longitude ($\bar{\psi}$), geocentric latitude ($\bar{\phi}$) and radial height (r) by integrating the geocentric velocity expression $V_E(0)_G$.

SECTION IV
TRAJECTORY KINEMATICS
(Continued)

A. Velocity and Positions (Continued)

$$[\dot{P}] = \begin{bmatrix} \dot{r} \\ \dot{\Phi} \\ \dot{\Psi} \end{bmatrix} = \begin{bmatrix} V_E(0)_{IG} \\ V_E(0)_{IG} / r \\ V_E(0)_{IG} \cos \Phi / r \end{bmatrix} \quad (36)$$

$$[P] = \begin{bmatrix} r \\ \Phi \\ \Psi \end{bmatrix} = \int_0^t [\dot{P}] dt + [P]_0 \quad (37)$$

The position of the body and tethered decelerator are considered identical in the above coordinates. The velocities, however, may differ considerably. The relative earth velocity of the tethered decelerator is,

$$V_E(d)_G = [T_{B \rightarrow G}] \left\{ V_I(0)_B + [T_{D \rightarrow B}] V_B(d)_D \right\} \quad (38)$$

B. Angle of Attack

The angle of attack defines the relative orientation between the body axes (body reference frame) and the wind vector. Assuming that there are no disturbing winds and that the atmosphere rotates with the planet, the wind vector is coincident with the earth related velocity vector $V_E(0)_G$.

The body angle of attack and its direction cosine are equated in

SECTION IV
TRAJECTORY KINEMATICS
(Continued)

B. Angle of Attack (Continued)

terms of the relative body velocity (see Figure III).

$$V_E(0)_B = [T_{G \rightarrow B}] V_E(0)_G \quad (39)$$

$$\mathcal{L} = \tan^{-1} \left\{ \frac{\sqrt{V_E(0)_{Bj}^2 + V_E(0)_{Bk}^2}}{V_E(0)_{Bi}} \right\} \quad (40)$$

$$\mathcal{S} = \tan^{-1} \left\{ \frac{V_E(0)_{Bj}}{V_E(0)_{Bk}} \right\}$$

$$\alpha_p = \tan^{-1} \left\{ \frac{V_E(0)_{Bk}}{V_E(0)_{Bi}} \right\} ; \beta = \tan^{-1} \left\{ \frac{V_E(0)_{Bj}}{\sqrt{V_E(0)_{Bi}^2 + V_E(0)_{Bk}^2}} \right\}$$

The total tethered decelerator angle of attack relationships (see Figure III) are defined in a similar manner.

$$V_E(d)_D = [T_{G \rightarrow D}] V_E(d)_G \quad (41)$$

$$\mathcal{L}_D = \tan^{-1} \left\{ \frac{\sqrt{V_E(d)_{Dj}^2 + V_E(d)_{Dk}^2}}{V_E(d)_{Di}} \right\} \quad (42)$$

$$\mathcal{S}_D = \tan^{-1} \left\{ \frac{V_E(d)_{Dj}}{V_E(d)_{Dk}} \right\} \quad (43)$$

$$\alpha_{Dp} = \tan^{-1} \left\{ \frac{V_E(d)_{Dk}}{V_E(d)_{Di}} \right\}$$

$$\beta_D = \tan^{-1} \left\{ \frac{V_E(d)_{Dj}}{\sqrt{V_E(d)_{Di}^2 + V_E(d)_{Dk}^2}} \right\}$$

SECTION IV
TRAJECTORY KINEMATICS
 (Continued)

C. Special Computations

The range traversed by the decelerator-body system over the planet surface is determined from the integral.

$$Range = \int_0^t R_{\Phi} \sqrt{\dot{\Phi}^2 + \dot{\Psi}^2 \cos^2 \Phi} dt + Range_0 \quad (44)$$

Where the oblate shape is approximated by:

$$R_{\Phi} = R_0 (1 - f \sin^2 \Phi) \quad (45)$$

R_{Φ} - local planet radius

R_0 - equatorial radius

f - oblateness parameter (earth = .003670034)

For spherical planet considerations, the oblateness parameter is equal to zero and $R_{\Phi} = R_0$.

The local altitude is determined from the relation,

$$h = r - R_0 (1 - f \sin^2 \Phi) \quad (46)$$

The Mach number M and dynamic pressure q are given by

$$M = V_{E(0)G} / V_s \quad (48)$$

$$q = \frac{1}{2} \rho V_{E(0)G}^2 \quad (49)$$

SECTION IVTRAJECTORY KINEMATICS
(Continued)C. Special Computations (Continued)

where V_s and ρ are the atmospheric properties of the velocity of sound and density respectively. The Mach number and dynamic pressure for the tethered decelerator is obtained by interchanging $V_E(d)_G$ with $V_E(0)_G$ in the above expressions. The atmospheric properties are determined in a subprogram which may be changed to incorporate any planetary atmosphere. A sample Martian atmospheric model is listed in Section VIII.

SECTION V
FORCES AND MOMENTS

The external forces are comprised of aerodynamic, gravity and cable tension force components. The force matrices are,

$$F_I(0)_B = F_I^A(0)_B - [T_{I \rightarrow B}] F_I^T(0)_D + [T_{G \rightarrow B}] F_I^G(0)_G \quad (50)$$

$$F_I(d)_D = F_I^A(d)_D + F_I^T(0)_D + [T_{G \rightarrow D}] F_I^G(d)_G \quad (51)$$

where

$F_I^A(0)_B$ - body aerodynamic force matrix

$F_I^A(d)_D$ - decelerator aerodynamic force matrix

$F_I^G(0)_G$ - body gravitational force matrix

$F_I^G(d)_G$ - decelerator gravitational force matrix

$F_I^T(0)_D$ - cable tension force matrix

The cable tension force also contributes to the body moments.

$$M_I(0)_B = M_I^A(0)_B + M_I^T(0)_B \quad (52)$$

where

$$M_I^T(0)_B = [T_{D \rightarrow B}] F_I^T(0)_D \times X_B(P)_B$$

A. Aerodynamics

The aerodynamic body force matrix is

$$\begin{aligned} F_I^A(0)_{iB} &= C_A(M, \alpha) q S' \\ F_I^A(0)_{jB} &= -C_N(M, \alpha) \sin(S) q S' \\ F_I^A(0)_{kB} &= -C_N(M, \alpha) \cos(S) q S' \end{aligned} \quad (53)$$

SECTION V
FORCES AND MOMENTS
(Continued)

A. Aerodynamics (Continued)

and the body moment matrix is

$$\begin{aligned} M_I^A(0)_{B_i} &= -C_{L_p}(M) \frac{W_I(0)_{B_i}}{|V_E(0)_G|} \frac{d^2 q}{d} S & (54) \\ M_I^A(0)_{B_j} &= F_I^A(0)_{B_j} \left(\frac{X_{CP}(M, \alpha)}{d} - \frac{X_{CG}}{d} \right) d - C_{m_{\dot{\eta}}}(M) \frac{W_I(0)_{B_j}}{|V_E(0)_G|} \frac{d^2 q}{d} S \\ M_I^A(0)_{B_k} &= -F_I^A(0)_{B_j} \left(\frac{X_{CP}(M, \alpha)}{d} - \frac{X_{CG}}{d} \right) d - C_{m_{\dot{\eta}}}(M) \frac{W_I(0)_{B_k}}{|V_E(0)_G|} \frac{d^2 q}{d} S \end{aligned}$$

The decelerator aerodynamic forces are similarly defined:

$$\begin{aligned} F_I^A(d)_{D_n} &= -C_{A_D}(M, \alpha) q_D S_D(t) & (55) \\ F_I^A(d)_{D_j} &= -C_{N_D}(M, \alpha) \sin(\delta_D) q_D S_D(t) \\ F_I^A(d)_{D_k} &= -C_{N_D}(M, \alpha) \cos(\delta_D) q_D S_D(t) \end{aligned}$$

where

- S - aerodynamic reference area
- d - aerodynamic reference length
- C_A - aerodynamic axial force coefficient
- C_N - aerodynamic normal force coefficient
- $C_{L_p}, C_{m_{\dot{\eta}}}$ aerodynamic moment damping coefficients
- X_{CP} - aerodynamic center of pressure along the longitudinal axis (distance from nose)
- X_{CG} - centroid location along the longitudinal axis (distance from nose)

SECTION V
FORCES AND MOMENTS
(Continued)

B. Gravitation

The earth gravitational potential considering the second spherical harmonic of the earth's oblateness is given by,

$$U(R, \Phi) = \frac{GM}{R} \left\{ 1 + \frac{J_2 R_0^2}{2 R^2} (1 - 3 \sin^2 \Phi) \right\} \quad (56)$$

where:

G - universal gravitational constant

M - mass of earth ($GM = 1.40786 \times 10^{16} \text{ ft}^3/\text{sec}^2$)

R_0 - equatorial earth radius (20,926,759 ft)

R - geocentric radius of body

Φ - geocentric latitude

J_2 - second harmonic term (1082.3×10^{-6})

The gravitational force matrix ($F_I^G(0)_G$) for the oblate earth is,

$$\frac{F_I^G(0)_G}{m} = \begin{bmatrix} -\frac{GM}{R^2} \left\{ 1 + \frac{3J_2}{2} \left(\frac{R_0}{R} \right)^2 (1 - 3 \sin^2 \Phi) \right\} \\ 0 \\ -\frac{GM}{R^2} \left(\frac{3J_2}{2} \left(\frac{R_0}{R} \right)^2 \right) \cos \Phi \sin \Phi \end{bmatrix} \quad (57)$$

For spherical planet shapes

$$\frac{F_I^G(0)_G}{m} = \begin{bmatrix} -g_0 \left\{ \frac{R_0}{R} \right\}^2 \\ 0 \\ 0 \end{bmatrix} \quad (58)$$

where g_0 is the value of sea level acceleration due to gravity.

SECTION VIDIGITAL TECHNIQUES AND EQUATION SOLUTIONSA. Matrix Routines

Four matrix subroutines were developed for use in the program.

These routines perform,

1. multiplication of a 3 x 3 matrix by another 3 x 3 matrix,
2. multiplication of a 3 x 3 matrix by a 3 x 1 column matrix,
3. multiplication using the transpose of a 3 x 3 matrix,
4. taking the cross product of two 3 x 1 column matrices.

The general matrix

$$X_B(P)_B = \begin{bmatrix} X \\ Y \\ Z \end{bmatrix}$$

is used to illustrate matrix operation notation. The cross product operator is,

$$[X_B(P)_B \times] = \begin{bmatrix} 0 & -Z & Y \\ Z & 0 & -X \\ -Y & X & 0 \end{bmatrix}$$

The transpose is,

$$\tilde{X}_B(P)_B = [X \ Y \ Z]$$

The scalar derivative is,

$$\dot{X}_B(P)_B = \begin{bmatrix} \dot{X} \\ \dot{Y} \\ \dot{Z} \end{bmatrix}$$

SECTION VIDIGITAL TECHNIQUES AND EQUATION SOLUTIONS
(Continued)A. Matrix Routines (Continued)

The inverse and transpose relationships are,

$$[T_{V \rightarrow B}][T_{V \rightarrow B}]^{-1} = [1] \text{ a unit matrix}$$

$$[T_{V \rightarrow B}]^{-1} = [\tilde{T}_{V \rightarrow B}] = [T_{B \rightarrow V}] \text{ for orthogonal transformation}$$

B. Numerical Integration

The fourth order Runge-Kutta numerical integration method is used with Earnest's (Reference 3) step size control scheme. The sequence of calculations performed in completing an integration step are

$$\begin{aligned}
 (1) \quad & f_{i0} = f_i(x_0, y_{10}, y_{20}, \dots, y_{m0}) \quad i = 1, 2, \dots, n \\
 & y_{i1} = y_{i0} + \frac{h}{2} f_{i0} \quad q_{i1} = f_{i0} \\
 (2) \quad & f_{i1} = f_i(x_0 + \frac{h}{2}, y_{11}, y_{21}, \dots, y_{m1}) \\
 & y_{i2} = y_{i0} + \frac{h}{2} f_{i1} \quad q_{i2} = q_{i1} + 2f_{i1} \\
 (3) \quad & f_{i2} = f_i(x_0 + \frac{h}{2}, y_{12}, y_{22}, \dots, y_{m2}) \\
 & y_{i3} = y_{i0} + h f_{i2} \quad q_{i3} = q_{i2} + 2f_{i2} \\
 (4) \quad & f_{i3} = f_i(x_0 + h, y_{13}, y_{23}, \dots, y_{m3}) \\
 & y_{i4} = y_{i0} + \frac{h}{6} (q_{i3} + f_{i3}) \quad q_{i4} = f_{i3} \\
 (5) \quad & f_{i4} = f_i(x_0 + h, y_{14}, y_{24}, \dots, y_{m4})
 \end{aligned} \tag{59}$$

$$T_i = h (f_{i4} - q_{i3}) \tag{60}$$

SECTION VIDIGITAL TECHNIQUES AND EQUATION SOLUTIONS
(Continued)B. Numerical Integration (Continued)

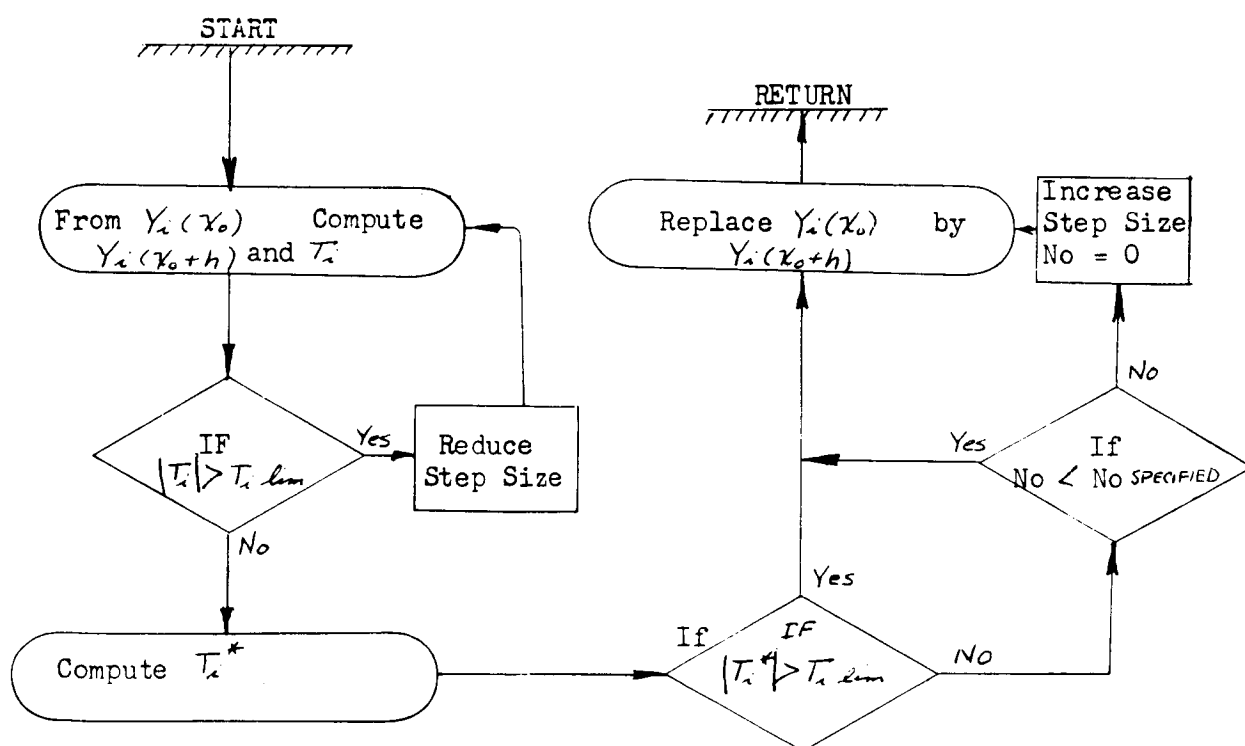
Where \overline{T}_i is the error estimate. The error estimate corresponding to the next larger step size h^* is approximated by

$$\overline{T}_i^* = f\left(\frac{h^*}{h}\right)^4 \overline{T}_i \quad (61)$$

Where h is the current step size and f is an input factor which causes \overline{T}_i^* to be overestimated to reduce time consuming premature increases in step size.

An incremental step size specified by the program input determines the amount of increase or decrease in (h) the step size. If the input factor is 2, the step size is halved if the truncation error (\overline{T}_i) is too large and doubled if the error is less than a preset magnitude limit (\overline{T}_{lim}) for a specified number of steps proves helpful for rotational motions where \overline{T}_i fluctuates.

Following is a flow chart showing the basic procedure.

SECTION VIDIGITAL TECHNIQUES AND EQUATION SOLUTIONS
(Continued)B. Numerical Integration (Continued)C. Computational Flow Chart

On the following page is a simplified diagram of the computational scheme for the complete computer program.



SECTION VII
COMPUTER INPUT-OUTPUT

An effort has been made to keep the input and output in conventional parameters. The output consists of parametric histories.

A. Input Format

The following format gives the sequence of the input parameter, their definitions and information concerning quantity, units, etc. The Fortran IV input formats are; for real variables F10.3 and for integer variables I5.

Type	Symbol	Definition	Units
1) <u>Index Settings</u>			
	I1	Type of decelerator; 1-tethered, 0-rigid	
	I2	No. of good integration steps before Δt is increased	
	I3	Planet shape; 1-cblate, 0-spherical	
	I4	Symbolic unit for output	
	I5	Symbolic unit for input	
	I6	No. of values in Mach No. scale (1-8)	
	I7	No. of values in angle of attack scale (1-8)	
	I8	No. of Mach No. values used for decelerator	
	I9	No. of angle of attack used for decelerator	
	I10	No. of stacked trajectory runs	
	I11	No. of differential equations 18-tethered 14-rigid	
	I12	No. of negligible values to reduce from 18-14 DOF	
	I13	No. of iterations per output	
	I14	Inflation: 0-inflation, 1-inflated	
	I15	Program parameter - must be zero	
	I16	Program parameter - must be zero	

SECTION VII
COMPUTER INPUT-OUTPUT
(Continued)

A. Input Format (Continued)

Type	Symbol	Definition	Units
<u>2) Body Aerodynamics</u>			
	M	Mach No. table (I6 values)	-
	α	Angle of attack table (I7 values)	deg.
	C_f	Body aerodynamic coefficient table The following sequence is used:	
		1. Read $C_A(M, \alpha)$ indexing Mach No. then angle of attack.	
		2. Read $C_N(M, \alpha)$	
		3. Read $X_{CP}(M, \alpha)$ from nose	ft.
	C_{lp}	Roll damping coefficient ($C_{lp}(M)$) I8 values	sec/deg.
	C_{mq}	Pitch and yaw damping coefficient ($C_{mq}(M)$) I8 values	sec/deg.
<u>3) Geophysics</u>			
	μ	Universal gravitational term (GM)	ft ³ /sec ²
	R_0	Equatorial radius	ft.
	J_2	Second harmonic constant	-
	g_0	Sea level gravity	ft/sec.
	Ω	Sidereal rotation rate of planet	rad/sec.
	f	Oblateness parameter	-
<u>4) Position</u>			
	t	Time	sec.
	Ψ	Geocentric longitude	deg.
	Φ	Geocentric latitude	deg.
	ϕ	Euler roll angle	deg.
	θ	Euler pitch angle	deg.
	ψ	Euler yaw angle	deg.
	R_n	Range	n. mi.

SECTION VII
COMPUTER INPUT-OUTPUT
(Continued)

A. Input Format (Continued)

Type	Symbol	Definition	Units
5)	<u>Body Rates and Orientation</u>		
	P	Body inertial roll rate	rad/sec.
	Q	Body inertial pitch rate	rad/sec.
	R	Body inertial yaw rate	rad/sec.
	α	Angle of attack	deg.
	β	Angle of sideslip	deg.
	X_{CG}	Center of gravity location from nose	cal.
	Alt	Attitude	ft.
	Vel	Velocity magnitude	ft/sec.

6) Configuration

	m	Mass	slugs
	I_x	Moment of inertia	slug-ft ²
	I_y	Moment of inertia	slug-ft ²
	I_z	Moment of inertia	slug-ft ²
	S'	Body aerodynamic reference area	ft ²
	d	Body aerodynamic reference length	ft.
	h_s	Altitude stop	ft.
	t_s	Time stop	sec.

SECTION VIICOMPUTER INPUT-OUTPUT
(Continued)A. Input Format (Continued)

Type	Symbol	Definition	Units
<u>7) Integration</u>			
	Δt	Initial time increment	sec.
	Δt_{min}	Minimum tolerable step size	sec.
	Δt_{max}	Maximum tolerable step size	sec.
	f	Integration step size factor (usually 2)	-
	$T_{i,lim}$	Error estimate limit table sequence is:	
		Range (1)	n. mi.
		[E] (3)	deg.
		$[\eta, \zeta]$ (2)	deg.
		$[\dot{\eta}, \dot{\zeta}]$ (2)	deg/sec.
		[P] (3)	ft.
		$V_x(\alpha)_s$ (3)	ft/sec.
		$\omega_x(\alpha)_s$ (3)	deg/sec.

Tethered Decelerator (If Required; i.e., if $I_1 = 1$)

C_f	Decelerator aerodynamic coefficient table. The following input sequence is used: 1. Read $C_A(M, \alpha)$ indexing Mach No. then angle of attack. 2. Read $C_N(M, \alpha)$	
X_P	Distance from body centroid to harness point	ft.
X_D	Tether cord length or distance from to decelerator centroid	ft.
m_D	Decelerator mass	slugs
ζ	Decelerator pitch angle	deg.
$\dot{\zeta}$	Decelerator yaw angle	deg.
$\dot{\zeta}$	Decelerator pitch rate	deg/sec.
$\dot{\eta}$	Decelerator yaw rate	deg/sec.
α_{Ds}	Negligibility limit on decelerator pitching motion	-
t_t	Time table for deployment sequence (4 values)	sec.
S_t	Decelerator aerodynamic reference area in accordance with the above table. (4 values)	ft ²

SECTION VII
COMPUTER INPUT-OUTPUT
 (Continued)

A. Input Format (Continued)

The input data sheets are:

Payload

(1) Index:

Format (16I5)

I1 I2 I3 I4 I5 I6 I7 I8 I9 I10 I11 I12 I13 I14 I15 I16

— — — — — — — — — — — — — — — 0 0

(2) Aerodynamics:

Format (8F10.3)

M_N

α

C_A

_____	_____	_____	_____	_____	_____	_____	_____
_____	_____	_____	_____	_____	_____	_____	_____
_____	_____	_____	_____	_____	_____	_____	_____
_____	_____	_____	_____	_____	_____	_____	_____
_____	_____	_____	_____	_____	_____	_____	_____
_____	_____	_____	_____	_____	_____	_____	_____
_____	_____	_____	_____	_____	_____	_____	_____
_____	_____	_____	_____	_____	_____	_____	_____
_____	_____	_____	_____	_____	_____	_____	_____
_____	_____	_____	_____	_____	_____	_____	_____

C_N

_____	_____	_____	_____	_____	_____	_____	_____
_____	_____	_____	_____	_____	_____	_____	_____
_____	_____	_____	_____	_____	_____	_____	_____
_____	_____	_____	_____	_____	_____	_____	_____
_____	_____	_____	_____	_____	_____	_____	_____
_____	_____	_____	_____	_____	_____	_____	_____
_____	_____	_____	_____	_____	_____	_____	_____
_____	_____	_____	_____	_____	_____	_____	_____
_____	_____	_____	_____	_____	_____	_____	_____
_____	_____	_____	_____	_____	_____	_____	_____

SECTION VII
COMPUTER INPUT-OUTPUT
(Continued)

A. Input Format (Continued)

Payload (Continued)

(2) Aerodynamics (Continued):

$\frac{CP}{D}$	_____	_____	_____	_____	_____	_____	_____
	_____	_____	_____	_____	_____	_____	_____
	_____	_____	_____	_____	_____	_____	_____
	_____	_____	_____	_____	_____	_____	_____
	_____	_____	_____	_____	_____	_____	_____
	_____	_____	_____	_____	_____	_____	_____
	_____	_____	_____	_____	_____	_____	_____
	_____	_____	_____	_____	_____	_____	_____
	_____	_____	_____	_____	_____	_____	_____
	_____	_____	_____	_____	_____	_____	_____
C_{lp}	_____	_____	_____	_____	_____	_____	_____
C_{mq}	_____	_____	_____	_____	_____	_____	_____

(3) Geophysics:

Format (8F10.3)

μ	R_0	J_2	g_0	Ω	f
_____	_____	_____	_____	_____	_____

(4) Position:

Format (8F10.3)

t	ψ	ϕ	ϕ	θ	ψ	R_n
_____	_____	_____	_____	_____	_____	_____

(5) Body Rates and Orientation:

Format (8F10.3)

P	Q	R	α	β	χ_0	Alt	Vel
_____	_____	_____	_____	_____	_____	_____	_____

SECTION VII
COMPUTER INPUT-OUTPUT
 (Continued)

A. Input Format (Continued)

Payload (Continued)

(6) Configuration:

Format (8F10.3)

m	I_x	I_y	I_z	S	d	h_s	t_s
_____	_____	_____	_____	_____	_____	_____	_____

(7) Integration:

Format (8F10.3)

	Δt	Δt_{min}	Δt_{max}	f			
	_____	_____	_____	_____			
	u	v	w	p	q	r	ϕ
	_____	_____	_____	_____	_____	_____	_____
T_{lim}	ψ	ϕ	θ	ψ	R_n	$\dot{\zeta}$	$\dot{\eta}$
	_____	_____	_____	_____	_____	_____	_____
	η						

SECTION VIICOMPUTER INPUT-OUTPUT
(Continued)A. Input Format (Continued)Decelerator

Format (8F10.3)

 C_A

_____	_____	_____	_____	_____	_____	_____	_____
_____	_____	_____	_____	_____	_____	_____	_____
_____	_____	_____	_____	_____	_____	_____	_____
_____	_____	_____	_____	_____	_____	_____	_____
_____	_____	_____	_____	_____	_____	_____	_____
_____	_____	_____	_____	_____	_____	_____	_____
_____	_____	_____	_____	_____	_____	_____	_____
_____	_____	_____	_____	_____	_____	_____	_____
_____	_____	_____	_____	_____	_____	_____	_____

 C_N

_____	_____	_____	_____	_____	_____	_____	_____
_____	_____	_____	_____	_____	_____	_____	_____
_____	_____	_____	_____	_____	_____	_____	_____
_____	_____	_____	_____	_____	_____	_____	_____
_____	_____	_____	_____	_____	_____	_____	_____
_____	_____	_____	_____	_____	_____	_____	_____
_____	_____	_____	_____	_____	_____	_____	_____
_____	_____	_____	_____	_____	_____	_____	_____
_____	_____	_____	_____	_____	_____	_____	_____

X_P	X_D	m_D	ζ	η	$\dot{\zeta}$	$\dot{\eta}$	α_{DS}
-------	-------	-------	---------	--------	---------------	--------------	---------------

_____	_____	_____	_____	_____	_____	_____	_____
t_{t1}	t_{t2}	t_{t3}	t_{t4}	S_{t1}	S_{t2}	S_{t3}	S_{t4}
_____	_____	_____	_____	_____	_____	_____	_____

SECTION VIICOMPUTER INPUT-OUTPUT
(Continued)B. Output Format

The program output consists of time histories of the various flight parameters. These flight parameters and their units are given below:

PAYLOAD

TIME	ALT	VELOCITY	MACH NO.	GAMMA
DT	LONG	U	VEL-S	ALPHA
MASS	LAT	V	DYN-PR	BETA
FN	RANGE	W	RHO	XCG
FX	MX	P	IX	PHI
FY	MY	Q	IY	THETA
FZ	MZ	R	IZ	PSI

DECELERATOR

TENSION	BETA	ALPHA	MASS	FA
VELOCITY	ETA	ZETA	HARNESS-L	FN
MACH NO.	ETAD	ZETAD	DYN-PR	CORD-L

PAYLOAD

TIME	-	Flight time (sec)
ALT	-	Altitude (ft)
VELOCITY	-	Relative earth velocity (ft/sec)
MACH NO.	-	Mach No.
GAMMA	-	Flight path elevation (deg)
DT	-	Time increment (sec)
LONG	-	Geocentric longitude (deg)
U	-	Relative velocity along body X axis (ft/sec)
VEL-S	-	Velocity of sound (ft/sec)
ALPHA	-	Angle of attack (deg)
MASS	-	Body mass (slugs)
LAT	-	Geocentric latitude (deg)
V	-	Relative velocity along body Y axis (ft/sec)
DYN-PR	-	Free stream dynamic pressure (lbs/ft ²)
BETA	-	Side slip angle (deg)
FN	-	Normal force (lbs)

SECTION VII
COMPUTER INPUT-OUTPUT
(Continued)

B. Output Format (Continued)

PAYLOAD (Continued)

RANGE	- Range (n. mi.)
W	- Relative velocity along body Z axis (ft/sec)
RHO	- Density (slugs/ft ³)
XCG	- Longitudinal centroid location (ft from nose)
FX	- Body longitudinal aerodynamic force (lbs)
MX	- Aerodynamic moment about body X axis (ft-lbs)
P	- Angular rate about body X axis (deg/sec)
IX	- Moment of inertia I _X (slug-ft ²)
PHI	- Euler bank angle (deg)
FY	- Body normal aerodynamic force, pitch (lbs)
MY	- Aerodynamic moment about body Y axis (ft-lbs)
Q	- Angular rate about body Y axis (deg/sec)
IY	- Moment of inertia I _Y (slug-ft ²)
THETA	- Euler pitch angle (deg)
FZ	- Body normal aerodynamic force, yaw (lbs)
MZ	- Aerodynamic moment about body z axis (ft-lbs)
R	- Angular rate about body Z axis (deg/sec)
IZ	- Moment of Inertia I _Z (slug-ft ²)
PSI	- Euler azimuth angle (deg)

DECELERATOR

TENSION	- Tether cord tension (lbs)
BETA	- Angle of side slip (deg)
ALPHA	- Angle of attack (deg)
MASS	- Decelerator mass (slugs)
FA	- Aerodynamic axial force (lbs)
VELOCITY	- Relative (earth) velocity (ft/sec)
ETA	- Pitch angle (deg)
ZETA	- Yaw angle (deg)
HARNESS-L	- Harness length, behind body CG (ft)
FN	- Aerodynamic normal force (lbs)
MACH NO.	- Mach Number
ETAD	- Pitch angular rate (deg/sec)
ZETAD	- Yaw angular rate (deg/sec)
DYN-PR	- Decelerator dynamic pressure (lbs/ft ²)
CORD-L	- Tether cord length to CG (ft)

NOMENCLATURE

<u>Symbol</u>	<u>Description</u>
X, Y, Z	Position coordinates
$[E]; \phi, \theta, \psi$	Euler angles
$[P]; r, \Phi, \Psi$	Geocentric planet coordinates; radial distance, latitude and longitude
Ω_E	Planet sidereal rotation rate
ζ, η	Tethered decelerator position angles
$\dot{\zeta}, \dot{\eta}$	Tethered decelerator relative pitch and yaw rates
H	Angular Momentum
$[T]$	Matrix transformation
$F_I(\omega)_B$	Sum of forces on the body; body axes components
$M_I(\omega)_B$	Sum of moments on the body; body axes components
m	Body mass
I	Moment of inertia
$V_I(\omega)_B$	Velocity of body relative to inertial space
$V_E(\omega)_B$	Velocity of body relative to the earth
$\omega_I(\omega)_B$	Inertial angular body velocity
$F_I(d)_D$	Sum of forces on the tethered decelerator
$V_I(d)_D$	Velocity of decelerator relative to inertial space
$\omega_I(\omega)_D$	Inertial angular decelerator velocity
$V_E(d)_D$	Velocity of decelerator relative to the earth
T	Tether cable tension force
λ	Flight path heading angle
γ	Flight path elevation

NOMENCLATURE (Continued)

<u>Symbol</u>	<u>Description</u>
h	Altitude
R_ϕ	Local radius of earth
α	Angle of attack
\mathcal{S}	Angle of attack direction cosine
C_A	Aerodynamic axial force coefficient
C_N	Aerodynamic normal force coefficient
X_{CP}	Aerodynamic longitudinal center of pressure location
C_{lp}, C_{mq}	Aerodynamic damping moments
g_0	Acceleration of gravity at sea level
ρ	Atmospheric density
V_s	Velocity of sound
M	Mach Number
q	Dynamic Pressure
X_{CG}	Longitudinal location of centroid from nose
X_P	Distance from body centroid to harness point
X_d	Distance from harness point to decelerator centroid
R_0	Planet equatorial radius

REFERENCES

1. Kolk, Richard W., "Modern Flight Dynamics," Prentice-Hall, Inc., Englewood Cliffs, N. J., 1961.
2. Birklein, K., "Preliminary Mars Trajectory Simulation Program," Goodyear Engineering Report No. GER 11525, March 1964.
3. Earnest, L. D., "Kutta Integration With Step Size Control," MIT Lincoln Laboratory.
4. Isakson, G., "Flight Simulation of Orbital Reentry Vehicles," ASD Technical Report 61-171(I), October 1961.
5. Schuler, J. M. and Pritchard, F. E., "Six Degrees-of-Freedom Equations of Motion for a Maneuvering Reentry Vehicle," Technical Report: NAVTRADEVCEEN801A, U. S. Naval Training Device Center, Port Washington, New York, June 1962.
6. Dennison, A. J. and Butler, J. F., "Missile and Satellite Systems Program for IBM 7090," General Electric Report No. 61SD170, February 1962.
7. Schlemmer, J. W. and Campbell, D. E., "A General Six Degrees of Freedom Trajectory Model for an IBM 11410 Digital Computer," Goodyear Engineering Report No. GER 10614, March 1962.